Soft condensates in hard confinement

– Structure and molecular mobility –

Mark Busch

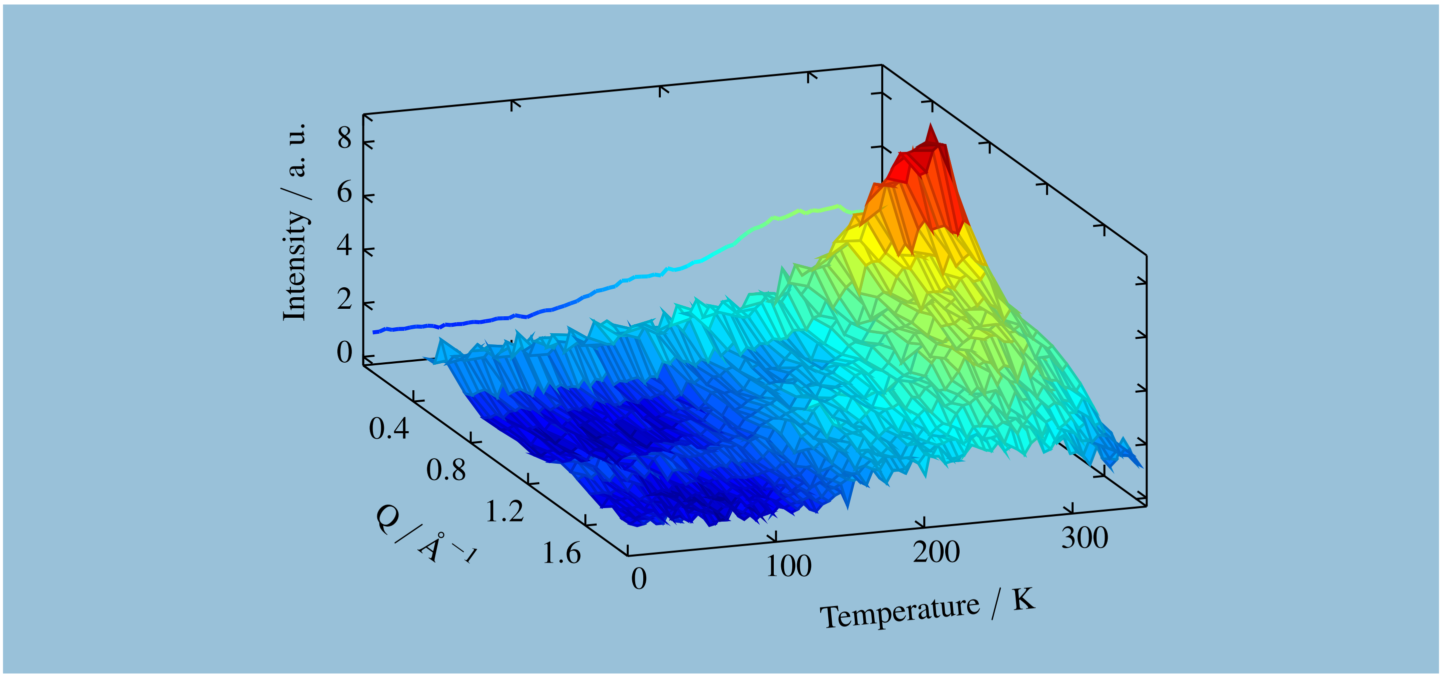

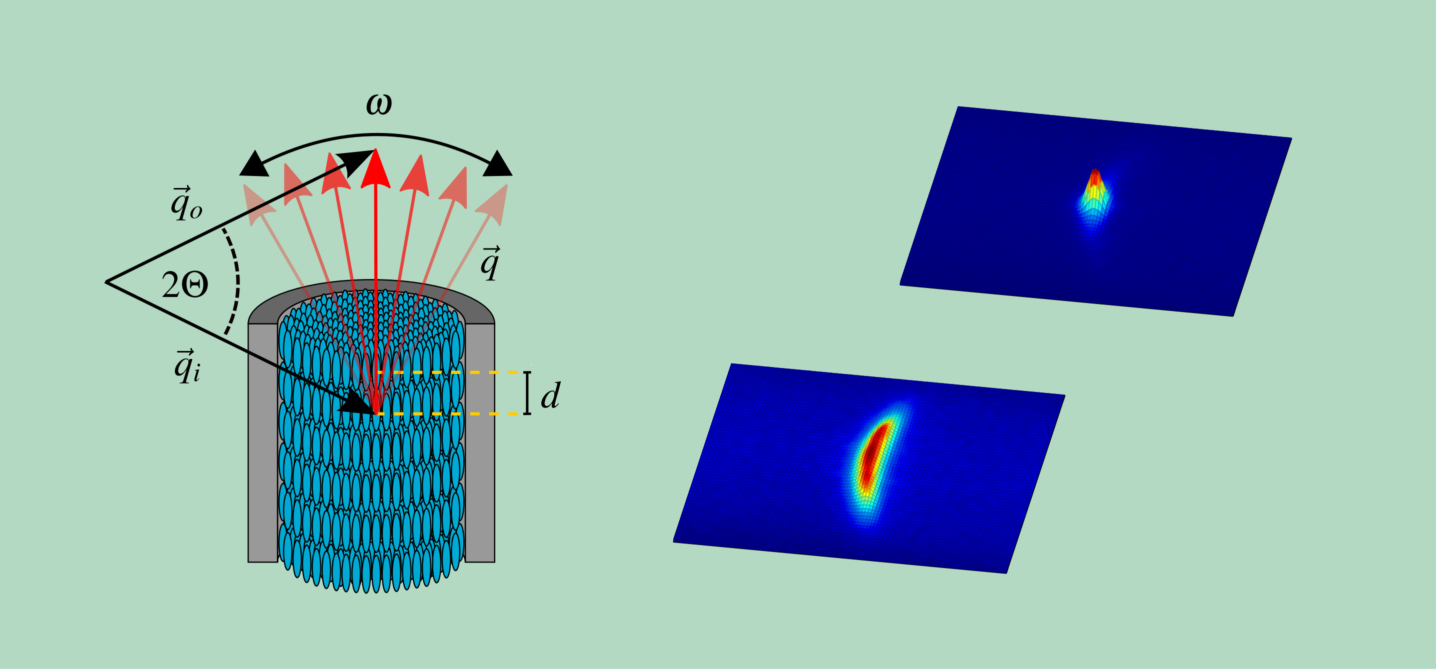

Digital Object Identifier (DOI):
10.15480/882.2546

Uniform Resource Name (URN):
urn:nbn:de:gbv:830-882.059855

Soft condensates in hard confinement
– Structure and molecular mobility –

Vom Promotionsausschuss der
Technischen Universität Hamburg

zur Erlangung des akademischen Grades

Doktor der Naturwissenschaften (Dr. rer. nat.)

genehmigte Dissertation

von

Hans Mark Busch

aus

Saarbrücken

2019

Gutachter:
Prof. Dr. rer. nat. Patrick Huber (Technische Universität Hamburg)
Prof. Dr. rer. nat. Andreas Schönhals (Technische Universität Berlin)

Vorsitz des Prüfungsausschusses:
Prof. Dr.-Ing. Bodo Fiedler (Technische Universität Hamburg)

Tag der mündlichen Prüfung: 16.12.2019

Summary

The properties of soft matter in the nanoscopic constriction within the voids of surrounding hard condensed matter are investigated. In this context the focus lies on its characteristics concerning the structure and the molecular mobility, dividing this work into two parts:
In the first part the cation self-diffusion dynamics of the room-temperature ionic liquid 1-N-butylpyridinium bis((trifluoromethyl)sulfonyl)imide ([BuPy][Tf_2N]) within the nanopores of carbide-derived carbons of different pore sizes are studied as a function of temperature using quasi-elastic neutron spectroscopy methods. It is shown that already the analysis of data from so-called fixed window scans, which allow a rapid investigation of a large temperature range, while acquiring one energy transfer value only, delivers a quite comprehensive picture of the confinement-induced changes of the cation's molecular dynamics. This is confirmed by the information gained from full spectroscopic data from two instruments with practically complementary dynamic range and resolution. These data reveal the existence of two translational diffusive processes, deviating by around one order of magnitude and obeying an Arrhenius temperature behaviour. Furthermore, the dynamics appear to slow down with decreasing confinement size. The ionic liquid confined in the nanoporous carbon is found to exhibit some molecular mobility already well below the melting point of the bulk liquid, but in contrast there is also a fraction of immobile cations at all investigated temperatures — even far above the bulk melting point.
The second part of this thesis analyses the structure and phase transition behaviour of two chiral thermotropic liquid crystals inside cylindrical polymer-surface-coated anodic aluminium oxide nanochannels (AAO) of different diameters. For the liquid crystal CE6 it is found that the chiral nematic $\rightleftharpoons$ smectic A* transition is continuous in the nanopores, while being of first order in the bulk state. In addition, the phase transition temperature is shifted to higher temperatures with decreasing confinement size. Furthermore, the critical exponent related to the smectic translational order parameter is determined for transitions in nanochannels of different diameter. In the case of the liquid crystal 2MBOCBC, its structure within the AAO nanochannels is investigated using neutron diffraction. On the transition from the smectic A* to the smectic C* phase the gradual formation of a rotational symmetric chevron-like smectic layer structure of the liquid crystal within these nanochannels is found. This process is fully reversible upon temperature cycling.

Contents

CHAPTER 1

Motivation

The control of soft condensed matter on the nanoscale has gained notable attention in recent years. A substantial fraction of research in this field is dedicated to investigate and control the properties of soft matter in the nanoscopic constriction within the voids of surrounding hard condensed matter. While this may appear to be only of academic interest on the first view, more and more technological applications arise. Nanopores serve for instance as sensors for the detection of complex molecules, like proteins, antigens and antibodies, viruses and DNA.[82, 96, 181, 197, 248] Especially the sequencing of DNA with recently available nanopore-based devices, allowing a fast, cheap and mobile DNA analysis, has been much noticed.[82] Not only for such applications the control of liquid flow through nanochannels is crucial. In this connection, there is the potential to build valves, pumps and other devices, influencing the liquid flow on the nanoscale or even generate electric energy from the liquid flow, on the basis of nanoporous materials.[123, 127, 254, 289] Drug delivery is another potential application, where nanopores can be loaded with hydrophilic as well as hydrophobic active agents and is well-suited for topical medication.[223, 256, 294] Due to their high surface-to-volume ratio, nanoporous materials are also very promising for the use as catalysts.[261, 265, 282] With regard to chemical reactions, there is even the possibility to do single molecule electrochemistry.[96] Other fields of application include the production of nanostructured materials utilising nanoporous templates [142, 257] or the use as mechanical sensors and actuators [62, 260]. Also for applications in photonics nanoporous materials are of relevance.[193, 233, 235] For instance there is the possibility to build lasers, whose wavelength can be tuned by influencing the structure of a liquid crystal in a confining pore space with an electric field.[193] As a last example of this non-exhaustive enumeration of potential applications of systems based on the interplay of soft condensed matter and nanoporous materials, devices for energy conversation and storage shall be mentioned. In that field their usage comprises fuel cells [64, 263], batteries [23, 46, 63, 188] and so-called super- or ultracapacitors [23, 46, 199, 250, 295, 297], all benefiting amongst others of the high specific surface area of nanoporous materials.

All the above mentioned applications have in common that their realisation requires a profound knowledge of the interaction of the soft matter with the hard confining walls as well as about the alterations of the structure, phase transition behaviour, dynamics and changes of other properties, induced by the nanometre-sized spatial restriction. This work is focussed to fundamental research on selected aspects of two different kinds of such systems, dividing this document into two parts.

The first part of this work is about the molecular dynamics of a room-temperature ionic liquid inside the nanometre-sized cavities of porous carbon. These salts, being liquid under ambient conditions, in combination with nanoporous carbon are regarded as possible candidates for the application in future high-performance electric energy storage devices. The self-diffusion and other dynamics of the ionic liquid within the carbon mirco- and mesopores, i.e. pores with less than 2 nm width and such between 2 nm and 50 nm [232], are studied employing quasi-elastic neutron spectroscopy methods.

In the second part of this thesis the focus is on the structure of chiral liquid crystals, when being restricted in nanochannels in contrast to the unconfined case. Of special interest in this connection is the temperature-dependent evolution of their structure, as well as their phase transition behaviour. This is investigated using X-ray and neutron diffraction methods.

Part I.

Molecular mobility

CHAPTER 2

Introduction to the dynamics of ionic liquids

In this first part the molecular mobility of an ionic liquid confined in the nanopores of carbon materials is investigated. This is predominantly done using quasi-elastic neutron scattering (QENS). This method is based on the analysis of the energy and momentum transfer of neutrons when being scattered at the molecules under investigation. Quasi-elastic scattering refers here to the fact that the energy transfer during the scattering process is low, i.e. the neutrons are almost elastically scattered. The reason why low-energy neutrons are chosen here is that their energy is comparable to the energies of molecular motions in soft matter and therefore the energy transfer when scattered at molecules in motion can be well measured. The wavelength of these neutrons is in the range of interatomic distances in condensed matter and gives therefore the additional possibility to gain structural information from these measurements. The fact that neutrons have no electric charge is furthermore essential, especially when dealing with charged matter like the ionic liquids investigated, here. In contrast to the X-rays scattering power, which increases with the number of electrons of an atom, i.e. with its atomic number, there is no such relation for the neutron scattering power. The latter varies seemingly randomly from isotope to isotope, which enables one to investigate also light elements in the presence of considerably heavier ones. This can be quite important for the investigation of soft matter, predominantly consisting of light elements, confined in hard condensates which might be composed of elements with comparably large atomic numbers.

2.1. Motivation

Despite the fact, that carbon-nanoconfined ionic liquids are interesting systems regarding their physical properties from a fundamental point of view, their investigation is additionally motivated by their prospective application in high-performance electric energy storage devices, such as electric double layer capacitors — so-called super- or ultracapacitors.[23, 46, 71, 250, 295, 297] These are expected to unite the power density of conventional capacitors with the energy density of batteries. Thus, these quickly chargeable devices are well-suited electric power supplies for a variety of applications, especially mobile ones. The choice of room-temperature ionic liquids in this connection is motivated by numerous advantages in comparison to other potential electrolytes. Their low volatility, good temperature stability and wide electrochemical window are just some of them.[6, 236, 250, 272, 297] The good (electro-)chemical stability, high electrical conductivity and large specific surface area motivate the use of nanoporous carbons as electrode material.[45, 46, 249] Furthermore, their pore size and shape, as well as their surface chemistry are well-tunable.[67, 70, 249]

Although, these systems are a very active field of research, the actual technical implementation as high-performance supercapacitors still remains challenging. One of the reasons is the relatively high viscosity of the ionic liquids [209, 236, 298], which results in slow ion dynamics — also already in the bulk.[218, 236] Intuitively, one might expect that the situation will be even worse within the nanopore restriction. However, there are some investigations finding increased dynamics for ionic liquids in carbon nanoconfinement [15, 39, 43, 44], while other studies indeed see a distinct slowdown of the ion motions.[69, 70, 180, 251] An additional detrimental effect on the ion mobility in nanopores, is the tendency of ionic liquids to form immobilised layers at the pore walls, while molecules within micropores often do not exhibit any discernible diffusion motion, anymore.[9, 43, 44, 68, 69] As a consequence the amount of mobile ions in relation to the total nanopore volume is reduced, which potentially diminishes the performance of such supercapacitors, since there the charge transfer involves diffusive processes.[88, 155]

In this connection, it becomes clear that it is essential to obtain a profound knowledge of the self-diffusion properties of ionic liquids in carbon nanoconfinement. It is obvious that investigations in this respect need to address the pore-size dependence of these dynamics, also in particular with regard to the above mentioned immobilised ion layers. However, there is another reason to have a look at different pore sizes. Interestingly, it is found that the capacitance of electrical double layer capacitors based on ionic liquids depends non-monotonically [81, 139, 176, 287], but in an oscillatory manner, on the pore width.[81, 139, 287] Thus, with respect to the pore size, the best trade-off between ion mobility and capacitance needs to be found. Another problem, with regard to the application of such supercapacitors is, that a decreasing temperature leads to a further slowdown of the ion dynamics and additionally the range of the liquid phase in the bulk state is usually quite limited for ionic liquids with respect to lower temperatures.[43, 236, 268, 297, 298] But it is known that nanoconfinement can change their phase transition behaviour.[107, 144, 285]

As a consequence of the above enlisted challenges, this work aims to contribute to their handling by studying the self-diffusion properties of an ionic liquid within carbon nanopores as a function of temperature and pore size.

2.2. Bulk ionic liquids and their heterogeneity

Before giving an overview of the current state of knowledge about room-temperature ionic liquids in nanoconfinement, the bulk state shall be shortly illuminated, since it exhibits some interesting peculiarities, which are of importance for the understanding of the dynamics in confining geometries. Diffraction patterns of ionic liquids commonly show two or three characteristic peaks [38, 146, 269], as exemplarily shown in the X-ray diffraction pattern of 1-N-butylpyridinium bis((trifluoromethyl)sulfonyl)imide in figure 2.1. These hint at certain kinds of molecular order within these ionic liquids. The peak at higher wave vector trans-

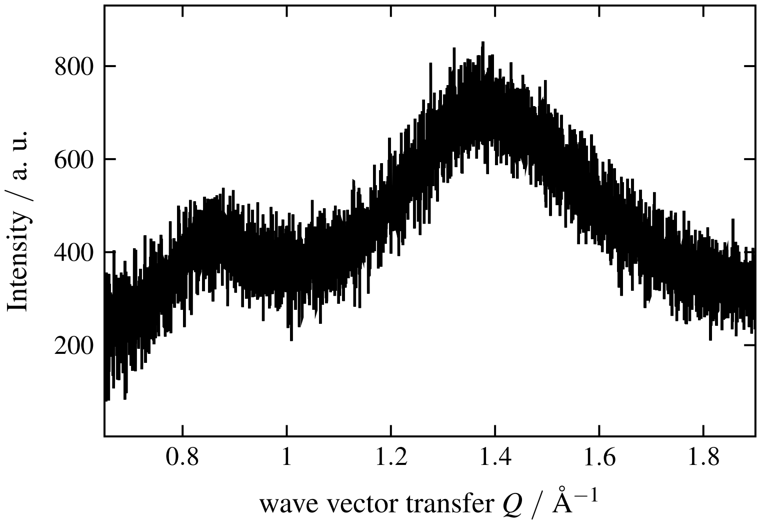

Figure 2.1.: X-ray diffraction pattern of the ionic liquid 1-N-butylpyridinium bis((trifluoromethyl)sulfonyl)imide ([BuPy][Tf$_2$N]) as a function of wave vector transfer Q, measured under ambient conditions.

fers Q is related to inter- and intramolecular adjacency correlations between neighbouring atoms.[4, 5, 191] The intermediate diffraction peak occurs often around 0.9 Å^{-1} and reflects the charge alternation within the ionic liquid, where especially anion–anion, cation head–cation head correlations and such between cation heads and anions contribute.[5, 146, 191] The first of these peaks, which often appears around $Q = 0.4$ Å^{-1} and below, is usually referred to as pre-peak or first sharp diffraction peak.[5, 38, 191] Contrary to the other two peaks [191], its position, width and intensity are usually relatively strongly influenced by the length of the alkyl tails.[4, 191, 270] With increasing length the peak sharpens, gains intensity and is shifted to lower Q-values [4, 191, 270], indicating an increase of the corresponding correlation length. While the existence of a pre-peak is not unique to ionic liquids [5, 38], its interpretation is controversial. Its origin is often ascribed to structural heterogeneities on the nanoscale [5, 191, 270], represented by the alternation of polar and apolar domains.[5, 37] In contrast, others ascribe the appearance of the pre-peak predominantly to the anisotropy of the ions, leading to a local distortion of their packing.[4, 119, 120, 146] Nevertheless, the existence of domains on the nanoscale in ionic liquids appears to be supported by numerous investigations [16, 28, 29, 37, 83, 191, 270, 290], while their presence is no necessary condition for the existence of a pre-peak.[4, 38]

The nanostructuration of ionic liquids has impact on various of their properties, especially on their molecular dynamics.[5, 16, 28, 29, 83, 121, 126, 191, 269, 270] Quasi-elastic neutron scattering experiments reveal that the translational diffusion of cations within an ionic liquid occurs not only as a single particle motion, but also involves a collective ion movement in the form of ionic aggregates, in coincidence with respective findings on the structure of the ionic liquid.[28, 29] As a consequence, the translational diffusion is found to be heterogeneous, as illustrated in figure 2.2: On the one hand, the cations can diffuse in the interspace between

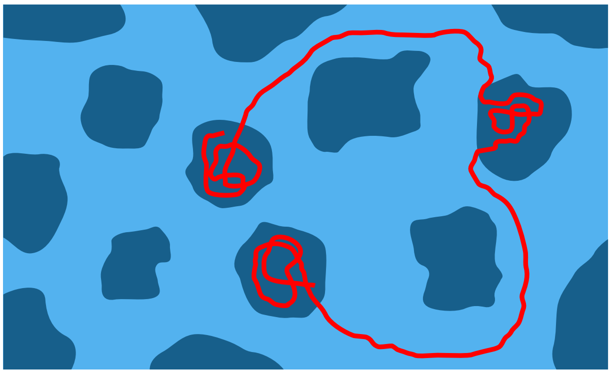

Figure 2.2.: Illustration of heterogeneous translational cation diffusion model in ionic liquids as proposed by Burankova et al. [30] / Ferdeghini et al. [83]: Cations diffuse (red line) localised within ionic aggregates (dark blue) and on longer distances in regions with lower density in between (light blue).

regions of higher density formed by ionic aggregates, resulting in an effectively longer path length, due to their meandering movement and therefore entail an apparently slower diffusion on the long distance.[16, 83] On the other hand, some cations also exhibit a diffusive motion within these aggregates and collectively with these clusters.[16, 28, 30, 83] This dynamical heterogeneity is also seen as an explanation for the deviating diffusion coefficients obtained with different techniques, like quasi-elastic neutron scattering, nuclear magnetic resonance spectroscopy (NMR) or dynamic light scattering, probing the molecular dynamics on different time scales.[15, 16, 83] In this way, NMR for instance delivers considerably smaller self-diffusion coefficients compared to QENS, since the measured time scale is orders of magnitude smaller in the latter case.[15, 16, 76, 83, 267] Certainly, the above described division into ion clusters and unbound ions is no static setting, but the cations bound within these aggregates can be dissolved again, like those initially diffusing in the free space in between might get trapped within such dense cation accumulations.[16, 28, 80, 83] Thus, the actual diffusive process in ionic liquids is more complex and additionally complicated through the fact that cations and anions have not necessarily the same translational diffusion dynamics, what amongst others originates from the different sizes of the two species and the heterogeneous cation environment.[191, 211, 271]

2.3. Ionic liquids in nanoconfinement

Investigations on ionic liquids in carbon nanotubes, which find increased translational self-diffusion dynamics, explain these faster motions with the disturbance of the ionic nanostructure.[15, 214] This argumentation is supported by the fact that the short range dynamics obtained by QENS remain practically unaltered under the confinement, while the diffusion on longer time scales, analysed by NMR, is increased.[15] This effect is stronger for an ionic liquid with a higher degree of self-organisation.[15] Other studies, also seeing an increased translational dynamic in the nanoconfinement of ordered mesoporous carbon, give further

possible reasons for the faster dynamics, such as structural changes induced by the pore walls and a lower cation concentration in the center region of the pores.[43, 44] Since they also find an appreciable fraction of immobile ions, which are attributed to molecules adsorbed at the pore walls [43, 44], an influence of the interplay between the ionic liquid and the pore walls on the structure and dynamics seems to make sense. Interestingly, two translational diffusive processes on the time scale of the applied QENS technique are found, here — both faster or comparable with the bulk dynamics, depending on the temperature.[43, 44]
Some molecular dynamics simulations of ionic liquids in carbon nanotubes in contrast find slower dynamics.[180, 203, 251, 252] Also here heterogeneous dynamics are observed: With decreasing distance to the tube walls, the molecules are showing considerably slower diffusion than those in the pore center, whose diffusivity can tend towards the bulk value.[180, 252] This is accompanied by an increased density of the molecules near the pore walls.[180, 252] Experimental studies and molecular dynamics simulations at an ionic liquid in hierarchical nanoporous carbon find a densification at the pore surface and especially within micropores, which is attributed to an interaction with the pore wall.[9, 10] It is known that the confinement in such small, conductive pores can lead to a disturbance of the ion coordination structure, going along with the breaking of the Coulombic charge ordering.[97, 153, 154, 199]
Like in the carbon nanoconfinement, studies of ionic liquids in silica nanopores also find no uniform picture concerning the impact of the nanopore restriction on the liquid's dynamics. While some find that these are slowed down in pores [129, 201], others find practically bulk-like dynamics [107] or even an increased molecular mobility [128]. The latter is observed with broadband dielectric spectroscopy at relatively low temperatures only, while at higher temperatures practically no difference is seen.[128] An investigation studying the dynamics of an ionic liquid in nanoporous silica as obtained by thermal oxidisation of porous silicon with untreated and silanised surface supports the above thesis of the influence of the pore wall surface on the molecular dynamics.[129] Although, in both cases the self-diffusion coefficients are lower than in the bulk ionic liquid, the respective one in the silanised silica nanopores is considerably higher than the one in the untreated pores.[129] This is attributed to the interaction of the molecules of the liquid with the hydrophilic silicon oxide of the non-silanised pore walls, which leads to the formation of bound surface layers.[129] In contrast, the latter are expected to be thinner and less strongly bound, i.e. more mobile, in the case of the modified pore surface.[129] However, it is clear that this effect depends on the particular chemistry of the ionic liquid and the pore surface. Thus, it is not surprising, that in the case of a different ionic liquid, no apparent difference in the dynamics between the both silica pore systems from above is found.[128] Also for the nanopores of carbide-derived carbons there are indications that see an influence of the surface chemistry on the mobility of the ionic liquid molecules within the pores.[69, 70] These hint at increased dynamics in the case of an oxidised pore surface, in comparison to a defunctionalised one.[69, 70] However, the data set is still relatively limited in this regard.

CHAPTER 3

Theory of neutron spectroscopy

In this chapter a short introduction into the physics behind neutron spectroscopy is given. Starting with some basic properties of neutrons and their scattering at nuclei, it is continued with answering the question, how it is possible to draw inferences from the scattered neutrons about the molecular dynamics of the system under investigation. Concluding, the characteristic form of the received spectra for specific molecular dynamic motions is given, as well as for their superposition.

3.1. Neutrons

Neutrons are nuclear particles, which are usually bound in the atomic cores. Free neutrons can for example be obtained through nuclear fission in nuclear reactors or by spallation, when shooting particles, e.g. protons from an accelerator, on them. In both cases the resulting free neutrons have a relatively high kinetic energy. Since for spectroscopic experiments the energy of the neutrons should be in the order of magnitude of those of the molecular dynamics and furthermore, especially for diffraction experiments, their wavelength needs to be in the range of the interatomic distances of the investigated condensed matter, the kinetic energy of the neutrons needs to be lowered. This is for instance done through moderation of the neutrons in liquid D_2O or for even 'colder' neutrons, i.e. with even lower energy, through a successive moderation with liquid deuterium. The energy of the neutrons is lowered through collisions with the moderator material. This results in neutrons having a Maxwellian distribution, when being in thermal equilibrium with the moderator.[13] A remarkable fact is that the neutrons used in spectroscopy experiments, like those presented in this work, have a velocity in the order of magnitude of meters per second. The fact that free neutrons are not stable is nevertheless no problem in this regard, because their lifetime of around 15 minutes [220] is still more than sufficient for conducting the experiments.
Neutrons possess no electric net charge and a very small, possibly vanishing [8, 222] electric dipole moment. This is an important fact, especially when neutrons are used as a probe to investigate charged matter, since they are insensitive to its charge distribution. That the neutrons possess a spin of $1/2$ and a magnetic moment, gives rise to further interesting experimental possibilities — also in neutron spectroscopy — which, however, are not of relevance for this work.

3.2. Neutron scattering cross sections

Neutrons approaching an atomic nucleus are either absorbed or scattered by that core. Here, the interaction takes place via magnetic and nuclear forces, while the latter is comparatively short-ranged in respect to the size of the nucleus and the wavelength of neutrons used in spectroscopy experiments.[13] As a consequence, the interaction potential between a neutron of mass m at a position $\vec{r}$ and a nucleus at r_j can be described by the Fermi pseudopotential

$$V(\vec{r}-\vec{r}_j) = \frac{2\pi\hbar^2}{m} b_j \delta(\vec{r}-\vec{r}_j) \tag{3.1}$$

and thus the scattering process at a bound atom (or ion) can be characterised by a single complex parameter, the bound scattering length b_j, also denoted as scattering amplitude.[13, 242, 258] Its imaginary part is related to the absorption process, while its real part is positive for an attractive interaction and negative for a repulsive one.[242] From this bound scattering length the coherent and incoherent bound cross sections, σ_{coh} and σ_{inc}, are derived:

$$\sigma_{\text{coh}} = 4\pi \langle b \rangle^2 \tag{3.2}$$

$$\sigma_{\text{inc}} = 4\pi \left(\langle b^2 \rangle - \langle b \rangle^2 \right) \,, \tag{3.3}$$

with the total bound scattering cross section

$$\sigma = \sigma_{\text{coh}} + \sigma_{\text{inc}} \,.[13] \tag{3.4}$$

The angle brackets $\langle \ldots \rangle$ denote an averaging over all spin states of the neutron and the nucleus, as well over all isotopes of a given sample.[13, 241, 242] The absorption cross section is given by

$$\sigma_{\text{a}} = \frac{4\pi}{k_0} \langle \text{Im}(b) \rangle \,, \tag{3.5}$$

with k_0 being the wave vector magnitude of the incident neutrons.[242] The dependence of the scattering power on the actual isotope, the neutron is scattered by, represents an important difference compared to X-ray scattering. While for the latter it increases monotonically with increasing atomic number, for neutrons it varies seemingly erratically from one isotope to another. The corresponding values for neutron scattering have been tabulated by Sears [242].

3.3. Differential scattering cross sections

The probability for an incident neutron with energy E_0 to be scattered into a solid angle element $\mathrm{d}\Omega = \sin(\Theta)\ \mathrm{d}\Theta\ \mathrm{d}\phi$ and to suffer an energy transfer such that its final energy lies between E_1 and $E_1 + \mathrm{d}E_1$, is given by the differential scattering cross section

$$\frac{\partial^2 \sigma(E_0, E_1, \Theta)}{\partial\Omega\, \partial E_1} \,.[186, 258] \tag{3.6}$$

This situation is illustrated in figure 3.1. First, the case of elastic scattering shall be considered,

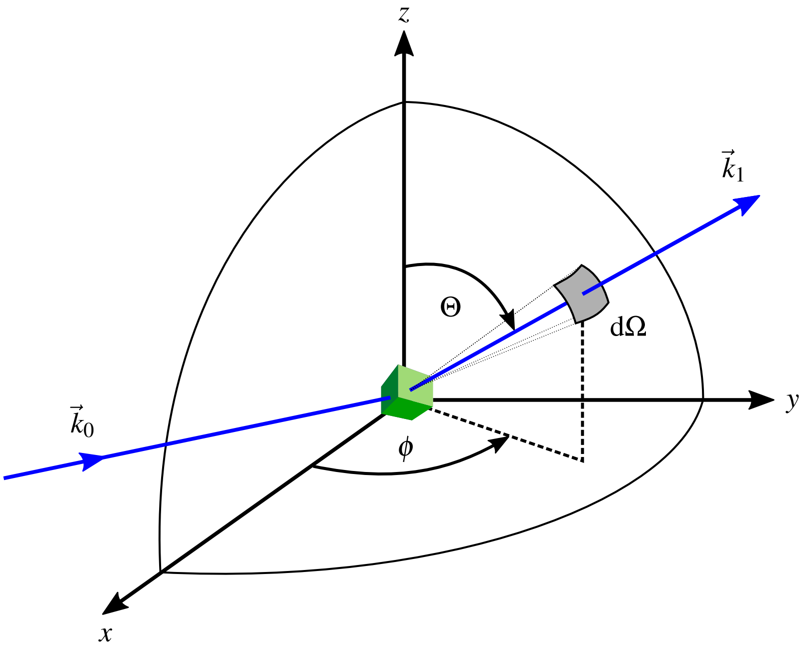

Figure 3.1.: Geometry of the scattering process at a target of a wave with the incident wave vector $\vec{k}_0$ and the outgoing wave vector $\vec{k}_1$ into the solid angle element $\mathrm{d}\Omega = \sin(\Theta)\ \mathrm{d}\Theta\ \mathrm{d}\phi$.

i.e. without the occurrence of any energy transfer. After Fermi's Golden rule the probability for the wave vector $\vec{k}_0$ of the neutron to be transferred to $\vec{k}_1$, with $E = \hbar\vec{k}_0^2/2m = \hbar\vec{k}_1^2/2m$, is given by

$$W_{\vec{k}_0\to\vec{k}_1} = \frac{2\pi}{\hbar}\left|\int \mathrm{d}\vec{r}\ \Psi^*_{\vec{k}_1} V \Psi_{\vec{k}_0}\right|^2 \cdot \rho_{\vec{k}_1}(E)\ .[186] \tag{3.7}$$

Here, $\Psi_{\vec{k}_l}$ (with $l = 0,1$) denote the wave functions

$$\Psi_{\vec{k}_l} = \frac{1}{L^{3/2}} \exp\left(i\vec{k}_l\vec{r}\right)\ , \tag{3.8}$$

normalised to the volume L^3 and with $\mathrm{d}\vec{k}_1 = k_1^2\ \mathrm{d}\Omega\ \mathrm{d}k_1 = k_0^2\ \mathrm{d}\Omega\ \mathrm{d}k_0$,

$$\rho_{\vec{k}_1}(E) = \left(\frac{L}{2\pi}\right)^3 \frac{\mathrm{d}\vec{k}_1}{\mathrm{d}E} = \left(\frac{L}{2\pi}\right)^3 \frac{mk_0}{\hbar^2}\ \mathrm{d}\Omega \tag{3.9}$$

describes the density of the final states after scattering.[186]
The cross section $\mathrm{d}\sigma$ is given by the quotient of the transition probability $W_{\vec{k}_0\to\vec{k}_1}$ and the flux of the incident neutrons $\hbar k_0/mL^3$:

$$\mathrm{d}\sigma = \left(\frac{mL^3}{2\pi\hbar^2}\right)^2 \left|\int \mathrm{d}\vec{r}\ \Psi^*_{\vec{k}_1} V \Psi_{\vec{k}_0}\right|^2 \mathrm{d}\Omega = \left|\left\langle \vec{k}_1 \middle| V \middle| \vec{k}_0 \right\rangle\right|^2 \mathrm{d}\Omega\ .[186] \tag{3.10}$$

Let H_0 be the Hamiltonian of the undisturbed system with eigenfunctions Ψ_n and associated energies E_n, such that

$$H_0\Psi_n = E_n\Psi_n \text{ .[258]} \tag{3.11}$$

The corresponding eigenvector to the state of the target is denoted as $|n\rangle$ with $\sum_n |n\rangle\langle n| = 1$ and hence the initial state of the initial, undisturbed system, i.e. of neutron and target, is written as $|\vec{k}_0\, n_0\rangle$.[186] Together with the momentum p_n of the neutron with mass m, and the interaction potential V between the nuclei and the scattered neutron, the total Hamiltonian of the system is expressed as

$$H = H_0 + \frac{p_n^2}{2m} + V \text{ .[258]} \tag{3.12}$$

The scattering process causes a change of the neutron's momentum from $\hbar\vec{k}_0$ to $\hbar\vec{k}_1$, where $\vec{k}$ is denoting the wave vector of the neutron and $\vec{Q} = \vec{k}_0 - \vec{k}_1$ is referred to as the scattering vector. Likewise its energy changes, such that

$$\hbar\omega = E_{n_1} - E_{n_0} = \frac{\hbar^2}{2m}\left(\left|k_1^2\right| - \left|k_0^2\right|\right) \tag{3.13}$$

gives the energy that is transferred between the neutron and the scattering nucleus.[258]
The partial differential cross-section, considering momentum and energy transfer, is described by

$$\frac{\partial^2\sigma\left(E_0, E_1, \Theta\right)}{\partial\Omega\, \partial E_1} = \frac{k_1}{k_0}\, \overline{\sum_{n_0,n_1} p_{n_0} \left|\left\langle \vec{k}_1\, n_1 \middle| V \middle| \vec{k}_0\, n_0 \right\rangle\right|^2 \delta\left(\hbar\omega + E_{n_0} - E_{n_1}\right)} \quad , \tag{3.14}$$

known as the first Born approximation, with $\sum_{n_0} p_{n_0} = 1$, where p_{n_0} is the statistical weight of the state n_0.[186] The horizontal bar over the above expression denotes the averaging over parameters relevant for the scattering process, such as orientation of the nuclear spin or the distribution of isotopes within the scatterer.[186]

3.4. Intermediate scattering function and scattering laws

The interaction of the neutrons with a target consisting of multiple nuclei with positions $\vec{R}_j$ is described by the potential

$$\frac{m}{2\pi\hbar^2} V(\vec{r}) = \sum_j V_j(\vec{r} - \vec{R}_j) \text{ .[186]} \tag{3.15}$$

With

$$\langle \vec{k}_1 | V | \vec{k}_0 \rangle = \sum_j V_j(\vec{Q}) \cdot e^{i\vec{Q}\vec{R}_j} \tag{3.16}$$

and

$$V_j(\vec{Q}) = \int \mathrm{d}\vec{r}\; e^{i\vec{Q}\vec{R}_j} \tag{3.17}$$

equation 3.14 becomes to

$$\frac{\partial^2\sigma}{\partial\Omega\,\partial E_1} = \frac{k_1}{k_0}\,\overline{\sum_{n_0,n_1} p_{n_0} \left|\left\langle n_1 \left| \sum_j V_j(\vec{Q}) e^{i\vec{Q}\vec{R}_j} \right| n_0 \right\rangle\right|^2}\,\delta\left(\hbar\omega + E_{n_0} - E_{n_1}\right) \quad .[186] \tag{3.18}$$

With the Fourier representation of the δ-distribution

$$\delta\left(\hbar\omega + E_{n_0} - E_{n_1}\right) = \frac{1}{2\pi\hbar}\int_{-\infty}^{\infty} \mathrm{d}t\; e^{-i\frac{t}{\hbar}(\hbar\omega + E_{n_0} - E_{n_1})} \tag{3.19}$$

and the Hamiltonian H_0 (see equation 3.11), one obtains [186, 258]

$$\begin{aligned}
\frac{\partial^2\sigma}{\partial\Omega\,\partial E_1} &= \frac{k_1}{k_0}\frac{1}{2\pi\hbar}\int_{-\infty}^{\infty} \mathrm{d}t\; e^{-i\omega t}\, \overline{\sum_{n_0,n_1} p_{n_0} \left\langle n_0 \left| \sum_j e^{-i\vec{Q}\vec{R}_j} V_j^{\dagger}(\vec{Q}) \right| n_1 \right\rangle} \\
&\qquad \cdot \overline{\left\langle n_1 \left| \sum_{j'} e^{i\frac{t}{\hbar}H_0} V_{j'}(Q) e^{i\vec{Q}\vec{R}_{j'}} e^{-i\frac{t}{\hbar}H_0} \right| n_0 \right\rangle} \\
&= \frac{k_1}{k_0}\frac{1}{2\pi\hbar}\int_{-\infty}^{\infty} \mathrm{d}t\; e^{-i\omega t}\, \overline{\sum_{j,j'} \left\langle e^{-i\vec{Q}\vec{R}_j(0)} V_j^{\dagger}(\vec{Q},0) V_{j'}(\vec{Q},t) e^{i\vec{Q}\vec{R}_{j'}(t)} \right\rangle} \quad .
\end{aligned} \tag{3.20}$$

For the last step the expression

$$V_j(\vec{Q},t) e^{i\vec{Q}\vec{R}_j(t)} = e^{i\frac{t}{\hbar}H_0} V_j(\vec{Q}) e^{-i\frac{t}{\hbar}H_0} e^{i\frac{t}{\hbar}H_0} e^{i\vec{Q}\vec{R}_j} e^{-i\frac{t}{\hbar}H_0} \;, \tag{3.21}$$

using time-dependent Heisenberg operators, and for the thermal average the notation $\langle \ldots \rangle = \sum_{n_0} p_{n_0} \langle n_0 | \ldots | n_0 \rangle$ has been used.[186, 258] The expression within the brackets is called correlation function.[186] Considering the thermal averaging being independent of the one over nuclear spin orientations and distributions, as well as from the nuclei type, one yields

$$\frac{\partial^2\sigma}{\partial\Omega\,\partial E_1} = N\frac{k_1}{k_0}\overline{\left|V_j(\vec{Q})\right|^2}\, \underbrace{\frac{1}{2\pi\hbar N}\int_{-\infty}^{\infty} \mathrm{d}t\; e^{-i\omega t} \sum_{j,j'} \left\langle e^{-i\vec{Q}\vec{R}_j(0)} e^{i\vec{Q}\vec{R}_{j'}(t)} \right\rangle}_{\equiv S(\vec{Q},\omega)} \tag{3.22}$$

for a scattering target consisting of N particles.[186] $S(\vec{Q},\omega)$ is the response function, often also denoted as dynamic structure factor or coherent scattering law, and possesses the dimension of reciprocal energy.[186] The summation $N^{-1}\sum_j$ can be omitted, if the scattering nuclei j are equal.[258]
The term

$$I(\vec{Q},t) = \frac{1}{N}\sum_{\substack{j=1\\ j'=1}}^{N} \left\langle e^{-i\vec{Q}\vec{R}_j(0)} e^{i\vec{Q}\vec{R}_{j'}(t)} \right\rangle \tag{3.23}$$

within $S(\vec{Q},t)$ in equation 3.22 is denoted as intermediate scattering function.[258] While it describes the interaction between neutrons scattered at different nuclei,

$$I_{\mathrm{s}}(\vec{Q},t) = \frac{1}{N}\sum_{j=1}^{N} \left\langle e^{-i\vec{Q}\vec{R}_j(0)} e^{i\vec{Q}\vec{R}_j(t)} \right\rangle \tag{3.24}$$

considers only scattered neutrons originating from the same nucleus.[258] The position of the respective nuclei might have changed in the observed time interval, in both cases. Its temporal Fourier transform

$$S_{\mathrm{inc}}(\vec{Q},\omega) = \frac{1}{2\pi\hbar}\int I_{\mathrm{s}}(\vec{Q},t)e^{-i\omega t}\mathrm{d}t \tag{3.25}$$

is called incoherent scattering law and is the one of primary interest in regard to the neutron spectroscopy methods used in this work.

3.5. Van Hove pair correlation function

An alternative representation of the scattering law can be expressed by the spatial and temporal Fourier transformation of the van Hove pair correlation function $G(\vec{r},t)$ [125, 258]:

$$S_{\mathrm{coh}}(\vec{Q},\omega) = \frac{1}{2\pi}\int e^{i(\vec{Q}\vec{r}-\omega t)}G(\vec{r},t)\,\mathrm{d}\vec{r}\mathrm{d}t\ , \tag{3.26}$$

$$S_{\mathrm{inc}}(\vec{Q},\omega) = \frac{1}{2\pi}\int e^{i(\vec{Q}\vec{r}-\omega t)}G_{\mathrm{s}}(\vec{r},t)\,\mathrm{d}\vec{r}\mathrm{d}t\ . \tag{3.27}$$

With

$$\delta(\vec{r}) = (2\pi)^{-3}\int \mathrm{d}\vec{Q}\,e^{i\vec{Q}\vec{r}} \tag{3.28}$$

the pair correlation function is determined from 3.23 and 3.26 as [258]:

$$G(\vec{r},t) = \frac{1}{N}\left\langle \sum_{j=1}^{N}\sum_{j'=1}^{N}\int \mathrm{d}\vec{r}'\,\delta(\vec{r}+\vec{r}_j(0)-\vec{r}')\delta(\vec{r}+\vec{r}_j(t))\right\rangle\ . \tag{3.29}$$

If the particles under consideration are distinguishable, it is possible to separate the pair correlation function into a so-called self and a distinct part [258]:

$$G(\vec{r},t) = G_{\mathrm{s}}(\vec{r},t) + G_{\mathrm{d}}(\vec{r},t)\ . \tag{3.30}$$

For the first part the summation in equation 3.29 is executed for $i = j$ only, while for the second one the terms with $i = j$ are considered. While in general the operators in the above equation do not commute, they do so under the assumption of a classical system, so that

$$G_{\mathrm{s}}(\vec{r},t) = \frac{1}{N}\left\langle \sum_{j}\delta(\vec{r}+\vec{r}_j(0)-\vec{r}_j(t))\right\rangle \tag{3.31}$$

and

$$G_{\mathrm{d}}(\vec{r},t) = \frac{1}{N}\left\langle \sum_{\substack{j,j'\\ j\neq j'}}\delta(\vec{r}+\vec{r}_j(0)-\vec{r}_{j'}(t))\right\rangle\ .[258] \tag{3.32}$$

These functions can be interpreted as follows: $G_{\mathrm{s}}(\vec{r}-\vec{r}',t-t')\,\mathrm{d}\vec{r}$ describes the ensemble averaged probability to find the same particle, which was at the time t' at the position $\vec{r}'$, at the coordinate $\vec{r}$ within the volume element $\mathrm{d}\vec{r}$ at the time t.[258] In the same way the expression $G_{\mathrm{d}}(\vec{r}-\vec{r}',t-t')\,\mathrm{d}\vec{r}$ gives the probability to find a different particle at the time t at the position $\vec{r}$, when another particle was at the time t' at $\vec{r}'$.[258]

3.6. Scattering law for continuous long-range diffusion

The van Hove self-correlation function $G_\mathrm{s}(\vec{r},t)$ allows to calculate the incoherent scattering law $S_\mathrm{inc}(\vec{Q},\omega)$, measured in quasi-elastic neutron scattering experiments, for the molecular dynamic processes in the sample under investigation. This shall briefly be shown in the following.

The concentration-gradient-induced spatial concentration fluctuations in a liquid can be related to its temporal evolution through the diffusion coefficient D and are described by Fick's second law

$$D \cdot \nabla^2 G_\mathrm{s}(\vec{r},t) = \frac{\partial}{\partial t} G_\mathrm{s}(\vec{r},t) \;.[13] \tag{3.33}$$

The diffusion coefficient can be expressed with the Stokes-Einstein relation in terms of the Boltzmann constant k_B, the temperature T, the friction coefficient of the liquid η and the radius R_p of the particles in a suspension, or alternatively, by the mean square displacement $\langle l^2 \rangle$ of the molecules within the time τ:

$$D = \frac{k_\mathrm{B} T}{6\pi\eta R_\mathrm{p}} = \frac{\langle l^2 \rangle}{6\tau} \;.[75] \tag{3.34}$$

Under the assumption that at the time $t = 0$ the center of mass of the particle is at the origin of the coordinate system, the boundary condition

$$G_\mathrm{s}(\vec{r},0) = \delta(0) \tag{3.35}$$

must hold for the solution of equation 3.33.[13, 75] As a further condition the particle can be expected to be somewhere in the space, at any time t:

$$\int G_\mathrm{s}(\vec{r},t)\, \mathrm{d}\vec{r} = 1 \;.[13] \tag{3.36}$$

With these assumptions the expression

$$G_\mathrm{s}(\vec{r},t) = (4\pi D t)^{-3/2} \cdot \exp\left(-\frac{r^2}{4Dt}\right) \tag{3.37}$$

can be found as a solution.[13, 75] This is the so-called Gaussian approximation.[274] A Fourier transformation in space and time according to equation 3.27 leads to the incoherent scattering law of the continuous diffusion

$$S_\mathrm{inc}(\vec{Q},\omega) = \frac{1}{\pi} \cdot \frac{DQ^2}{\omega^2 + (DQ^2)^2} \;.[13, 26, 274] \tag{3.38}$$

That means that the half width at half maximum DQ^2 (or $\hbar DQ^2$ in terms of energy transfer) of this Lorentzian-shaped curve gives direct access to the diffusion coefficient D.[13]

Unfortunately, this law holds only for diffusional motions, where the random displacements are very small and the interactions between the particles are very weak, as it can be found for instance in liquid argon.[13] For more complex liquids, for example already for water, this description of the diffusion process is not sufficient.

3.7. Singwi-Sjölander jump-diffusion model

Contrary to the continuous motion of the molecules assumed above, the Singwi-Sjölander jump-diffusion model [253] divides the diffusion into two separate processes: In a first step, the molecule is assumed to perform an oscillatory motion during a mean time τ_0 [253], around a fixed position in space. Afterwards it continuously diffuses for a mean time τ_1.[253] These two steps, whose motions are considered to be uncorrelated, are then perpetually repeated.[253] Through this description, where the molecule does not only diffuses by continuous motions, but also executes oscillatory motions without actually diffusing, crystalline features are ascribed to the liquid.

Under the assumption that the jump lengths l of the molecules possess a broad statistical distribution $l \cdot \exp(-l/\langle l \rangle)$ the half width at half maximum of the Lorentzian is determined as

$$\Gamma = \frac{\hbar Q^2 D}{1 + Q^2 D \tau_0} \tag{3.39}$$

by the Singwi-Sjölander jump-diffusion model.[73, 258] For large wave vector transfers Q the width saturates towards $\hbar/\tau_0$. If the time τ_1 during which the molecule is diffusing continuously is much larger than the residence time τ_0, where the molecule oscillates around a fixed position, i.e. $\tau_1 \gg \tau_0$, the model yields the continuous diffusion model from above, with the half width at half maximum of $\Gamma = \hbar Q^2 D$.

The macroscopic self-diffusion coefficient D is given here by

$$D = \frac{1}{6} \frac{\langle R_0^2 \rangle + \langle l^2 \rangle}{\tau_0 + \tau_1} , \tag{3.40}$$

where $\langle l^2 \rangle$ is the mean square displacement of a particle during the time τ_1 and $\langle R_0^2 \rangle$ the mean square radius of the thermal cloud corresponding to the oscillatory motion.[253]

Aside from the jump-diffusion model of Singwi and Sjölander [253], described here, a variety of further jump-diffusion models exist, like the ones of Hall and Ross [116] or of Chudley and Elliott [48], which however are not of relevance for this work.

3.8. Localised molecular motions

Some molecular dynamics are restricted to a finite space volume, like the rotation of the whole molecule or the dynamics of certain side groups of the molecule (e.g. methyl groups). In this case the van Hove self-correlation function can be subdivided into two parts,

$$G_s(\vec{r},t) = G_s(\vec{r},\infty) + G_s'(\vec{r},t) , \tag{3.41}$$

with the stationary part $G_s(\vec{r},\infty)$ and the time-dependent one, $G_s'(\vec{r},t)$, decaying to zero for $t \to \infty$.[174, 258] This leads to the following form of the incoherent scattering function:

$$S(\vec{Q},\omega) = S_{\mathrm{el}}(\vec{Q}) \cdot \delta(\omega) + S_{\mathrm{inel}}(\vec{Q},\omega) \text{ .[14, 174]} \tag{3.42}$$

The first term, originating in the stationary part of the van Hove correlation function above, corresponds to purely elastical scattering.[14, 258] The second, inelastic term, where a finite energy transfer occurs, leads to a quasi-elastic broadening of the obtained spectrum.[14, 258] The resulting scattering functions for such localised or confined molecular motions have the form

$$S(\vec{Q},\omega) = A_0(\vec{Q})\delta(\omega) + \sum_{j=1}^{n} A_j(\vec{Q})\frac{1}{\pi}\frac{\Gamma}{\Gamma^2+\omega^2}\ , \tag{3.43}$$

where $A_0(\vec{Q})$ is the so-called elastic incoherent structure factor (EISF) of the localised dynamics.[175]. The elastic incoherent structure factor is the ratio of the integrated elastic intensity to the sum of the integrated elastic and inelastic intensity for a specific wave vector transfer $\vec{Q}$:

$$\mathrm{EISF}(\vec{Q}) = \frac{I_{\mathrm{el}}(\vec{Q})}{I_{\mathrm{el}}(\vec{Q}) + I_{\mathrm{inel}}(\vec{Q})}\ .[13,\ 14] \tag{3.44}$$

It delivers information about the structure of the localised motions.[174]
For the prefactors $A_j(\vec{Q})$ of the Lorentzians in equation 3.43 the relation

$$\sum_{j=1}^{n} A_j(\vec{Q}) = 1 - \mathrm{EISF}(\vec{Q}) \tag{3.45}$$

is valid.[175]

3.9. Combination of different dynamics

When dealing with soft condensed matter systems, there is usually more than one kind of molecular dynamics present. For instance, molecules of a liquid can not only diffuse in a translatory way, but they can also rotate and with increasing complexity of the molecules also the motion of its single parts, for example side groups, must be considered. For the description of the single dynamics, the models described in the above sections are valid. However, they need to be combined in order to gain a scattering law, describing the whole system.
In terms of intermediate scattering functions, this is done by multiplying the scatterings laws $I^j_{\mathrm{inc}}(\vec{Q},t)$ for the individual dynamics:

$$I_{\mathrm{inc}}(\vec{Q},t) = \prod_j I^j_{\mathrm{inc}}(\vec{Q},t)\ .[13] \tag{3.46}$$

Consequently, the total incoherent scattering law is given by

$$S_{\mathrm{inc}}(\vec{Q},\omega) = \bigotimes_j S^j_{\mathrm{inc}}(\vec{Q},\omega)\ , \tag{3.47}$$

i.e. by the successive convolution of the scattering laws $S^j_{\mathrm{inc}}(\vec{Q},\omega)$ corresponding to the different dynamics being present in the system under investigation.[13]
Prerequisite to combine the motions in the way presented here, is the assumption that the various molecular dynamics of the molecules are independent from each other.[13] For liquids this can be usually assumed.[13]

CHAPTER 4

Quasi-elastic neutron scattering instrumentation

In this chapter the neutron spectroscopy instruments used for the analysis of the molecular dynamics of an ionic liquid confined in nanoporous carbons are introduced and their working principle is described for a better understanding of the experimental data presented in chapter 6. Two different kinds of spectrometers are used, which do not only differ in the way the energy exchange of the neutrons with the sample is determined, but also in the maximum detectable energy transfer and their resolution. Thus, they are probing the dynamic processes of the system under investigation at different time scales. While the time-of-flight spectrometer FOCUS in its used configuration has an observation time in the picosecond range, the one of the backscattering spectrometer IN16B adjoins to that one of FOCUS and reaches observation times up to the nanosecond range.

4.1. Time-of-flight spectrometer FOCUS

The time-of-flight spectrometer FOCUS is situated at the continuous flux spallation source SINQ at the Paul Scherrer Institute in Villigen, Switzerland. The free neutrons, obtained through spallation of lead atomic nuclei by shooting highly accelerated protons onto the lead target, are moderated with liquid deuterium and delivered to the instrument by a neutron guide, whose end is vertically converging.[200] A disc chopper divides the continuous neutron beam into pulses of a defined length and time lag between successive pulses.[136, 200] These neutron bunches then arrive at a vertically and horizontally focusing monochromator, consisting of a doubly curved assembly of single crystal pieces.[138, 200] From the different available monochromator crystal configurations [200], the pyrolytic graphite 002 reflex is used here for monochromatisation to a wavelength of 6.00 Å. After the monochromator the neutrons are passing a Fermi chopper [84], i.e. a fast rotating plate collimator.

The combination of the monochromator with a Fermi chopper allows for two operation modes of the instrument: monochromatic or time focusing.[200] While in the monochromatic focusing mode the resolution of the instrument is good over a wide energy transfer range, it is so in the time focusing mode only for a comparatively small range, but a considerably higher intensity is obtained.[137, 200] Since in the latter mode it is possible to optimise the resolution for a certain energy transfer, this mode is suitable for quasi-elastic measurements to obtain a good resolution around the elastic line of the spectrum, while still having the possibility to access a relatively wide dynamic range.[137] The changeover between the two operation modes is done by varying the distance between the monochromator and the sample, which equals the distance between the end of the beam guide of the monochromator in the monochromatric focusing mode, but does not in the time focusing mode.[137, 200] As a consequence, in the time focusing mode a broader wavelength band exits the monochromator, which leads to a degradation of the energy resolution. Since in neutron spectroscopy experiments only the energy transfer is of interest, this can be partly counterbalanced by the subsequent Fermi chopper.[137, 200, 239] Depending on its current orientation it lets neutrons from different positions of the monochromator pass, and thus allows to let slow neutrons start before faster ones, in a way that the elastically scattered neutrons arrive at the same time at the detectors.[137, 200, 239] While the Fermi chopper velocity must be well tuned in this case, it has to run at its maximum speed in the monochromatic focusing case.[200]

After passing the Fermi chopper the neutrons are impinging on the sample, being housed in an aluminium sample cell. For the here presented experiments the latter was mechanically connected to the cold head of a closed cycle helium refrigerator system, which allows to access a sample temperature range between around 30 K and 600 K [301]. From there the neutrons are scattered trough a radial collimator and an argon filled space to a detector array in a distance of 2.5 m around the sample with a large angular range.[137, 200] From the particular angular position of the detectors, the respective wave vector transfer Q can be determined. The spectroscopic information, i.e. the energy transfer of the incident neutrons with the sample, is obtained from the deviation of the flight time of the scattered neutrons, from the time that would be needed by neutrons with the original, unaltered velocity to travel the pathway of known distance within the spectrometer. At this point it also becomes clear, why it was necessary to divide the continuous neutron beam into discrete bunches of defined time lag, because otherwise the neutron flight time could not be determined.

4.2. Neutron backscattering spectrometer IN16B

The neutron backscattering experiments [32] have been performed at the IN16B spectrometer at the Institut Laue-Langevin in Grenoble, France. A sketch of this instrument can be seen in figure 4.1. Eponymous for this kind of neutron spectroscopy is the backscattering from the monochromator and analyser crystals [189], i.e. that part of the neutron beam that matches the Bragg condition is reflected back under a Bragg angle of 90°. As it can be easily seen from Bragg's law in its differential form, the wavelength spread $\Delta\lambda$ of the back-reflected neutrons becomes minimal in that case, leading to an optimised energy resolution. The resolution function of IN16B has a Gaussian shape [91] with a full width at half maximum of around 0.85 μeV.

The working principle of the IN16B neutron backscattering spectrometer is as follows: The 'white' beam of cold neutrons coming from the nuclear reactor after moderation with liquid deuterium, passes a mechanical velocity selector (see sketch of the instrument in figure 4.1), before it is reflected from the neutron beam guide to the instrument by a pyrolytic graphite (002) deflector [93]. Note, that the latter is only the case, when the instrument is used in the

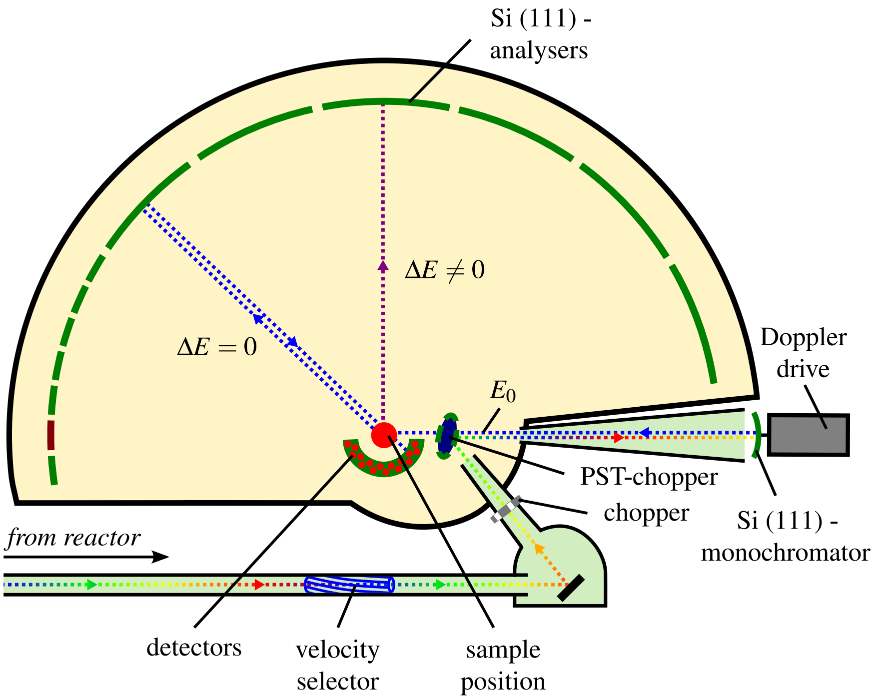

Figure 4.1.: Sketch of the IN16B neutron backscattering spectrometer.

low background configuration, as it has been done during the experiments presented later in this work. By contrast, in the high flux configuration, the spectrometer would be situated at the tail of the neutron beam guide, such that the deflector is not necessary. After the deflector the neutrons are passing a first chopper, whose purpose is to keep the background low. The choppers are fast rotating disks with an alternating arrangement of wings and slits in between the latter, letting the neutrons pass or not, depending on the current position of the opening. Thereafter, they are impinging on the so-called phase space transformation chopper (PST-chopper), from which they are reflected towards the monochromator, composed of spherically arranged silicon (111) single crystals. From there only such neutrons are reflected back parallel to the surface normal that fulfil the Bragg condition, thus resulting in a monochromatic neutron beam with a wavelength of 6.27 Å. The purpose of the phase transformation chopper is twofold. First, it enables to have practically perfect backscattering [94], i.e. the neutrons are impinging the monochromator crystals and leaving them again in direction of the sample under an angle of 90° with respect to the monochromator surface, as already stated before. But it does more than simply reflecting the neutrons onto the monochromator. The incoming neutron beam has still a quite broad velocity distribution, even though that distribution has been already shrinked by the initial velocity selector. Furthermore, that neutron beam has a relatively small divergence. On the surface of the chopper wings, which reflect the neutrons towards the monochromator crystals, pyrolytic graphite mosaic crystals are attached. The reflection from these very fast moving mosaic crystals leads to a phase space transformation of the corresponding phase space element of the reflected neutrons, such that the outgoing beam has a much narrower energy distribution, but a larger divergence.[94, 95, 238] This phase space transformation is in consistency with the Liouville theorem, since the phase space volume is conserved.[94, 238] Such a conversion is favourable here, because the monochromator crystals reflect only a very narrow wavelength interval, but through the use of a spherically curved crystal surface it does so also for the whole divergent beam.[94, 238] Consequently, this leads to a seizable intensity gain.[94, 108, 238] Furthermore, the mismatch in divergence between the beam at the monochromator and that one at the analysers is reduced.[103, 238]

The neutron beam from the monochromator passes the opening of the phase space transformation chopper, from which it had been reflected to the monochromator crystals before, and hits the sample. In the case of the present work the sample is encased in an aluminium cell, which is placed in a cryofurnace, enabling a temperature control of the sample within a range from around 2 K up to 560 K [92]. However, this range is possibly limited to much lower temperatures through the used materials, for example for the cell sealing. The neutrons that are scattered by the sample, having exchanged energy and momentum with it, are flying through the vacuum chamber of the instrument until they are impinging on large analyser crystals. These consist of silicon (111) single crystals, like the monochromator, and therefore reflect only such neutrons with same energy as those coming from the monochromators, if all crystals have the same temperature and are static. The neutrons that are backscattered from the analysers are then partly passing the sample a second time and are finally hitting the detector tubes. However, the second passage through the sample necessitates only minor correction and contributes as a flat background in the measurement signal.[94] At this point one can see the necessity of a pulsed neutron beam, since it has to be avoided that new neutrons are reaching the samples or detector, while a preceding neutron pulse has not reached the latter, yet.

With the instrument as described above, only elastically scattered neutrons, i.e. such that have not exchanged energy with the sample, could be detected, since the analysers and the monochromator consist of the same silicon (111) crystals. For doing spectroscopic measurements, the monochromator is mounted at a linear drive, which enables one to move it fast with a defined velocity profile, perpendicular to its surface plane. Consequently, the incoming neutrons see an altered lattice constant, because the lattice planes are moving away or towards the neutrons. This causes a kind of Doppler effect, which leads to the fact that the wavelength of the reflected neutrons is shifted.[94] Now, such neutrons are reflected by the analysers, whose energy exchange with the sample is ΔE, when the energy shift of the neutrons at the monochromator was ΔE away from the energy E_0 of the neutrons in case of the static monochromator. Since the velocity and therefore the flight time of the neutron packets within the spectrometer is known, it is possible to correlate the neutrons at the detector with a certain energy transfer. The detector position, which is connected with the analyser position, gives information about the wave vector transfer Q.

A description of the experiments carried out at this neutron backscattering spectrometer, together with a delineation of the data analysis is found in the experimental section, chapter 6.

CHAPTER 5

Materials & sample preparation

In the following the materials that are used for the investigation of the ionic liquid molecular dynamics within a geometrically restricting geometry, are presented. Furthermore, a description of their preparation for the quasi-elastic neutron scattering experiments is given.

5.1. Carbide-derived carbons

Nanoporous carbide-derived carbons serve as confining geometry for the ionic liquid in the here presented experiments on its molecular dynamics. These porous carbons were produced by Boris Dyatkin from the working group of Yury Gogotsi at Drexel University (U.S.A.). As a precursor for the production [226] of these porous carbide-derived carbons, molybdenum (Mo_2C), boron (B_4C) and silicon (SiC) carbide microparticles with a size of 1–5 µm were used.[33] The metal from molybdenum and boron carbide precursors was selectively etched out with Cl_2 gas at 900 °C, while in the case of the silicon carbide a temperature of 1000 °C was used.[33] Note, that a certain percentage of metals nevertheless remains at the end within the produced carbide-derived carbons.[66] The halogen etching procedure was followed by an annealing in H_2 gas at 600 °C.[33] Before the carbide-derived carbons were finally vacuum annealed at 10^{-6} torr and 1400 °C, all specimens, except BC-no-9, have been oxidised at air at a temperature of 425 °C.[33] The final vacuum annealing step removed all functional groups from the surface of the carbon material and thus lead to a practically identical surface chemistry of all samples.[33] All preceding steps are determinant for the pore widths of the nanoporous carbide-derived carbons.[33]

Figure 5.1 shows the pore size distribution of these samples, which were determined by Boris Dyatkin by employing quenched solid density functional theory models [210] for the analysis of corresponding nitrogen sorption isotherm measurement data. Own measurements at these samples obtained similar results. For almost all samples slit pores were assumed for the analysis. An exception is only sample MoC-21, where a combination of slit, cylindrical and spherical pores lead to a better fit of the model and a more reasonable pore volume. The specific surface area of the characterised carbons was determined to lie in a range between 1000–1400 m^2/g.[66] All four carbide-derived carbons possess a high amount of micropores, especially such below one nanometre in diameter, which constitute a comparatively high part

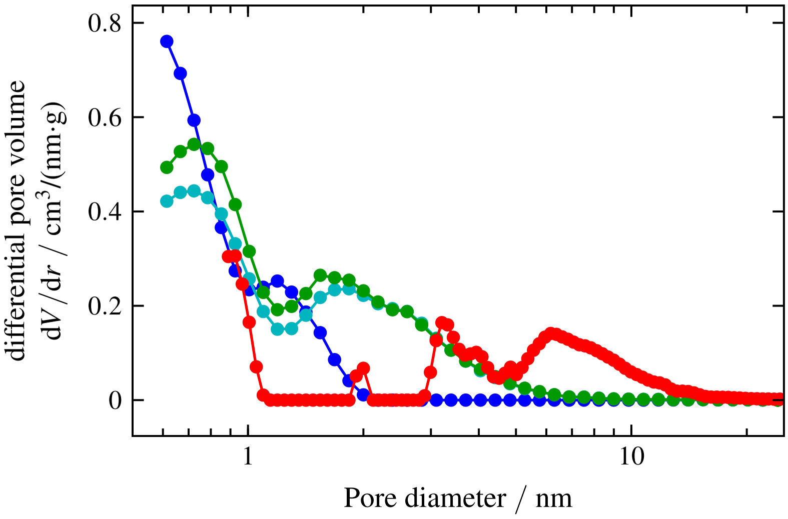

Figure 5.1.: Pore size distributions of the four nanoporous carbide-derived carbon samples, ● MoC-21, ● BC-no-9, ● BC-9 and ● SiC-2. The lines, connecting the data points, serve as guide for the eyes.[33]

of the total pore volume. Furthermore, most of the samples have a quite broad distribution of pore diameters, which reaches up to around 21 nm in the case of MoC-21. Samples BC-no-9 and BC-9 have smaller pores and the corresponding distributions are very similar for both. The narrowest pore diameter distribution with a maximum width of around 2 nm has sample SiC-2.

The numbers at the end of the sample designators indicate the maximum pore size for each specimen. This is indented as an orientation and for a better discriminability of the samples. Note however, that this quantity is not necessarily the one that is of importance to describe the dynamical processes of the ionic liquid, which are investigated in the following sections. For this purpose, one needs to consider the whole distribution, where probably the most frequent pores size, excluding very small pores, is of most importance. Since however, the pore size distribution of sample MoC-21 exhibits some artefacts, where the differential pore size is exactly zero, the determination of an average pore size is not meaningful. Because of this, the maximum pore width has been chosen for the specimen designators.

Except the granulate material SiC-2, all carbide-derived carbons are powders. As can be exemplarily seen from the scanning electron micrograph in figure 5.2 (a) for sample BC-no-9, the size of the powder grains is up to approximately 15 µm. In the case of the granular carbon sample SiC-2, shown in figure 5.2 (b), the grains have diameters in the range of several hundred micrometres.

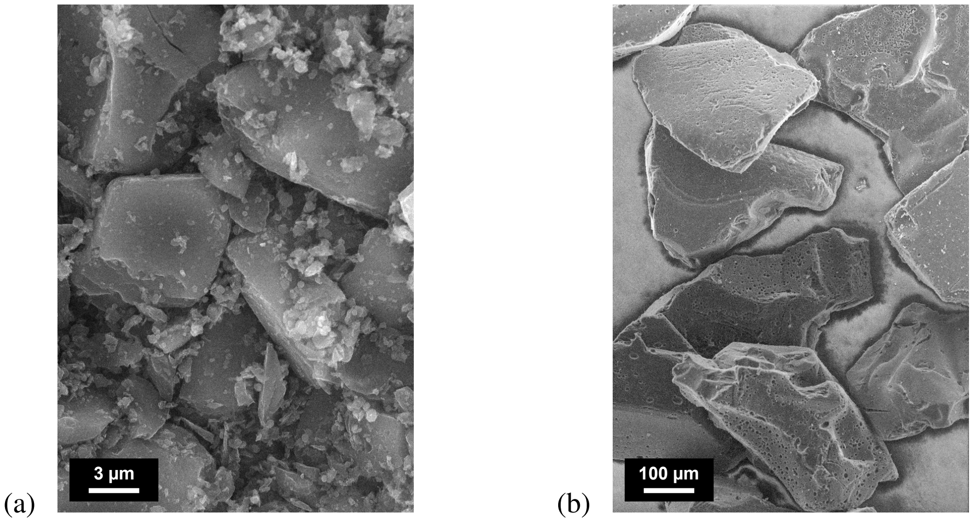

Figure 5.2.: Scanning electron micrographs of nanoporous carbide-derived carbon particles: (a) powder grains of sample BC-no-9, (b) grains of granular sample SiC-2.

5.2. Ionic liquid [BuPy][Tf$_2$N]

The room-temperature ionic liquid, whose molecular dynamics are investigated by means of quasi-elastic neutron scattering in this work, especially in the nanoconfinement of the pores of the above described carbide-derived carbons, is denominated as 1-N-butylpyridinium bis((trifluoromethyl)sulfonyl)imide. Because of its long name the ionic liquid will be referred to as [BuPy][Tf$_2$N] in the following. The first part [BuPy] corresponds to the cation of this ionic liquid, consisting of a pyridinium ring, where a butyl chain is attached to the nitrogen atom, as can be seen in the structural formula in figure 5.3. [Tf$_2$N] on the other hand refers to the anion bis((trifluoromethyl)sulfonyl)imide, whose structural formula is also depicted in figure 5.3. This anion is also frequently termed [TFSI] in the literature.

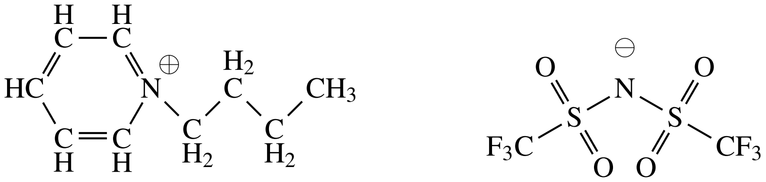

Figure 5.3.: Structural formula of the cation (*left*) and the anion (*right*) of the ionic liquid 1-N-butylpyridinium bis((trifluoromethyl)sulfonyl)imide.

Looking at the neutron scattering cross sections of the elements the ionic liquid [BuPy][Tf$_2$N] is consisting of, weighted with the natural abundance of the isotopes, as shown in table 5.1, one finds that the incoherent cross section σ_{inc} of the cation $C_9H_{14}N$ is 1124.24 barn = 112424 fm^2. In contrast, the incoherent neutron scattering cross section of the anion $C_2F_6NO_4S_2$ is only

Table 5.1.: Neutron scattering cross sections of the isotopes [BuPy][Tf$_2$N] is consisting of, as tabulated by Sears [242]. In case no atomic mass number is given, the specified values are weighted over all isotopes of the respective element according to their natural abundance. All values given in barn = 100 fm^2.

Isotope	σ_{inc}	σ_{coh}
^{1}H	80.27(6)	1.17583(10)
^{2}H	2.05(3)	5.592(7)
H	80.26(6)	1.7568(10)
C	0.001(4)	5.550(2)
N	0.50(12)	11.01(5)
O	0.000(8)	4.232(6)
F	0.0008(2)	4.017(14)
S	0.007(5)	1.0186(7)

0.53 barn, i.e. less than 0.5 ‰ of the one of the cation. As stated in chapter 3, the incoherent scattering of the nuclei is important for the analysis of the single-particle molecular dynamics using quasi-elastic neutron scattering spectroscopy. Consequently, it is the mobility of the cation this technique is sensitive to, while the anion dynamics are almost neglectable in the measurement signal. The coherent neutron scattering cross sections σ_{coh} of the cation and the anion are with 85.56 barn and 65.19 barn comparatively small in contrast to the respective incoherent cross sections. This means that the incoherent scattering is the dominating process here and the influence of the coherent scattering on the measurement results can be expected to be small. However, in the analysis of the dynamic processes in the bulk ionic liquid, the coherent contribution to the total measurement signal, arising from collective motions, has shown to be not completely neglectable.[30, 31]

Another important point for the study of the molecular dynamics of [BuPy][Tf$_2$N] in the confinement of the nanoporous carbide-derive carbon, are the phase transition properties of the bulk ionic liquid. These are like most other physicochemical properties influenced by impurities, for example water, so that deviating data are found in different publications. However, most specify the melting point of [BuPy][Tf$_2$N] at 299.00–299.15 K, determined by differential scanning calorimetry at a heating rate of 10 K/min [185, 211, 267] or 5 K/min [167], respectively. Here, it should be noted that except in one case [185], where the melting point is given with 299.05 K, the values are specified without decimal places, suggesting a comparatively lower accuracy. However, with respect to the crystallisation temperature and a possible glass transition of the ionic liquid [BuPy][Tf$_2$N], the situation is ambiguous in the literature. Tokuda et al. [267] detected no glass transition during differential scanning calorimetry measurements at a scanning rate of 10 K/min, however, at 50 K/min they observed a supercooling of the liquid, as well as a glass transition at 197 K. Lall-Ramnarine et al. [167] give a glass transition temperature of 192 K, measured with a rate of 5 K/min. Noda et al. [211] observed a relatively fast crystallisation, as well as a glass transition during cooling scans, but do not specify a temperature for the latter. However, they also describe the observation of an exothermic peak, corresponding to a crystallisation process, on heating scans with 10 K/min with an onset temperature of 224 K.[211] Other publications [27, 30, 185] do not detect a glass transition. Instead, Burankova et al. [30] specify a crystallisation temperature of 254.2 K and 236.2 K for cooling rates of 5 K/min and 10 K/min, respectively.[27, 30] Concluding, it should be mentioned that the supercooling well below the melting temperature is quite prevalent for ionic liquids, as well as that they may present uncommon phase sequences, like a glass-to-crystalline transition on heating.[87]

The ionic liquid [BuPy][Tf_2N] possesses as other ionic liquids a relatively high viscosity. Its dynamic viscosity is for instance 181.810–182.1 mPa·s at 278.15 K [209, 215], 48.11–49.4 mPa·s at 303.15 K [18, 169, 215, 293] and 10.59–10.9 mPa·s at 353.15 K [169, 215, 293]. Here, the temperature dependence of the dynamic viscosity follows a Vogel-Fulcher-Tammann law.[18, 209, 211, 215, 267] In comparison, the dynamic viscosity of water is only 0.798 mPa·s at 303.15 K [55], what exemplifies how viscous the ionic liquid [BuPy][Tf_2N] is. The density of [BuPy][Tf_2N], which is important for the sample preparation, as described in the next section, is 1.4440–1.4506 g/cm^3 [18, 169, 185, 215, 293] at 303.15 K, while its surface tension at this temperature is 33.2–34.5 mN/m [18, 185]. Both parameters are found to linearly decrease with increasing temperature.[18, 185, 209, 215, 293]

5.3. Sample preparation for the quasi-elastic neutron scattering experiments

A proper filling procedure of the carbide-derived carbons with the ionic liquid is crucial for the neutron spectroscopic investigation of the ionic liquid's molecular dynamics in the nanoconfinement. Not only a preferably complete pore filling should be achieved, but first and foremost bulk ionic liquid between the carbon grains must be avoided. The reason is that the measurement signal from the latter would superimpose the one from the nanoconfined liquid and render the analysis of its dynamics very challenging.

As a consequence, only such an amount of ionic liquid is used, that it equals the pore volume as determined by the nitrogen sorption isotherm characterisation of the carbide-derived carbons (see section 5.1). That volume of [BuPy][Tf_2N] is mixed in a first step with ethanol with a purity of $\geq 99.9\,\%$ in a volume ratio of 1 to 2. Afterwards, this liquid is blended with the respective nanoporous carbon. The compound is then distributed in the flat aluminium sample holder. To remove the remaining ethanol and to accelerate the capillary imbibition of the highly viscous [BuPy][Tf_2N] into the nanovoids of the carbon, the sample is stored inside a drying cabinet at a temperature of 348 K and at an absolute pressure of 8 mbar for 2.5 hours. After that the carbon powders have changed their visual appearance back to that of the empty, dry carbon powder samples. An exception was here the granular sample SiC-2, where the large carbon grains appeared to be a bit adherent. The filling procedure of the samples has been randomly verified by weighting the empty, as well as the ionic-liquid-filled, dried carbon samples. The above procedure is orientated at one that has been already successfully applied at similar systems.[43]

Following the drying of the specimens, the sample container is closed by attaching the top cover, while the gap to the bottom part is sealed with indium wire or lead wire, respectively. For the sealing of the sample containers of the experiment at the time-of-flight spectrometer FOCUS mainly lead was used, while for the experiment at the neutron backscattering spectrometer IN16B solely indium has been used. In the latter experiment the indium wire and the screws, connecting both parts of the sample container, were shielded from the neutron beam with a cadmium sheet around the respective parts of the sample cell. In both experiments the slab-like cells made of pure aluminium had a volume of around 0.45 cm^3, while the slab thickness was 0.4 mm in the case of IN16B and 0.6 mm in that of FOCUS.

For the reference measurements of the bulk ionic liquid at IN16B, the same kind of flat sample cells like for the [BuPy][Tf_2N]-filled carbons was used, to avoid measurement geometry related effects. The same is true for the measurements of vanadium at both spectrometers, which are used for detector efficiency normalisation of the data.

CHAPTER 6

Experimental results & discussion

In the following the analysis of the temperature- and pore-size-dependent molecular dynamics of the room-temperature ionic liquid within the carbon nanoconfinement is presented. This analysis starts with applying a technique that enables one to get a first brief, but already quite detailed overview of the dynamic processes in a wide temperature interval. Following, a more in-depth analysis of the dynamics at selected temperatures is conducted, employing the information provided by quasi-elastic neutron scattering (QENS) spectra obtained from two spectrometers with practically complementary dynamic range and resolution.

6.1. Fixed window scans

The neutron backscattering spectrometer IN16B at the Institut Laue-Langevin offers the powerful possibility to perform so-called fixed window scans. With these, it is possible to quickly vary a specimen parameter, e.g. the temperature, while acquiring the scattered intensity with respect to a certain, fixed energy transfer between the incoming neutrons and the sample. For the acquisition of a full energy spectrum, the monochromator of the instrument is moved with a sinusoidal velocity profile, so that it is continuously changing the energy transfer it is sensitive to (see section 4.2 for a brief description of the instrument and its working principle). On the contrary, when doing a fixed window scan, the monochromator is at rest all the time, when measuring at an energy transfer of $\Delta E = 0\,\mu\text{eV}$ or it moves after a very fast acceleration for a relative long period at a constant velocity for measurements at $\Delta E \neq 0\,\mu\text{eV}$. In the first case, when observing elastically scattered neutrons, i.e. $\Delta E = 0\,\mu\text{eV}$, these measurements are denoted as elastic fixed window scans in the following, while measurements where $\Delta E = \text{const.} \neq 0\,\mu\text{eV}$, i.e. the neutrons are inelastically scattered, are named inelastic fixed window scans. Since at the fixed window scans the monochromator is for a relatively long time at a certain constant velocity, the intensity, integrated over the measurement time interval, is much higher, compared to the case, when acquiring full spectroscopic information, where only for a short period of time neutrons are registered for a certain energy transfer. This is the reason, why it is possible to quickly scan a large temperature range of the sample, while observing a certain energy exchange with the impinging neutrons, to get an overview of dynamic processes being activated at specific temperatures. While the acquisition of a full quasi-elastic spectrum at a single temperature takes several hours to achieve a reasonable signal-to-noise ratio, one data point, i.e. one temperature, is only a matter of minutes in the case of the fixed window scans.

In this work, the sample was heated continuously with a rate of 1 K/min from a temperature of 2 K up to 355 K, while alternately acquiring for 1 minute the intensity of the elastically scattered neutrons and for 3 minutes those that experience an energy exchange of $\Delta E = \pm 2\,\mu\text{eV}$ with the specimen. The fact that the energy transfer spectrum is symmetric around $\Delta E = 0\,\mu\text{eV}$, allows one to sum up the intensity that is measured on advancing and receding motion of the monochromator, i.e. for $\Delta E = -2\,\mu\text{eV}$ and $\Delta E = +2\,\mu\text{eV}$, respectively. Because the data of the energy channels are registered separately, it was possible to verify the equivalence of the intensity for $\Delta E = \pm 2\,\mu\text{eV}$. The available wave vector transfer range is limited to $Q = 0.44\,\text{Å}^{-1}$ to $1.90\,\text{Å}^{-1}$ in the case of the fixed window scans, since the two analysers at small angles, corresponding to the lowest Q-values, are inclined with respect to the perfect backscattering condition. Thus, they deliver a shifted energy transfer spectrum, which is no problem, when acquiring a full spectrum, but in the case of the fixed window scans, where only one specific ΔE is considered. Therefore, the data from these analysers are omitted for the fixed window scans.

Before analysing the dynamics of the ionic liquid [BuPy][Tf_2N] in the confinement of the nanoporous carbide-derived carbons, the bulk ionic liquid is investigated as a reference concerning its temperature-dependent dynamics with the help of the fixed window scans. Figure 6.1 shows the intensity of the elastically scattered neutrons as a function of temperature, when heating the bulk [BuPy][Tf_2N] with a rate of 1 K/min from 2 K to 355 K. The shown

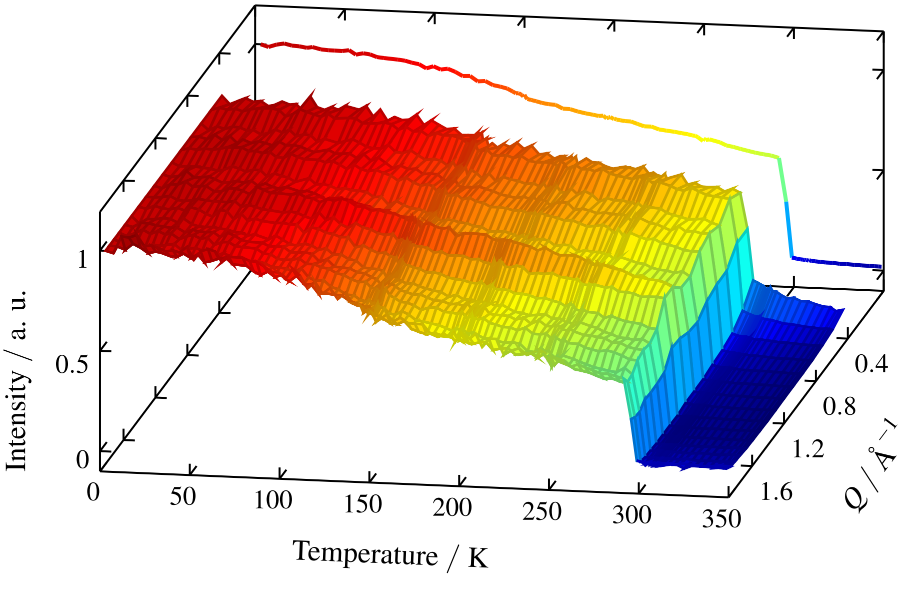

Figure 6.1.: Elastic fixed window scan, i.e. the intensity of neutrons, elastically scattered at the molecules of the bulk [BuPy][Tf_2N], while heating from 2 K to 355 K with a rate of 1 K/min. *Foreground*: Intensity as a function of temperature and wave vector transfer Q. *Back panel*: Over the available Q-range averaged intensity as a function of temperature.

data of this elastic fixed window scan are normalised for each wave vector transfer Q to the intensity at 2 K, where it is maximal, since all diffusive dynamics are not active at this temperature. With increasing temperature the intensity is expected to decrease also without the presence of diffusive processes according to the Debye-Waller factor [61, 280], due to lattice vibrations. The line plot in the back panel of graph 6.1 shows the over Q averaged intensity. Changes in the slope of this curve in the temperature range between approximately 100 K and 200 K give a first hint at the activation of dynamic processes in this ionic liquid, while the abrupt drop in the elastic intensity at about 295 K indicates the melting of the crystallised liquid. But before this is further analysed using the inelastic fixed window scan data, the mean square displacement of the scattering nuclei as a function of temperature is determined from the elastic fixed window scan.

6.1.1. Mean square displacement

As one can see from the three-dimensional intensity plot in figure 6.1, the intensity is sloped along the Q-axis. Assuming a harmonic vibration, the Q-dependence of the intensity can be described as

$$I(Q) = I_0 \cdot e^{-\frac{1}{3}\langle u^2\rangle Q^2} \cdot I_{\mathrm{c}} \,, \tag{6.1}$$

where I_0 is the intensity at $Q = 0$ (if $I_{\mathrm{c}} = 1$) and $\langle u^2\rangle$ the mean square displacement. [13, 94] This relation is usually referred to as Gaussian approximation.[302] The offset $I_{\mathrm{c}} = \exp(c_{\mathrm{f}})$ allows for effects like multiple scattering.[94] It should be noted that there are more sophisticated methods to handle multiple scattering effects and for the determination of the mean square displacement from elastic fixed window scans in general, which reduce the underestimation of the latter by the above simple model, especially at higher temperatures.[302, 303] However, for a first impression of the temperature-dependent dynamics the widely used Gaussian approximation is sufficient. With a fit of this model to the elastic intensity at each measured temperature the mean square displacement $\langle u^2\rangle$ is determined and shown together with c_{f} in figure 6.2 for all measured samples. The curves are shown until $\ln(I(Q^2))$ gets visibly nonlinear, i.e. equation 6.1 is no longer valid. This is at the latest the case when the molecular motions are getting an increasing complexity, which happens for example for the bulk liquid upon the transition from the crystalline to the liquid state. As a reference figure 6.2 shows also the result for the empty carbon matrix of sample MoC-21, which has been measured on rapid cooling with an uncontrolled cooling rate. From this curve one can see that the contribution of the nanoporous carbon to the total averaged mean square displacement of the filled carbon matrices is low. The mean square displacement of all ionic-liquid-filled samples and the bulk one is at latest from around 100 K on clearly above the one of the empty carbon powder. The ionic-liquid-filled porous carbon with the smallest pore size, SiC-2, has a mean square displacement that is almost indistinguishable from the one of the crystallised bulk sample. In contrast, the mean square displacement of the two other samples with larger pores has higher values for temperatures above 150 K. This can be seen as a first indication for altered dynamics in the case of nanoconfinement. In contrast, the constant contribution c_{f} is quite similar for all three samples of the confined ionic liquid, but deviates strongly from the bulk one. The introduction of c_{f} is necessary, since with increasing temperature, the intensity as a function

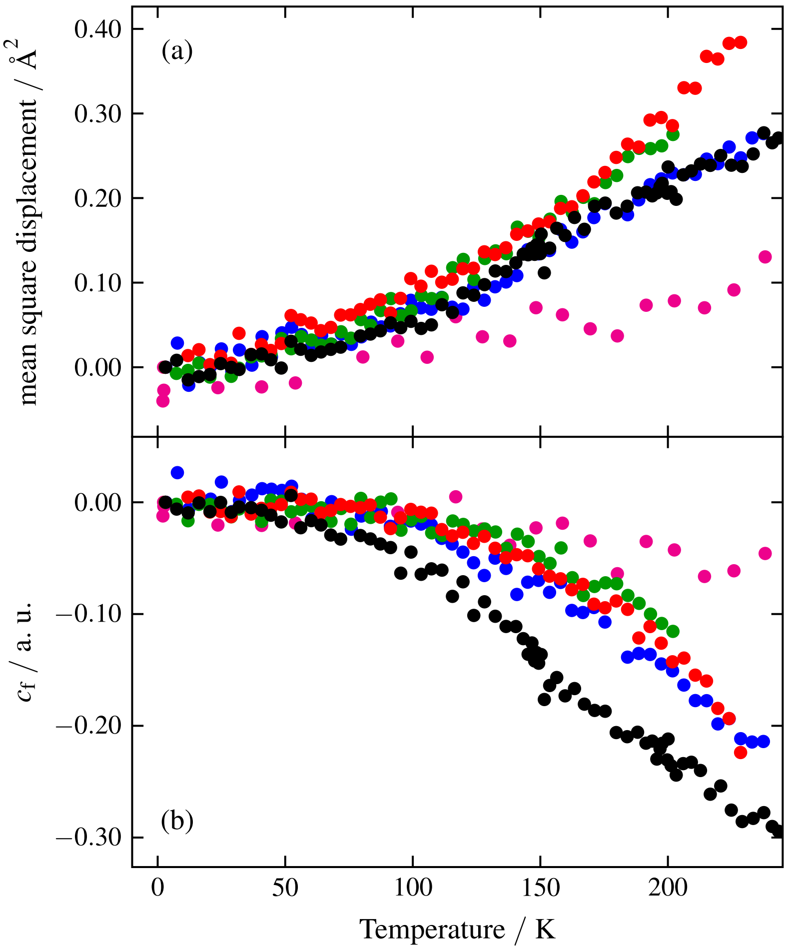

Figure 6.2.: (a) Mean square displacement $\langle u^2 \rangle$ as a function of temperature and (b) constant contribution c_f for each temperature for the ● bulk [BuPy][Tf$_2$N], as well as confined in the nanoporous carbide-derived carbon samples ● MoC-21, ● BC-no-9 and ● SiC-2, derived from the elastic fixed window scan, as described in the text. For reference the result for the ● empty carbon matrix of MoC-21, measured on rapid cooling, is shown.

of Q^2, i.e. $\ln(I(Q^2))$, is no line through the origin any more.
Although this analysis of the mean square displacement averaged over all scatters within the sample, predominantly protons, gives first hints of the cation dynamics, more detailed information will be deduced in the following from the data of the inelastic fixed window scans.

6.1.2. Qualitative overview of the dynamic landscape

Figure 6.3 shows the intensity as a function of temperature and wave vector transfer Q as a result of the inelastic fixed window scan with $\Delta E = \pm 2\,\mu\text{eV}$. Here, the intensity is normalised for each Q independently to the respective intensity at 2 K of the corresponding elastic fixed window scan, where all dynamic processes, aside from lattice vibrations, can be considered to be frozen. The graph in the back panel of figure 6.3 shows the intensity of the three-dimensional plot in the front, averaged over the whole for the fixed window scans available Q-range. Already here, the potential of the inelastic fixed window scans becomes apparent. More clearly than from the elastic fixed window scan, one can see the thermal activation of a first kind of dynamics starting from around 100 K on in this inelastic fixed window scan. A former investigation of the bulk [BuPy][Tf$_2$N] cation dynamics sees in this temperature range the onset of methyl group dynamics.[27, 30] The sudden rise in the inelastic intensity with $\Delta E = \pm 2\,\mu\text{eV}$ at around 295 K can be ascribed to the melting of the crystalline [BuPy][Tf$_2$N] and corresponds to the elastic intensity drop, as seen above in figure 6.1. By the way, the elastic fixed window scan curve of the bulk [BuPy][Tf$_2$N] shows that the heating rate of

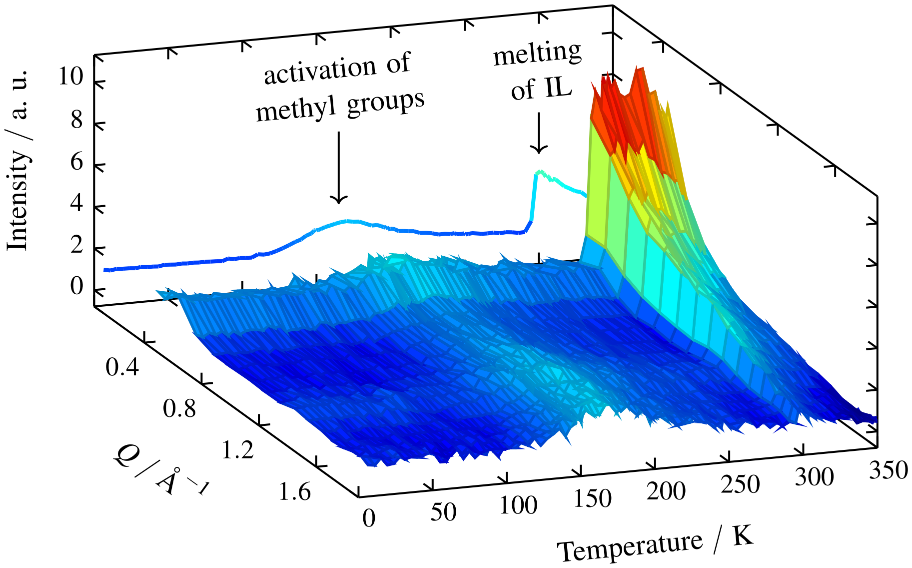

Figure 6.3.: Inelastic fixed window scan with an energy transfer of $\Delta E = \pm 2\,\mu\text{eV}$ from 2 K to 355 K of the bulk [BuPy][Tf$_2$N], clearly showing the activation of different dynamic processes in the temperature course. *Foreground*: Intensity as a function of temperature and wave vector transfer Q. *Back panel*: Mean intensity over the available Q-range as a function of temperature.

1 K/min is well-chosen: Although, the bulk fixed window scan possesses the peculiarity that it was stopped at several temperatures in order to acquire full quasi-elastic spectra for several hours, the curve is still smooth at these points. This would not be expected, if the heating rate would be too fast, because then the sample would reach its thermal equilibrium only when keeping it for a longer time at a certain temperature and thus the observed dynamics would be different before and after the stop.

That the inelastic intensity for the low-temperature dynamics, as well as for the melting, first rises and than falls again with increasing temperature might appear a little bit counter-intuitive at first glance. However, the reason is that with rising temperature the dynamics are getting faster and consequently the energy transfer spectrum of the scattered neutrons becomes broader, since the maximum energy transfer between the neutrons and the scattering nuclei increases. As a result, the constant quantity of scattered neutrons is distributed on a wider energy range, thus resulting in a decrease in intensity of the neutrons with a lower energy transfer, as for example those in the 2 μeV energy channel, here.

Having a look at the wave vector transfer dependence of the inelastic intensity in the two afore described temperature ranges with different dynamics, one observes only a very weak Q-dependence for the low-temperature dynamics, which are starting to get active from around 100 K on. Contrary, after the melting, above 295 K, the ionic liquid shows a very strong wave vector transfer dependence in the considered 2 μeV energy channel of the scattered neutrons. This fact will become important for the systematic investigation of the inelastic fixed window scans with respect to the cation dynamics, below.

Prior to that, a qualitative overview of the differences in the temperature-dependent cation dynamics of the bulk [BuPy][Tf_2N] in comparison to the ones in the nanoconfinement of the carbide-derived carbons shall be obtained. Therefore, the Q-averaged intensities of the respective elastic and inelastic fixed window scans, shown in figure 6.4, are examined. Clear differences between the cation dynamics of [BuPy][Tf_2N] in the bulk and in the case of the nanoconfinement with different pore sizes are observed: While the bulk shows a well-defined abrupt first-order crystalline-to-liquid phase transition, there is no such in the case of the confined [BuPy][Tf_2N]. Instead, a continuous transition is taking place, starting at much lower temperatures and being indicated by a broad peak in the inelastic fixed window scans. Furthermore, the peaks are shifted to higher temperatures with decreasing pore size.

Such a changeover to a continuous phase transition, together with its pore-size dependence and a strong melting point depression, is a common phenomenon of liquids within nanoporous media.[1, 47, 134, 264] From the Gibbs-Thomson equation a shift of the melting temperature is predicted which scales with the inverse of the pore diameter.[1, 134] The direction of the melting temperature shift depends on the surface tension between the pore wall and the liquid phase in comparison to that between the pore wall and the solid phase.[1] The melting point is depressed, if the latter is the larger one.[1] However, it should be noted that this equation is strictly valid only for sufficiently large pores, such that the crystalline structure of the solidified liquid within these pores is not disturbed and still identical with that in the bulk.[1, 134] The observed massive broadening of the melting transition has most likely several reasons: First of all, from the above-mentioned, it is reasonable to suppose that the ionic liquid in pores of different diameters has different melting temperatures. Remembering the broad pore size distributions of the used carbide-derived carbons, as shown in figure 5.1 in section 5.1, it can

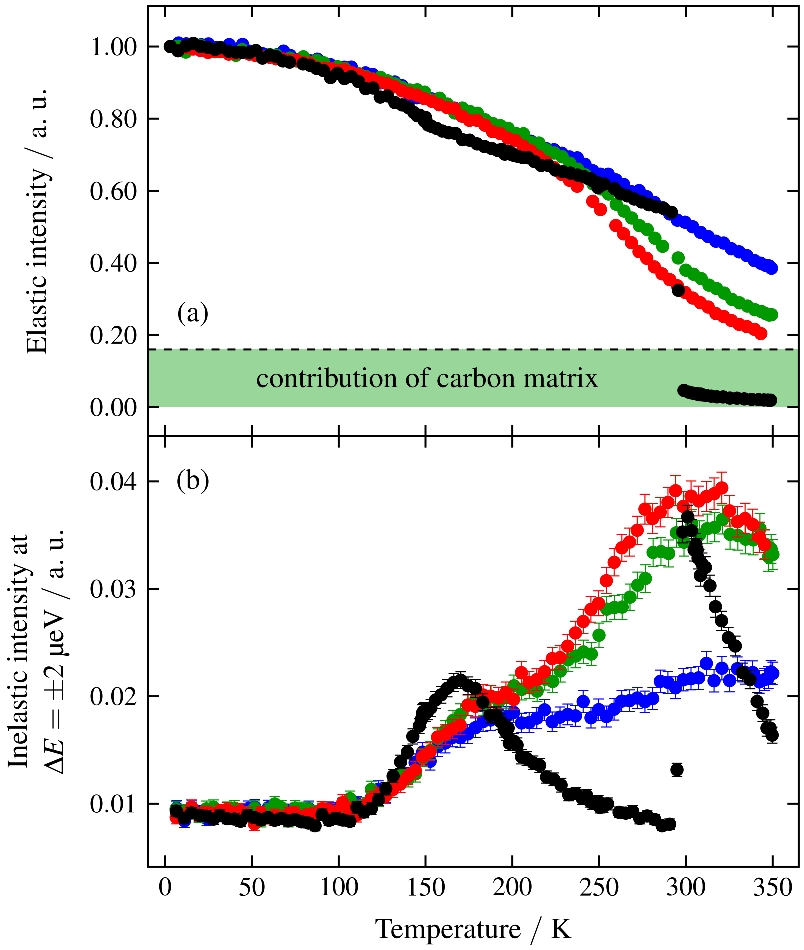

Figure 6.4.: Intensity of the (a) elastic and (b) inelastic fixed window scans, averaged over the available wave vector transfer range. Differences in the temperature course illustrate the altered dynamics between cations of the ● bulk and those in the nanoconfinement of ● MoC-21, ● BC-no-9 and ● SiC-2, i.e. with decreasing pore size.

be assumed that this leads also to a wide distribution of melting temperatures. An additional effect that needs to be considered is the fact that surface adsorbed films often start to melt at the respective interface well below the bulk melting temperature [1, 47, 300], as for example water at the interface to SiO_2 [78], graphite or talc [192]. This interfacial liquid layer then growths in thickness, when the temperature further approaches the bulk melting point.[1, 47, 78, 192] It is obvious that this has a strong impact on the phase transition behaviour of liquids in pores on the nanoscale, due to the high surface-to-volume ratio. There, the liquid in the pores starts to melt at the pore walls and the liquid phase then advances successively towards the pore centre. [1, 47] As a consequence, this leads to a broadening of this phase transition with respect to the temperature range.[1] The phase transition properties are further affected by the geometry of the porous medium, including surface roughness, which both might vary

locally, such that not only the phase transition temperature is shifted, but also the transition might be further broadened.[1, 17, 192] A complexification of the phase transition behaviour in confining geometries, together with a shift of the respective phase transition temperature, is also known from ionic liquids in silica [107, 144] and carbon [285] nanopores.
Likewise the peaks in the graph 6.4 (b) are shifted to higher temperatures with decreasing pore size, their maximum intensity is decreasing. This hints together with an increasing elastic scattering fraction in narrower pores (see figure 6.4 (a)), to a growing portion of immobilised cations concerning the diffusive motion. As an orientation also the contribution of the carbon matrix to the elastic scattering is drawn in panel (a) of figure 6.4, which was estimated as described in appendix C. The peak that is expected to be related to the diffusion of the whole cation and the one corresponding to the localised dynamics overlap now, whereas they are well separated in the bulk. The first of the two peaks, belonging to localised motions, seems to be also affected by the nanoconfinement, since its maximum also appears to be shifted to higher temperatures and is decreasing with decreasing pores size.

6.1.3. Quantitative analysis of the cation dynamics employing inelastic fixed window scan data

Now, on the basis of the inelastic fixed window scans, a first quantitative analysis of the molecular dynamics of [BuPy][Tf_2N] in the carbon nanoconfinement shall be undertaken, starting with an investigation of the bulk as a reference, to be able to judge on the confinement-induced alterations. Due to the limited number of data points, the diffusive cation motion in the high-temperature region can not be adequately analysed for the bulk [BuPy][Tf_2N], such that in this case the investigation is limited to the localised motions, at low temperatures.

Localised dynamics of bulk [BuPy][Tf_2N]

As described above, the localised low-temperature motions and those after the melting do not interfere in the inelastic fixed window scan data of the bulk material, such that they can be analysed independently. For the relaxation time $\tilde{\tau}_{\text{local}}(T)$ of these motions an Arrhenius temperature dependence,

$$\tilde{\tau}_{\text{local}}(T) = \tilde{\tau}_{\infty;\text{local}} \cdot \exp\left(\frac{E_{\text{a;local}}}{RT}\right) , \tag{6.2}$$

is assumed, where $\tilde{\tau}_{\infty;\text{local}}$ is the high-temperature limit of this relaxation time, R the universal gas constant and $E_{\text{a;local}}$ the activation energy of this dynamic process.[90, 111] The relaxation time provides a measure for the reorientation time scale of a molecule.[231] The scattering law of the localised dynamics can be expressed as

$$S_{\text{local}}(Q,T,\omega) = A(Q)\delta(\omega) + (1 - A(Q)) \cdot \frac{1}{\pi} \frac{\gamma_1(Q,T)}{\gamma_1^2(Q,T) + \omega^2} \ . \tag{6.3}$$

The elastic incoherent structure factor $A(Q)$ (EISF) of the localised motions is considered to be temperature independent, here.[13] Note, that also slow dynamic processes that lead to an energy transfer lower than the resolution of the respective instrument appear to be elastic. The half width at half maximum (HWHM) γ_l of the Lorentzian function is given as the inverse of the above relaxation time, i.e. $\gamma_l(T) = 1/\tilde{\tau}_{\mathrm{local}}(T)$.[90, 111] Thus, this half width is regarded as wave vector transfer independent, here. That there is no such Q-dependence for the methyl group dynamics, was not only shown in the past for a polymer [40], but is also found here in a respective analysis of the data. The latter is presented in appendix A.1.2. As a result for the analysis of the localised, low-temperature dynamics of [BuPy][Tf$_2$N] the over Q averaged intensity, as already shown as black curve in figure 6.4 (b), is considered in the following. Resulting from the above model this temperature-dependent intensity can be described by

$$I(T) = e^{-a\cdot T} \cdot \left[I_0 \cdot \frac{1}{\pi} \frac{\tilde{\tau}_{\mathrm{local}}(T)}{1 + \tilde{\tau}^2_{\mathrm{local}}(T) \cdot \omega^2_{\mathrm{IFWS}}} + c_0 \right] , \qquad (6.4)$$

which is evaluated for $\omega_{\mathrm{IFWS}} = \pm 2\,\mu\mathrm{eV}/\hbar$ and fits the data very well, as can be seen from graph 6.5. Within the parameter I_0 an intensity factor and the elastic incoherent structure

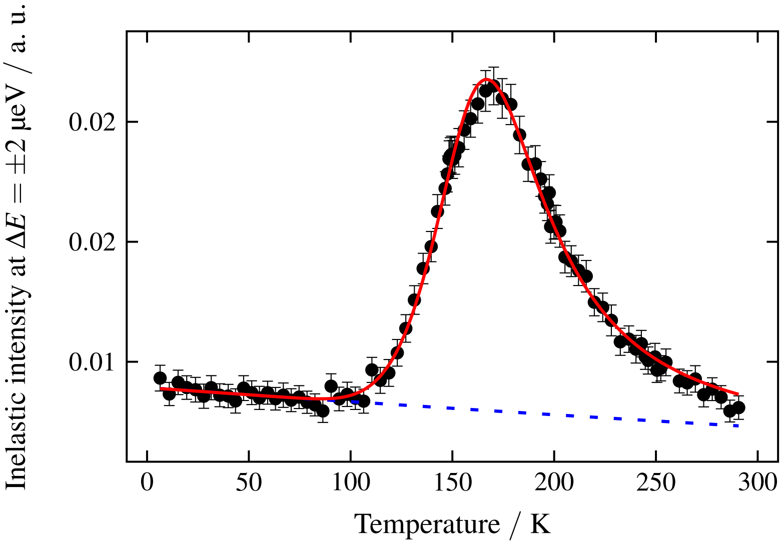

Figure 6.5.: Fit of the model for the localised, low-temperature dynamics of the bulk [BuPy][Tf$_2$N] to the temperature-dependent intensity data as obtained by the inelastic fixed window scan at $\Delta E = \pm 2\,\mu\mathrm{eV}$, averaged over the available wave vector transfer range. Dashed line indicates background, determined as described in appendix A.1.1.

factor from equation 6.3 are subsumed, while the delta part of this equation does not play a role here, since it can be considered to be outside the considered $\pm 2\,\mu\mathrm{eV}$ energy channel. The exponential prefactor, corresponding to a temperature dependence of the Debye-Waller factor, and the offset c_0 are determined from the low-temperature region of the elastic and inelastic fixed window scan data, respectively, where no disturbing dynamics can be observed in the latter, yet. The appropriate procedure for the determination of these two parameters is described at length in the appendix A.1.1.

The described analysis of the inelastic fixed window scan data yields an activation energy of 9.7 kJ/mol for the localised dynamics in [BuPy][Tf$_2$N]. This value is smaller than those obtained by Burankova et al. [30] by employing a three-site jump and a rotational diffusion model for the analysis of their elastic fixed window scan data, yielding 6.5 kJ/mol and 7.0 kJ/mol, respectively.[27, 30] Additionally, their determined values for the high-temperature limit of the relaxation time are around one order of magnitude higher than the one obtained, here. Disregarding that they employed other models for their analysis and utilised the data of an elastic instead of an inelastic fixed window scan, as it is done here, they also used a partially deuterated [BuPy][Tf$_2$N] sample. The protons of the pyridinium ring of their molecules were replaced by deuterium atoms. The incoherent scattering cross section of the latter is much smaller than that of ^{1}H, as can be seen from table 5.1. Consequently, there is practically no incoherent scattering contribution from the dynamics of that part of the molecule to the quasi-elastic neutron scattering signal, any more.

The attempt to use the three-site jump and the rotational diffusion model to analyse the elastic fixed window scan of the fully protonated cations, succeeds only for the three-site jump model (see appendix in section A.2 for details). However, also here, the results deviate from those of Burankova et al. [30], what is ascribed to the fact that apart from the methyl group rotations and segmental rotations of the butyl chain, also motions of the pyridinium might play a role. Since this comprises that the applicability of the three-site jump model is limited in this case and because of the very well agreement of the above model for the localised motions (see equation 6.4) with the respective data of the inelastic fixed window scan, the latter model is also used in the following analyses of the localised dynamics in the case of the nanoconfined [BuPy][Tf$_2$N]. Therefore, values for the activation energy and the relaxation time will be compared to the one obtained by that model only, for a better comparability.

Cation dynamics in carbon nanoconfinement of various pore sizes

As already mentioned above in the qualitative discussion of the dynamics in the confinement, the localised motions can not be considered independently from those of the diffusive one, here. As a result, a combined ansatz needs to be chosen. Mathematically this is done by convoluting the scattering laws of both dynamics (see also section 3.9):

$$S(Q,T,\Delta E) = S_{\mathrm{local}}(Q,T,\Delta E) \otimes S_{\mathrm{global}}(Q,T,\Delta E) \ , \tag{6.5}$$

such that the intensity of the inelastic fixed window scan is described by

$$I(Q,T,\Delta E) = e^{-a\cdot T} \cdot [I_0(Q) \cdot S(Q,T,\Delta E) + c_0(Q)] \ . \tag{6.6}$$

The first of the two components of this model describes the localised motions, fully analogous to above:

$$S_{\mathrm{local}}(Q,T,\Delta E) = A(Q)\delta(\Delta E) + (1 - A(Q)) \cdot \frac{1}{\pi} \frac{\Gamma_1(Q,T)}{\Gamma_1^2(Q,T) + \Delta E^2} \ , \tag{6.7}$$

where $\Gamma_1(Q,T) = \Gamma_1(T) = \hbar/\tilde{\tau}_{\mathrm{local}}(T)$ with the temperature-dependent relaxation time as defined in equation 6.2. The second component is the dynamic structure factor of the centre-of-mass diffusion of the cation, given by

$$S_{\mathrm{global}}(Q,T,\Delta E) = \frac{1}{\pi} \frac{\Gamma_2(Q,T)}{\Gamma_2^2(Q,T) + \Delta E^2} \ . \tag{6.8}$$

While the corresponding HWHM Γ_2 depends on the wave vector transfer Q, the half width Γ_1 is in analogy to the analysis of the localised dynamics of the bulk [BuPy][Tf$_2$N] above Q-independent. Since however, the number of free parameters would exceed the numbers of equations that need to be solved, further assumptions need to be taken into account. For bulk [BuPy][Tf$_2$N] Embs et al. [76] find in a QENS study that the HWHM Γ_2 of the global component is described by the Singwi-Sjölander jump-diffusion model [253], i.e.

$$\Gamma_2(Q) = \frac{\hbar D Q^2}{1 + D Q^2 \tau_0} \ . \tag{6.9}$$

Additionally, the self-diffusion coefficient D obeys an Arrhenius-like temperature dependence [76],

$$D(T) = D_\infty \cdot \exp\left(-\frac{E_{\mathrm{a;global}}}{RT}\right) \ , \tag{6.10}$$

while these data suggest in addition that also the corresponding residence time τ_0 exhibits such a temperature dependence, i.e.

$$\tau_0(T) = \tau_\infty \cdot \exp\left(\frac{E_{\mathrm{a;global}}}{RT}\right) \ . \tag{6.11}$$

This model is fitted to the inelastic fixed window scan data sets. The fitting procedure is performed simultaneously for all 16 wave vector transfers Q, available for the fixed window scans. This is done with a set of common parameters for all Qs, together with few that are Q-dependent. The high-temperature limits of the self-diffusion coefficient and the residence time, D_∞ and τ_∞, the activation energies of the diffusive and the localised dynamics, $E_{\mathrm{a;global}}$ and $E_{\mathrm{a;local}}$, and the relaxation time corresponding to the localised motions are the same for all Q. In contrast, the intensity factor I_0 and the EISF A are individual parameters for each Q (see also sections A.1.3 and A.1.4). The exponential prefactor and the background c_0 are determined as described in section A.1.1 of the appendix.

The temperature course of the intensity of the inelastic fixed window scans is very well reproduced by the above model. Figure 6.6 shows this exemplarily for representative wave vector transfers Q in case of the dynamics of the ionic liquid in the nanpores of the MoC-21 carbon sample. The black line is the best fit of the model to the measurement data (red triangles), while the background $\exp(-a \cdot T) \cdot c_0(Q)$ is plotted as blue dotted line. Respective curves for the two other nanoporous carbons, BC-no-9 and SiC-2, filled with [BuPy][Tf$_2$N] can be found in figure A.5 and A.4 in section A.1.3 of the appendix. The obtained activation energies and relaxation times for the localised dynamics, as well as the activation energies for the translational diffusive motion, are listed in table 6.1 for all analysed samples. The activation energy of the localised motions is found to be notably smaller in the case of the nanoconfinement, compared to the bulk. But more interestingly, it further decreases with decreasing pore size. The same trend is observed for the activation energy of the centre-of-mass diffusion of the cation. However, there is no decline from the value of the bulk liquid (taken from Burankova et al. [28, 31], Embs et al. [76, 77]) to the one corresponding to the cation diffusion within the nanoporous carbide-derived carbon sample with the largest pore size. At first glance it may appear counter-intuitive that the activation energies are successively reduced in the nanopore confinement, although the maxima of the curves from the inelastic fixed window scans

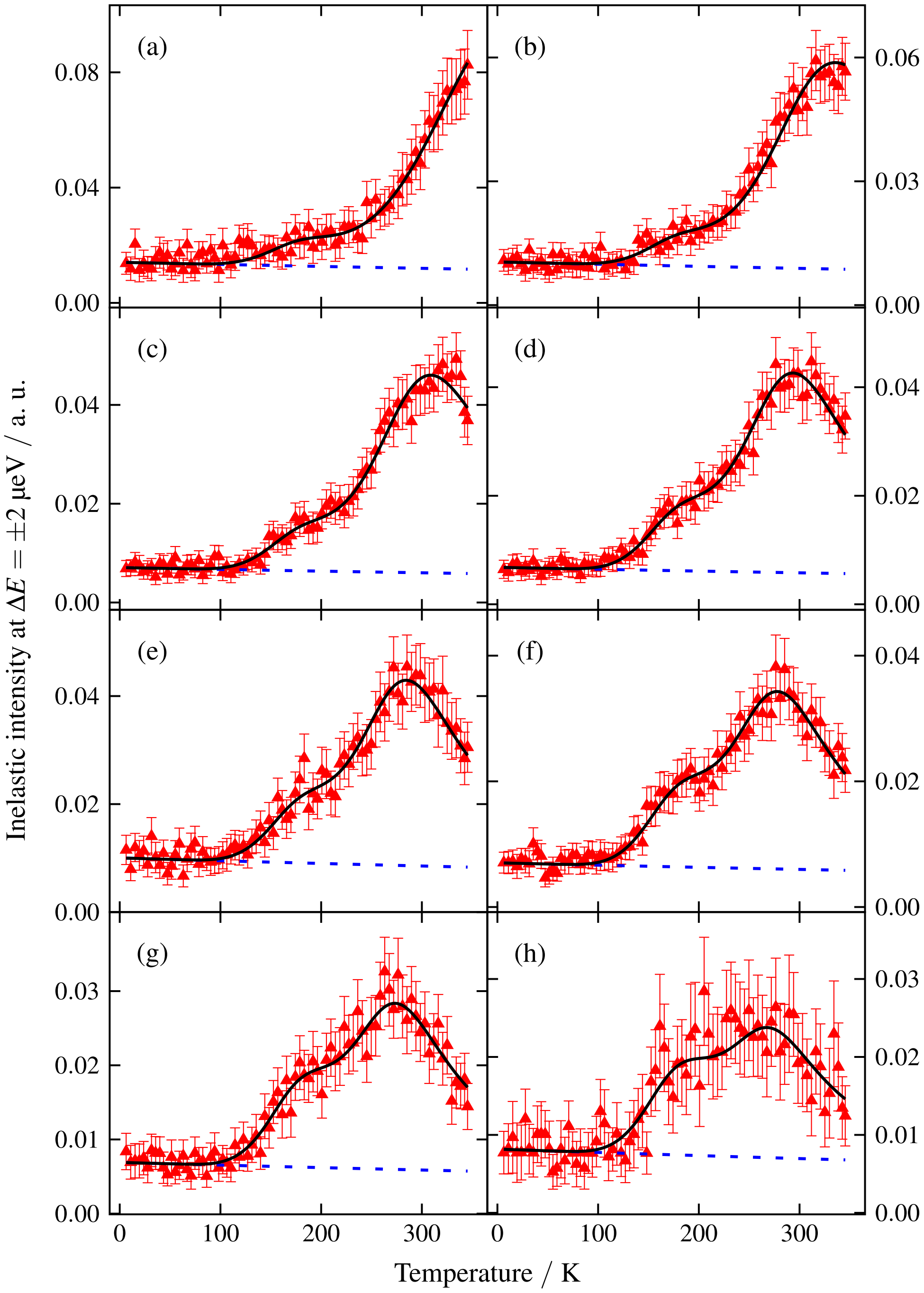

Figure 6.6.: Result of the fit as described in the text to the data of the inelastic fixed window scan of [BuPy][Tf_2N] in the nanopores of MoC-21, shown for eight representative wave vector transfers Q: (a) $0.44\,\text{Å}^{-1}$, (b) $0.70\,\text{Å}^{-1}$, (c) $0.95\,\text{Å}^{-1}$, (d) $1.18\,\text{Å}^{-1}$, (e) $1.39\,\text{Å}^{-1}$, (f) $1.57\,\text{Å}^{-1}$, (g) $1.72\,\text{Å}^{-1}$ and (h) $1.90\,\text{Å}^{-1}$.

Table 6.1.: Activation energies of the localised and diffusive dynamics, together with the relaxation times of the localised motions of [BuPy] in bulk and in the nanoconfinement of carbide-derived carbons (ordered by decreasing pore size). All data are obtained from the inelastic fixed window scans, except the bulk value of $E_{\mathrm{a;global}}$ (taken from [28, 31, 76, 77]).

	localised dynamics		diffusive dynamics
	$E_{\mathrm{a;local}}$ [kJ/mol]	$\tilde{\tau}_{\infty;\mathrm{local}}$ [ps]	$E_{\mathrm{a;global}}$ [kJ/mol]
bulk IL	↑ 9.7	0.3	12.3–14.8
MoC-21 + IL	7.1	3.6	↑ 15.1
BC-no-9 + IL	6.9	4.4	14.9
SiC-2 + IL	6.0	↓ 7.6	12.0

(see figure 6.4) are shifted to higher temperatures with decreasing pore size. But since by contrast the relaxation time $\tilde{\tau}_{\infty;\mathrm{local}}$ (see equation 6.2) increases (see table 6.1) at the same time, the connected line width Γ_1 decreases nevertheless. This HWHM Γ_1, as obtained from the inelastic fixed window scan analysis with the above models, is plotted in figure 6.7 as a function of temperature. Note, that this HWHM is also for the bulk considerably smaller than the one inferred by Embs et al. [76] from full energy transfer spectra of the bulk ionic liquid. The reason may lie in the fact that the simple model for the analysis of the inelastic fixed window scans subsumes all localised motions being activated over a large temperature range, starting already at very low temperatures. The spectra [76], however, were measured at only one, relatively high temperature, which is in addition higher as the highest temperature for the analysis of the localised dynamics of bulk [BuPy][Tf_2N] with the inelastic fixed window scans. Thus, it is possible that both data describe to some extent different dynamics.

An increase of the methyl group relaxation time in nanopore confinement is also known from other substances, like polymers [89, 240] and toluene [89, 204], where it is ascribed to the interaction of the confining pore walls with an immobilised surface layer. Also concerning the ionic liquid within the restriction of the carbon nanopores, such an influence of the pore walls appears to be reasonable. A reduction of the pore size entails a growth of the surface-to-volume ratio and thus strengthens the role of surface-interaction-induced effects. This corresponds with the found increase of the relaxation time with decreasing pore size (see table 6.1). Similarly, also the residence time τ_0 concerning the jump-diffusion process of the cation increases, while the corresponding diffusion coefficient D decreases, with decreasing pore size. This is shown in figure 6.8 (open circles) for selected temperatures. As a consequence of the slower diffusion, the corresponding line width Γ_2 (see equation 6.9) is smaller for the ionic liquid in narrower pores. Thus, the respective intensity maximum of the inelastic fixed window scans in figure 6.4 is shifted towards higher temperatures. Such a behaviour appears reasonable, since the increasing confinement in smaller pores hinders the molecular motions and thus prolongates the corresponding relaxation times and slows down the diffusion of the molecules. A further intensification of this effect occurs due to a growing fraction of immobile molecules at the pore walls, what lessens the volume of mobile ions, as will be discussed at length in section 6.2.4.

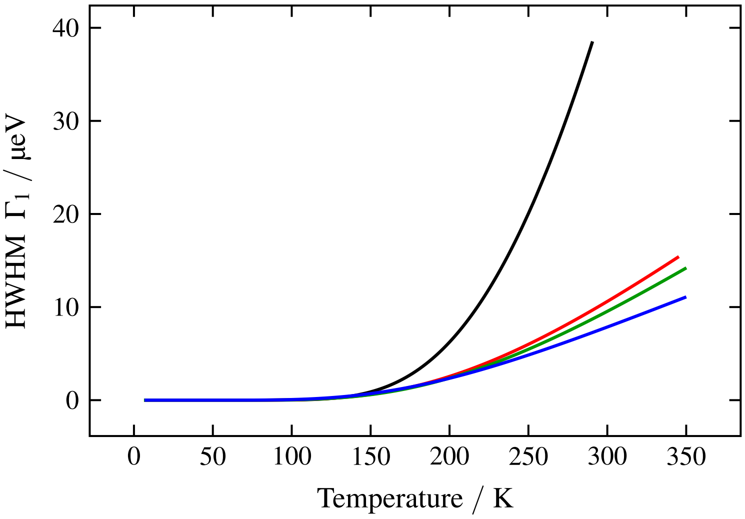

Figure 6.7.: Half width at half maximum Γ_1 as a function of temperature of the localised dynamics of [BuPy][Tf$_2$N] in — bulk and in the nanoconfinement of — MoC-21, — BC-no-9 and — SiC-2, as obtained from the inelastic fixed window scan analysis.

6.2. Full quasi-elastic spectra

The analysis of the fixed window scans delivers already a quite comprehensive picture of the molecular dynamics of [BuPy][Tf$_2$N] inside the nanopores of the carbide-derived carbons. However, it is intelligible that the data derived from only two energy transfer values can not contain as much information as complete energy transfer spectra do. For this reason, such full spectra were acquired at temperatures selected on the basis of the fixed window scans. This has been done at two spectrometers: The time-of-flight spectrometer FOCUS and the backscattering spectrometer IN16B, whose working principles are described in chapter 4. At IN16B spectra up to 350 K were measured. With the measurements at FOCUS a temperature range from 310 K to 390 K is covered. FOCUS possesses, compared to IN16B, a wider energy window, but a lower resolution, such that slow motions at low temperatures can not be resolved. In contrast, others are too fast to fit into the energy window of IN16B and contribute there in the spectra only as an approximately flat background. However, in this regard, the two spectrometers are practically complementary: IN16B with a resolution of 0.85 µeV allows for a maximum energy transfer of ±31 µeV with available Q-range from 0.19 Å^{-1} to 1.90 Å^{-1}, while FOCUS gives access to an energy transfer range of ±1.00 meV with a simultaneously accessible wave vector transfer range between 0.32 Å^{-1} and 1.64 Å^{-1} and a full width at half maximum of its resolution function of 39 µeV.

6.2.1. Dynamic structure factors for the analysis of the spectra

It is found that the QENS spectra can be analysed with the following dynamic structure factor

$$S(Q,\Delta E) = f \cdot \delta(\Delta E) + (1-f) \cdot S_{\text{dyn}}(Q,\Delta E) \quad , \tag{6.12}$$

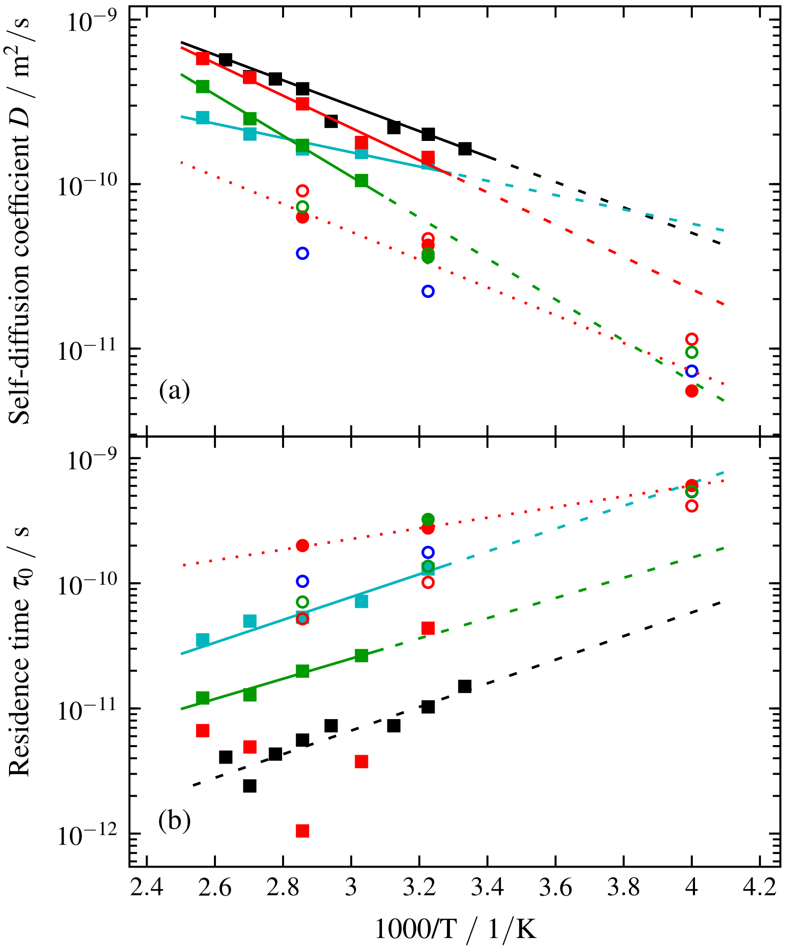

Figure 6.8.: (a) Self-diffusion coefficients D and (b) residence times τ_0 of the [BuPy] cation, as a function of temperature, determined using the Singwi-Sjölander jump-diffusion model, for ■ bulk [BuPy][Tf$_2$N] (taken from Embs et al. [76]) and confined in ■/●/○ MoC-21, ■/●/○ BC-no-9, ■ BC-9 and ○ SiC-2. Two translational diffusive processes on different time scales are observed. Squares denote data from the FOCUS time-of-flight spectrometer and circles such from the IN16B backscattering spectrometer, at which open circles show values derived from the inelastic fixed window scans. Solid lines are fits with an Arrhenius temperature dependence (see equation 6.10 and 6.11). Dashed/dotted lines serve as guides for the eye.

where

$$S_{\mathrm{dyn}}(Q,\Delta E) = S_1(Q,\Delta E) \otimes S_2(Q,\Delta E) \quad . \tag{6.13}$$

Within this scattering law a fraction f of immobile scatterers is incorporated, which accounts to the observation of a notable portion of elastically scattered neutrons in the spectra. This elastic fraction is ascribed to both dynamic components, in order to keep the model computationally as stable as possible. However, one should keep in mind that this is a simplification, since it assumes that the molecules stay immobile with respect to the motions related to both components at the same time. A further practically temperature-independent contribution to the elastic scattering intensity comes from the carbon matrix, while it however does not appreciably contribute to the quasi-elastic signal, as it was verified with measurements of the empty carbide-derived carbon powder.
The scattering laws

$$S_1(Q,T) = A(Q)\delta(\Delta E) + (1-A(Q)) \cdot \frac{1}{\pi} \frac{\Gamma_1(Q,T)}{\Gamma_1^2(Q,T) + \Delta E^2} \tag{6.14}$$

and

$$S_2(Q,T) = \frac{1}{\pi} \frac{\Gamma_2(Q,T)}{\Gamma_2^2(Q,T) + \Delta E^2} \tag{6.15}$$

are in principle fully analogous to S_{local} and S_{global} from the inelastic fixed window scan data analysis. However, the HWHM Γ_1 and Γ_2 are now treated as free parameters and the kind of dynamics they describe may differ from above, as will be seen below. With this dynamic structure factor the intensity of the spectra is described as

$$I(Q,\Delta E) = I_0(Q) \cdot S(Q,\Delta E) \otimes R(Q,\Delta E) + c_1(Q) \cdot \Delta E + c_0(Q) \quad , \tag{6.16}$$

where $I_0(Q)$ is an intensity factor and $c_1(Q) \cdot \Delta E + c_0(Q)$ is a linear background. I_0 also contains the Debye-Waller factor, which is not explicitly included here, since it would further increase the number of parameters. The dynamic structure factor $S(Q,\Delta E)$ is convoluted with the measured resolution function $R(Q,\Delta E)$ of the respective instrument. For IN16B the resolution function is acquired by a measurement of the respective sample at 2 K, and at 40 K in the case of FOCUS. At these temperatures there are no molecular dynamics, aside from lattice vibrations, being anyway outside the energy window. The model function 6.16 for the intensity is then fitted to the measured data using self-written software. The latter became necessary, because the available software did not meet the requirements. More information regarding this can be found in appendix B. The basic data reduction and detector efficiency calibration using a vanadium standard are done before this fitting procedure, using the software packages DAVE (FOCUS) [7] and LAMP (IN16B) [228]. Also corrections, like for multiple scattering and the subtraction of empty aluminium cell measurements in the case of IN16B are performed in this way.

6.2.2. Analysis of the spectra from the FOCUS spectrometer

For the data acquired at the FOCUS spectrometer the fit with the above model yields a line width Γ_1 of around 60–250 μeV, depending on the temperature. The HWHM Γ_1 is plotted

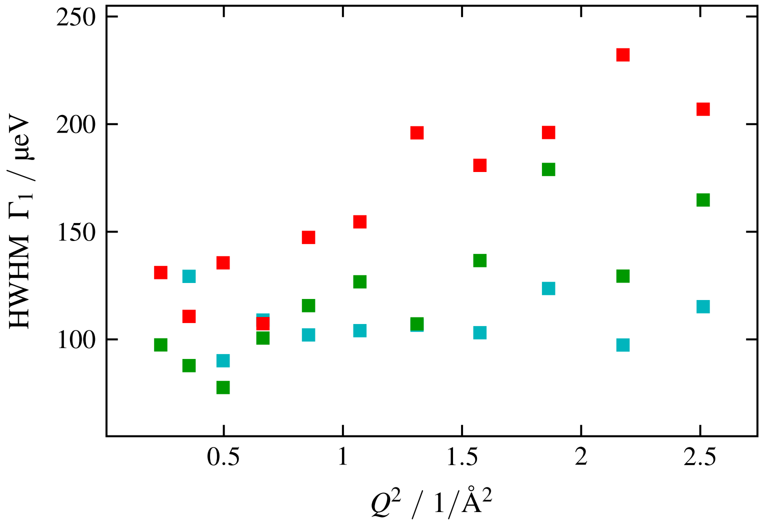

Figure 6.9.: HWHM Γ_1 ascribed to the localised dynamics of [BuPy][Tf$_2$N] as a function of Q^2. Data derived from FOCUS spectra measured at 370 K for the samples 🟥 MoC-21, 🟩 BC-no-9 and 🟦 BC-9.

exemplarily for a temperature of 370 K in figure 6.9 for the different ionic-liquid-filled carbon samples. Although for this example temperature the HWHM seems to depend on Q for the samples with large pores, it shows no distinct wave vector transfer dependence, in general. Its non-vanishing width towards low Q-values hints at spatially restricted motions. As in the case of the bulk ionic liquid [76], this component of the QENS spectra is ascribed to localised motions of the molecules, like for example the rotation of methyl end groups.[76]. Its magnitude is comparable with the one observed for the bulk liquid [28, 76], with a tendency to lower values in the confinement. Furthermore, as can be seen from figure 6.9, it exhibits a certain pore-size dependence, which hints towards decreased dynamics in narrower pores. The effect appears to be more pronounced at higher temperatures. The reduced line width in confinement and in smaller pores is in accordance with the results from the inelastic fixed window scans above. However, both findings disagree in their absolute values. One of the reasons might be the different analysis methods, as already explicated above for the deviations in the case of the bulk liquid (see section 6.1.3). But also the different energy resolution of both instruments can lead to this discrepancy. While slow dynamics are not resolved by the FOCUS spectrometer, the inelastic fixed window scans at IN16B are supposed to average over these slow as well as faster dynamics, up to a certain extent. When being thermally activated, also the faster dynamics are within the energy window of the inelastic fixed window scans, until they become faster with rising temperature. Consequently, they significantly contribute to the inelastic fixed window scans only when their HWHM is still comparatively narrow. In that way, this might lead to the considerably smaller values in case of the inelastic fixed window scans, where the applied model does not account for a possible heterogeneity of the localised dynamics.

In comparison to the line width Γ_1, the HWHM Γ_2 of the second component is notably smaller. Its wave vector transfer dependence follows the Singwi-Sjölander jump-diffusion model [253] (see equation 6.9). Figure 6.10 shows the best fit of this model to the line width as a function of Q^2 for the cation dynamics of [BuPy][Tf_2N] within the nanopores of MoC-21, BC-no-9 and BC-9 at different temperatures. Also for the ionic liquid in the pores of SiC-2, i.e. the granular carbon with the smallest pores, such QENS spectra were acquired. However, the dynamics concerning the diffusive component appear to be that weak that the resulting quasi-elastic line broadening is close to the resolution of the FOCUS spectrometer. Thus, it is not possible to determine self-diffusion coefficients from these data.

The self-diffusion coefficients D and corresponding residence times τ_0 for all other samples resulting from the jump-diffusion model are plotted as squares in figure 6.8. As one can see from this graph, these self-diffusion coefficients are considerably lower than those of the bulk (bulk values taken from Embs et al. [76]) and exhibit a distinct pore-size dependence, as they decrease with decreasing size of the confinement. In contrast, the residence time shows the opposite behaviour and increases with shrinking pore size. Both, the self-diffusion coefficient and the residence time, exhibit an Arrhenius temperature dependence, as can be seen from the lines in graph 6.8, representing respective fits to the data. However, the resulting activation energies diverge. They are different for the Arrhenius distribution of the self-diffusion coefficients and the residence times. This is in contrast to what was assumed for the analysis of the fixed window scans and might thus explain the different results obtained by the analysis of the spectra.

There, in contrast to the inelastic fixed window scans, no clear trend with respect to a possible pore-size dependence of the activation energies of the three analysed samples is identifiable — also not in comparison to the bulk value of 12.3–14.8 kJ/mol [28, 31, 76, 77]. For the self-diffusion coefficient related activation energy of the translational diffusive dynamics of [BuPy][Tf_2N] within the nanopores of MoC-21, as observed with FOCUS, a value of 19 kJ/mol is found. For BC-no-9 and BC-9 the determined activation energies are 23 kJ/mol and 8 kJ/mol, respectively. According to the sample characterisation (see section 5.1) BC-no-9 and BC-9 possess a very similar pore size distribution. However, since the two porous carbon materials underwent different synthesis pathways, it is reasonable to assume that they might exhibit differences in their pore wall roughness and pore morphology. Molecular dynamics simulations hint indeed towards altered dynamics as a consequence of such differences.[203] Bañuelos et al. [10] point out the importance of pore surface roughness and the surface morphology in general for the structure of ionic liquids inside nanoporous carbons. It appears plausible that such structural changes might go along with a modification of the ion's dynamics. Note additionally that the pore shape of BC-no-9 and BC-9 was assumed to be identical for the quenched-solid-density-functional-theory-model-based analysis of the nitrogen sorption isotherms. Thus, due to possible differences in the pore morphologies, the pore size distributions might deviate stronger in reality, than the ones obtained by this analysis.

All used carbide-derived carbon samples exhibit a considerably broad distribution of pore widths. As a consequence, the observed dynamics are a kind of average over those in pores of different size. Hence, also the associated activation energies underlie such an averaging. Interestingly, while the activation energies in the case of the MoC-21 and BC-no-9 carbons are higher than the bulk, the one for BC-9 is smaller. About the reasons one can only speculate, but it might again originate from structural changes of the ionic liquid induced by the pore

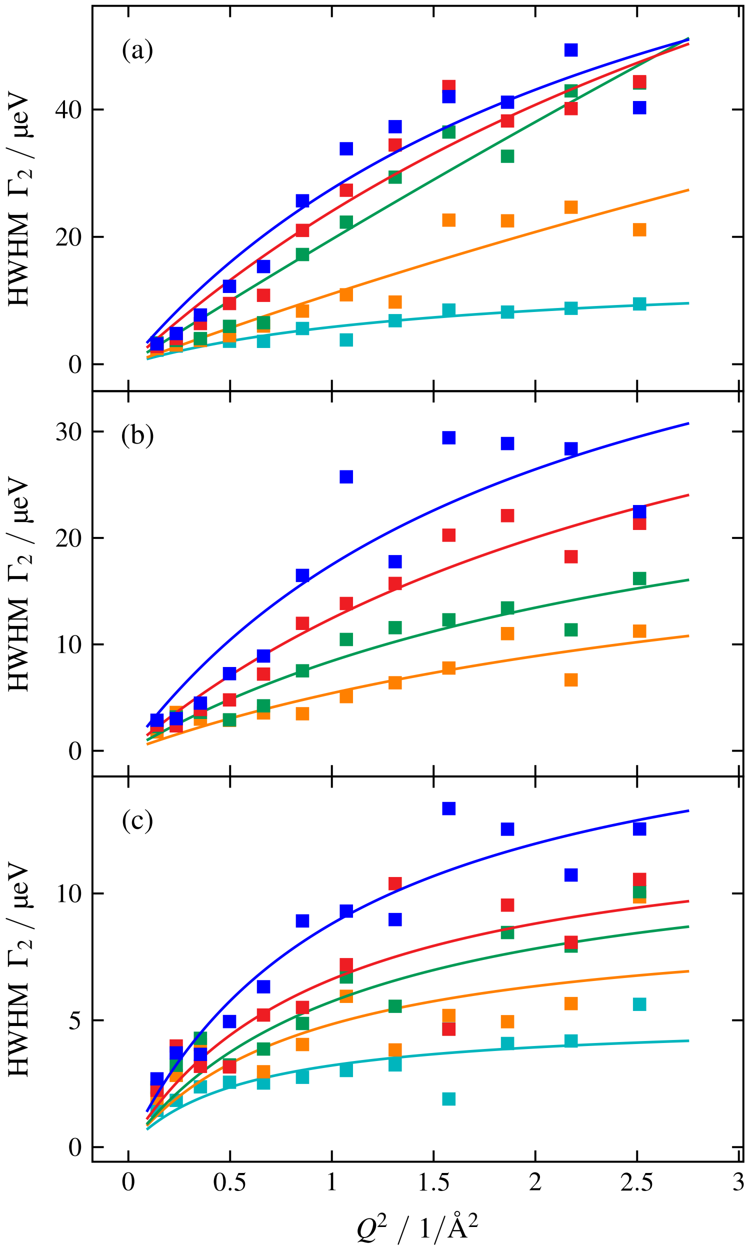

Figure 6.10.: HWHM Γ_2 of the diffusive motion of [BuPy] as a function of Q^2, as obtained from the analysis of the spectra acquired with the FOCUS spectrometer for a sample temperature of ■ 310 K, ■ 330 K, ■ 350 K, ■ 370 K and ■ 390 K, for [BuPy][Tf_2N] within the nanopores of (a) MoC-21, (b) BC-no-9 and (c) BC-9. Lines are fits with the Singwi-Sjölander jump-diffusion model.

morphology or interactions with the pores walls. Such a reduction of the activation energy concerning the translational diffusion in confinement compared to the bulk liquid has been for example already observed for hexane in porous silica, where the activation energy is even further reduced with decreasing pore width.[12] Also for supercooled water in silica nanopores such a pore-size dependence of the activation energy is observed.[184]

6.2.3. Analysis of the spectra from the IN16B spectrometer

Also the analysis of the full quasi-elastic spectra acquired with the IN16B backscattering spectrometer, which possesses a higher resolution, but smaller dynamic range than the FOCUS time-of-flight spectrometer, yields two dynamic components. The fit of the model from equation 6.16 above to the spectra together with the corresponding residuals is exemplarily shown in figure 6.11 for one wave vector transfer $Q = 1.28\,\text{Å}^{-1}$. Due to its HWHM, the broader

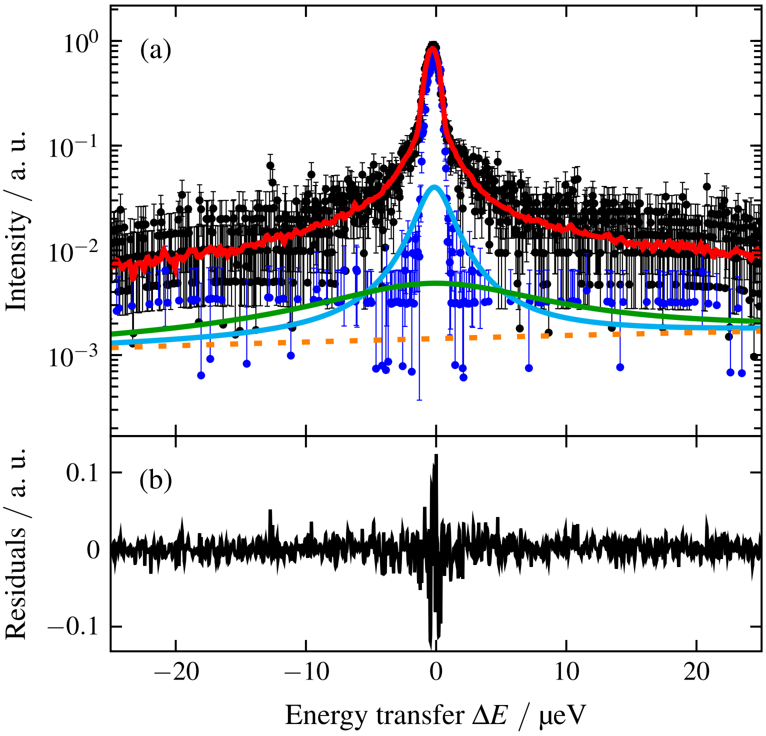

Figure 6.11.: (a) Fit to the ● spectrum acquired at IN16B for [BuPy][Tf$_2$N] in the nanopores of MoC-21 at 310 K and $Q = 1.28\,\text{Å}^{-1}$ with the model as described in section 6.2.1, where the — fit function is composed of a — narrow and a — broad Lorentzian together with a - - linear background, which are convoluted with the measured ● resolution function. (b) Residuals.

of the two Lorentzians is ascribed to the superposition of translational diffusive motions, as observed with FOCUS, and the slow localised dynamics, as derived from the inelastic fixed window scans. However, since both exhibit a comparable HWHM, a separation of the two

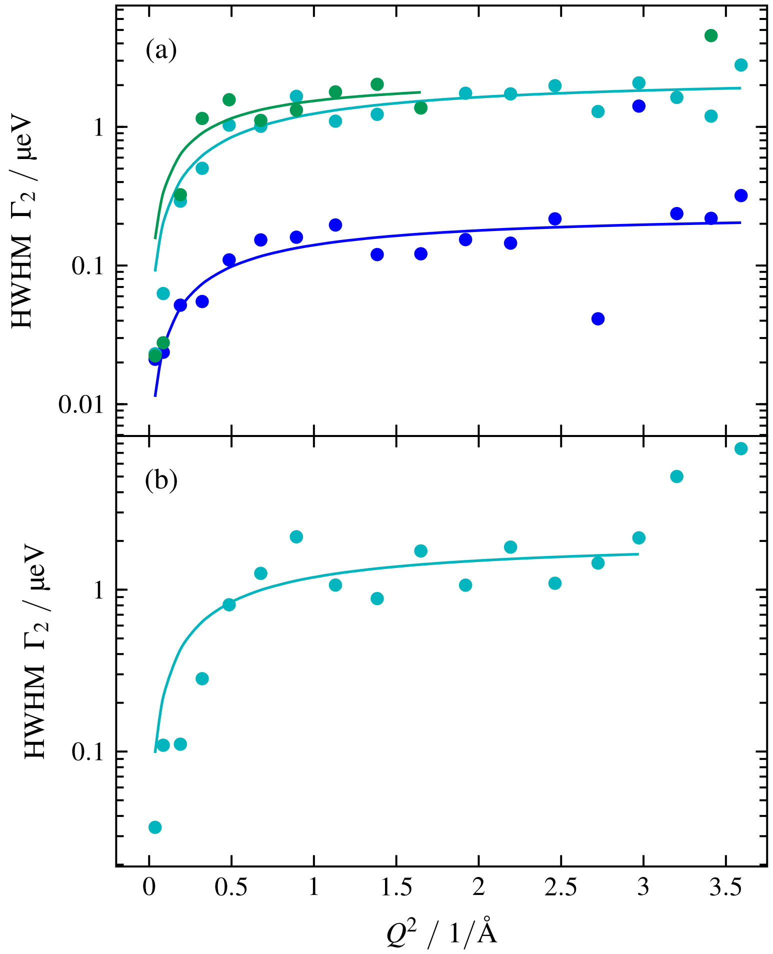

Figure 6.12.: HWHM Γ_2 as a function of Q^2 of the diffusive motion of the [BuPy][Tf$_2$N] cation, derived from the spectra acquired with the IN16B spectrometer with the model function as described in the text. Lines are fits with the Singwi-Sjölander jump-diffusion model to the data at ● 250 K, ● 310 K and ● 350 K for the samples (a) MoC-21 and (b) BC-no-9, filled with the ionic liquid.

components is quite challenging. Hence, the analysis of the spectra is focussed to their second, much narrower component.

The dynamics corresponding to the latter are found to be of diffusive nature and its HWHM is again following the Singwi-Sjölander jump-diffusion model, as can be seen from the respective fits in figure 6.12 for the ionic-liquid-filled carbons MoC-21 and BC-no-9 measured at different temperatures. There are several things that shall not be concealed at this point: For the IN16B spectra the fit procedure with the model from equation 6.16 is not completely stable, but may lead to different, though similar, results, depending on different starting parameters. As a consequence, the Singwi-Sjölander jump-diffusion model is applied to all reasonable results obtained with various initial parameters. The resultant parameters are then averaged for each sample and temperature. In this respect, the HWHM data shown in figure 6.12 are exemplarily selected curves. For the ionic liquid within the pores of SiC-2 no reliable self-diffusion coefficients could be derived from the quasi-elastic spectra, as it was also the case for the other two samples at lower temperatures. Furthermore, as in the case of [BuPy][Tf_2N] inside the pores of MoC-21 measured at 350 K, where the acquired spectra have poor statistics, due to a comparatively short measurement time, the obtained HWHM Γ_2 rises from a certain Q-value on suddenly to relatively high values. This is considered as an artefact or at least not to be related with the translational diffusion of the cation. Thus, the fit to the data with the Singwi-Sjölander model is performed over a respectively limited Q-range in these cases. This should be kept in mind, when interpreting the data, since it may affect the reliability of these data points.

However, the here determined self-diffusion coefficients (see solid circles in figure 6.8 (a)) are in a very good agreement with those derived from the inelastic fixed window scans (see open circles in figure 6.8 (a)) in section 6.1.3. Yet, the dynamic properties inferred from the inelastic fixed window scans are the result of a simplified model, containing only one component for each, the localised dynamics and the centre-of-mass diffusion of the whole cation, respectively. Hence, the derived parameters characterising the cation dynamics need to be considered as averaged over the fast diffusing species, as observed with FOCUS, and the slower one, as seen with IN16B.

6.2.4. Further discussion of the observed molecular dynamics

Heterogeneous dynamics

The self-diffusion coefficients of the slowly diffusing molecules inferred from the IN16B spectra (see solid circles in figure 6.8 (a)) are almost one order of magnitude smaller than those found with FOCUS (see solid squares in figure 6.8 (a)), where the molecular motions are observed on a different time scale. In the same way, the respective residence times τ_0 are increased by one order of magnitude, as can be seen from figure 6.8 (b). This is very interesting, because it means that two translational diffusive motions at different time scales exist in the carbon nanoconfined [BuPy][Tf_2N]. Moreover, as the results of the inelastic fixed window scans at IN16B in combination of the findings from the FOCUS spectrometer suggest, there is also a coexistence of fast and slow localised dynamics, amongst others ascribed to methyl group motions. It appears reasonable to assume that cations that exhibit sluggish translational diffusive motions are also those that correspondingly possess slow localised dynamics.

An existence of several translational diffusive motions at different time and length scales has been already observed for ionic liquids in 9 nm wide pores of ordered mesoporous carbon.[43, 44] But also in the bulk state such a dynamic heterogeneity is not unusual for ionic liquids.[16, 29, 83] Even for bulk [BuPy][Tf_2N] such a behaviour is observed.[28] In these cases one dynamic component is regarded as long-range translational diffusive motion of ions in the interspace of ionic aggregates, while the ions bound in these clusters move within them and diffuse collectively[1] [16, 28, 29, 80, 83].

---

[1] See section 2.2 of the introduction for a more detailed description of a proposed diffusion mechanism of ionic liquids forming such heterogeneous environments and its consequences for the ascertained diffusion coefficients with different techniques.

In this connection, Monte Carlo simulations and X-ray diffraction experiments find a disturbance of the ionic liquid's Coulombic ordering inside conductive pores like those of nanoporous carbons.[97, 153] There, image forces lead to a shielding of the electrostatic interaction between the ions [153, 154] and thus make the pairing of ions with the same charge more likely [97, 153, 154], at which this effect is observed to be stronger in smaller pores [97, 154, 155].

A further interpretation approach for heterogeneous diffusive cation dynamics is delivered by molecular dynamics simulations: These find that ions in molecular layers closer to the pore walls exhibit considerably decreased self-diffusion coefficients compared to those ions in the pore centre.[180, 252] Also Monte Carlo simulations on supercooled liquids find that molecules close to rough surfaces have notably larger relaxation times, where the influence of the surface reaches deeper into the liquid with decreasing temperature.[237] However, Scheidler et al. [237] further argue that as a result of the very broad distribution of relaxation times in such a case, experimental data might be misinterpreted towards the existence of a surface layer with drastically reduced dynamics, despite an underlying continuous distribution of relaxation times.

Although there are several reasonable explanation approaches for the observed dynamic heterogeneity, it is hard to trace it back to any particular effects within the scope of the available data. Presumably, there is even a complex interplay between several of these mechanisms. Furthermore, the observed dynamics are a superposition of the cation dynamics in different pores of these carbon materials with complex pore morphologies and wide pore size distributions.

Immobile ions

At all temperatures, the quasi-elastic spectra from both spectrometers contain a considerable fraction of neutrons that are elastically scattered within the time frame of the resolution of the respective instrument. Only a comparatively small part of this is contributed by the carbon matrix, as it is indicated in the figures 6.4 and 6.13 (see appendix C for the details on the estimation of this contribution). The predominant portion of the elastic scattering however originates from non-moving cations of the ionic liquid [BuPy][Tf_2N] within the pores. The immobile fraction decreases with increasing temperature. But even at 390 K, which is around 90 K above the bulk melting point, a notable fraction of immobilised cations exists.

Immobile surface layers, adsorbed at the pore walls, are a well-known phenomenon for complex molecules in nanoconfinement [89, 124, 159] and are also observed for ionic liquids in nanoporous carbons [9, 44, 68, 69]. Comparing the fraction of immobile ions within the different carbon samples, shown in figure 6.13, reveals only little differences between the specimens, although they differ in their pore size distribution. One of the reasons could be the fact that all carbon samples possess micropores, whose volume is comparatively large. Cations adsorbed within these micropores might be expected to remain largely immobile. Though, it appears that there is a weak tendency towards a higher amount of immobile ions in samples with smaller pores, at which one should be aware of the uncertainties due to the contributions of the carbon matrix (see appendix C). However, such a tendency would be reasonable, because the surface-to-volume ratio is higher in narrower pores and consequently a higher fraction of the overall pore volume is occupied by these immobile layers.

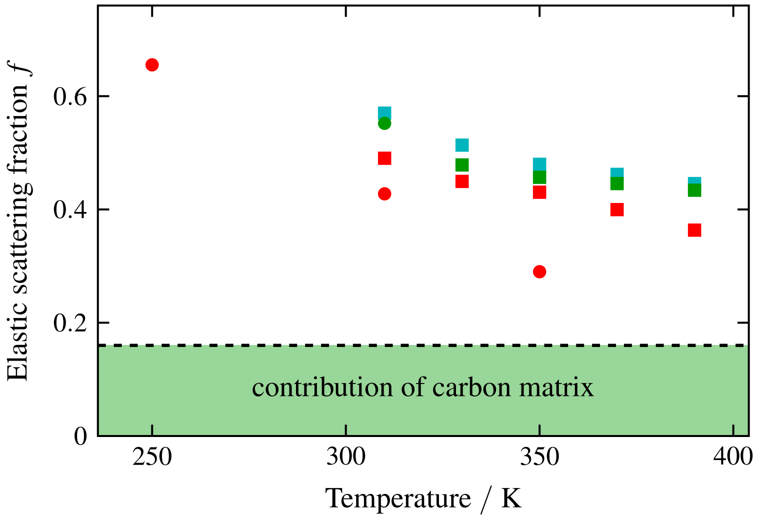

Figure 6.13.: Fraction f of the elastically scattered neutrons in the quasi-elastic spectra, measured at the FOCUS (solid squares) and IN16B (solid circles) spectrometer, as a function of temperature for the [BuPy][Tf_2N] ionic liquid within the nanopores of 🟥/🔴 MoC-21, 🟩/🟢 BC-no-9 and 🟦 BC-9.

Furthermore, such a pore-size dependence of the immobile fraction is also supported by the comparison of the elastic fixed window scans in figure 6.4 (a) of the ionic liquid in the pores of the different carbon samples. While the elastic intensity of MoC-21 with [BuPy][Tf_2N] in its comparatively large pores appears to saturate at high temperatures only somewhat above the elastic contribution of the carbon matrix, the saturation value of the elastic intensity for the samples with smaller pores is notably higher and besides increases with decreasing pore width. The immobile fraction concerning those molecules that exhibit the slower of the two translational diffusive motions (measured with IN16B; solid circles in figure 6.13) in the nanoconfinement appears to be lower than that of the faster diffusing cations (found with FOCUS; solid squares in figure 6.13). This can be ascribed to the fact that the time scale of the slow dynamics is below the resolution of FOCUS and thus they appear to be immobile there, giving rise to a seemingly elastic contribution to the scattering signal, while they are seen as mobile within the higher resolution of IN16B.

CHAPTER 7

Conclusions & outlook

The molecular mobility of the room-temperature ionic liquid [BuPy][Tf_2N] within the nanopores of carbide-derived carbons was investigated using quasi-elastic neutron spectroscopy methods. There, the focus is on the self-diffusion dynamics of the cation, comparatively studying its motions in pores of different sizes and at various temperatures.
A first but already quite conclusive overview about the dynamic landscape within this system is obtained from the analysis of so-called elastic and inelastic fixed window scans at the neutron backscattering spectrometer IN16B. These enable one to quickly scan one sample environment parameter, so that a wide temperature range from 2 K to 355 K is covered for the investigation of the dynamics. During these scans no full quasi-elastic spectra are measured, but only data at fixed energy transfer values are acquired. Nevertheless, it is shown that the application of suitable models for the analysis of these data delivers quite reliable results on the molecular dynamics. This is confirmed by the subsequent comparison with the results from full quasi-elastic spectra.
These spectra were acquired at selected temperatures on two instruments — IN16B (Institut Laue-Langevin, Grenoble) and the time-of-flight spectrometer FOCUS (Paul Scherrer Institute, Villigen) — with practically complementary resolution and dynamic range. The analysis of these spectra employing the Singwi-Sölander jump-diffusion model points towards the existence of heterogeneous dynamics with two translational diffusive motions. These are deviating by one order of magnitude in their self-diffusion coefficients and residence times, which furthermore obey an Arrhenius temperature behaviour. This dynamic heterogeneity of the carbon-confined ionic liquid is ascribed to the complex interplay of intrinsic properties of the ionic liquid and several confinement-induced effects.
The temperature-dependent analysis of the nanoconfined ionic liquid further reveals that their cation's molecular mobility is already activated well-below the melting point of the bulk liquid, which is of interest concerning possible technical applications of such systems. However, at all considered temperatures, i.e. also for example around 90 K above the melting temperature of the bulk, a considerably temperature-dependent fraction of immobile ions is found, too.
Overall, the results show that the molecular dynamics of [BuPy][Tf_2N] exhibit a dependence on the pore width of the nanoconfinement. The mobility decreases with decreasing pore size. However, the derivation of a detailed pore-diameter dependence is difficult. This is owed to

the very broad and multimodal pore size distribution of the carbide-derived carbons, together with the ill-defined shape of their pores. These carbide-derived carbons are therefore not well-suited as model systems to study pore-size-dependent effects. Nevertheless, this study delivers valuable insights into a technically relevant system, since the carbide-derived carbons are being regarded as potential candidates for applications like supercapacitors.

Future investigations dealing with the pore-size dependence of the ionic liquid dynamics should utilise carbons with more defined pore size distribution and morphology. An alternative might be for example ordered mesoporous carbons [72, 166, 198, 283] with hexagonally arranged cylindrical pores [198].

Another interesting approach would be the use of monolithic porous carbons [122, 143, 291]. If the presence of macropores and macroscopic cracks can be excluded, then this would facilitate the filling procedure with the ionic liquid. It would not be necessary anymore to exactly match the pore volume with the volume of the liquid. Therefore, there would be no problem with possible under- or overfilling, where the latter would lead to bulk liquid in between the grains of powder samples, possibly dominating the measurement signal. Furthermore, since any free liquid between the carbon can be avoided, there would be the possibility to study the ion dynamics under an electrical potential, where the monolithic carbons serve as electrodes. It would not only be of fundamental interest to investigate the influence of electrified pore surfaces on the mobility of these charged molecules, but it is also important with regard to the application of such systems as electrochemical charge storage devices.

The systematic study of the dependence of the ion dynamics on different pore surface chemistries in conjunction with a variation of the chemical composition of the ionic liquids would be also interesting. As already noted in the introduction, some publications [69, 70, 129] have already observed some notable effects in this respect. For instance there are hints that the ionic liquid dynamics in carbide-derived carbons with an oxidised pore surface are increased in contrast to such with a defunctionalised one.[69, 70] Also the surface silanisation of silica nanopores leads to an increase of the ionic liquid dynamics in contrast to the untreated pore surface.[129] In addition to the influence of the pore wall chemistry on the dynamics, the one of its roughness needs more attention.

For the disentanglement of the single molecular motions as found with this quasi-elastic neutron scattering study, not only the above proposed experiments with very well-defined pores would be beneficial, but also such employing neutron spin-echo and diffuse scattering spectrometers. The latter allow, through a polarisation analyis of the neutrons, a separation of the coherent and spin-incoherent contribution to the scattering signal.[28, 29] Thus, possibly collective ion motions could be identified, while the last mentioned instrument type delivers further information about the structure.[28, 29] In this way it might be possibly to find out, whether there are still ionic clusters in the carbon nanoconfinement, as they exist in the bulk [28], and how they influence the confined ion dynamics.

Furthermore, concerted computer simulations on these systems of carbon nanoconfined ionic liquids could be enlightening. Especially, they are expected to bring insights into the nature of the observed two translational diffusive motions on different time and length scales. However, due to the comparatively large molecules within the nanopores, a realistic modelling of the structure of the ions and the porous carbons would be necessary. This could be complemented by a more sophisticated analysis of the quasi-elastic neutron scattering data, taking more complex molecular motions, as well the distribution of pore sizes, into account.

Part II.

Structure of confined liquid crystals

CHAPTER 8

Motivation for the analysis of confined liquid crystals

Liquid crystals exhibit many interesting properties, which make them well-suited for applications like organic electronics, energy conversion, tunable lasers, drug delivery and template-assisted synthesis of nanomaterials.[54, 133, 164, 170, 244, 281, 288] However, the most prominent usage of this versatile class of materials is the one in displays, where liquid crystals electrically switchable control the transmittance of light. One type of liquid crystals considered for the application in special purpose displays, such as fast, high-resolution microdisplays, are so-called ferroelectric liquid crystals.[3, 141, 165, 255, 296] These displays take advantage from the fast bistable electro-optical switching in thin, micrometre-sized cells, enabled by the special molecular arrangement of these ferroelectric liquid crystals.[49, 53, 141, 165, 255]

Liquid crystals distinguish themselves by certain kinds of collective molecular order, depending on the mesogens and boundary conditions, as described in the next chapter. The direction in which their molecules collectively align through self-organisation is arbitrary in space, if the liquid crystal is in the bulk state. However, in contact to a surface the situation is different. It has been shown, that these substrates can predominate the molecule's alignment direction.[207] Interestingly, their spontaneous alignment into a certain direction can be induced by macroscopic structures on the respective surface, as well as by interactions on the microscale.[207] It is evidently clear, that this effect is of great importance for most of the above mentioned applications — especially those, where the liquid crystals are confined in small cells, entailing a high interface-to-volume ratio.

The molecular arrangement of liquid crystals is even more affected if the confinement size is decreased to the nanoscale, where not only the surface-to-volume ratio is further increased, but also the spatial restriction has the potential to hinder the (re-)orientation of the liquid crystal molecules.[130, 234] Furthermore, these effects influence the temperature-induced changeover between different molecular orders of the respective liquid crystals within the confining environment.[60, 130, 227, 234]

For instance, the respective phase transition temperatures are frequently found to be shifted in the nanoconfinement, while the transition is furthermore often broadened.[113, 160–162, 227] Also a complete suppression of a phase transition is possible.[113] Although, it appears that a majority of the studies of liquid crystals within nanopores find a downward shift of the phase transition temperature [113, 160–162], there are competing effects which can drive the transition temperature in the one or the other direction.[60, 227] While disorder through finite size effects or rough pore walls is expected to decrease the phase transition temperatures, an enhanced order as a result of a strong surface anchoring of the mesogens has the opposite effect.[60, 227] The impact of the surface alignment of the liquid crystals becomes also apparent from the fact that it can lead to the formation of a so-called paranematic phase, where the molecules within a certain distance to the surface align parallel to the latter, while the rest of the liquid crystal can be still in the isotropic phase with randomly oriented molecules.[131, 148, 246, 247] However, the anchoring of the liquid crystal molecules at the confining surface does not only influence the phase transition behaviour, but also leads to interesting changes in the arrangement of the mesogens within the confined volume — as will be seen later in this work.

In the context of the above non-exhaustive enumeration of interesting effects of nanoscale confinement on the properties of liquid crystals, this second part of the thesis is concerned with the phase transition properties and the structure of thermotropic, chiral liquid crystals within the confining geometry of cylindrical nanochannels. Compared to the unordered, interconnected pore networks in whose voids the liquid crystals are investigated in several of the above cited studies [160–162, 227], the here used nanochannels have the advantage that there are no curved segments or junctions of pores, which might perturb the order of the liquid crystal molecules. Consequently, the number of influencing factors on the properties of the confined liquid crystal is reduced. Thereby, they allow the study of more uniform structures, so that for instance the dependence on the confinement size can be better ascertained. The structure and the phase transition behaviour of the nanochannel-confined liquid crystals in this work is studied as a function of temperature and pore size by an X-ray and neutron diffraction-based analysis of the structural arrangement of the molecules within the pores.

CHAPTER 9

Brief introduction to liquid crystals

In this chapter some fundamentals of liquid crystals important for the understanding of the results presented in the following sections are introduced. The main focus lies on the two types of liquid crystals that are investigated in this work. These are cholesteric and ferroelectric liquid crystals, both consisting of chiral, rod-like molecules. However, at this point only a brief introduction to liquid crystals can be given. For a deeper understanding of the theory of liquid crystals the interested reader is referred to the large variety of textbooks on this topic.

9.1. Types of order of liquid crystals

While being an isotropic liquid at elevated temperatures, liquid crystals start to exhibit particular types of order when being cooled under a certain temperature, specific for each liquid crystal. So-called thermotropic liquid crystals additionally show phase transitions between different order types under temperature variation. In the following some types of liquid crystalline order are introduced. While there exist considerably more, only those types of order relevant for this work are presented.

9.1.1. Nematics

In the so-called nematic phase the molecules exhibit no long-range translational order, similiar to conventional liquids and also their flow characteristics are alike.[106] However, they orient parallel to a common axis (see sketch in figure 9.1 (a)), whose direction defining unit vector $\vec{n}$ is commonly denoted as 'director'.[106] In principle this direction is arbitrary, however, it is often affected by exterior influences.[106] Especially in the case of strong confinement as inside the nanoporous media later in this work (see chapter 11), this fact is of great importance. The nematic phase shows an optical anisotropy. Nematics of uniaxial symmetry for instance possess two different refractive indices, with the optical axis parallel to the director $\vec{n}$, and exhibit an optical birefringence. Concerning the director there is no physical distinction between the directions $\vec{n}$ and $-\vec{n}$.[106] In systems consisting of chiral molecules, i.e. such that can not be brought in congruence with its mirror image, no nematic phase occurs (an exception are 1:1, called racemic, mixtures of the constituent molecules of opposing chirality).[106]

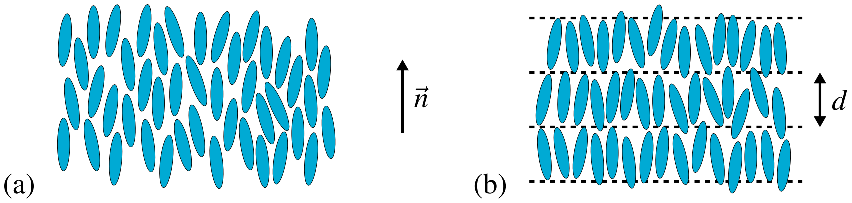

Figure 9.1.: Sketch of the arrangement of molecules in the (a) nematic and (b) smectic liquid crystalline phase.

9.1.2. Cholesterics

Liquid crystals formed by chiral molecules, however, constitute a similar structure like the nematic phase, i.e. with an absence of long-range translational order and a preferred orientation along a director $\vec{n}$.[106] However, in this cholesteric (or chiral nematic) phase the latter is not constant, but alters its direction in space.[106] Thereby, the preferred formation is helical and the components of the director $\vec{n}$ are defined as [106]

$$\begin{aligned} n_x &= \cos(g_0 z + \phi) \\ n_y &= \sin(g_0 z + \phi) \\ n_z &= 0\,. \end{aligned} \tag{9.1}$$

The axis of the helix, here the z-direction, as well as the phase ϕ are arbitrary.[106] The indistinguishability between the $\vec{n}$ and $-\vec{n}$ director state leads to the fact that the length of the periodicity of this system is the half of the pitch length $2L$, i.e.

$$L = \frac{\pi}{|g_0|}\,.[106] \tag{9.2}$$

The typical periodic length is here often in the range of optical wavelengths, but can also be much larger.[106, 149] The handedness of the helix is determined by the sign of the twist g_0 and is always the same for a given temperature, but it can undergo a phase transition from left- to right-handed or vice versa when the system undergoes a change in temperature.[106]

9.1.3. Blue phases

In chiral nematic liquid crystals additional types of molecular order can arise. If the chirality of the system is high enough, up to three different so-called blue phases can form in the temperature range between the nematic and the isotropic phase.[149] They are denominated as blue phase I to blue phase III in sequence with increasing temperature, in which all phase transitions of the bulk liquid crystal are of first order.[106] While a cubic symmetry is exhibited by the blue phases I (body-centred cubic) and II (simple cubic), the symmetry of the blue phase III with a short range chiral order resembles the one of the isotropic phase.[106, 149]

9.1.4. Smectics

Another type of molecular order in liquid crystals is the so-called smectic phase (see sketch in figure 9.1 (b)), which commonly occurs at lower temperatures compared to the nematic phase.[106] This phase is more ordered than the nematic phase since it exhibits a layer structure in one dimension. The molecules inside these layers show no long-range order, being therefore a two-dimensional liquid, and are collectively aligned parallel to a director $\vec{n}$, as already described for the nematics.[106] The layer structure and the respective interlayer distance d can be studied using X-ray and neutron diffraction techniques, as described in the following chapters. For the smectic order several subtypes are differentiated, which have additional characteristic properties. Again only those of relevance for this work are presented.

Smectic A phase

In the smectic A phase the director is parallel to the normal vector $\vec{z}$ of the layer plane and the states $\vec{n}$ and $-\vec{n}$ are again physically equivalent.[106] This structure is rotationally symmetric around the $\vec{z}$-axis and it is optically uniaxial [106], in which the optical axis is along the director $\vec{n}$ as for the nematics and coincides with the smectic layering direction $\vec{z}$, here. Consequently, such a structure is birefringent. If a smectic A phase is formed by chiral molecules it is often referred to as smectic A* phase.

Smectic C and C* phase

The molecules in the layers of the smectic C phase in contrast to the smectic A phase are collectively tilted by an angle ϑ with respect to the normal vector of the layers. Such a phase possesses in general an optical and electrical biaxiality.[106] Consequently, there are three principal refractive indices, in which two, being orthogonal to each other, are lying in the tilt plane and the third one is perpendicular to them. In liquid crystals where also a smectic A phase exists, the smectic C phase usually appears at temperatures below the smectic A phase.[149]

If the liquid crystal consists of chiral molecules (except racemic mixtures), the tilt angle is not constant along the layer normal vector, but performs a precession around the same.[106] The resulting helical structure, distinguished from the cholesterics by the presence of a layer structure, is called smectic C* phase.[106] The last-mentioned structural peculiarities lead to special physical properties, described in section 9.3.

9.2. Order parameters

In real liquid crystalline systems the molecules are not perfectly collectively aligned with their long axis parallel to the director $\vec{n}$. Rather the director represents the average molecular orientation, while the molecules are statistically tilted away from that direction by a small angle ϑ.[277] A measure for the degree of orientational order in liquid crystals is therefore the orientational order parameter

$$S = \frac{1}{2}\langle 3\cos^2(\vartheta) - 1\rangle \ , \tag{9.3}$$

being zero in the totally unordered, i.e. isotropic state, and one if all molecules are perfectly aligned parallel to $\vec{n}$ with their long axis.[106, 277, 304] In actual liquid crystals the order parameter S can be expected to be always smaller than one and it will likely decrease with rising temperature.[172, 277] This has consequences for the smectic layer thickness: For instance, as it will be also seen in section 11.2, the layer thickness in the smectic A phase can not only be smaller than the length of the molecules, but it can also possess a temperature dependence, although the director is still perpendicular to the smectic layer planes, i.e. the smectic A structure is still preserved.[277]

The orientational order parameter S only describes the order with respect to the orientational deviation of the molecules in relation to their predominant direction $\pm\vec{n}$. It is often referred to as nematic order parameter, since it is the defining characteristic of the nematic phase. In the smectic phases however, at least one second type of order is added: The arrangement of the molecules in a layered structure that can be described by a density modulation orthogonal to the layers along $\pm\vec{z}$:

$$\rho(z) = \rho_0 + \sum_m \rho_m \cos\left(\frac{2\pi m z}{d} - \Phi\right) \ , \tag{9.4}$$

where Φ is an arbitrary phase.[22, 106] From the infinite number of coefficients ρ_m of the density modulation harmonics, ρ_1 of the first harmonic is usually referred to as smectic or translational order parameter:

$$\rho_1 = \langle\cos\left(\frac{2\pi z}{d}\right)\rangle \ . \text{[106, 151, 152, 194, 195]} \tag{9.5}$$

In the nematic or isotropic state, which do not possess a translational order along the $\vec{z}$-axis, ρ_1 is zero, while it would be one if a perfect translational order would exist parallel to that axis.[163]

In smectic phases, layer fluctuations can occur, which yield for the layer displacement $u(\vec{r})$

$$\Phi(\vec{r}) = -\frac{2\pi}{d} u(\vec{r}) \ . \text{[106]} \tag{9.6}$$

Fluctuations of the modulation intensity ρ_1 have to be taken into account in the vicinity of a phase transition.[106] These circumstances are incorporated in the complex order parameter

$$\Psi(\vec{r}) = \rho_1(\vec{r})\, e^{i\Phi(\vec{r})} \ . \text{[104, 106, 195, 196]} \tag{9.7}$$

In the absence of distortions only the real part of the order parameter, i.e. ρ_1, as shown in equation 9.5, is used in practice. The complex order parameter describes the smectic order on the macroscale and it seems that it is not suitable for the modelling of smectic phases on the nanoscale.[224] However, for this work this is not crucial. Although the liquid crystals are confined in nanochannels (see section 10.3 and chapter 11, respectively), the employed

experimental techniques, like the X-ray and neutron diffraction or the optical measurements, average over a comparatively large volume. This means that they are acting on the macroscale, although investigating nanoscale properties.
Note, that in general, there is a coupling between the orientational and the translational order parameter whose strength varies between different liquid crystalline systems.[22, 106, 152, 194, 195] This coupling can have a great impact on their properties, especially on their phase transition behaviour, as discussed in section 11.1.

9.3. Ferroelectric liquid crystals

There are solid dielectric crystals exhibiting a permanent polarisation, which can be significantly altered by an external electric field. This phenomenon is known as ferroelectricity. However, this effect is not limited to solid crystals but also exists with a sort of liquid crystals, the so-called ferroelectric liquid crystals. The origin of the spontaneous polarisation in these liquid crystals is their composition of chiral molecules [149], as an occurring polarisation can not be cancelled out by any symmetry operation, for example a rotation of the molecules [106]. However, there is no direct relation between the ferroelectric characteristics and the helical structure, i.e. ferroelectricity can also exist without the presence of a helical structure and vice versa.[149]
The spontaneous polarisation originates from the permanent dipole moment of the liquid crystal molecules.[149] Due to symmetry reasons there is no net polarisation in untilted phases (e.g. smectic A), but only in such where the molecules are tilted with respect to the layer normal.[149] Since the molecules inside the layers exhibit fluid properties, they have respective degrees of freedom of molecular motion especially rotation around certain axes, while still maintaining the superordinate collective structure. Consequently, one needs to consider the time-averaged dipole moment, whose component parallel to the tilt plane averages to zero, while there is a finite moment remaining for the component perpendicular to it.[149] The direction of the consequential spontaneous polarisation $\vec{P}$ is perpendicular to the just mentioned tilt plane spanned by the director $\vec{n}$ and the smectic layer normal $\vec{z}$, i.e. it points in the direction $\pm(\vec{z} \times \vec{n})$, in which a positive sign describes a right-handed system and a negative sign consequently a left-handed one.[149] The magnitude of the spontaneous polarisation depends in general in a non-linear manner on the tilt angle ϑ.[21, 149] Since in the smectic C* phase the direction of $\vec{n}$ is changing from layer to layer, describing a helical structure, also the direction of the spontaneous polarisation changes in this manner. Although in general, this leads in sum to a vanishing macroscopic spontaneous polarisation, in special cases, e.g. where an electric field or a micrometre-sized slab confinement leads to a distortion of the helix, a non-zero polarisation is observed.
There are smectic liquid crystals where the spontaneous polarisation suffers a sign inversion at a particular temperature (see e.g. references [74, 110]). However, most liquid crystals do not show such a behaviour, but are having either a positive or negative sign over the complete temperature range of the smectic C* phase.[149]

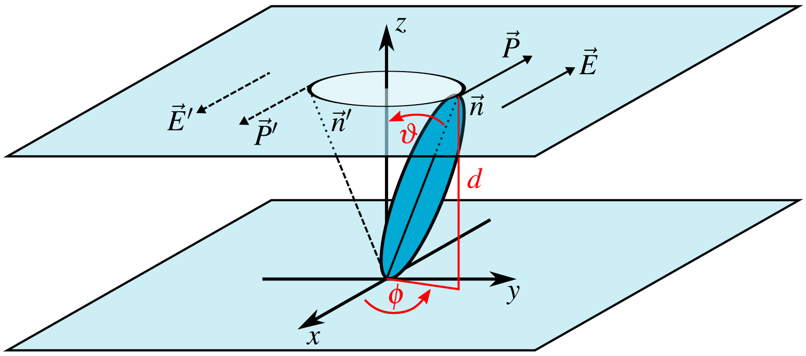

Figure 9.2.: Field-induced director reorientation in a ferroelectric liquid crystal: Large electric fields $\vec{E}$ force the polarisation $\vec{P}$ of the smectic layer planes to align parallel to $\vec{E}$ causing an adjunctive molecular reorientation. On inverting the electric field $\vec{E}$ to $\vec{E}'$, the director $\vec{n}$ is switched to $\vec{n}'$ while ending up in the same plane perpendicular to $\vec{E}$. For small electric fields the director moves on the surface of a cone coinciding with the smectic layer boundary plane, thereby varying the azimuth angle ϕ while the tilt angle ϑ stays constant in the smectic C* phase.

9.3.1. Dielectric properties

The predominant influences on the dielectric properties of the ferroelectric smectic C* phase at a low-frequency electric field are the so-called soft and the Goldstone mode.[149] While the soft mode has its origin in a varying tilt and polarisation magnitude, the Goldstone mode results from changes in the direction of the aforementioned quantities.[149] In the smectic C* phase the Goldstone mode dominates over the soft mode.[149] But in the smectic A* phase the Goldstone in contrast to the soft mode does not exist, because the molecules are untilted in this phase.[149] The origin of the Goldstone mode are electric-field-induced variations in the local direction of the spontaneous polarisation.[149]

In this context, the application of a small electric field perpendicular to the smectic layering direction $\vec{z}$ entails a slight distortion of the helix structure and therefore a non-vanishing net polarisation in direction of the applied electric field.[149] On the field-induced reorientation of the molecules an energy dissipation occurs, which is described by the rotational viscosity, which determines the reorientation velocity.[21] Here, the rotational viscosity can be divided into a component relating to changes of the azimuthal angle of the director ϕ and its tilt angle ϑ, respectively (see figure 9.2).[21] Deep in the smectic C* phase, i.e. far from the transition temperature to the smectic A* phase, the tilt angle ϑ is only neglectably influenced by the electric field, because its variation would cause an energetically unfavorable density change.[21, 106] Consequently, the Goldstone mode, associated with the variations of the azimuthal director angle ϕ, plays the most important role here. In this connection, the director $\vec{n}$ moves as sketched in figure 9.2 on the surface of a cone coinciding with the smectic layer boundary plane, since ϑ practically stays constant. The soft mode, corresponding to changes in the director tilt angle ϑ, is only weakly present, here. This, however, changes near the transition to the smectic A* phase and the tilt angle becomes influenceable by the electric

field, the so-called electroclinic effect.[21] Also in the smectic A* phase, where the molecules are in principle untilted, they can be forced to tilt this way.
Large electric fields $\vec{E}$ of constant polarity — contrary to the small fields considered above — dissolve the helical structure, because the field compels in every smectic layer an alignment of the polarisation along $\vec{E}$.[149] Consequently, the direction of the tilt of the molecules in the individual layers is perpendicular to $\vec{E}$ and at the same time the director $\vec{n}$ lies in a plane perpendicular to $\vec{E}$.[149] The reorientation of the molecules in this connection takes place in a way that the spontaneous polarisation vector $\vec{P}$ is compelled parallel to the electric field vector $\vec{E}$, with the above described relation between polarisation, tilt and layering direction.[149] This situation is sketched in figure 9.2, as well as the switching of the tilt direction when switching the polarity of the field. Thereby, the tilt angle ϑ of the molecules is inverted, that is tilted about an angle 2ϑ into the opposite direction, while the director $\vec{n}$ stays within the aforementioned plane perpendicular to the electric field $\vec{E}$.[149]

9.3.2. Electro-optics

The above described changes of the molecular director orientation, regardless whether it is only a distortion of the helix structure or a complete reorientation of the molecules, alters the optical properties of the liquid crystalline system. Here, the ferroelectric smectic C* phase can be considered as approximately uniaxial concerning its dielectric behaviour at optical frequencies, since its biaxiality is usually weak.[21, 109] The electric-field-induced structural changes then lead to a variation of the two the uniaxility defining refractive indices, thus entailing an alteration of the birefringence, quantitatively described by the difference of both indices. Such changes of this quantity can, for example, be measured by irradiating the liquid crystalline structure with a monochromatic light beam of known polarisation under a certain angle out of the optical axis and measuring the phase difference of the two outgoing beams. The variations in the birefringence on the application of electric fields, as well as those only induced by temperature-related structural changes, are often very small and necessitate appropriate elaborate measurement methods [20, 21, 34, 202].

CHAPTER 10

Materials & methods

The materials and the instruments used in this part of this thesis are described in the following. First the liquid crystals CE6 and 2MBOCBC together with some relevant bulk phase properties are introduced, followed by the surface-treated nanoporous anodic aluminium oxide membranes, hosting the liquid crystals for the study of confinement effects on their thermotropic structure. Afterwards the temperature-dependent X-ray and neutron diffraction methods for this purpose are described.

10.1. The cholesteric liquid crystal CE6

The liquid crystal S-(+)-4-(2-methylbutyl)phenyl-4-decyloxybenzoate, also known under its trivial name CE6, is a thermotropic liquid crystal composed of chiral molecules whose structural formula is depicted in figure 10.1. Beside a chiral nematic, i.e. cholesteric, and a smectic A* phase the bulk liquid crystal also exhibits the blue phases I-III.[56, 112, 276] The phase transition between the crystalline and the smectic A* phase occurs at 315.0 K, while at 315.4 K the latter transforms into the chiral nematic phase.[112] At around 318.43 K CE6 finally changes its state from cholesteric to isotropic.[112, 276] But before, in the close vicinity to this phase transition the blue phase I appears at around 317.92 K, followed by the blue phase II at around 318.31 K and the blue phase III at around 318.38 K.[276]

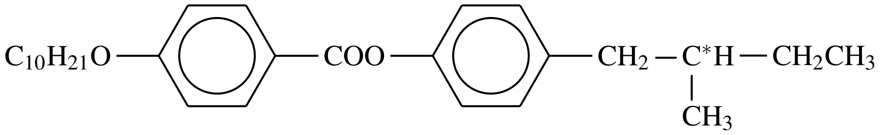

Figure 10.1.: Structural formula of the cholesteric liquid crystal CE6.[225]

10.2. The ferroelectric liquid crystal 2MBOCBC

The liquid crystal (S)-2”-methylbutyl-4’-n-octylcarbonyloxy-(1,1’-biphenyl)-1-carboxylate is denominated the trivial names 2MBOCBC or IS-2424. Figure 10.2 shows its structural

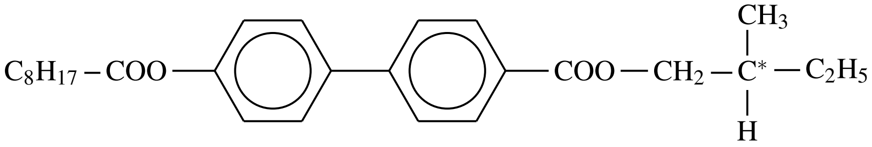

Figure 10.2.: Structural formula of the ferroelectric liquid crystal 2MBOCBC.[206]

formula. The bulk liquid crystal exhibits four different phases: crystalline, smectic C*, smectic A* and isotropic.[19, 110, 206] The transition from the crystalline to the smectic C* phase occurs at 309–310 K [110, 206], the following one to the smectic A* phase takes place at 315–316 K [74, 110, 206] and finally the phase transition to the isotropic phase occurs at 333 K [19, 110, 206]. On cooling there is a hysteresis in relation to the recrystallisation temperature: It was found that, depending on the cooling rate, it can start well below 293 K [206] and was found by Goodby et al. [110] to occur at 260.1 K, when cooling with $10\,\mathrm{K\,min^{-1}}$. The chiral liquid crystal 2MBOCBC is ferroelectric in the smectic C* phase.[110, 206] With respect to its spontaneous polarisation it possesses the peculiarity that its sign changes during temperature variation in the smectic C* phase at $291\,\mathrm{K} \pm 1\,\mathrm{K}$.[74, 110, 135] Optical measurements suggest a vanishing molecular tilt angle at this point when also the polarisation is zero.[74, 110, 135] On the other hand, X-ray diffraction studies confirm that the molecules are still tilted with respect to the smectic layer normal.[135, 206] Moreover the angle between the alkyl tail and the phenyl core of the molecule remains unchanged within the smectic C* phase.[135] Thus the layer shrinkage upon temperature variation in this phase is a consequence of the tilting of the molecule as a whole with respect to smectic layer normal.[135] The explanation for the vanishing spontaneous polarisation is therefore another. It is ascribed to a temperature-dependent change in the concentration of different conformers of the molecule with opposite polarisation sign, thus leading to the cancellation of the spontaneous polarisation at a certain point, followed by a change in its sign.[109, 219]

10.3. Nanoporous anodic aluminium oxide

The nanoporous anodic aluminium oxide (AAO) membranes serve as a host material for the investigation of the properties of liquid crystals under nanoconfinement in this work. They are produced by electrochemical etching of pure aluminium sheets, in which a self-organising process leads to the formation of pores, arranged on a hexagonal lattice (see figure 10.3 (a)). After the anodisation the sheets are crossed by channels perpendicular to the surface plane (see figure 10.3 (b)) with a controlled width, usually in the range between a few tens up to several hundred nanometres, depending of the etching parameters. The remaining material in between the channels is thereby transformed into the ceramic aluminium oxide. Its structure is amorphous and some electrolyte-derived anions are incorporated into the channel walls, thus influencing their properties.[177] Owing the latter fact and because the exact oxidation state is unknown, the membranes are here referred to as nanoporous AAO instead of the also commonly used term nanoporous alumina (denominating Al_2O_3). At the end of the etching process a porous AAO film is obtained that is still attached to the rest of the aluminium sheet

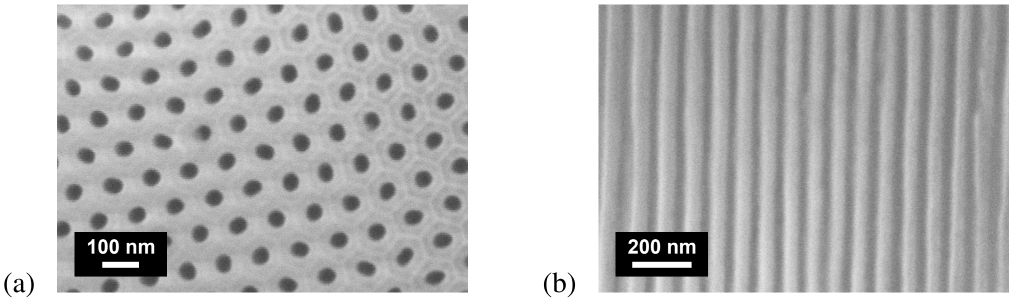

Figure 10.3.: Scanning electron micrographs of the untreated nanoporous anodic aluminium oxide membrane with 42 nm pore diameter: (a) surface and (b) cross-sectional view.

it is produced from. In the final steps the remaining aluminium and the barrier aluminium oxide layer, closing the bottom end of the channels, are dissolved, leading to free-standing nanoporous AAO sheets. There are additional post-treatments available to further tune the pore size of the resulting membranes. For some of the membranes used in this work, the pore size of the membranes has been adjusted using such a method. The nanoporous AAO membranes that were used for the measurements presented in this thesis are commercial ones, purchased with different pore sizes.

The pore diameters were analysed using nitrogen adsorption-desorption isotherms and for selected membranes they were further justified using scanning electron microscopy. For the evaluation of the nitrogen sorption isotherms a commercial implementation of the BJH model [11] has been used here. This model assumes cylindrical channels and uses the Kelvin equation for calculating the diameter of the pores being emptied in each desorption step while also considering the concurrent reduction of the layer thickness of the adsorbate at the channel walls of the larger pores, already having been emptied in the preceding steps.[11] Consequently, the model is applied to the desorption branch of the isotherm, delivering a distribution of pore sizes existing in the membrane. The pore diameters determined in such a way for the membranes used here, are 20 nm, 30 nm and 42 nm.

10.4. Surface treatment of the anodic aluminium oxide and melt infiltration of the liquid crystals

Since optical birefringence studies have shown that the as-prepared surface of the pores does not lead to a defined and stable (under temperature variation) molecular order of the liquid crystal molecules inside the pores [34], a special polymer surface coating is used prior to the filling of the membranes with the liquid crystal.[36] Therefore, the polyimide resin SUNEVER-130 (later referred to as SE-130) from Nissan Chemical Industries, also used as an alignment coating in the liquid crystal display industry, are utilised. It leads to a tangential anchoring of the CE6 and 2MBOCBC molecules with respect to the pore walls.[34, 36] Especially in cases where the interplay of the liquid crystal molecules with the surface chemistry of the pore walls is studied, it would be however more favourable to use a polymer with a

well-defined and well-known chemical composition.
Before starting the surface treatment of the membranes, they are heated to 200 °C for two hours, in order to remove surface adsorbates, like water. Afterwards, the still 100 °C hot membranes are immersed into a 1 % solution of SE-130 in water-free dimethylformamide and kept inside for around 24 hours. On removal from the solution the excess polymer solution at the membrane surface is absorbed with some tissue. After letting them dry under ambient conditions for 2–3 hours the membranes are further dried on a 50 °C warm heating plate for additional two hours. In a final step the membranes are heated to 190 °C for 30 minutes to polymerise the surface film with a subsequent slow cool down to a temperature below 50 °C. The resulting polymer coating thickness formed by such a procedure was estimated to be less than 2 nm with measurements of the membrane's optical birefringence [36] and with nitrogen sorption isotherms — comparing the uncoated and coated sample.
The filling of the polymer-coated nanoporous AAO membranes with the liquid crystal is done by melt infiltration. The liquid crystal is heated to a temperature slightly above the phase transition temperature to the isotropic phase, while the membrane is heated to around 95 °C on a second heating plate, until it is brought into contact with the liquid crystal. The channels of the membrane become thus filled by the liquid crystal via capillary action. After the filling procedure the surplus material on the surface is removed by careful polishing of the membranes with soft lens tissue at a temperature of around 50 °C.
While particularly those samples for the neutron scattering experiments have been prepared within the scope of this work, the surface coating and filling of the membranes for some of the other experiments has partly been done in the group of Andriy Kityk, Częstochowa University of Technology, Poland.

10.5. X-ray diffraction

The wide-angle X-ray diffraction experiments have been performed at an in-house X-ray diffractometer, using Bragg-Brentano geometry and Cu-Kα radiation with a wavelength of 1.5406 Å. The sample is placed inside a cell that is temperated via a Peltier cooler and a resistance heater, controlled by a precision temperature controller. This, the sample enclosing beryllium cylinder is surrounded by a second larger cap with polyimide windows. With this set-up a uniform heat distribution and temperature stability inside the sample cell is ensured.
Prior to each temperature-dependent measurement series, the sample's position is adjusted relative to the X-ray beam and it is subsequently slowly heated above the respective phase transition temperature to the isotropic phase of the liquid crystal. There, it is kept for at least 30 further minutes to ensure that the whole sample is in thermal equilibrium.
The measurement is started with a Θ-2Θ-scan at the aforementioned temperature. After each scan the next temperature step is approached with a cooling or heating rate of 1 K/min. A subsequent waiting time of 2 minutes before the start of the next scan again ensures the thermal equilibrium of the entire sample. After having reached the lowest desired temperature, the measurements are continued as described before until the isotropic phase is reached again. In this way complete heating and cooling cycles are measured.

10.6. Neutron diffraction

The neutron diffraction experiments presented in section 11.2 have been performed at the membrane diffractometer at the V1 beamline of the BERII research reactor at the Helmholtz-Zentrum Berlin. The incident neutron beam with a flux of 10^7 neutrons/(cm^2·s) had a wavelength of 4.567 Å. It impinged a stack of 38 closely packed, SE-130-surface-coated, nanoporous AAO membranes, filled with the liquid crystal 2MBOCBC. Each of the membranes had a thickness of 100 µm and an area of 10 mm × 10 mm. The samples were situated inside a temperature-controlled aluminium cell, allowing measurements in reflection and transmission geometry, respectively. An insulating vacuum around the sample cell ensured the temperature stability. The scattered neutrons are detected by a 128 × 128 pixel area detector (1.5 mm pixel width) in a distance of 1025.7 mm from the sample. Figure 10.4 shows a sketch of the scattering geometry of the neutron diffraction experiment.

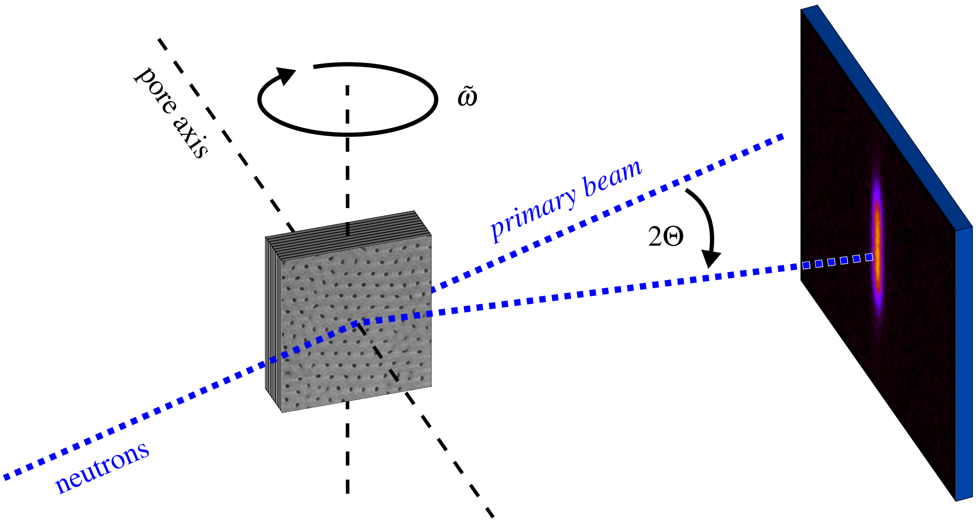

Figure 10.4.: Sketch of the scattering geometry of the neutron diffraction at the V1 membrane diffractometer.

The sample is rotated around an axis that is perpendicular to the long AAO nanochannel axis, as well as to the incoming neutron beam, while the detector is situated at a fixed position, centred at the 001 smectic Bragg peak position at $2\Theta = 9.4°$. For convenience the angle ω is defined over $\tilde{\omega} = \omega + \Theta$, where the rotation angle of the sample $\tilde{\omega}$ equals zero if the surface of the membranes is parallel to the direction of the incident neutron beam. As a consequence, ω is zero in the maximum of the smectic layering Bragg peak. In one degree $\tilde{\omega}$-rotation steps, 60 diffraction patterns like the one exemplary depicted in figure 10.4 are acquired for each temperature step. These two-dimensional diffraction patterns are integrated perpendicular to the indicated 2Θ-direction (see figure 10.4) forming one ω-line of the resulting intensity maps as function of ω and 2Θ (see figure 11.4 in section 11.2.1). With the help of these so-called ω-scans the structure of the liquid crystal molecules with respect to the pore axis, more precisely the orientation of the smectic layers, is analysed as a function of temperature.

Between those ω-rocking scans coupled ω-2Θ-scans are conducted from time to time with $\Delta\omega = \Delta\Theta$ over a 2Θ range from 10° up to 100° and different ω-angle starting points. By this means, possibly occurring additional structures in the temperature course, not being encompassed by the above measurements, can be detected.

Additionally neutron diffraction experiments with a different scattering geometry are executed in order to investigate the in-plane arrangement of the liquid crystal molecules in the smectic layers. For this purpose deviating from the scattering geometry shown in figure 10.4 the membrane stack is turned by an angle of 90° in a way that the long nanochannel axis is now parallel to the ω rotation axis. Measurements with 2Θ ranging from 5° to 100° and fixed ω, as well as ω-scans, i.e. with fixed 2Θ, are done at different temperatures to monitor possible structural changes, e.g. an occurring crystallisation of the liquid crystal.

CHAPTER 11

Experimental results & discussion

In this chapter the results of X-ray and neutron diffraction experiments, studying the structure and phase transition behaviour of the thermotropic liquid crystals CE6 and 2MBOCBC in bulk and confined in mesoporous anodic aluminium oxide (AAO) membranes, are presented and discussed.

11.1. Liquid crystal CE6

The smectic A* $\rightleftharpoons$ chiral nematic phase transition of the chiral liquid crystal CE6 is studied in this section in the bulk as well as in the confined state. For the latter the liquid crystal is embedded in nanoporous AAO membranes with SE-130 polymer wall coating, as described in section 10.3. All samples are heated to the isotropic phase of the liquid crystal at the beginning of the measurement to ensure to have the system in a defined state and to exclude possible hysteretic effects. Note however, that studies of these confined liquid crystal samples measuring the optical birefringence, which is a measure of a collective orientation of the liquid crystal molecules due to their optical anisotropy, have shown that even far above the isotropic phase transition temperature a small residual birefringence asymptotically approaching zero with rising temperature is detected.[36] This is attributed to the formation of a so-called paranematic state where indeed the predominant part of the liquid crystal molecules are in the isotropic phase, but in the proximity of the channel walls there is a small quantity that has still a preferred molecular orientation, depending on the surface anchoring type.[36, 247]

11.1.1. Structure and phase transition in the bulk phase

First the bulk phase is studied using X-ray diffractometry (see section 10.5) as a reference for the following investigations on the confined CE6 liquid crystal. The liquid crystal is placed on a polished silicon wafer support, which had been afore cleaned using piranha solution [266]. The scattering geometry of these experiments is depicted in figure 11.1. It is chosen in a way that the scattering vector $\vec{q}$, defined by the angle 2Θ between the wave vector of the incoming and outgoing X-ray beam, $\vec{q}_i$ and $\vec{q}_o$, probes a periodicity along the surface normal of the substrate or along the long axis of the nanochannels in the confined case, respectively.

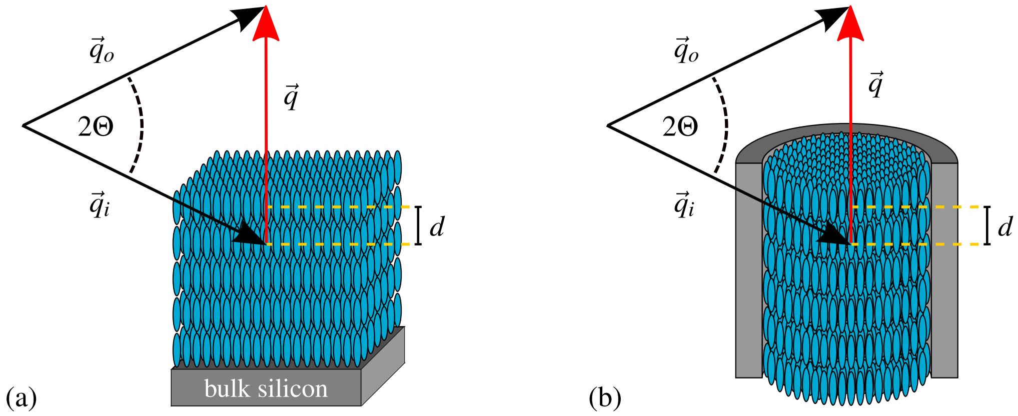

Figure 11.1.: Scattering geometry of the diffraction experiments in the case of the (a) bulk and the (b) confined liquid crystals.

Here, the thermal evolution of the smectic layering thickness d is of interest. The integrated intensity of the corresponding 001 smectic A* layering Bragg peak of bulk CE6 as a function of temperature is shown in figure 11.2 (a). On stepwise cooling from the isotropic phase a first-order phase transition occurs at 314.7 K, as suddenly the smectic layering peak appears. This is in accordance with the McMillan model [194], which predicts such a first-order phase transition for liquid crystals with such high ratios between the smectic-A-to-nematic and the nematic-to-isotropic phase transition temperature, i.e. with a comparatively small nematic temperature range. Also from the analogue of a superconductor in a weak magnetic field, the cholesteric-to-smectic-A transition is predicted to be always of first order [118, 187], but by now it is known that such a transition can be in principle also a second-order transition.[243] After the abrupt intensity jump, the layering peak intensity subsequently rises slightly on further cooling. The inverse, congruent behaviour is shown during the following heating of the sample back to the isotropic phase, i.e. the peak disappears abruptly at the same temperature it had appeared before. This behaviour stays reproducible during several repeated heating and cooling cycles (not shown in the figure). The inset of figure 11.2 (a) shows the smectic layering peak at 313.0 K centred at a wave vector transfer $q_{001} = 0.216\,\text{Å}^{-1}$, corresponding to an interlayer distance of $d = 29\,\text{Å}$. This finding is in accordance with the values determined by Cordoyiannis et al. [58]; however, it should be noted that their values refer to a mixture of CE6 with a small percentage of nanoparticles.

11.1.2. Structure and phase transition in cylindrical nanoconfinement

Figure 11.2 (b) shows the integrated X-ray intensity of the 001 Bragg peak originating from the smectic A* layering of the CE6 liquid crystal confined in pores with a diameter of 42 nm of mesoporous AAO, with SE-130 wall surface coating. Contrary to the cholesteric $\rightleftharpoons$ smectic A* phase transition of the bulk liquid crystal, the transition in the case of the confined liquid crystal is not any more of first order, but continuous. This is reflected by

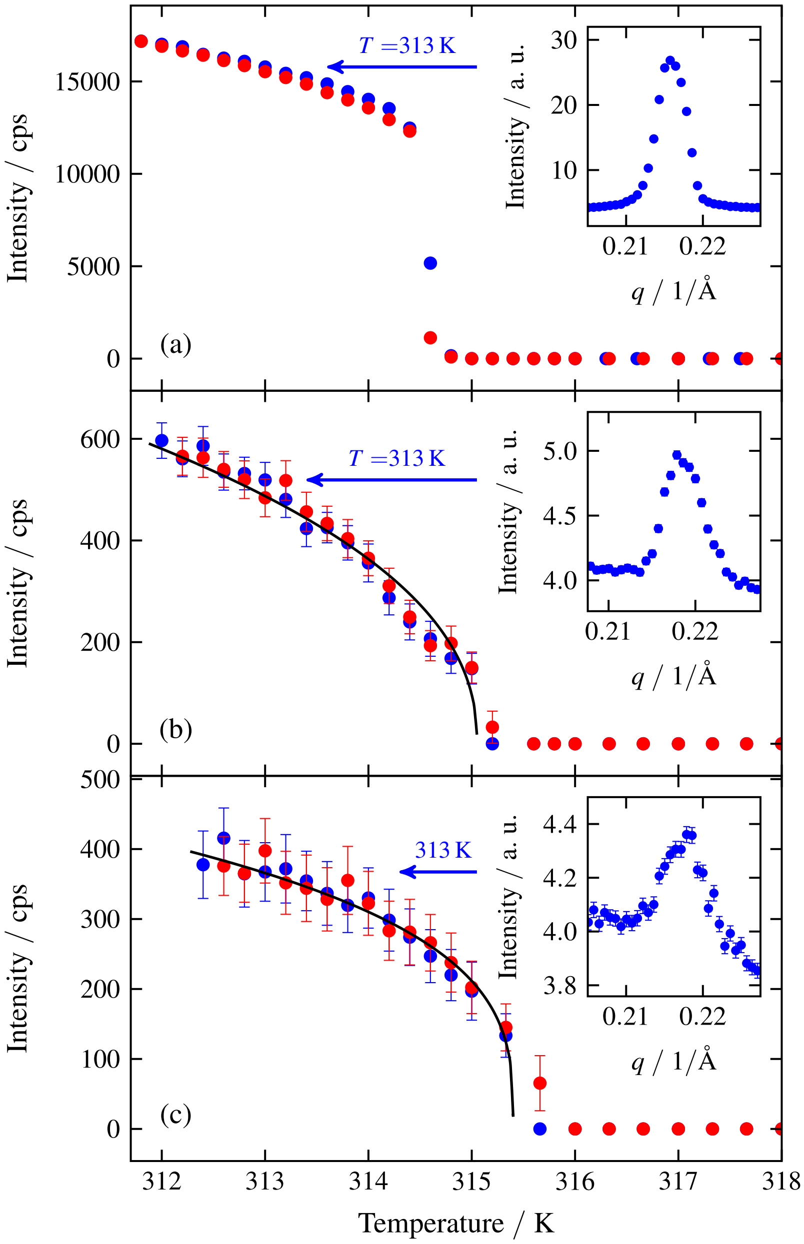

Figure 11.2.: Integrated X-ray intensities of the Bragg peak corresponding to the smectic layering for (a) the bulk CE6 liquid crystal and CE6 confined in mesoporous AAO membranes, surface-coated with SE-130, in pores with a diameter of (b) 42 nm and (c) 30 nm, respectively (red curves belong to heating, blue ones to cooling cycles). The insets respectively show the smectic layering peak at 313.0 K, measured in the cooling cycle.

the continuous growth of the Bragg peak intensity starting from zero intensity, which replaces its afore discontinuous rise, i.e. the sudden appearance of that peak. Additionally, the phase transition temperature is shifted to a higher temperature, namely 315.1 K. The smectic peak position, however, remains in the limits of measurement accuracy the same than in the bulk phase (see insets in figure 11.2). This means that the layer distance equals the one of the bulk liquid crystal and therefore there is especially no tilting of the molecules inside the smectic layers. That means the smectic A* structure of the bulk phase is also presevered in the confinement of these tubular nanochannels with an SE-130 surface coating favouring a tangential anchoring at the channel walls.

For mesoporous AAO membranes with SE-130 pore wall coating and a pore diameter of 30 nm one observes a comparable behaviour (see figure 11.2 (c)) as for the 42 nm membranes described above. However, the phase transition temperature between the cholesteric and the smectic A* phase is shifted further to higher temperatures and occurs now at 315.4 K.

The smoothing of the phase transition from a first order to a continuous transition for the CE6 liquid crystal embedded in the AAO membranes can be explained by geometric confinement and so-called quenched disorder, originating in small perturbations, e.g. roughness of the channel walls.[114, 130, 132, 147] However, the shift to higher phase transition temperatures can not be traced back to quenched disorder, since the latter usually causes a shift to lower temperatures.[130, 132] In fact, a large number of experimental studies, investigating the nematic $\rightleftharpoons$ smectic A phase transition of liquid crystals confined in the voids of materials such as controlled pore glasses, aerosil networks or cellulose membranes, find a downward shift of the respective phase transition temperature with respect to the unconfined bulk phase.[59, 115, 130, 147, 160–162, 168, 182, 227, 299] But not in all of these cases there is a clear trend that the phase transition temperature is further shifted down with decreasing pore size or with an increasing degree of disorder caused by the confinement, respectively.[59, 182, 227] It seems that the deviations especially occur for small void sizes and a comparatively high degree of disorder. This shows that there are presumably several mechanisms in combination and in competition responsible for the shift of the phase transition temperature, like elastic distortions, random field and finite size effects, as well as surface order and disorder.[227] For instance there is a competition between the surface-induced disordering, which causes a downward shift of the phase transition temperature and the surface-induced ordering, which leads to a shift to higher temperatures, analogous to a spin system, affected by an external magnetic field.[227] The latter might be an explanation for the phase transition temperature shift to higher temperatures observed for CE6 confined in the SE-130-surface-treated AAO membranes. The coating of the channel walls, which forces a planar alignment of the rod-like liquid crystal molecules with respect to it, probably leads to such a strong ordering field, acting on the confined liquid crystals, that the effects leading to a lower phase transition temperature are overcompensated. Consequently, this leads to an upward shift of the chiral nematic $\rightleftharpoons$ smectic A* phase transition temperature.

It is interesting that it is even further postponed to higher temperatures, if the channel diameter is decreased from 42 nm to 30 nm. This can be considered to support the above argumentation, since that way it is easier to impose the surface-induced ordering to the molecules in the centre volume of the nanochannels. However, one might speculate that at one point on further decreasing the diameter of the channels other effects like surface-induced disorder due to surface roughness might start to dominate and thus stop the trend towards higher phase transition temperatures, if the transition will not be even totally suppressed on attaining a critical pore size.

11.1.3. Critical exponent of the smectic order parameter

The measured X-ray intensity presented above in figure 11.2 can be further analysed to learn more about the phase transition behaviour of the CE6 liquid crystal in the interplay of the surface-coated AAO nanochannel confinement. From the temperature-dependent integrated X-ray intensity of the 001 smectic layering Bragg peak $I(T)$ the smectic order parameter (see equation 9.5 in section 9.2) can be determined. The latter is given by

$$\rho_1^2(T) = \frac{I(T)}{I_0} \, , \tag{11.1}$$

where I_0 describes the intensity of a perfectly translationally ordered smectic phase.[145, 171, 194] This proportionality arises from the definition of the order parameter (see section 9.2), relating it to the electron density of the liquid crystalline system and from the proportional dependence of the X-ray scattering intensity on the corresponding structure factor.[25] Assuming the following power-law dependence of the smectic order parameter ρ_1 on the temperature T, the second-order phase transition temperature $T_c > T$ and the critical exponent $\beta > 0$

$$\rho_1(T) = \left(1 - \frac{T}{T_c}\right)^{\beta} \, , \tag{11.2}$$

the temperature dependence of the 001 smectic Bragg peak intensity $I(T)$ can be described as

$$I(T) = I_0 \cdot \left(1 - \frac{T}{T_c}\right)^{2\beta} \, , \tag{11.3}$$

using equation 11.1.[145]

It is challenging to determine the absolute value of the smectic order parameter, since I_0 is unknown, for a start. However, there are methods for the determination of the smectic order parameter absolute value: For the method of Leadbetter and Norris [171] the measurement of higher-order Bragg diffraction peaks corresponding to the smectic layers is necessary, together with sophisticated calculation of the molecular structure factors. Another technique [145] uses an extrapolation of the temperature-dependent Bragg peak intensity $I(T)$ of the 001 smectic layering peak to $T = 0\,\mathrm{K}$, where $I(0\,\mathrm{K}) = I_0$, analogous to the method employed by Haller [117] in a similar context. This could be done using equation 11.3 for a fit to the X-ray diffraction intensity data shown in figure 11.2. Although it would be interesting to determine the order parameter of the confined liquid crystal in comparison to the one of the bulk, there are some arguments why it is not possible or at least not meaningful, here. For the first method the intensities of the diffraction peaks in case of the confined liquid crystals are too low for a detection of the necessary higher-order peaks. The second method uses an extrapolation to determine I_0 at the absolute zero point, assuming that the temperature dependence of the 001 smectic layering peak intensity evolves in a way that it represents a perfect smectic translational order at this point. This might be an acceptable assumption for bulk liquid crystals, but in the confined cases it can a priori not be expected to hold. The reason is that the nanochannels whose total interface area with the liquid crystal is comparatively large, impose a certain disorder to its host material. Thus even at the absolute zero point, the system should not be expected to find to a perfect smectic order, so that it can not be used as a reference point for the determination of I_0. An obvious loophole would be to take the bulk liquid crystal and its corresponding I_0 value as a reference. However, in order to be able to do this, one would need to have an accurate knowledge of the amount of liquid crystalline material in the sphere of influence of the X-ray beam, to get a correct scaling of the respective intensities. But also this is prone to errors due to the shielding, as well as the scattering of the AAO membranes. Beyond that, there are further methods [2, 79] for the ascertainment of the translational order parameter, which possess certain drawbacks and prerequisites, not permitting their application, here. Consequently, the following analysis will spare the determination of absolute values for the smectic order parameter and focus on the determination of the critical exponent β.

The critical exponent β for the second-order phase transition of CE6 confined in the SE-130-surface-coated nanochannels of AAO membranes, where a continuous development of the smectic order takes place, is determined by a fit with equation 11.3 to the temperature-dependent 001 smectic Bragg peak intensity of the cooling cycle and is shown as a black line in figure 11.2 (b) and (c), respectively. For the AAO membranes with 42 nm channels this yields a critical exponent $\beta = 0.22 \pm 0.05$ and $\beta = 0.15 \pm 0.03$ for the 30 nm channels. Before these values are interpreted a short review on the critical behaviour of liquid crystals in bulk and confinement is given below.

Following from the renormalisation group theory the critical behaviour of a phase transition is only determined by the dimension of the corresponding order parameter and the space.[25] Since the complex smectic order parameter is a two-dimensional function of the amplitude and phase of the density modulation of the smectic layers and therefore of order two, while the space is three-dimensional, the critical behaviour of the nematic-to-smectic A phase transition can be described by means of the three-dimensional XY theory, in analogy to the fluid-to-superfluid and conducting-to-superconducting transition.[25, 104, 105, 292] Indeed, for various bulk liquid crystalline systems an accordance of the respective critical exponents with the ones predicted for the 3D XY universality class is found experimentally.[24, 42, 99–102, 213] However, this is not true for all liquid crystals.[42, 102, 292] Especially for liquid crystals with a small nematic range, i.e. a large McMillan ratio, like the liquid crystal CE6 investigated in this study, a deviation from the 3D XY behaviour is predicted and found in experiments.[25, 42, 102, 292] This is explained by strong temperature-induced variations of the orientational order parameter in the vicinity to the isotropic $\rightleftharpoons$ nematic phase transition, which influence through the coupling between the orientational and the translational order parameter also the phase transition from the nematic to the smectic phase.[25, 102] An increasing nematic range therefore changes the critical behaviour of the nematic-to-smectic A phase transition from 3D XY and from being a second-order transition, to a first-order phase transition via a Gaussian tricritical point with tricritical values for the critical exponents in the crossover region.[25, 102] Also splay deformations, i.e. director fluctuations can cause such an effect due to the coupling between the two order parameters.[25, 102, 118]

The situation changes if the liquid crystals are confined to a limited space. The quenched disorder weakens the coupling between the nematic and the smectic order parameter, in which the effect seems to be the stronger, the higher the degree of disorder induced by the confinement or the smaller the pore size is.[130, 162, 182, 227] Thus, it has a similar impact on the critical exponents related with this phase transition as their dependence on the McMillan ratio.[168, 179, 182, 227] The weakened orientational and translational order parameter coupling additionally explains the changeover from the first-order bulk phase transition to the continuous transition in confinement, as observed above for the liquid crystal CE6. Furthermore, the whole critical behaviour of the phase transition is influenced through the confinement or the introduction of disorder, respectively. While there is a variety of liquid crystalline systems, whose bulk phase critical behaviour does not fit into the 3D XY universality class, it is found that the increasing spatial confinement often drives them successively towards the 3D XY behaviour.[130, 160–162, 168, 179, 227, 299] There, the bulk liquid crystals often possess a near tricritical phase transition behaviour.[130, 162, 179, 227] In contrast, if the bulk liquid crystals already exhibit 3D XY critical behaviour, this is found to be not altered due to the introduction of disorder or confinement.[227, 299]

The tricritical value of the critical exponent β, corresponding to the order parameter, is calculated to $\beta = 0.25$ [179], while renormalisation group delivers a critical exponent $\beta = 0.35$ for the 3D XY universality class.[41] Both strongly differ from the value $\beta = 0.5$ given by the mean-field theory.[41] If one compares now the critical exponents determined above for the two pore diameters, one notices that the value for the comparatively large 42 nm channels with $\beta = 0.22$ most likely fits to the one expected for the tricritical behaviour. Interestingly, the changeover to smaller channels, i.e. with 30 nm diameter, does not lead to an approximation towards the 3D XY value, but entails an even smaller critical exponent of $\beta = 0.15$. Thus, while already the one for the 42 nm pores was below the tricritcal value, the critical exponent for the 30 nm channels is even smaller. Note however, that such small values are also observed for some liquid crystals in the bulk phase.[57, 145, 275] The trend of critical exponents that are moving away from the 3D XY value with decreasing pore size, instead of approaching it, is in contradiction to the above cited studies. But also among them there are some, where this tendency is broken in the case of high aerosil particle densities, i.e. high degree of disorder, as well as for comparatively small void sizes.[168, 227] Furthermore, it should be emphasised that the majority of the above publications that find the liquid crystals to approach the 3D XY behaviour with decreasing confinement size or increasing disorder, investigate the phase transition behaviour of the same liquid crystal 8CB [160–162, 179, 227, 299], but only some of them additionally study a second one [168, 227, 299]. In addition, these liquid crystals are achiral, in contrast to the here investigated CE6.

Again, like the above discussed chiral nematic $\rightleftharpoons$ smectic A* phase transition that was shifted to higher instead of lower temperatures, the explanation for the observed evolution of the critical exponent might be found in the interplay of several competing effects. Note in this connection, that the void sizes in the majority of the above cited investigations are often much larger than the channel diameters in the AAO membranes, here. However, the mentioned deviations from the trend towards 3D XY phase transition behaviour with decreasing confinement size, occur in these publications for the smallest pores, whose size is in the same order of magnitude than the AAO nanochannels. Anew, this correlation suggests an increasing dominance of surface-induced effects. This would be comprehensible due to the shrinked liquid crystal volume in the small channels, which are here additionally coated to increase the surface alignment strength.

11.2. Liquid crystal 2MBOCBC

The structure of the liquid crystal 2MBOCBC (see section 10.2) confined in the channels of nanoporous AAO having different widths between 20 nm and 42 nm is studied in this section under temperature variation, covering the isotropic, the smectic A*, as well as the smectic C* phase. Being necessary for a reproducible and stable surface anchoring [34] of the liquid crystal molecules at the channel walls, the AAO membranes are SE-130-surface-coated prior to the melt infiltration of the 2MBOCBC liquid crystal, as described in section 10.3.

11.2.1. Neutron diffraction experiments

In a neutron diffraction study the orientational order of the smectic layers is studied. The description of the experimental set-up (see sketch in figure 10.4) and procedure can be found in section 10.6. With the ω-rocking scans described there, the arrangement of the smectic layer planes with respect to the nanochannel axis can be studied by tilting the AAO membranes with respect to the incoming beam with wave vector $\vec{q}_i$ and thus inclining the scattering vector $\vec{q} = \vec{q}_o - \vec{q}_i$ ($\vec{q}_o$: wave vector of the scattered neutrons) concerning the aforementioned axis. This is sketched in figure 11.3 for the example of an individual nanochannel containing an idealised smectic A layer arrangement with layers perpendicular to the channel axis. The direction of the scattering vector $\vec{q}$ is parallel to the layering direction, i.e. to the surface normal, of the possible smectic layers, being probed.

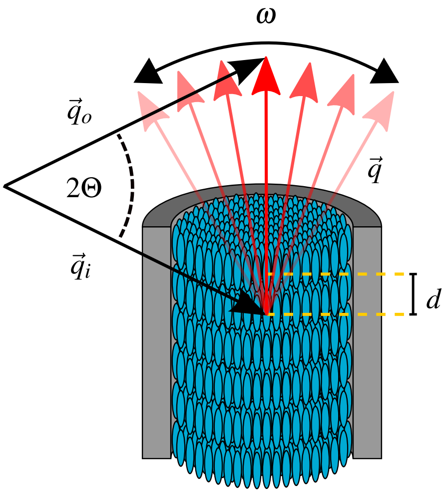

Figure 11.3.: Scattering geometry of the ω-scans of the neutron diffraction experiment at the liquid crystal 2MBOCBC confined in the channels of nanoporous AAO membranes.

These measurements are performed for different temperatures from $T = 337.65\,\mathrm{K}$ in the isotropic phase stepwise down to $T = 276.15\,\mathrm{K}$ and in the same manner back again to the isotropic state. Figure 11.4 shows the result for such measurements for two selected temperatures, $T = 279.15\,\mathrm{K}$ and $T = 324.15\,\mathrm{K}$, as a function of 2Θ and sample rotation $\tilde{\omega} = \omega + \Theta$ (compare sketch of the experimental set-up in figure 10.4), as a two-dimensional intensity colormap. The just mentioned shift concerning the zero-point of the ω-axis label with respect to the rotation angle of the sample is done by reason of a clearer representation of the thermal evolution of the diffraction peak.

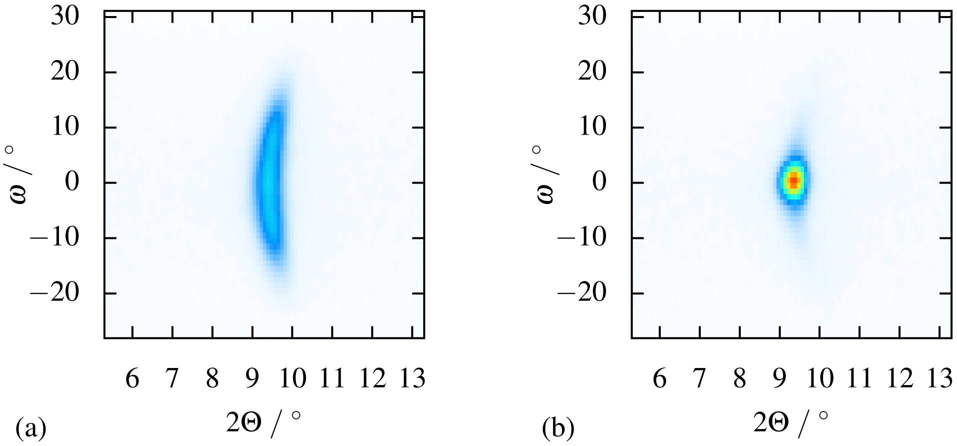

Figure 11.4.: Intensity of the smectic layering Bragg peak as a function of sample rotation $\tilde{\omega} = \omega + \Theta$ and 2Θ as indicated in the sketch of the experimental set-up (see figure 10.4) for (a) $T = 279.15\,\mathrm{K}$ and (b) $T = 324.15\,\mathrm{K}$.

11.2.2. Diffraction pattern analysis

To further analyse the peak shape, its thermal evolution and therefore the changes of the smectic layer structure under temperature variation, the data, as seen exemplarily in figure 11.4, are integrated over 2Θ. The resulting curves are then fitted by one or two pseudo-Voigt functions, respectively (see figure 11.5). Within these fits, a fixed background is considered, which is determined in the isotropic phase where no Bragg peak is present. In order to achieve a stable fitting procedure during the two-peak fits the width and the area (i.e. intensity) of both peaks are coupled to the same value, respectively. Due to symmetry reasons of the investigated structure, as will be seen later, the agreement between the fitted curve and the data is still very good. Furthermore, it should be stressed that the centre position of the individual peaks is independent in this procedure and not subject to any limitations.

The integrated intensity of the Bragg peak as a function of temperature determined by the two-peak pseudo-Voigt fit is shown in figure 11.6 (a). While it is zero in the isotropic phase due to the absence of any layer structure, on cooling it steeply rises from around 330.5 K on, clearly indicating the formation of smectic layers. After this relatively steep rise, it subsequently rises in a much slower manner as a sign of increasing smectic order until a kink at approximately

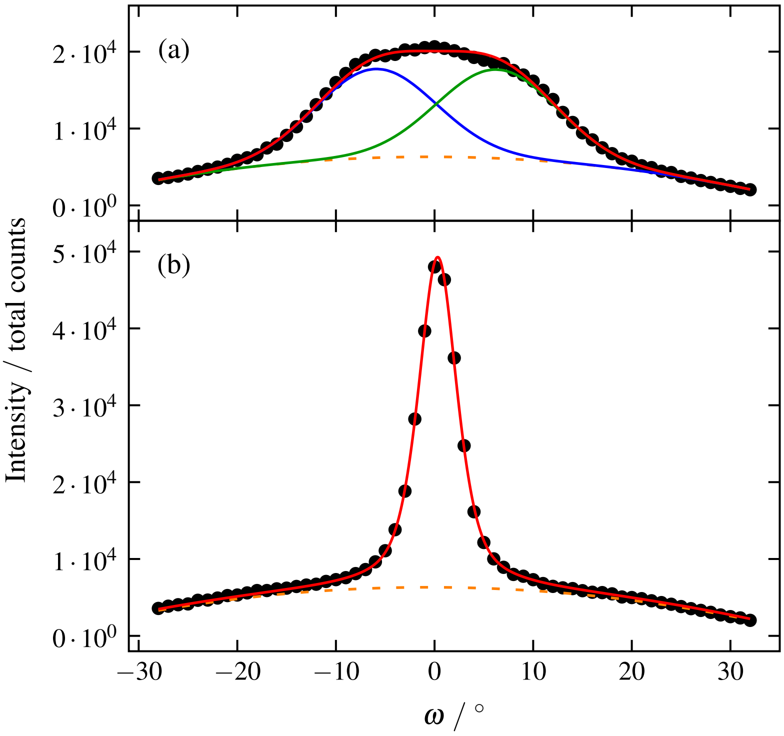

Figure 11.5.: Integrated intensity of the ω-scans (compare figure 11.4) for (a) $T = 279.15\,\mathrm{K}$ and (b) $T = 324.15\,\mathrm{K}$. Red lines are the total fit functions composed of the single peaks (blue and green lines) and a fixed background (dashed orange curve).

309.5 K occurs. From there on it stays almost constant, but still slightly rising. Upon heating the intensity is congruent with its evolution on cooling, with the exception of a hysteresis at the transition to the isotropic phase. There the intensity drop is shifted to higher temperatures, however being steeper than its rise upon cooling.

This is compatible with the thermal evolution of the optical retardation, showing the same behaviour at this phase transition.[34] This optical retardation is a consequence of the collective molecular ordering of the liquid crystal molecules along the channel axis in the smectic phases, rendering the liquid crystal inside the AAO membrane birefringent. Note, that there is also a small birefringence in the isotropic phase, whose origin is the refractive index difference between the confining AAO matrix and the isotropic liquid crystal in conjunction with the geometric boundary conditions of parallel straight channels, as well as molecules in the paranematic state in the proximity of the pores walls.[34] While it is known that the thermodynamic pathways of such phase transitions can be different depending on the direction of the transition, the exact reason of the hysteresis, as well as the overall shift to lower temperatures compared with the bulk phase, remains unclear within the scope of this study and needs further investigation.[34] Although, the investigation of the birefringent properties are evidencing the collective molecular ordering of the liquid crystal upon cooling it down from the isotropic phase, a clear determination of its structure, including the distinction of the smectic phases from the nematic phase, necessitates the here presented diffraction experiments.

Correlation between peak shape and smectic layer structure

On formation of the smectic layers at the transition from the isotropic phase, the corresponding Bragg peak is quite sharp with respect to variations in ω, as can exemplarily be seen in figures 11.4 (b) and 11.5 (b) for a temperature some Kelvin below this point. In figure 11.6 (b) this peak width as a function of temperature is shown. It is determined from the results of the two-peak fits, summing up the respective full width at half maximum of both peaks while considering their overlap. The width of the peak is almost constant in the range from the isotropic $\rightleftharpoons$ smectic A* phase transition on until approximately 309.5 K, where also the kink in the integrated peak intensity occurs. However, at that point it starts to gradually increase from around 6° to almost 27° at lower temperatures. To understand the reason for this peak broadening it necessitates a more detailed analysis of the peak shape. Whereas until 309.5 K where the peak starts to widen the peak shape can be described by one pseudo-Voigt peak function (see figure 11.5 (b)), two of those functions are needed to reproduce the peak form at lower temperatures (see figure 11.5 (a)). If one envisions again the scattering geometry in figure 11.3, it is obvious that this separation into two peaks, which increases with decreasing temperature, is attributed to a tilting of the smectic layer planes in two opposing directions. Thus it suggests the formation of a chevron-like layer structure, as it is depicted in figure 11.7 (a) in a simplified two-dimensional drawing. Since the position of the two peaks belonging to each layer tilting direction symmetrically moves away from the centre position, as plotted in figure 11.6 (c), thus indicating that the corresponding tilt angle has the same absolute value, the chevron structure is expected to be rotational symmetric around the long channel axis. This is also supported by the fact that the intensity of both peaks being united to the total peak form is the same, i.e. both orientations have the same incidence. The layer tilt angle gradually increases from 0° at the beginning of the chevron-like layer buckling until it saturates at about ±6.3°, negligibly decreasing on further cooling below approximately 288 K.

11.2.3. Origin of chevron-like smectic layer structure

The formation of chevron-like layer structures in liquid crystalline systems is a well-known phenomenon since their first observation in the 1970/80s. They were found in slab geometries consisting of two glass plates, separated by a gap in the micrometre range, thus being at least around two orders of magnitude larger then the nanochannel diameters in this work.[50, 171, 216, 221, 229] Such textures exist not only in the smectic C* phase of ferroelectric liquid crystals [216, 229], but also in achiral smectic C [85] and even in smectic A phases [190, 217, 262], depending on the mesogens. Also for 2MBOCBC within a micrometre-sized slab geometry the appearance of chevron-like molecular arrangements has been described.[135]
But what are the reasons for such a drastic change in the orientation of the smectic layer structure? The emergence of chevron-like structures in smectic C and C* phases is explained as a consequence of the smectic layer thinning caused by the collective tilting of the molecules within it — characteristic for the smectic C/C* phase.[229] The structural reformation of the

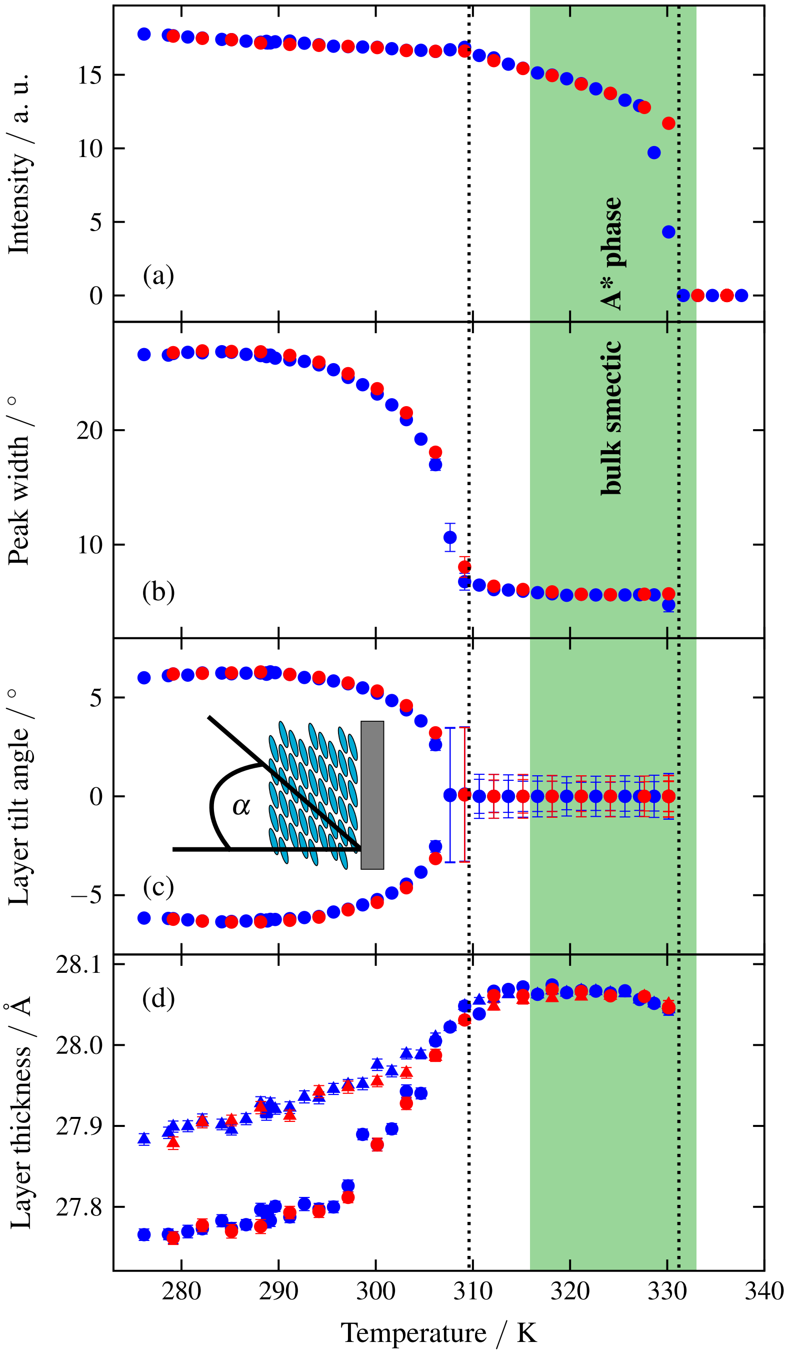

Figure 11.6.: Neutron diffraction measurements as function of temperature for the 42 nm AAO membranes: (a) integrated neutron scattering intensity of the 001 smectic layering peak, (b) overall peak width along ω (compare figure 11.4), (c) smectic layer plane tilt angle, (d) smectic layer thickness (see text for explanation). Blue and red symbols correspond to cooling and heating cycles, respectively.

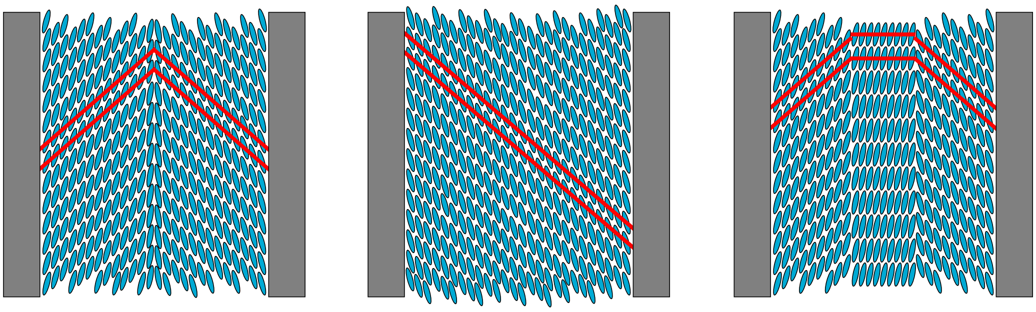
(a) (b) (c)

Figure 11.7.: Idealised sketch of different possible smectic C* structures inside the AAO membranes with tilted layers, neglecting the helix structure in favour of a clearer visualisation: (a) chevron-like structure, (b) only one layer tilt direction in each channel, (c) chevron-like structure with untilted layers in the core region. Red lines illustrate the smectic layer planes.

layers, i.e. their tilting towards chevrons, here conduces to a certain extent the preservation of the original smectic layer distance, hence reducing the strain induced by the thinning layers and leading to an energetically more favourable state.[156, 208, 229] This is expected to be facilitated by molecules anchored at the confining glass plates (or in our case the channel walls), still having a smectic-A-layer-like periodicity and imposing it on the neighbouring molecules.[35, 65, 183, 229, 245]

In contrast, in the smectic A phase the molecules do not collectively tilt and therefore there is consequently no associated layer thinning. Hence, the reason for the creation of chevron-like patterns in a smectic A phase is somewhat different, although the overall argumentation is quite similar. Also in this case, the core of the reasoning forms a decreasing layer thickness, but much less pronounced, nevertheless being sufficient to provoke the chevron structure generation.[183, 217, 262] However, as chevron formation in the smectic A phase is not relevant in the context of the measurements presented here, it will not be further discussed at this point.

A calculation by Kralj et al. [157] shows that chevron structures are expected to be less probable in the case of cylindrical confinements. Nevertheless, experimentally it is found that such structures develop for example in the smectic A phase of 8CB within micrometre-sized glass capillaries [190] or even in the smectic C phase of an achiral liquid crystal confined in AAO nanochannels [178].

11.2.4. Discussion of further possible structures

Concerning the neutron diffraction pattern from which the presence of the chevron-like structure is deduced here, it should be noted that such an arrangement of the smectic layers is not the only one that is compatible with it. A structure where only one tilt direction per pore is present (see figure 11.7 (b)) and whose tilt direction differs from channel to channel, thus resulting in a statistical distribution of layer tilt directions, would deliver the same result of the diffraction experiment. Even multiple domains with different tilt directions inside individual channels can not be really excluded. But there is one strong argument against such structures in favour of the chevron-like structure: The crux is that there is a transformation from a structure where the layers are perpendicular to the channel walls, to one where their surface normal is tilted by a certain angle with respect to it. This makes a shift of molecules necessary — either in the case of the chevron structure (see figure 11.7 (a)) in the inside of the channel where liquid crystal molecules shear against each other or at the pore walls in the case of a layer tilt in only one direction in each pore (see figure 11.7 (b)) having in consequence that the molecules need to shear along the channel walls. The molecules in the proximity of the channel walls are however more strongly bound and therefore rather not expected to slide [35, 65, 150, 156, 286], making the latter case appear less probable. The chevron formation in contrast seems to be more likely, since here the molecules close to the pore walls stay in place and only the ones in the interior of the channels are sheared. In fact, when looking again at the studies of liquid crystals in slab geometries, such a structure is the predominant one, while the one with collectively tilted smectic layers is only rarely observed.[156, 217] This makes the above argumentation even more striking, because the surface-to-volume ratio in the case of the nanochannels is dramatically higher than in such slab geometries. Even though some theoretical works have found that the collectively tilted layer configuration should be in principle favourable, amongst others because being energetically advantageous, a closer examination confirms that the chevrons are a thermodynamic equilibrium structure and yet substantiate the strong influence of the anchored near-boundary molecules and possible roughness of the confining walls.[156, 273, 284] The fact that the chevron structure is fully symmetric here is not too surprising, since such a symmetric one is also the most common in slab geometries, because the anchoring conditions can not be preserved at both surfaces by asymmetric chevron structures.[165]

If one has a further, more thorough look on the shape of the diffraction pattern in the region where the chevron-like structure is present, e.g. in figure 11.5 (a), a third peak in the middle of the two shown in the figure becomes imaginable. An appropriate fit to the data shows that this possibility can not be excluded with regard to the neutron scattering pattern. This would correspond to a molecular arrangement with untilted layers in the middle of the channels, while the layers at the circumference tilt similar to the chevron structure formation. An idealised picture of this situation is sketched in figure 11.7 (c). Again, conformations where single domains of either untilted or tilted layers with a statistical distribution are formed are in principle also compatible with the shown data. Three-armed chevron structures, as described here, have been also observed in micrometre-sized slab geometries.[85, 86, 205, 217] Furthermore, theoretical considerations as well as experiments on liquid crystals in nanochannels suggest the existence of a chevron tip with a finite width.[178, 273] However, a theoretical examination finds that especially far from the smectic-A-to-smectic-C phase transition the width of the tip is expected to be around three orders of magnitude smaller than the gap of the confining cell.[273]

Looking at the onset temperature of the chevron formation and the phase transition data of the 2MBOCBC bulk liquid crystal (see section 10.2), one notices that the transition temperature from the crystalline to the smectic C* phase accords well with the temperature where in the AAO nanochannels the structural change from chevrons back to the bookshelf structure, or vice versa, occurs. However, respective neutron diffraction experiments on the in-plane

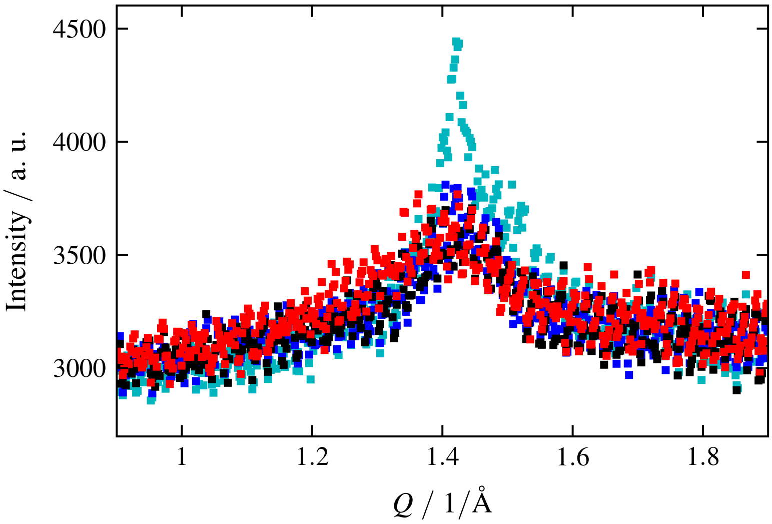

Figure 11.8.: Neutron diffraction Bragg peak of the liquid-like order within the smectic layers of the AAO-nanoconfined 2MBOCBC molecules measured at 🟥 313 K, ⬛ 273 K, 🟦 368 K and ■ 258 K.

smectic molecular order were carried out as described in section 10.6. These deliver a diffraction peak belonging to the intermolecular distance within the smectic layers. This Bragg peak is shown in figure 11.8 for different temperatures. It is found to be quite broad in the whole temperature range investigated above, as it is characteristic for the diffraction at liquids. Only below around 268 K an onset of crystallisation can be observed, but even ten Kelvin lower the smectic layers still possess remains of liquid-like properties. Therefore, it can be excluded that the above structural changes are triggered by a starting crystallisation of the liquid crystal.

11.2.5. Temperature-dependent smectic layer thickness

The above argumentation that the buckling of the layers towards chevrons sustains to some extent the original smectic layer spacing is corroborated by the determined thickness of the tilted layers of 2MBOCBC in mesoporous AAO, investigated here. This layer thickness is ascertained by determining the smectic diffraction peak centre via a pseudo-Voigt-shaped fit to the intensity as a function of 2Θ at the ω-angle associated with the respective layer tilt angle. Or in other words, the slice along 2Θ of an ω-rocking scan as depicted in figure 11.4 whose ω equals the tilt angle of the layers (compare figure 11.6 (c)) is considered for the determination of their thickness. The peak position is related to the layer spacing via Bragg's equation. The results for the layers that form the wings of the chevrons upon cooling are shown as a function of temperature in figure 11.6 (d) as round dots. Contrary to the bulk state, where a marked increase of the smectic layer thickness is observed in the smectic A* phase upon cooling until the transition to the smectic C* phase [110, 206], in the nanoconfinement of the AAO channels this effect is hardly perceptible in the same temperature range, as can be seen from figure 11.6 (d). However, at the transition to the smectic C* phase the layer thickness starts to decrease. This effect becomes much stronger and faster starting at around 309.5 K, when also the chevron formation sets in, having a saturation tendency resembling somewhat that of the layer tilt angle in the panel above. This again might be considered as an evidence of the influence of the smectic C* molecular tilt on the layer tilting and therefore the genesis of chevrons. The overall magnitude of the decrease in layer thickness though is around a factor of three less compared to the one observed in the bulk smectic C* phase in the same temperature range, found in the literature and confirmed by own X-ray diffraction measurements.[110, 135, 206] Thus, the finding that the smectic layer distance of the tilted layer planes does not strongly reduce when chevrons are formed is also confirmed in the case of nanoconfinement in the channels of AAO.

The temperature course of the layer thickness of the potential untilted centre smectic layers, as determined from the diffraction peak position at $\omega = 0°$ (compare figure 11.4), is shown as triangles in panel (d) of figure 11.6. It is noteworthy, that there the layer thickness decrease on cooling is significantly smaller than the one of the tilted layers. Note also, that the round dots in the same graph show the results of the two-peak fits to the data assuming only tilted layers and the outcome when considering additional untilted layers in the centre is even somewhat more pronounced concerning the decrease of the thickness of the tilted layers.

11.2.6. Reversibility upon temperature cycling and reproducibility

It should be emphasised that not only the layer thickness, but also the layer tilt angle with the associated chevron-like structure development is fully reversible throughout the whole temperature cycle, while cooling and heating (see figure 11.6). Moreover, it is reproducible in consecutive measurements. Solely, the temperature course of the integrated intensity has, as already mentioned, a hysteresis in the transition between the isotropic and smectic phase (see figure 11.6 (a)). Such a reproducibility of the chevron formation where the structure is the same on cooling and heating can not offhandedly be regarded as naturally given. At least for chevron structures evolving out of the smectic A phase in a slab geometry a hysteresis is reported [217, 262], which is amongst others attributed to possible surface memory effects [52, 156]. The amplitude of the hysteresis in this context is found to shrink with decreasing micrometre-sized slab distance [156, 217], therefore supporting the absence of a hysteresis in the case of nanochannels confining the liquid crystal, as presented here.

In addition to the reversibility of the temperature-induced structural changes of the liquid crystal within the nanochannels, the measurements on this system exhibit a remarkable reproducibility. Figure 11.9 shows the integrated intensity of the 001 smectic layering Bragg peak from the above neutron diffraction experiment in comparison to the one obtained from X-ray diffraction measurements at one arbitrarily chosen sample from the membrane stack of the neutron scattering experiment. Note, that in contrast to the integrated Bragg peak intensity shown in panel (a) of figure 11.6, here the intensity of the peak is not integrated over the complete measured ω-range (compare e.g. figure 11.4), but only for $\omega = 0°$, since that corresponds to the scattering geometry of the X-ray diffraction experiments (see section 10.5). As a consequence, the intensity course below the starting point of the formation of the chevron-like layer structure at around 309.5 K is different now, because due to the tilting of the layers the intensity is distributed over a larger ω-range. Therefore, at $\omega = 0°$ there are less smectic

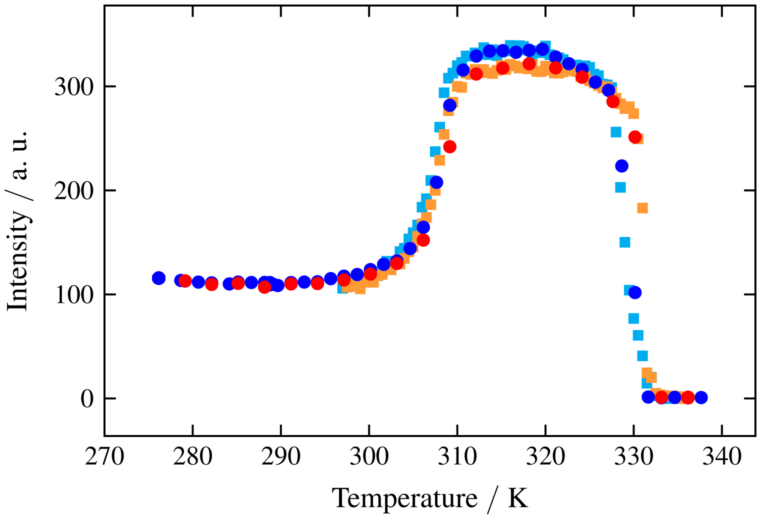

Figure 11.9.: Integrated intensity of the 001 smectic layering Bragg peak from ●/● neutron (for $\omega = 0°$) and ■/■ X-ray diffraction data. Blue/cyan and red/orange symbols denote cooling and heating cycle, respectively.

layers contributing to the diffraction signal and thus the intensity decreases. As can be seen from figure 11.9, the temperature courses of both diffraction experiments match very well in all details, like the hysteresis in the vicinity to the transition to the isotropic phase or that in a certain temperature range the intensity during cooling is always higher than the one on heating. The latter might hint at small differences in the structure, for instance that the bookshelf structure is not (completely) restored in a minority of pores on heating. That this can not be seen from figure 11.6 is simply a consequence of the different ways the integrated intensity is determined, since the corresponding fits as shown in figure 11.5 might underestimate changes of the intensity at a single ω-value, especially at $\omega = 0°$. As a conclusion, these measurements show not only their reproducibility and the long-term stability of the samples, but also that already such relatively simple laboratory-scale X-ray diffraction experiments can give valuable first hints at the complex structural changes of the nanoconfined liquid crystals. This is discussed in more detail in appendix D, where also preliminary X-ray diffraction experiments on 2MBOCBC within AAO nanochannels of different widths are presented.

11.2.7. Results in the context of electro-optical experiments

The above structural findings elucidate the results of concerted electro-optical experiments on identical membranes [34], performed by the group of Andriy Kityk (Częstochowa University of Technology, Poland). There, an applied electric field causes changes in the orientation of the molecules and therefore a change in its birefringence (see section 9.3 for theoretical background), which can be detected by a suitable optical technique. This method can be regarded as an analogue to dielectric spectroscopy.[158, 278, 279]

An alternating sinusoidal voltage with a frequency of 124 Hz and 10 V amplitude is applied with electrodes separated around 1 mm from each other, creating a virtually homogeneous electric field perpendicular to the long channel axis of the liquid crystal filled nanopores.[34] At the same time the sample is penetrated by an elliptically polarised laser beam with an angle of around 35–45° to the surface normal of the membrane, which is subsequently analysed by a polariser and photodetector (see Busch et al. [34] for a sketch and a more detailed description of the experimental set-up). In this way the response of the liquid crystalline structure on the application of the external electric field — manifesting in its optical properties — is measured. The chosen frequency corresponds to the quasi-static regime.[34] That means that the variations of the electric field are such slow that its impact on the liquid crystal molecules resembles the one of a static field of the corresponding strength. In principle the application of an electric field as it is done here, can lead to a deformation of the chevron-like layer structure up to a complete transformation back to a bookshelf structure.[135, 140, 212, 259] However, the required electric field strength is usually much higher than the one applied in the here presented experiments.[135, 140, 212, 259]

Starting from the isotropic-to-smectic A* transition the real part of the linear electro-optical response starts to rise [34], as can be seen from figure 11.10 (a). This increase becomes steeper on approaching the transition to the smectic C* phase.[34] The already remarkably increasing electro-optical response in the range of the smectic A* phase is attributed to the fact that this phase is in actuality superseded by a parasmectic C* phase, which is characterised by already slightly tilted molecules.[34] This is also the assumptive explanation for a much higher optical activity in this range, compared to the bulk ferroelectric liquid crystal, whose origin is in the helical structure normally not being present in the smectic A* phase due to the absence of collectively tilted molecules.[34] The presence of a helix structure in the nanochannels is a very interesting finding, since in micrometre-sized slab geometries with planar surface anchoring, a reduction of the confinement in the range of the pitch length of the helix usually leads to an unwinding of the ladder.[149, 165] Interestingly, here the optically activity even increases with decreasing nanochannel diameter.[34]

Soon after the temperature is reached, where the bulk smectic-A*-to-smectic-C* phase transition occurs, the electro-optical response of 2MBOCBC confined in AAO starts to saturate and reaches its maximum. When cooling the system further down the response begins to decline. In principle a decrease is expected on chilling the sample, because interfacial interactions and the rotational viscosity at a progressive rate hinder the field-induced molecular reorientation.[34] However, the effect of a reducing optical response is much stronger than one would expect in such a case. In addition, as one can see from the comparison of panel (a) and (b) of figure 11.10, the starting point of its strong abatement at 309.5 K very well coincides with the onset of the chevron-like layer transformation, accompanied by the steep increase of the diffraction peak width and the kink in its intensity course (see figure 11.6). This chevron-like layer buckling has now two consequences on the spontaneous polarisation of the confined smectic layers: Since the spontaneous polarisation $\vec{P}$ is parallel to the smectic layer plane, the tilting of these planes causes also a respective change in the direction of $\vec{P}$, which is not longer perpendicular to the long channel axis of the hosting AAO membranes. Furthermore, the rotational symmetry of the chevron arrangement around the channel axis entails conically-shaped smectic C* layers and thus a uniform direction of the spontaneous polarisation, as it would be the case in planar smectic layers, can not be expected. In general,

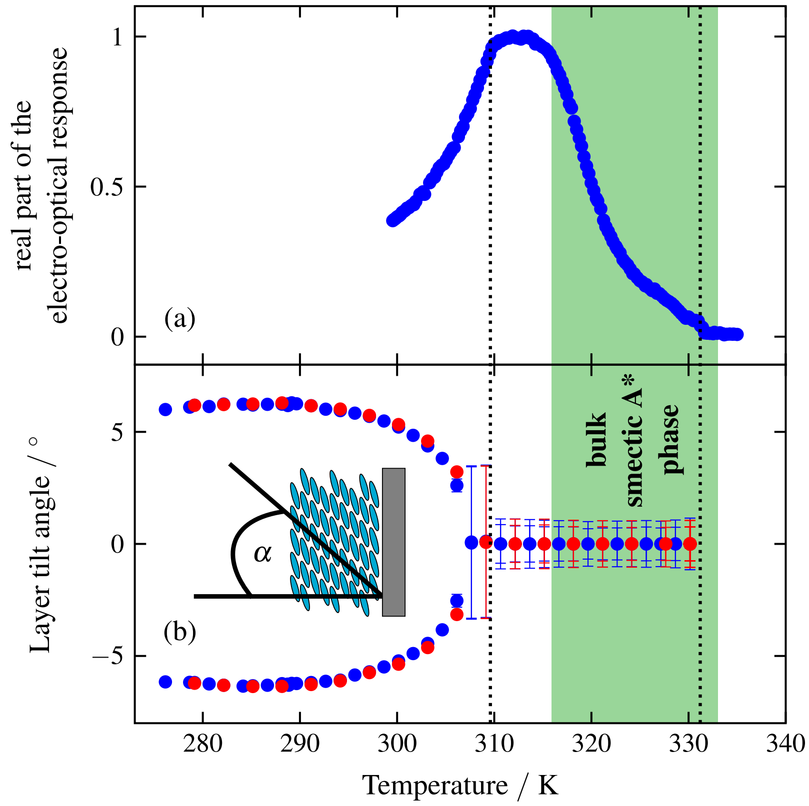

Figure 11.10.: Relation between structure and electro-optical response: (a) real part of electro-optical response and (b) smectic layer tilt angle (identical with panel (c) of figure 11.6) as a function of temperature.

it is well known that the formation of chevrons has a great impact on the response of a confined ferroelectric liquid crystal on the application of an external electric field.[51, 165] The fact that the electro-optical response does not vanish completely supports the above described statement that there is presumably a certain range of untilted smectic layers in the channel centre.[34]

CHAPTER 12

Conclusions & outlook

The temperature-dependent structure and phase transition behaviour of two chiral, thermotropic liquid crystals within anodic aluminium oxide (AAO) nanochannels have been studied using X-ray and neutron diffraction techniques.

12.1. Liquid crystal CE6

The chiral nematic $\rightleftharpoons$ smectic A* phase transition of the liquid crystal CE6 has been investigated in polymer-surface-coated AAO nanochannels as a function of channel width with X-ray diffraction. The findings were compared to analogous measurements of CE6 in the bulk state. While the cholesteric $\rightleftharpoons$ smectic A* phase transition is of first order in the bulk state, the transition is continuous in the case of the AAO nanoconfinement, where the smectic layers orient perpendicular to the long nanochannels axis. The transition temperature in the confinement is shifted towards higher temperatures and further increases with decreasing nanochannel diameter. In parallel, the critical exponent of the smectic translational order parameter that is related to this phase transition was found to decrease, instead of approaching the value predicted by the 3D XY theory, as it is found for the achiral liquid crystal 8CB and few others [130, 160–162, 168, 179, 227, 299].
Although possible explanations were discussed, the ultimate reason for the observed upward shift of the chiral nematic $\rightleftharpoons$ smectic A* phase transition temperature, going along with the shrinking values for the smectic translational order parameter related critical exponent, could not be given here. For a further investigation of these findings, experimental studies at more membranes with different channel diameters — larger and smaller ones — might be helpful. Furthermore, an additional variation of their surface chemistry and roughness would be necessary in order to review whether surface-induced effects are responsible for the above findings. For example, such a study of the nematic-to-isotropic phase transition of the achiral liquid crystal 5CB in AAO nanochannels of different diameters with and without surface modification finds that the phase transition temperature is shifted to lower temperatures as a result of the surface coating, to which a disordering effect is ascribed.[113] This shows again the importance of investigating the interplay between the liquid crystal and the its confining surface for different material combinations, because contrary to the cited study a surface-induced or-

dering effect is ascribed to the polymer coating that is used in the investigation of the confined CE6 liquid crystal, here (see section 11.1.2).

Concerted with the above proposed experiments, theoretical studies, as well as computer simulations, could additionally lead to a deeper understanding of the perceived phenomena. In this context, an analysis of the influence of the confinement and pore wall surface on the coupling of the smectic and the orientational order parameter might be interesting.[59, 98] Finally, an investigation of the molecule's chirality and the resultant helix structure in the chiral nematic phase with regard to their role concerning the phase transition behaviour in the bulk and the confined states could deliver important new insights.

12.2. Liquid crystal 2MBOCBC

The liquid crystal 2MBOCBC, which consists as CE6 also of chiral molecules, was investigated in AAO nanochannels concerning its temperature-dependent structure, using neutron diffraction. The surface of the channels was coated with a polymer in order to ensure a tangential alignment of the molecules with respect to these pore walls. The isotropic $\rightleftharpoons$ smectic A* phase transition is found to exhibit a hysteresis between the heating and cooling cycle. But more interesting is the transition of the smectic A* to the smectic C* phase. When the molecules within the smectic layers start to tilt, also the afore perpendicular to the long nanochannels axis oriented smectic layers start to gradually tilt up to an angle of more than 6°. Several possible structural arrangements within these 42 nm wide AAO nanochannels were discussed, from which the formation of a rotational symmetric chevron-like smectic layer structure with a supposable untilted core region is found to be the most likely one. Furthermore, the development of this structure is fully reversible without any hysteresis and additionally reproducible on consecutive temperature cycles. The tilt of the liquid crystal molecules within the smectic C* layers leads to a corresponding shrinkage of the layer's thickness, which is however less pronounced than the one observed in the bulk state. If considering a region of untilted smectic layers in the core region of the nanochannels, it is found that there the layer thickness is even less reduced than the one in the surrounding chevron wings.

It would be very interesting to continue the investigation of the structure of the liquid crystal 2MBOCBC inside AAO nanochannels of other — especially smaller — diameters. Preliminary X-ray diffraction experiments that are shown in appendix D demonstrate not only that already such simple experiments give valuable hints on the formation of the above described chevron-like layer structure, but indeed suggest that there might be also the development of such structures in AAO nanochannels with considerably smaller diameters.

Since concerted optical experiments by a collaborating working group find an enhanced optical activity that hints towards the existence of a helical supermolecular structure even in the chevron regime [34], it would be very interesting to study this structure in more detail on a microscopic level. Especially, the analysis of the interplay between the helical structure related to the molecules' chirality and the dynamics of smectic layer tilting with the corresponding formation of a chevron-like smectic layer structure, as well as the interaction with the channel walls, appears desirable and could be investigated using for example computer simulations.

Appendix

APPENDIX A

Fixed window scan data treatment and analysis

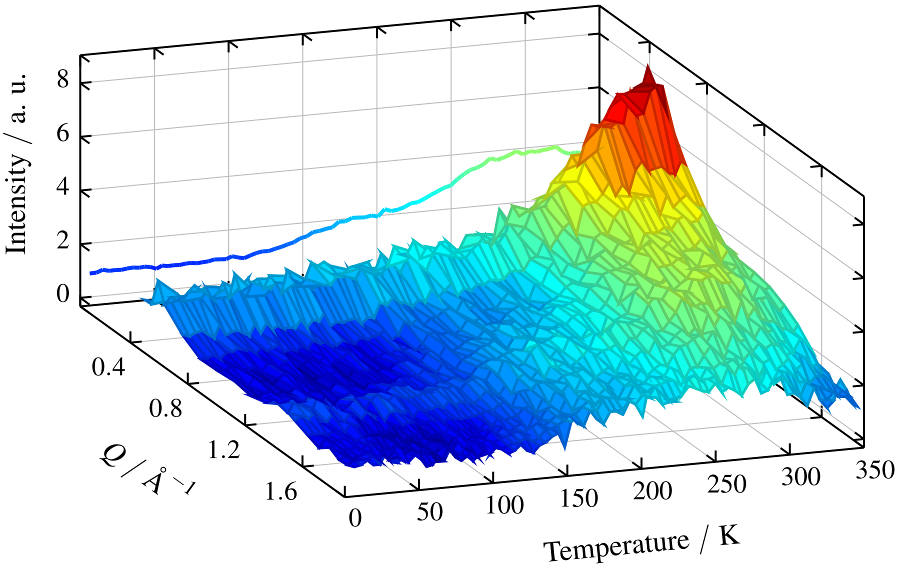

Figure A.1.: Intensity of the inelastic fixed window scan on MoC-21 filled with the ionic liquid at an energy transfer of ±2 µeV as a function of temperature and wave vector transfer Q (foreground) and over the available Q-range averaged intensity as a function of temperature (back panel).

The so-called fixed window scans measured with the neutron backscattering spectrometer IN16B, whose working principle and acquisition are described in section 6.1, deliver a dataset containing the intensity of scattered neutrons that have exchanged a defined amount of energy with the sample, as a function of wave vector transfer Q and temperature T. In contrast to the full quasi-elastic spectra, where the normalisation on the detector efficiency is done using a measurement on vanadium, here for the normalisation the low temperature measurement, where all dynamics are frozen, is used. That means, that the measured intensity for all temperatures in the elastic and inelastic fixed window scans is respectively divided by the intensity

recorded in the elastic fixed window scan of the respective sample at the lowest measured temperature around 2 K, for each wave vector transfer Q separately. As an example the resulting normalised intensity as a function of wave vector transfer Q and temperature T from the inelastic fixed window scan measurement of the carbon sample MoC-21 filled with the ionic liquid, is shown in the three-dimensional plot in figure A.1. The Q-range available in the fixed window scans is smaller compared to the one of the quasi-elastic spectra, since the analysers corresponding to the two lowest wave vector transfers are slightly skewed out of the backscattering condition. In such a way they deliver data that correspond to another energy transfer as the intended one and are therefore omitted in case of the fixed window scans, while for the full quasi-elastic spectra it leads to an manageable shift of the energy transfer scale.
For the representation of the data as a function of temperature, as shown in graph 6.4 in section 6.1.2 the intensity is normalised and subsequently averaged over the whole for this measurement mode available wave vector transfer range, which is $0.44\,\text{Å}^{-1}$ to $1.90\,\text{Å}^{-1}$. This is exemplarily shown for the inelastic fixed window scan in figure A.1, where the graph in the back panel shows the intensity of the 3D graph in the front, summed up over all Q and divided by 16, i.e. the number of different Q-values.

A.1. Model fits to the inelastic fixed window scans

Though being a comparatively simple, but excellent tool to study the molecular dynamics over a wide temperature range, the analysis of the received data from the fixed window scans is more complex as it might appear on the first view or even in its description in the experimental section (see page 31 ff.), where not every detail can be described.
In the most cases information are gained from the wave vector transfer dependence of the intensity. Therefore, for these analyses the intensity is not averaged over Q, as it is done for a first qualitative representation of the data, described above. An exception is the fit to the inelastic fixed window scan curve of the low-temperature dynamics of the crystalline bulk ionic liquid, where a Q-dependence of the width of the corresponding quasi-elastic spectrum is neither expected [40], nor found here, as shown in section A.1.2 of this appendix.

A.1.1. Handling of the background of the data

Since the incorporation of the background intensity, present in the data, into the fit procedure of the molecular dynamics would not only entail a more complex and therefore less stable routine, but also possibly leads to wrong results. Hence, the background is determined as follows for each Q-value separately before the fit to the data with the model describing the molecular dynamics, and kept unaltered during the latter. First, the temperature dependence of the background is appointed by the assumption that its intensity diminishes with rising temperature according to the Debye-Waller factor. Assuming the applicability of its harmonic approximation [173] a temperature-dependent Debye-Waller factor,

$$DWF = e^{-\tilde{a}\cdot T\cdot Q^2} = \frac{I(Q,T)}{I(Q,T=0\,\text{K})} \quad \text{with } \tilde{a} = \text{const.,} \tag{A.1}$$

is used for the description of the temperature dependence of the measurement signal in the absence of any dynamics apart from lattice vibrations. Because its dependence on the wave vector transfer Q will be already implicitly included in the later determined offset, this Debye-Waller factor is split into two parts and only the one describing its temperature dependence, $\exp(-a \cdot T)$ (with $a = \text{const.}$), will be estimated here. This is done by a fit to the integrated intensity of the elastic fixed window scan corresponding to the analysed inelastic one. To do this, initially, a range in the elastic fixed window scan must be identified, where the reduction of the measured intensity is only due the Debye-Waller factor and not cause of any dynamic processes, like diffusion. The presence of such dynamics would lead to inelastically scattered neutrons and thus to less elastically scattered ones, since the overall amount of neutrons is of course conserved. The procedure is shown in figure A.2 at the example of the measurement at MoC-21 filled with the ionic liquid. From the integrated inelastic fixed window scan a range at low temperatures is chosen (see rectangle B in panel (b)), where no perturbing dynamics are present, i.e. which is relatively far away from any rise of the inelastically scattered intensity — at least with the considered energy transfer. Thereafter, the temperature dependence of the Debye-Waller factor is determined through a fit with

$$e^{-a \cdot T} = \frac{I(T)}{I(T = 0\,\mathrm{K})} \quad \text{with } a = \text{const.}, \tag{A.2}$$

to the data of the over Q averaged elastic fixed window scan in the same temperature range (see rectangle A in panel (a) of graph A.2). This temperature dependence is subsequently used for the background of all curves of the respective sample, for all wave vector transfers Q. Because the intensity of the inelastic fixed window scan is normalised on that of the elastic fixed window scan the intensity prefactor $c_0(Q) = I(Q, T = 0\,\mathrm{K})$ for the background BG

$$BG = c_0(Q) \cdot e^{-a \cdot T} \tag{A.3}$$

is determined for each of the 16 inelastic fixed window scan curves, corresponding to different wave vector transfers Q from $0.44\,\text{Å}^{-1}$ to $1.90\,\text{Å}^{-1}$, separately. This is done by fitting equation A.3 with fixed constant a, as determined above, to the data of the inelastic fixed window scan in the same temperature range, marked with the rectangle B in figure A.2 (b), that was also used for the determination of the temperature dependence of the Debye-Waller factor. The background in the inelastic fixed window scan data might amongst others originate from remains of the resolution function, because the 2 µeV energy channel lies relatively close to the elastic line. Interestingly, the background offset $c_0(Q)$ shows also in the cases of the carbon nanoconfinement clear indications of the structure factor of the ionic liquid.

For the wave-vector-independent fit to the data of the bulk ionic liquid inelastic fixed window scan, the specification of the background is done fully analogous to above, with the difference that here the fit is applied to the data that are averaged over the available Q range, since also the subsequent fit of the dynamics is done in such a way.

A.1.2. Model fits of the localised dynamics of the bulk ionic liquid

In the next step a model describing the dynamics of the system under consideration is fitted to the data. The dynamic structure factor for localised dynamics of the bulk ionic liquid, as

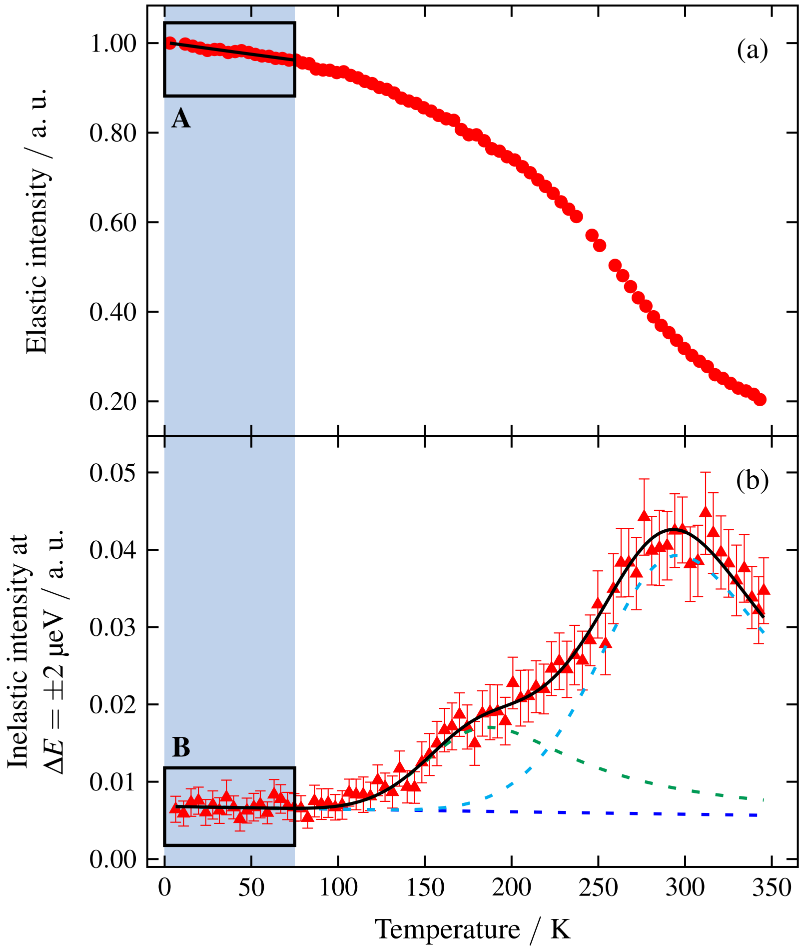

Figure A.2.: Fixed window scans on MoC-21, filled with the IL: (a) Elastic fixed window scan integrated over the available Q-range with fit of the temperature-dependent Debye-Waller factor (see A). (b) Inelastic fixed window scan data at a wave vector transfer $Q = 1.18\,\text{Å}^{-1}$ with fit composed of different contributions, as described in the text.

those of the methyl groups or possibly segmental rotations of the butyl group, reads

$$S_{\text{local}}(Q,T,\omega) = A(Q)\delta(\omega) + (1 - A(Q)) \cdot \frac{1}{\pi} \frac{\gamma_1(Q,T)}{\gamma_1^2(Q,T) + \omega^2} \quad , \tag{A.4}$$

where $A(Q)$ describes the elastic incoherent structure factor (EISF) of these localised motions and is considered to be temperature-independent, here.[13] It should be pointed out that also slow motions, which appear to be immobile within the resolution of the instrument, give rise to an elastic contribution. The half width at half maximum γ_1 is the inverse of the relaxation time of the considered dynamics and the latter is assumed to follow an Arrhenius temperature dependence:

$$\frac{1}{\gamma_1(T)} = \tilde{\tau}_{\text{local}}(T) = \tilde{\tau}_{\infty;\text{local}} \cdot \exp\left(\frac{E_{\text{a;local}}}{RT}\right) \quad , \tag{A.5}$$

with the universal gas constant R, the high-temperature limit $\tilde{\tau}_{\infty;\mathrm{local}}$ of the relaxation time and the activation energy $E_{\mathrm{a;local}}$ of these dynamics.[90, 111] The intensity measured in this inelastic fixed window scan experiment is then given as

$$I(Q,T) = e^{-a\cdot T} \cdot \left[I_0(Q) \cdot (1 - A(Q)) \cdot \frac{1}{\pi} \frac{\tilde{\tau}_{\mathrm{local}}(Q,T)}{1 + \tilde{\tau}^2_{\mathrm{local}}(Q,T) \cdot \omega^2_{\mathrm{IFWS}}} + c_0(Q) \right] , \tag{A.6}$$

since the delta part of equation A.4, related to the elastic scattering, is not registered by the energy channels corresponding to $\omega_{\mathrm{IFWS}} = \pm 2\,\mu\mathrm{eV}/\hbar$. The given intensity factor I_0 (and the offset c_0) also contains the additional intensity due to the convolution of the above scattering law with the resolution function.[90] As already stated above, the relaxation time $\tilde{\tau}_{\mathrm{local}}(T)$ and consequently the half width is assumed to be wave vector transfer independent. This is confirmed by fitting equation A.6 to the bulk ionic liquid inelastic fixed window scan data for all available wave vector transfers Q in parallel with common parameters, only differing in the background offset $c_0(Q)$ and the intensity scaling factor $I_0(Q) \cdot (1 - A(Q))$. The background offset and the exponential prefactor, describing the temperature dependence of the Debye-Waller factor, were determined before this fit as described in the preceding section. The result of the fit procedure with equation A.6 is shown in figure A.3 for various Q values. A Q-dependent half width would entail a Q-dependent peak shift. However, such a shift is not visible here, but instead the model function fits the data very well for all wave vector transfers. Also fits with other models allowing the peak to shift with respect to the temperature do not show a systematic wave vector transfer dependence of the related half width of the quasi-elastic line broadening.

Therefore, the data can alternatively also analysed by averaging the intensity of this inelastic fixed window scan over Q and fitting the model in equation A.6 to this single curve, having now only a single intensity factor and background offset. The results of this method are presented in figure 6.5 in section 6.1.3 and show only minor deviations concerning the numerical results of the obtained activation energy $E_{\mathrm{a;local}}$ and the high-temperature limit of the relaxation time $\tilde{\tau}_{\infty;\mathrm{local}}$.

A.1.3. Model fits of the combination of various dynamics

In contrast to the bulk ionic liquid, where the localised and global dynamics are separated with regard to the temperature range of the inelastic fixed window scan, there is a superposition of both dynamics in the case of the confinement in the nanoporous carbon. Thus a model describing localised dynamics, as well as such on a longer length scale, is needed. In principle the same model is used, which is also applied to the full quasi-elastic spectra. This model consists of two components.

The first one describes the localised dynamics, which are here, amongst others, attributed to the dynamics of the methyl groups and is described by the same dynamic scattering law as above (see equation A.4). Again the Arrhenius distribution from equation A.5 for the temperature-dependent relaxation time $\tilde{\tau}_{\mathrm{local}}(T)$ is used and thus also the corresponding half width at half maximum $\Gamma_1(T)$ follows an Arrhenius temperature dependence through the relation $\Gamma_1(T) = \hbar/\tilde{\tau}_{\mathrm{local}}(T)$.

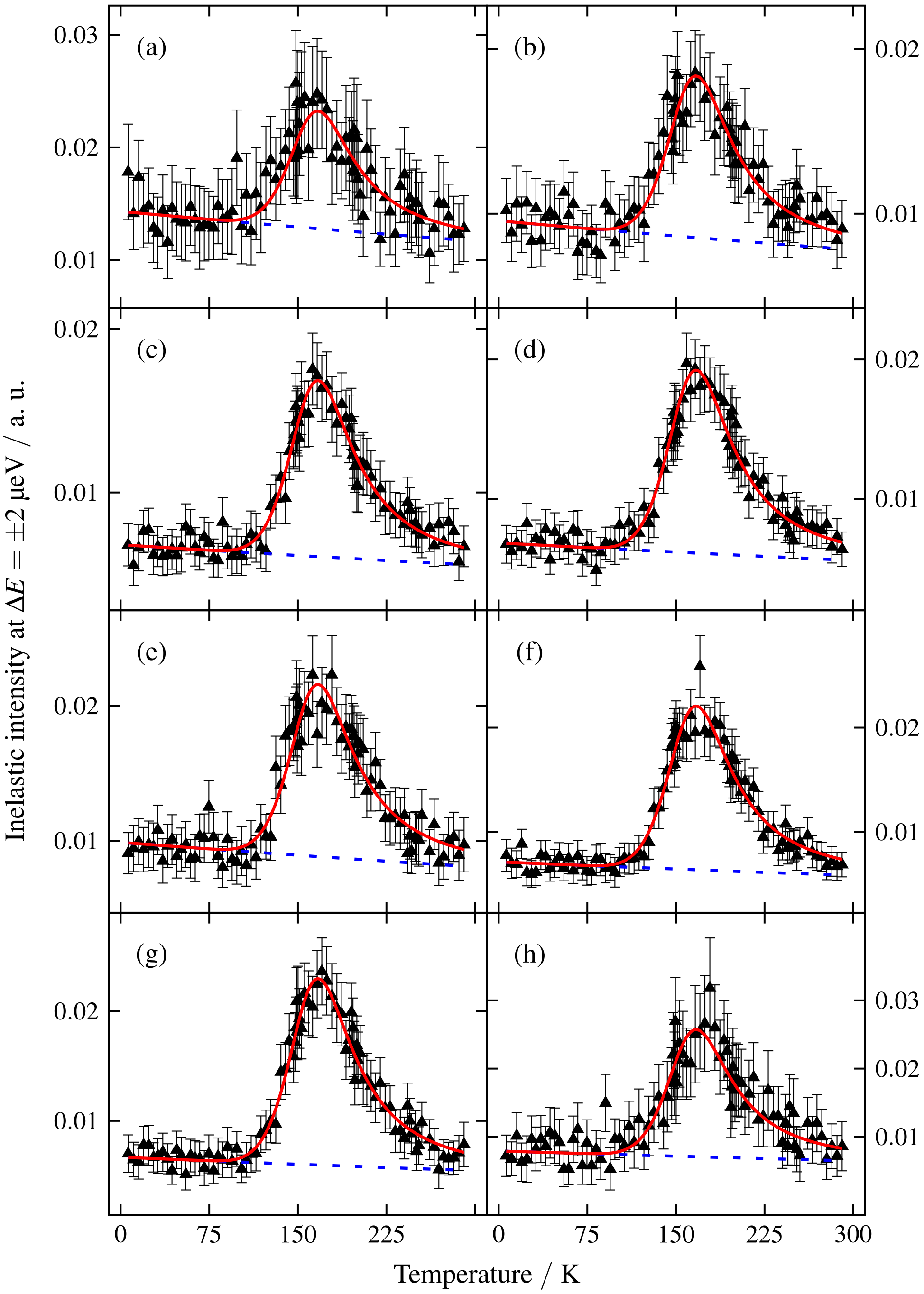

Figure A.3.: Result of the simultaneous fit with the model from equation A.6 to the data of the inelastic fixed window scan on the bulk ionic liquid for eight representative wave vector transfers Q of (a) 0.44 Å^{-1}, (b) 0.70 Å^{-1}, (c) 0.95 Å^{-1}, (d) 1.18 Å^{-1}, (e) 1.39 Å^{-1}, (f) 1.57 Å^{-1}, (g) 1.72 Å^{-1} and (h) 1.90 Å^{-1}.

The second component

$$S_{\text{global}}(Q,T,\Delta E) = \frac{1}{\pi} \frac{\Gamma_2(Q,T)}{\Gamma_2^2(Q,T) + \Delta E^2} \tag{A.7}$$

is related to the diffusion process of the molecule as a whole. Here, in opposition to the fits to the full quasi-elastic spectra, only one such component is considered. In principle, it would be possible to include more than one of such components into the fit procedure. However, since the information content is limited compared to the full spectra, an increasing number of parameters would not only lead to a decreased stability of the fit procedure, but also reduce the reliability of the gained outcome. Thus, the information about the mass diffusion of the whole molecule obtained here, is considered as an average of the different diffusive processes of this kind.

For the fit to the data the two components above are convoluted, scaled with an intensity factor $I_0(Q)$ and supplemented with the background, as determined in section A.1.1 above:

$$I(Q,T,\Delta E) = e^{-a \cdot T} \cdot \left[I_0(Q) \cdot \left\{ S_{\text{local}}(Q,T,\Delta E) \otimes S_{\text{global}}(Q,T,\Delta E) \right\} + c_0(Q) \right] \ . \tag{A.8}$$

Because the inelastic fixed window scan data are merely acquired for an energy transfer of $\Delta E = \pm 2\,\mu\text{eV}$, the obtained expression is evaluated for this energy value, only.

When doing a fit to the data, the number of data points determines the number of equations to be solved in the corresponding system of equations. Since the size of such a system limits the number of free variables that might be extracted from the data set (although the actual number should be well below this value), the number of these free parameters must be reduced. Therefore, certain assumptions are made:

The half width at half maximum $\Gamma_2(Q,T)$ is considered to follow the Singwi-Sjölander jump-diffusion model [253]

$$\Gamma_2(Q) = \frac{\hbar D Q^2}{1 + D Q^2 \tau_0} \ , \tag{A.9}$$

which has been found to hold for the bulk ionic liquid.[76] Additionally, Embs et al. [76] observed an Arrhenius-like temperature dependence of the self-diffusion coefficient D in case of the bulk liquid:

$$D(T) = D_\infty \cdot \exp\left(-\frac{E_{\text{a;global}}}{RT} \right) \ . \tag{A.10}$$

In addition, the results in this publication [76] also suggest a similar temperature dependence for the corresponding residence time τ_0

$$\tau_0(T) = \tau_\infty \cdot \exp\left(\frac{E_{\text{a;global}}}{RT} \right) \ , \tag{A.11}$$

which is used here as necessary assumption, to further reduce the number of free parameters. The resulting model function for the intensity of the inelastic fixed window scan is now fitted to the data for all available wave vector transfers Q in parallel, having common fit parameters, except the intensity factor $I_0(Q)$ and the EISF $A(Q)$. The background offset $c_0(Q)$ and the exponential prefactor, describing the temperature dependence of the Debye-Waller factor, are determined before (see section A.1.1) and kept fixed during this fit procedure.

The resulting best fit to the data is shown for example for the ionic-liquid-filled MoC-21 at a wave vector transfer of $Q = 1.18\,\text{Å}^{-1}$ in panel (b) of figure A.2. For a better understanding of the fit the three terms obtained after performing the convolution in equation A.8 are shown in equation A.12 below and delineated in the graph.

$$\begin{aligned} I(Q,T,\Delta E) = {} & e^{-a\cdot T}\cdot I_0(Q)\cdot A(Q)\cdot\frac{1}{\pi}\frac{\Gamma_2}{\Gamma_2^2+\Delta E^2} && \Big\}\ \text{(I)} \\ & + e^{-a\cdot T}\cdot I_0(Q)\cdot(1-A(Q))\cdot\frac{1}{\pi}\frac{\Gamma_1+\Gamma_2}{(\Gamma_1+\Gamma_2)^2+\Delta E^2} && \Big\}\ \text{(II)} \\ & + e^{-a\cdot T}\cdot c_0(Q) && \Big\}\ \text{(III)} \end{aligned} \tag{A.12}$$

The term (I) expresses the intensity of the Lorentzian corresponding to the diffusion of the cation as a whole, weighted with the EISF $A(Q)$ of the localised component, and is drawn as cyan dashed line. The green dashed line (term (II)) shows the convolution of the Lorentzians corresponding to the two dynamics, resulting in a Lorentzian, whose width is the sum of those of the individual ones. Each of the two graphs contains also the background term (III), which is plotted additionally as dark blue dashed line into the graph.

Fit curves for further wave vector transfers Q together with the respective inelastic fixed window scan measurement data of [BuPy][Tf$_2$N] within the carbon nanopores of MoC-21 are shown in figure 6.6 in section 6.1.3. Respective data for the cation dynamics of the ionic liquid confined within SiC-2, i.e. the carbon sample with the smallest pores, are presented in figure A.4. Figure A.5 shows the same kind of data for BC-no-9.

A.1.4. Intensity factor in the inelastic fixed window scan analysis

There is one important point that must be considered when analysing the inelastic fixed window scans as described above: The intensity at a fixed energy transfer is the only indicator for the shape of the underlying quasi-elastic energy transfer spectrum. When this spectrum broadens as a function of wave vector transfer Q, the intensity (i.e. the number of neutrons) is distributed over a wider energy transfer range and thus the intensity measured at a specific energy transfer value decreases. In that way, this intensity gives a direct measure for the width of the spectrum, if the underlying physical processes and therefore the fundamental shape of the curve are known. The application of suitable models that describe the Q and temperature dependence of the energy transfer spectra thus allow to trace the peak shape and the related model parameters back to the measured intensity. However, the crucial point is that the variance of the intensity as a function of Q is not only due to the dynamic processes of interest that are described by the employed model, but also caused by other effects. As a consequence, an intensity factor was chosen here that is individual, i.e. a free parameter, for each wave vector transfer. This, however, might disturb the correlation between the measured intensity and the Q-dependence of the peak shape as given by the applied model.

The analysis the Q-dependence of this intensity factor as obtained by the above model fits reveals that its course can be described to a large extent with a Debye-Waller factor. Hence,

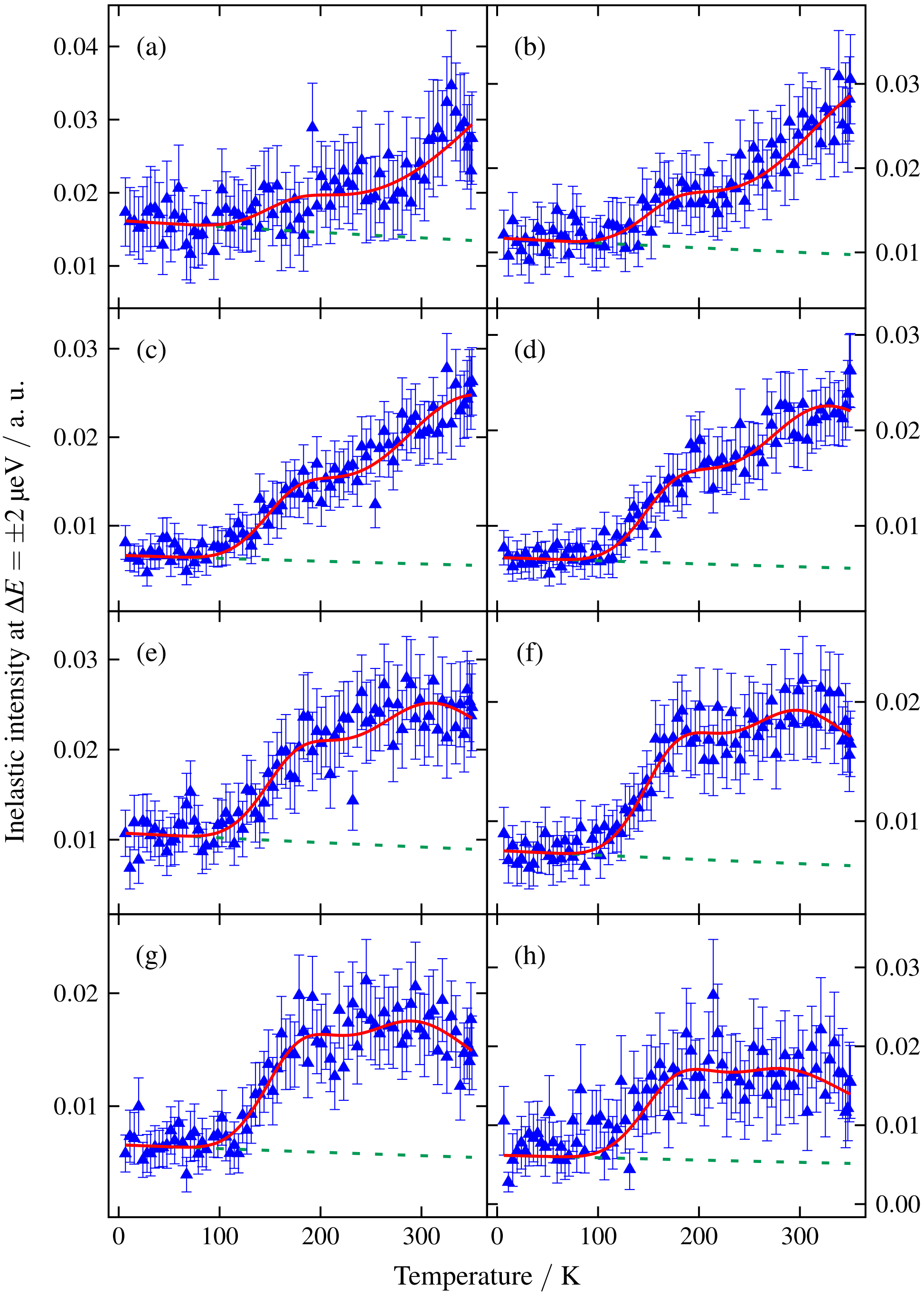

Figure A.4.: Result of the fit of the model from section A.1.3 to the inelastic fixed window scan data of [BuPy][Tf$_2$N] confined within SiC-2, for eight exemplary wave vector transfers Q: (a) 0.44 Å^{-1}, (b) 0.70 Å^{-1}, (c) 0.95 Å^{-1}, (d) 1.18 Å^{-1}, (e) 1.39 Å^{-1}, (f) 1.57 Å^{-1}, (g) 1.72 Å^{-1} and (h) 1.90 Å^{-1}.

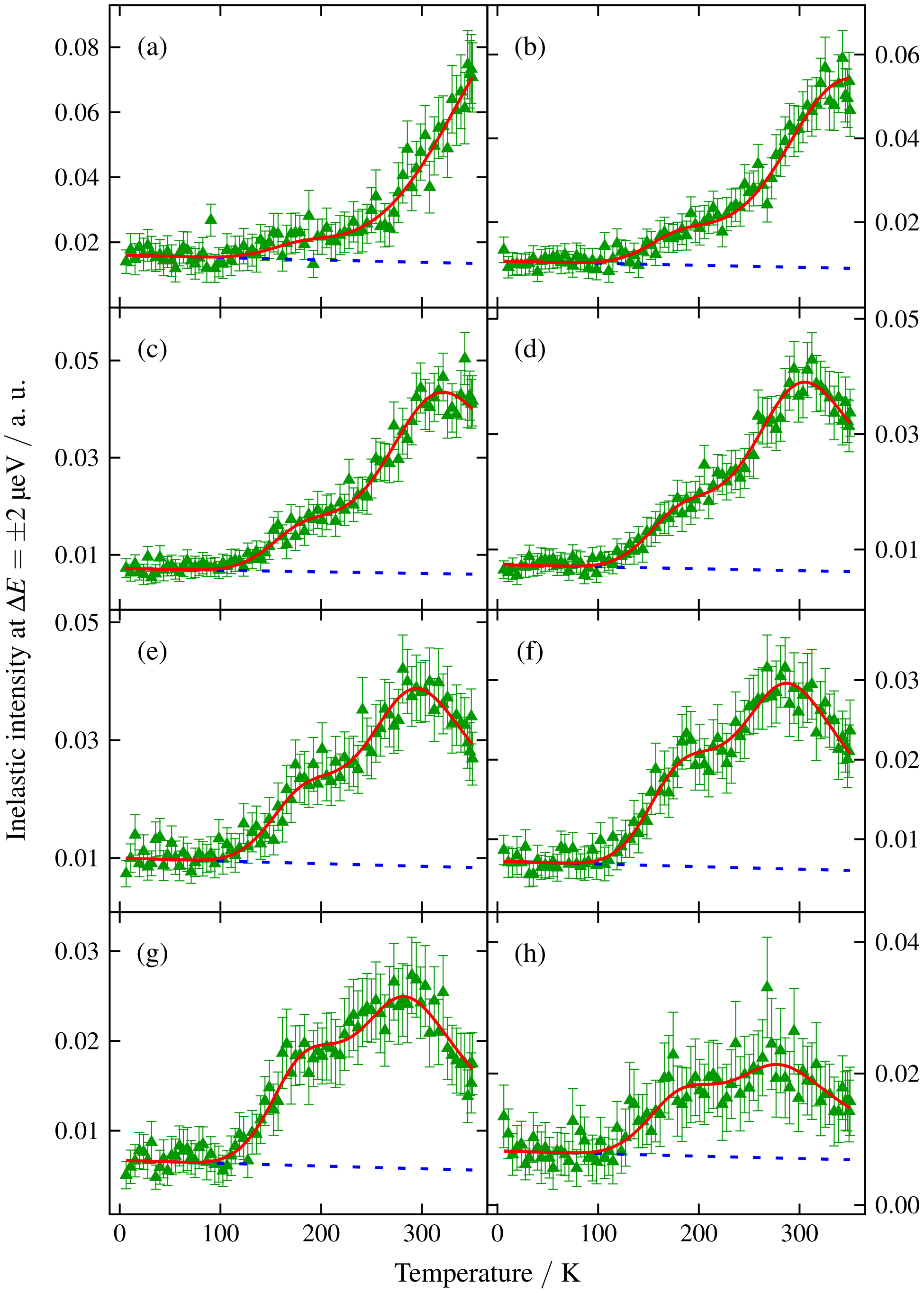

Figure A.5.: Result of the fit of the model from section A.1.3 to the inelastic fixed window scan data of [BuPy][Tf$_2$N] confined within BC-no-9, for eight exemplary wave vector transfers Q: (a) 0.44 Å^{-1}, (b) 0.70 Å^{-1}, (c) 0.95 Å^{-1}, (d) 1.18 Å^{-1}, (e) 1.39 Å^{-1}, (f) 1.57 Å^{-1}, (g) 1.72 Å^{-1} and (h) 1.90 Å^{-1}.

an alternative approach is to keep the intensity factor Q-independent and to model its wave vector transfer dependence completely by a Debye-Waller factor. Due to the reduced number of parameters this gives the additional opportunity to also incorporate the offset and the temperature dependence of the Debye-Waller factor within the fit procedure of the model. Indeed, it was found that such an approach with an explicitly given Debye-Waller factor leads in principle to comparable results with respect to the determined parameters. However, one might question that this procedure leads to more reliable results in general. The reason is that apart from the Debye-Waller factor, there are other parameters influencing the Q-dependence of the intensity. For instance there can be multiple scattering effects [302, 303] (see also the determination of mean square displacement from fixed window scans in section 6.1.1) or an influence of the structure factor of the analysed sample. It seems that signs of the latter can also be found in the above determined Q-dependent intensity factor. As a consequence of these effects, again the measured intensity and the one prescribed by the applied model might be wrongly correlated to a certain extent, leading to possible deviations in the determined parameters of the system from the actual ones.

In summary, it appears admissible to treat the intensity factor as a free, wave vector transfer dependent parameter, although it would be more favourable to predetermine it with a suitable model, what, however, is challenging because of the interplay of several effects. Nevertheless, it is essential to carefully examine whether the course of this intensity factor is physically meaningful. Additionally, one has to keep in mind that both approaches have the potential to distort the wave vector transfer dependence of the employed model, whose applicability therefore has to be thoroughly reviewed.

A.2. Model fits to the bulk elastic fixed window scan

The elastic fixed window scan data of the bulk ionic liquid is analysed using a rotational diffusion and a three-site jump model. These models describe the intensity of the elastic fixed window scans as a function of temperature T and wave vector transfer Q as

$$I_{\mathrm{el}}(T,Q) = I_0(Q) \cdot e^{-\tilde{a}TQ^2} \cdot \left[f + (1-f) \cdot \left(j_0^2(Qr_{\mathrm{s}}) + \sum_{k=1}^{\infty} \frac{(2k+1) j_k^2(Qr_{\mathrm{s}}) \Gamma_{\mathrm{res}}}{\Gamma_{\mathrm{res}} + \frac{k(k+1)\hbar}{6\tau'(T)}} \right) \right] , \tag{A.13}$$

in the case of the rotational diffusion model and as

$$\begin{aligned} I_{\mathrm{el}}(T,Q) = I_0(Q) \cdot e^{-\tilde{a}TQ^2} \cdot \Bigg[f + (1-f) \cdot \Bigg\{ & \frac{1}{3} \left(1 + 2 j_0 \left(Q r_{\mathrm{s}} \sqrt{3} \right) \right) \\ & + \frac{2}{3} \left(1 - j_0 \left(Q r_{\mathrm{s}} \sqrt{3} \right) \right) \Bigg\} \cdot \frac{\Gamma_{\mathrm{res}}}{\Gamma_{\mathrm{res}} + \frac{3\hbar}{2\tau'(T)}} \Bigg] , \end{aligned} \tag{A.14}$$

for the three-site jump model.[30, 230] Here, $I_0(Q)$ is an intensity factor, the exponential term a temperature-dependent Debye-Waller factor, f the fraction of immobile scatterers, j_k are spherical Bessel function of the first kind and Γ_{res} is the HWHM of the resolution function.

The relaxation time $\tau'(T)$ is assumed to possess an Arrhenius temperature dependence, analogous to equation A.5. Contrary to the inelastic fixed window scans above, the Debye-Waller factor is fitted directly with the rest of the model function to the data. The intensity factor $I_0(Q)$, which is chosen to be individual for each Q, is found to be practically 1 for all Qs, what is expected due to the normalisation of the data.

Burankova et al. [30] use both models from above to analyse an elastic fixed window scan of [BuPy][Tf_2N] with deuterated pyridinium ring, which was acquired at a spectrometer with a comparable energy resolution. They find that both models fit the data at least in a limited temperature range before the melting of the liquid and ascribe the observed dynamics to the motion of the methyl group, due to the fraction of mobile protons, found to be around one third.[30] The radius r_s of the motions is obtained to be 1.1 Å for both models, while the activation energy is 6.5 kJ/mol for the three-site jump model and 7.0 kJ/mol for the rotational diffusion model.[30] The high-temperature limit of the relaxation time is however found to deviate distinctly.[30]

The attempt to apply these models to the elastic fixed window scan of the fully protonated [BuPy][Tf_2N] obtained at IN16B in this work yields that only with the three-site jump rotation model a description of the data is possible. However, depending on the wave vector transfer Q the model fits the measurement data not nearly as well as the inelastic fixed window scans above by the respective models. Figure A.6 shows a representative selection of measurement curves and the respective result of the fit, where both — those that show a good agreement between model and data and those that do not — are chosen. The fit procedure is carried out simultaneously for all 16 Qs within a temperature range between 3 K and 246 K, while the plot shows the whole temperature range before the melting of [BuPy][Tf_2N]. The data points that do not contribute to the fit are marked with a grey background. This analysis yields an activation energy of 5.0 kJ/mol, a radius r_s of 3.4 Å and a fraction f of immobile scatterers of 0.5, in deviation from the results of the above cited reference [30]. The predominant reason for the observed differences are ascribed to the fact that there a partially deuterated molecule was investigated, while here all parts of the cation contribute to the incoherent scattering signal. That means, that apart from methyl group rotations and segmental rotations of the butyl chain, also motions of the pyridinium ring might be observed. This would be an explanation for the deviation of the above parameters, but would also make this model less applicable here. This, together with the very well agreement of the model presented in section A.1.2 with the respective bulk ionic liquid inelastic fixed window scan data, is one of the reasons, why the latter model is used for the analysis of the temperature dependence of the localised dynamics in bulk and in the case of the carbon nanoconfinement.

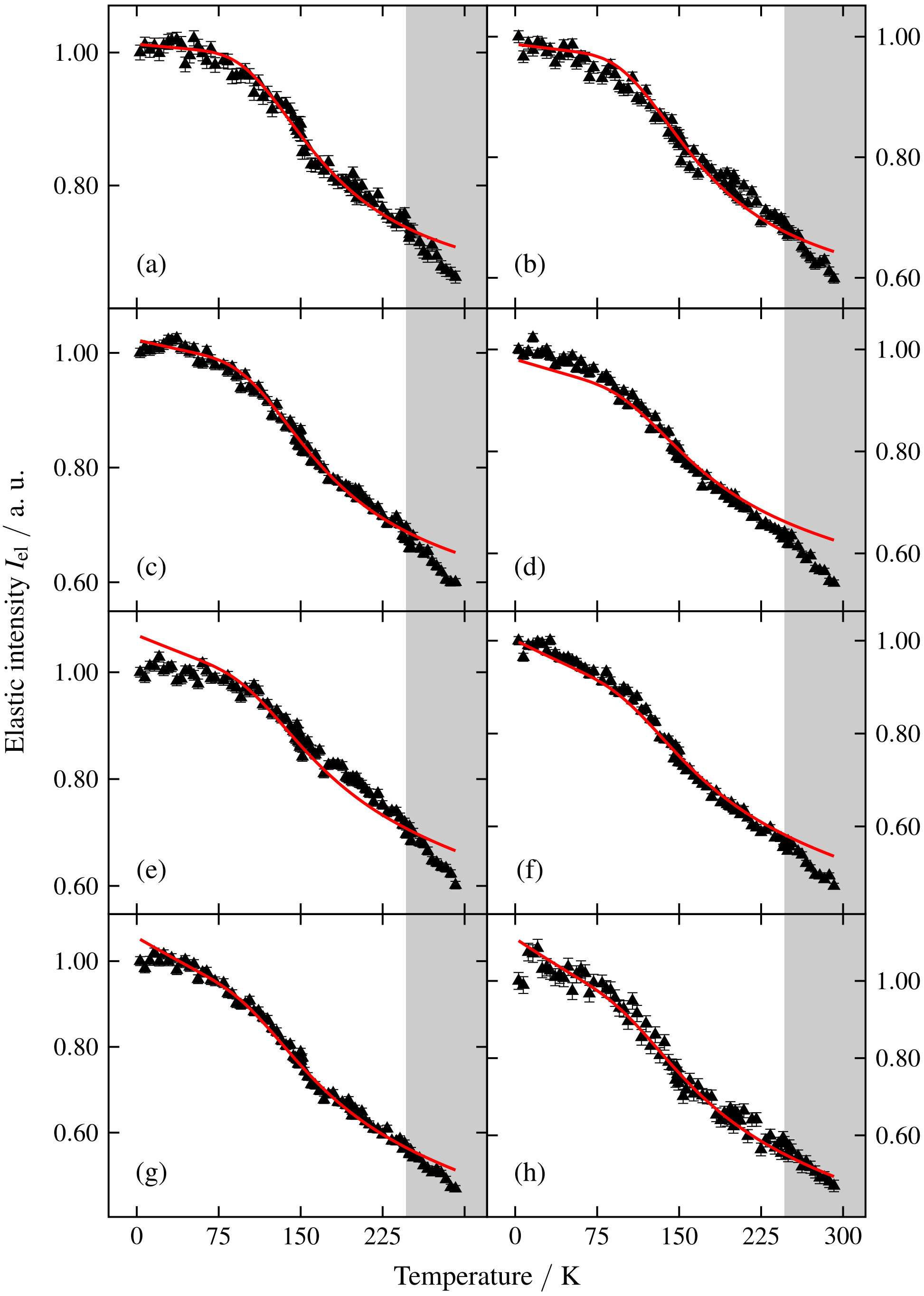

Figure A.6.: Representative results of simultaneous fit to the elastic fixed window scan data of bulk [BuPy][Tf_2N] with the three-site jump model in the temperature range from 3 K to 246 K (data outside this range marked with grey background) for a wave vector transfer Q of: (a) 0.57 Å^{-1}, (b) 0.70 Å^{-1}, (c) 0.95 Å^{-1}, (d) 1.18 Å^{-1}, (e) 1.28 Å^{-1}, (f) 1.57 Å^{-1}, (g) 1.72 Å^{-1} and (h) 1.90 Å^{-1}.

APPENDIX **B**

Data analysis program for quasi-elastic neutron scattering spectra

Only the basic data reduction of the quasi-elastic neutron scattering data was done using existent software. For the FOCUS spectra data reduction the DAVE [7] software package was used, while the data acquired with IN16B was reduced with LAMP [228], provided by the Institut Laue-Langevin. For any further data analysis self-written programs were used — for the analysis of the fixed window scans (see appendix A) and especially for the analysis of the full quasi-elastic spectra. The program for the latter is described in the following.

The necessity for this program arose from the requirements for the data analysis, which were not satisfied by the available software. There was the need to be able to fit flexibly chosen, complex model functions to the data — if necessary in parallel to all spectra with different wave vector transfers of a particular measurement. The latter enables the implementation of models implying a certain wave vector dependence. Such models have the potential to render the fits more stable by reducing the number of free parameters, however with the drawback of anticipating a certain result with respect to the kind of molecular motions and are therefore less universal. Another demand to the software was to be able to set individual start parameters for each spectrum, which is surprisingly not possible with several available curve fit tools, like some of the software packages mentioned above.

Data import and corrections

The program exists in different versions, optimised for the peculiarities of the respective spectrometer. In the case of IN16B the data are imported from binary files that are in the Hierarchical Data Format (HDF), in which they are exported from LAMP. For FOCUS the data are imported in form of ASCII files.

After some elementary data integrity checks, certain corrections are necessary due to instrument/data reduction software specific peculiarities, in order to ensure a faultless fit procedure. The IN16B spectra delivered by LAMP contain numerous values, being exactly zero, as well as their respective errors. The latter is problematic for the error weighting during the fit procedure. Thus, these error values are treated here in a way that they behave neutral related to the error weighting. The FOCUS data, reduced with DAVE, can have the peculiarity that, if the available energy transfer range for a certain wave vector transfer Q is not large enough, the values outside this range are exported as constant negative values. It is apparent that these values must be excluded, when fitting the model to the data. Such a function is implemented in the program.

Fit procedure

As already described in the requirements for the program, it is possible to freely define a model function, which is fitted to the data. The corresponding parameters, which can be limited to a certain range of values, can be individual for each spectrum (i.e. for each Q) or common for all. This can be decided for each single parameter, independently. Before fitting the model to the data, the respective function is numerically convoluted with the measured resolution function. The energy range of the data and the resolution, that is considered for the convolution and the fit, can be chosen, respectively. The fit procedure uses the Levenberg-Marquardt algorithm with error weighting and can be performed as a simultaneous fit for all spectra in parallel, or individually, depending whether the parameters are chosen wave-vector-dependent or independent. Furthermore, there is the possibility to restrict the Q-range for the fit. For the case, that an elastically scattering fraction of atoms needs to be incorporated within the model, a delta function is approximated numerically. It is chosen to be a narrow Gaussian function, because also the measured resolution functions are of Gaussian shape and the convolution of two such functions delivers again a Gaussian function, such that the overall shape of the resolution data is not altered. For the reason of numerical stability the width of such a delta function needs a certain minimum width, but is chosen here to be as narrow as possible to avoid an unnecessary broadening of the line width after the convolution. Note, that the width of the Gaussian to approximate the delta peak is different for FOCUS and IN16B, due to a different energy data spacing. One of the reasons to use such an approximation of the delta function, instead of simply using the resolution data as they are, is to have the possibility to smoothly shift the data with respect to the zero point regarding the energy transfer, during the fit. A side effect is a slight smoothing of the resolution function.

Output of fit results

For a direct inspection, the results of the fit are displayed in a graphical interface. For each spectrum the resulting best fitting function is plotted over the measurement data and is shown in different representations together with the corresponding residuals. Additionally, all important parameters of the used model function are displayed as a function of wave vector transfer.

All data are written into an HDF file. This includes not only the final fit parameters, but also the corresponding function with the associated residuals, as well as the measurement data, including the measured resolution function. Additionally, the energy range, over which the fit is executed and the start parameters are stored within this file. The latter can be read into the program again, if necessary. Furthermore, it is possible to load the results of a fit from such a file, which causes them to be displayed, like they are directly after the fit. If the desired tolerance was not reached within the preceding run, because it had stopped after the defined maximum number of iterations, the fitting procedure can be continued from this point on, now.

APPENDIX C

Contribution of the carbon matrices to the elastic scattering in the QENS data

The contribution of the carbon matrix to the elastic scattering fraction, drawn in panel (a) of figure 6.4 in section 6.1.2 and figure 6.13 in section 6.2.4, is estimated from the comparison of the elastic scattering intensity from an empty carbide-derived carbon matrix and one that is filled with the ionic liquid. Both full energy transfer spectra were measured at 2 K, where all neutrons are practically elastically scattered on the time scale of the used instrument. Since this comparison is complicated by coherent scattering, especially from the empty porous matrix, an additional comparison of the calculated scattering cross sections of both samples, weighted with the respective particle numbers, is done. The latter calculations confirm the value of the immobile fraction deduced from the measurement data. Note however, that the value sketched in the above mentioned graphs is only an average value of the estimated immobile fraction, which lies in the range between 0.1 and 0.2. The specific pore volume of the here used carbon samples is smaller for such with the smaller pores, what entails a higher carbon-to-ionic-liquid ratio. Consequently, the elastic scattering contribution from the carbon matrix is expected to be higher for samples with smaller pores, which is for example the case for the granular carbon SiC-2 in comparison with the other samples. However, it appears that this affects the elastic scattering fraction less than the observed differences, as shown for instance in figure 6.4. Furthermore, the remaining metal within the carbide-derived carbons also contributes to the elastic scattering, such that there is no general scaling of the latter with the porous carbon content of the ionic-liquid-filled samples.

The above mentioned coherent scattering, which leads to comparatively high intensities for certain wave vector transfers Q, is also the reason, why it is not possible to simply subtract the measured spectra of the empty matrices from those that are filled with the ionic liquid, since this would lead to erroneous results, which include negative intensities.

APPENDIX **D**

Temperature-dependent structure of the liquid crystal 2MBOCBC in AAO nanochannels of different widths

In section 11.2 neutron diffraction experiments on the liquid crystal 2MBOCBC confined in the 42 nm channels of anodic aluminium oxide (AAO) membranes are described. It would be desirable to perform these neutron diffraction experiments also for such AAO membranes with other channel diameters, in order to investigate how the increasing nanoconfinement affects the observed temperature-dependent structure. Unfortunately, the high number of equal membranes needed for this kind of experiment and the limited access to these large scale facilities due to high user demand leads to the fact that the following pore-size-dependent diffraction experiments are limited to laboratory scale X-ray diffraction, as those already presented in section 11.1 for the liquid crystal CE6. However, with these X-ray diffraction experiments a full analysis of the structure as done above is not realisable. One of the reasons is that at already relatively low layer tilt angles, a measurement in reflection geometry would not be possible anymore due to the short X-ray wavelength, why the smectic layering Bragg peak is at relatively low angles. Additionally, due to the lack of an area detector, the acquirement of the necessary data comprising ω-rocking scans at every 2Θ-position would be quite cumbersome. However, these X-ray diffraction experiments still give valuable insights into the temperature-dependent evolution of the liquid crystalline structure in the nanoconfinement of the AAO membranes, comparing different pore sizes, as will be seen in the following.

Figure D.1 shows the integrated intensity of the 001 smectic layering peak for the bulk state of the liquid crystal 2MBOCBC on a silicon substrate, as well as in the confinement of AAO nanopores with channel diameters of 42 nm, 30 nm and 20 nm. The AAO nanochannels used here are coated with the polymer SE-130 (see section 10.3) in order to achieve a tangential anchoring of the liquid crystal molecules at the pore walls. In panel (a) of figure D.1 the respective data for the bulk liquid crystal on a silicon substrate, which was cleaned with piranha solution [266] before the deposition of 2MBOCBC, are shown. On cooling from the isotropic phase, smectic A* layers are being formed at around 333 K in a first-order phase transition, thus giving rise to a sudden increase of the smectic layering diffraction peak intensity. At around 315 K the transition to the smectic C* phase occurs, which manifests in a small downward kink in the former almost constant intensity. After that point the integrated intensity slightly rises again and saturates on a constant value on further cooling until at least 285 K.

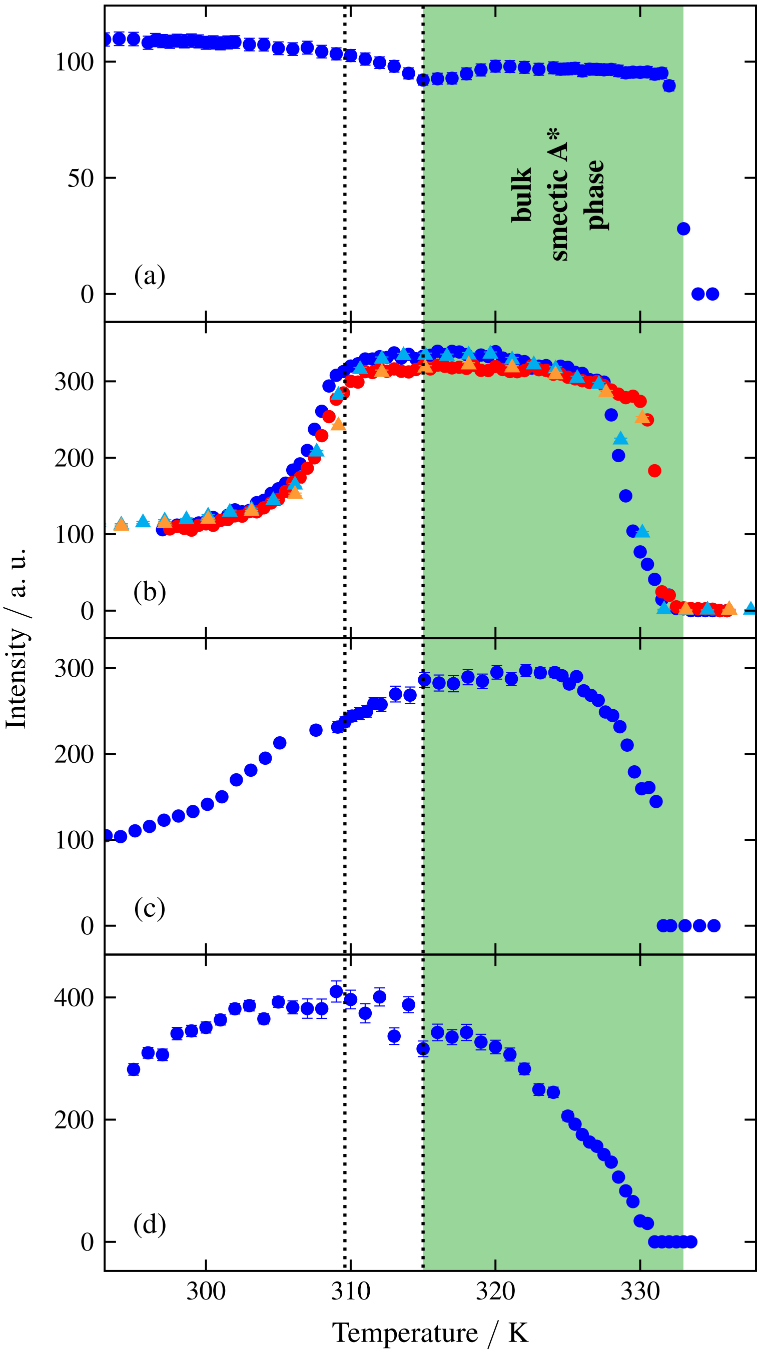

Figure D.1.: Integrated X-ray diffraction intensity of the smectic layering peak for (a) bulk 2MBOCBC on silicon substrate and confined in nanoporous AAO with (b) 42 nm (▲/▲: neutron diffraction data for comparison), (c) 30 nm and (d) 20 nm channel diameter, each surface-coated with SE-130. Blue/cyan and red/orange curves show cooling and heating cycles, respectively.

The integrated intensity of the smectic layering diffraction peak of 2MBOCBC confined in the AAO nanochannels with 42 nm diameter in contrast has a different course in the same temperature range. As it can be seen in figure D.1 (b), the X-ray scattering intensity behaves completely in the same way as the intensity of the neutron scattering experiment from section 11.2. This demonstrates again the reproducibility of the measurements, especially because here only an X-ray diffraction measurement at one arbitrarily chosen membrane from the neutron diffraction experiment is shown. Interestingly, also the fact that the diffraction intensity for the cooling cycle lies above the one measured during heating for temperatures below the end of the hysteresis is reproduced. Note, that here in contrast to the neutron diffraction data in graph 11.6 (see section 11.2) and in analogy to the X-ray diffraction measurement geometry, only the integrated neutron scattering intensity of the smectic layering peak for $\omega = 0^\circ$ is plotted, and not the one that is additionally integrated over the entire measured ω-range. That is why the intensity course in figure D.1 (b) behaves differently on the formation of the chevron structure: Instead of a kink (see figure 11.6 (a)) it decreases continuously from around 309.5 K on, until it saturates like the smectic layer tilt angle (see figure 11.6 (c)). This is simply a consequence of the fact that as a result of the layer buckling the diffracted intensity is now distributed over a larger ω-range and therefore the one at $\omega = 0^\circ$ is lowered, as it can be seen in figure 11.4. Or in other words, upon chevron-like layer structure formation, there are less smectic layer planes fulfilling the Bragg condition for $\omega = 0^\circ$, leading to a lower diffraction intensity compared to the smectic A* phase. Accordingly, such a decrease in intensity on cooling the confined 2MBOCBC down within the smectic C* phase might be interpreted as a hint at the evolution of a chevron-like layer structure.

Indeed, also in the case of the 30 nm membrane in figure D.1 (c) and the 20 nm one in panel (d) of the same graph, such a decrease in the integrated intensity of the smectic C* layering related diffraction signal is observed. However, with decreasing channel diameter this decline becomes more smooth and possibly also shifts to lower temperatures. In the case of the smallest pore diameter, 20 nm, there is only a small intensity decrease in the measured temperature range, so that the situation is not completely clear. It should be also noted that for the 20 nm and 30 nm membranes there are unfortunately not enough measurements on different samples available to draw final conclusions.

It is also interesting to have a look on the temperature-dependent width of the smectic layering Bragg peak. Figure D.2 shows the full width at half maximum (FWHM) of that peak in the case of the confined 2MBOCBC within the 42 nm channels of the AAO membranes. From the formation of smectic layers on cooling from the isotropic phase at around 332 K till the formation of the chevron-like layer structure at around 309.5 K (see section 11.2) the FWHM remains at a constant level. However, on further cooling it starts to rise steeply. Although in general, it is not a sufficient criterion for the existence of a chevron-like structure formation, in this case it can nevertheless serve as an indicator for this structural rearrangement.

Despite the fact that such molecular reorganisations likely entail also structural changes that cause a peak broadening, the prevailing contribution can certainly be ascribed to the divergence of the X-ray beam. As a consequence, also some tilted layers partially contribute to the scattering signal, but at different diffraction angles and thus lead to a broadening of the Bragg peak.

For the two membranes with the smaller nanochannel diameters the situation is — as already in the case of the above intensity considerations — ambiguous. In the high-temperature region the FWHM is not constant as for the AAO membrane with the 42 nm channels. However, at least for the 30 nm channels the width rises below 309 K and also for the 20 nm ones there might be such a rise at even lower temperatures. Likewise the temperature dependence of the smectic layering Bragg peak intensity, this course of the FWHM may suggest a possible chevron-like layer formation also in these small channels, but possibly shifted to lower temperatures. However, due to the quality and limited number of the measurements the situation is not completely clear. Further experiments on such membranes with nanochannel diameters smaller than 42 nm should be carried out in the future to resolve the molecular arrangement of the liquid crystal molecules within these narrow pores — especially with respect to the potential appearance of chevron-like tilted smectic layers.

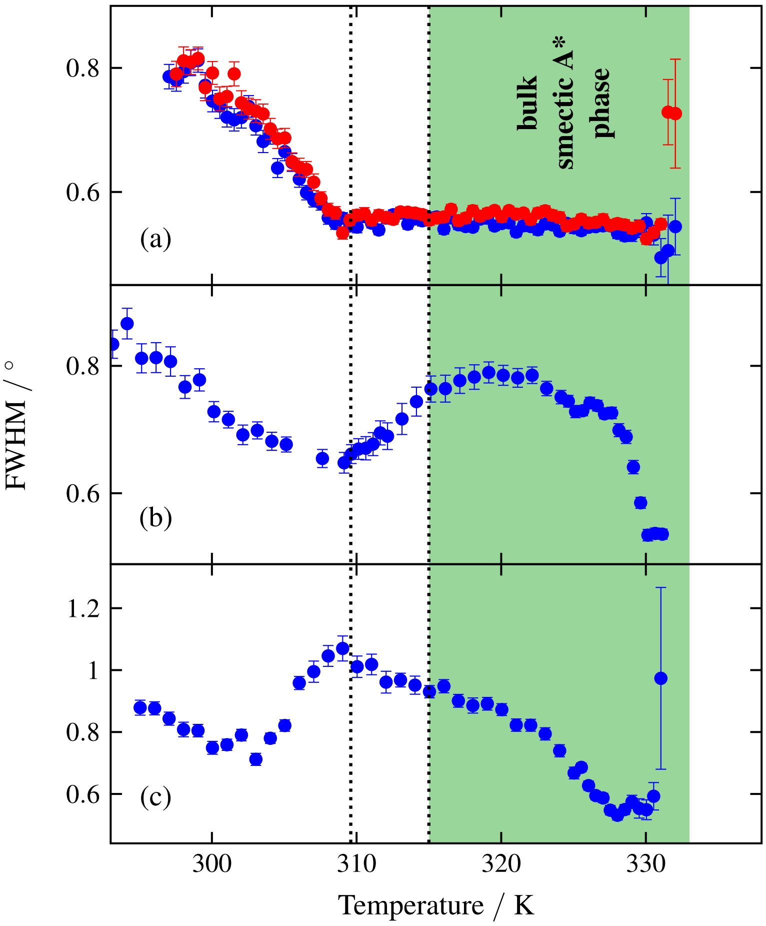

Figure D.2.: FWHM of the 001 smectic layering peak of 2MBOCBC confined in AAO membranes with (a) 42 nm, (b) 30 nm and (c) 20 nm nanochannel width as a function of temperature, as measured by X-ray diffraction.

Bibliography

[1] ALBA-SIMIONESCO, C. ; COASNE, B. ; DOSSEH, G. ; DUDZIAK, G. ; GUBBINS, K. E. ; RADHAKRISHNAN, R. ; SLIWINSKA-BARTKOWIAK, M.: Effects of confinement on freezing and melting. In: *Journal of Physics: Condensed Matter* 18 (2006), January, No. 6, pp. R15–R68

[2] ALEXANDER, G. G. ; KING, S. M. ; RICHARDSON, R. M. ; ZIMMERMANN, H.: Determination of the translational order parameter for smectic liquid crystals using small-angle neutron scattering. In: *Liquid Crystals* 37 (2010), July, No. 6–7, pp. 961–968

[3] ANDREEV, A. L. ; ANDREEVA, T. B. ; KOMPANETS, I. N. ; STARIKOV, R. S. ; ZALYAPIN, N. V.: Novel FLC- Materials Open New Possibilities for FLCoS Based Microdisplays and Video Projectors. In: *Physics Procedia* 73 (2015), pp. 87–94. – 4th International Conference of Photonics and Information Optics, PhIO 2015, 28-30 January 2015, Moscow, Russian Federation

[4] ANNAPUREDDY, Harsha V. R. ; KASHYAP, Hemant K. ; DE BIASE, Pablo M. ; MARGULIS, Claudio J.: What is the Origin of the Prepeak in the X-ray Scattering of Imidazolium-Based Room-Temperature Ionic Liquids? In: *Journal of Physical Chemistry B* 114 (2010), December, No. 50, pp. 16838–16846

[5] ARAQUE, Juan C. ; HETTIGE, Jeevapani J. ; MARGULIS, Claudio J.: Modern Room Temperature Ionic Liquids, a Simple Guide to Understanding Their Structure and How It May Relate to Dynamics. In: *The Journal of Physical Chemistry B* 119 (2015), October, No. 40, pp. 12727–12740

[6] ARMAND, Michel ; ENDRES, Frank ; MACFARLANE, Douglas R. ; OHNO, Hiroyuki ; SCROSATI, Bruno: Ionic-liquid materials for the electrochemical challenges of the future. In: *Nature Materials* 8 (2009), July, No. 8, pp. 621–629

[7] AZUAH, Richard Tumanjong ; KNELLER, Larry R. ; QIU, Yiming ; TREGENNA-PIGGOTT, Philip L. W. ; BROWN, Craig M. ; COPLEY, John R D. ; DIMEO, Robert M.: DAVE: A Comprehensive Software Suite for the Reduction, Visualization, and Analysis of Low Energy Neutron Spectroscopic Data. In: *Journal of Research of the National Institute of Standards and Technology* 114 (2009), November, No. 6, pp. 341–358

[8] BAKER, C. A. ; DOYLE, D. D. ; GELTENBORT, P. ; GREEN, K. ; GRINTEN, M. G. D. van der ; HARRIS, P. G. ; IAYDJIEV, P. ; IVANOV, S. N. ; MAY, D. J. R. ; PENDLEBURY, J. M. ; RICHARDSON, J. D. ; SHIERS, D. ; SMITH, K. F.: Improved Experimental Limit on the Electric Dipole Moment of the Neutron. In: *Physical Review Letters* 97 (2006), September, No. 13, pp. 131801–1–131801–4

[9] BAÑUELOS, José Leobardo ; FENG, Guang ; FULVIO, Pasquale F. ; LI, Song ; ROTHER, Gernot ; AREND, Nikolas ; FARAONE, Antonio ; DAI, Sheng ; CUMMINGS, Peter T. ; WESOLOWSKI, David J.: The influence of a hierarchical porous carbon network on the coherent dynamics of a nanoconfined room temperature ionic liquid: A neutron spin echo and atomistic simulation investigation. In: *Carbon* 78 (2014), November, pp. 415–427

[10] BAÑUELOS, José Leobardo ; FENG, Guang ; FULVIO, Pasquale F. ; LI, Song ; ROTHER, Gernot ; DAI, Sheng ; CUMMINGS, Peter T. ; WESOLOWSKI, David J.: Densification of Ionic Liquid Molecules within a Hierarchical Nanoporous Carbon Structure Revealed by Small-Angle Scattering and Molecular Dynamics Simulation. In: *Chemistry of Materials* 26 (2014), January, No. 2, pp. 1144–1153

[11] BARRETT, Elliott P. ; JOYNER, Leslie G. ; HALENDA, Paul P.: The Determination of Pore Volume and Area Distributions in Porous Substances. I. Computations from Nitrogen Isotherms. In: *Journal of the American Chemical Society* 73 (1951), No. 1, pp. 373–380

[12] BAUMERT, J. ; ASMUSSEN, B. ; GUTT, C. ; KAHN, R.: Pore-size dependence of the self-diffusion of hexane in silica gels. In: *Journal of Chemical Physics* 116 (2002), June, No. 24, pp. 10869–10876

[13] BÉE, Marc ; MILLEN, D. J. (Ed.): *Quasielastic Neutron Scattering - Principles and Applications in Solid State Chemistry, Biology and Materials Science*. Bristol and Philadelphia : Adam Hilger, 1988

[14] BÉE, Marc: Localized and long-range diffusion in condensed matter: state of the art of QENS studies and future prospects. In: *Chemical Physics* 292 (2003), August, No. 2-3, pp. 121–141

[15] BERROD, Q. ; FERDEGHINI, F. ; JUDEINSTEIN, P. ; GENEVAZ, N. ; RAMOS, R. ; FOURNIER, A. ; DIJON, J. ; OLLIVIER, J. ; ROLS, S. ; YU, D. ; AL. et: Enhanced ionic liquid mobility induced by confinement in 1D CNT membranes. In: *Nanoscale* 8 (2016), No. 15, pp. 7845–7848

[16] BERROD, Quentin ; FERDEGHINI, Filippo ; ZANOTTI, Jean-Marc ; JUDEINSTEIN, Patrick ; LAIREZ, Didier ; GARCÍA SAKAI, Victoria ; CZAKKEL, Orsolya ; FOUQUET, Peter ; CONSTANTIN, Doru: Ionic Liquids: evidence of the viscosity scale-dependence. In: *Scientific Reports* 7 (2017), May, No. 1, pp. 2241–1–2241–8

[17] BIENFAIT, Michel: *Two Dimensional Phase Transitions in Classical Van Der Waals Films Adsorbed on Graphite*. Chap. 2, pp. 29–64. In: DASH, J. G. (Ed.) ; RUVALDS, J. (Ed.): *Phase Transitions in Surface Films*. Boston, MA : Springer US, 1980

[18] BITTNER, Bożena ; WROBEL, Rafal J. ; MILCHERT, Eugeniusz: Physical properties of pyridinium ionic liquids. In: *The Journal of Chemical Thermodynamics* 55 (2012), December, pp. 159–165

[19] BLINC, R. ; ČOPIČ, M. ; DREVENŠEK, I. ; LEVSTIK, A. ; MUŠEVIČ, I. ; ŽEKŠ, B.: Order parameter fluctuations in ferroelectric liquid crystals. In: *Ferroelectrics* 113 (1991), January, No. 1, pp. 59–76

[20] BLINOV, L. M. ; BAIKALOV, V. A. ; BARNIK, M. I. ; BERESNEV, L. A. ; POZHIDAYEV, E. P. ; YABLONSKY, S. V.: Experimental techniques for the investigation of ferroelectric liquid crystals. In: *Liquid Crystals* 2 (1987), No. 2, pp. 121–130

[21] BLINOV, L. M. ; CHIGRINOV, V. G.: *Electrooptic Effects in Liquid Crystal Materials*. Springer-Verlag New York, 1994 (Partially Ordered Systems)

[22] BLINOV, Lev M.: *Structure and Properties of Liquid Crystals*. Springer, 2011

[23] BORCHARDT, Lars ; ZHU, Qi-Long ; CASCO, Mirian E. ; BERGER, Reinhard ; ZHUANG, Xiaodong ; KASKEL, Stefan ; FENG, Xinliang ; XU, Qiang: Toward a molecular design of porous carbon materials. In: *Materials Today* 20 (2017), December, No. 10, pp. 592–610

[24] BOUWMAN, W. G. ; JEU, W. H. de: 3D XY behavior of a nematic-smectic-A phase transition: Confirmation of the de Gennes model. In: *Physical Review Letters* 68 (1992), February, No. 6, pp. 800–803

[25] BOUWMAN, Wim G. ; DE JEU, Wim H.: Critical behaviour of the nematic to smectic A phase transition. In: BUKA, Agnes (Ed.): *Modern Topics in Liquid Crystals*. Singapore : World Scientific Publishing Co. Pte. Ltd., 1993, pp. 161–186

[26] BROCKHOUSE, B. N.: Structural dynamics of water by neutron spectrometry. In: *Il Nuovo Cimento* 9 (1958), March, No. Supplement 1, pp. 45–71

[27] BURANKOVA, Tatsiana: *Dynamics and Structure of Ionic Liquids by Means of Neutron Scattering*, Universität des Saarlandes, Phd Thesis, 2014

[28] BURANKOVA, Tatsiana ; HEMPELMANN, Rolf ; WILDES, Andrew ; EMBS, Jan P.: Collective Ion Diffusion and Localized Single Particle Dynamics in Pyridinium-Based Ionic Liquids. In: *Journal of Physical Chemistry B* 118 (2014), December, No. 49, pp. 14452–14460

[29] BURANKOVA, Tatsiana ; MORA CARDOZO, Juan F. ; RAUBER, Daniel ; WILDES, Andrew ; EMBS, Jan P.: Linking Structure to Dynamics in Protic Ionic Liquids: A Neutron Scattering Study of Correlated and Single-Particle Motions. In: *Scientific Reports* 8 (2018), November, No. 1, pp. 16400

[30] BURANKOVA, Tatsiana ; REICHERT, Elena ; FOSSOG, Verlaine ; HEMPELMANN, Rolf ; EMBS, Jan Peter: The dynamics of cations in pyridinium-based ionic liquids by means of quasielastic- and inelastic neutron scattering. In: *Journal of Molecular Liquids* 192 (2014), April, pp. 199–207

[31] BURANKOVA, Tatsiana ; SIMEONI, Giovanna ; HEMPELMANN, Rolf ; MORA CARDOZO, Juan F. ; EMBS, Jan P.: Dynamic Heterogeneity and Flexibility of the Alkyl Chain in Pyridinium-Based Ionic Liquids. In: *The Journal of Physical Chemistry B* 121 (2017), January, No. 1, pp. 240–249

[32] BUSCH, Mark ; EMBS, Jan P. ; FRICK, Bernhard ; HOFMANN, Tommy ; HUBER, Patrick: *Dynamics of an ionic liquid confined in nanoporous carbon substrates*. May 2015. – Institut Laue-Langevin (ILL): Grenoble, 2015; DOI:10.5291/ILL-DATA.6-02-558

[33] BUSCH, Mark ; HOFMANN, Tommy ; FRICK, Bernhard ; EMBS, Jan P. ; DYATKIN, Boris ; HUBER, Patrick: Ionic liquid dynamics in nanoporous carbon: A pore-size- and temperature-dependent neutron spectroscopy study on supercapacitor materials. In: *(under review)* (2019)

[34] BUSCH, Mark ; KITYK, Andriy V. ; PIECEK, Wiktor ; HOFMANN, Tommy ; WALLACHER, Dirk ; CAŁUS, Sylwia ; KULA, Przemysław ; STEINHART, Martin ; EICH, Manfred ; HUBER, Patrick: A ferroelectric liquid crystal confined in cylindrical nanopores: Reversible smectic layer buckling, enhanced light rotation and extremely fast electro-optically active Goldstone excitations. In: *Nanoscale* 9 (2017), December, No. 48, pp. 19086–19099

[35] CAGNON, M. ; DURAND, G.: Positional anchoring of smectic liquid crystals. In: *Physical Review Letters* 70 (1993), May, No. 18, pp. 2742–2745

[36] CAŁUS, Sylwia ; BUSCH, Mark ; KITYK, Andriy V. ; PIECEK, Wiktor ; HUBER, Patrick: Chiral Phases of a Confined Cholesteric Liquid Crystal: Anchoring-Dependent Helical and Smectic Self-Assembly in Nanochannels. In: *The Journal of Physical Chemistry C* 120 (2016), June, No. 21, pp. 11727–11738

[37] CANONGIA LOPES, José N. A. ; PÁDUA, Agílio A. H.: Nanostructural Organization in Ionic Liquids. In: *The Journal of Physical Chemistry B* 110 (2006), February, No. 7, pp. 3330–3335

[38] CASTNER, Edward W. ; MARGULIS, Claudio J. ; MARONCELLI, Mark ; WISHART, James F.: Ionic Liquids: Structure and Photochemical Reactions. In: *Annual Review of Physical Chemistry* 62 (2011), May, No. 1, pp. 85–105

[39] CHABAN, Vitaly V. ; PREZHDO, Oleg V.: Nanoscale Carbon Greatly Enhances Mobility of a Highly Viscous Ionic Liquid. In: *ACS Nano* 8 (2014), August, No. 8, pp. 8190–8197

[40] CHAHID, A. ; ALEGRIA, A. ; COLMENERO, J.: Methyl Group Dynamics in Poly(vinyl methyl ether). A Rotation Rate Distribution Model. In: *Macromolecules* 27 (1994), June, No. 12, pp. 3282–3288

[41] CHAIKIN, P. M. ; LUBENSKY, T. C.: *Principles of condensed matter physics*. Cambridge University Press, 1995

[42] CHAN, K. K. ; PERSHAN, P. S. ; SORENSEN, L. B. ; HARDOUIN, F.: X-ray studies of transitions between nematic, smectic-A_1, -A_2, and -A_d phases. In: *Physical Review A* 34 (1986), August, No. 2, pp. 1420–1433

[43] CHATHOTH, S. M. ; MAMONTOV, E. ; DAI, S. ; WANG, X. ; FULVIO, P. F. ; WESOLOWSKI, D. J.: Fast diffusion in a room temperature ionic liquid confined in mesoporous carbon. In: *Europhysics Letters* 97 (2012), March, No. 6, pp. 66004–p1–66004–p6

[44] CHATHOTH, S. M. ; MAMONTOV, E. ; FULVIO, P. F. ; WANG, X. ; BAKER, G. A. ; DAI, S. ; WESOLOWSKI, D. J.: An unusual slowdown of fast diffusion in a room temperature ionic liquid confined in mesoporous carbon. In: *Europhysics Letters* 102 (2013), April, No. 1, pp. 16004–p1–16004–p5

[45] CHEN, Tao ; DAI, Liming: Carbon nanomaterials for high-performance supercapacitors. In: *Materials Today* 16 (2013), July, No. 7-8, pp. 272–280

[46] CHERUSSERI, Jayesh ; KUMAR, Kowsik Sambath ; CHOUDHARY, Nitin ; NAGAIAH, Narasimha ; JUNG, Yeonwoong ; ROY, Tania ; THOMAS, Jayan: Novel mesoporous electrode materials for symmetric, asymmetric and hybrid supercapacitors. In: *Nanotechnology* 30 (2019), March, No. 20, pp. 202001

[47] CHRISTENSON, Hugo K.: Confinement effects on freezing and melting. In: *Journal of Physics: Condensed Matter* 13 (2001), March, No. 11, pp. R95–R133

[48] CHUDLEY, C. T. ; ELLIOTT, R. J.: Neutron Scattering from a Liquid on a Jump Diffusion Model. In: *Proceedings of the Physical Society* 77 (1961), February, No. 2, pp. 353–361

[49] CLARK, N. A. ; HANDSCHY, M. A. ; LAGERWALL, S. T.: Ferroelectric Liquid Crystal Electro-Optics Using the Surface Stabilized Structure. In: *Molecular Crystals and Liquid Crystals* 94 (1983), No. 1-2, pp. 213–233

[50] CLARK, N. A. ; LAGERWALL, S. T.: Structures and Applications of SSFLC Devices. In: *Japan Display '86: Proceedings of the 6th International Display Research Conference* Soc. for Information Display (Org.), 1986, pp. 456–458. – Playa del Rey, Calif.

[51] CLARK, N. A. ; RIEKER, T. P.: Smectic-C "chevron," a planar liquid-crystal defect: Implications for the surface-stabilized ferroelectric liquid-crystal geometry. In: *Physical Review A* 37 (1988), February, No. 3, pp. 1053–1056

[52] CLARK, Noel A.: Surface memory effects in liquid crystals: Influence of surface composition. In: *Physical Review Letters* 55 (1985), July, No. 3, pp. 292–295

[53] CLARK, Noel A. ; LAGERWALL, Sven T.: Submicrosecond bistable electro-optic switching in liquid crystals. In: *Applied Physics Letters* 36 (1980), June, No. 11, pp. 899–901

[54] COLES, Harry ; MORRIS, Stephen: Liquid-crystal lasers. In: *Nature Photonics* 4 (2010), September, pp. 676–685

[55] COLLINGS, A. F. ; BAJENOV, N.: A High Precision Capillary Viscometer and Further Relative Results for the Viscosity of Water. In: *Metrologia* 19 (1983), January, No. 2, pp. 61–66

[56] COLLINGS, P. J.: Comment on "Chiral-racemic phase diagram of a blue-phase liquid crystal". In: *Physical Review A* 33 (1986), March, No. 3, pp. 2153–2154

[57] CONRAD, H. M. ; STILLER, H. H. ; FRISCHKORN, C. G. B. ; SHIRANE, G.: Smectic A order parameter measurements and critical scattering near the smectic A $\leftrightarrow$ nematic phase transition in CBOOA. In: *Solid State Communications* 23 (1977), August, No. 8, pp. 571–575

[58] CORDOYIANNIS, George ; RAO JAMPANI, Venkata Subba ; KRALJ, Samo ; DHARA, Surajit ; TZITZIOS, Vassilios ; BASINA, Georgia ; NOUNESIS, George ; KUTNJAK, Zdravko ; PATI TRIPATHI, Chandra Shekhar ; LOSADA-PÉREZ, Patricia ; JESENEK, Dalija ; GLORIEUX, Christ ; MUŠEVIČ, Igor ; ZIDANŠEK, Aleksander ; AMEINITSCH, Heinz ; THOEN, Jan: Different modulated structures of topological defects stabilized by adaptive targeting nanoparticles. In: *Soft Matter* 9 (2013), No. 15, pp. 3956–3964

[59] CRUCEANU, F. ; LIANG, D. ; LEHENY, R. L. ; GARLAND, C. W. ; IANNACCHIONE, G. S.: High-resolution calorimetric study of the nematic to smectic-A transition in aligned liquid crystal–aerosil gels. In: *Physical Review E* 79 (2009), January, No. 1, pp. 011710–1–011710–8

[60] DADMUN, M. D. ; MUTHUKUMAR, M.: The nematic to isotropic transition of a liquid crystal in porous media. In: *The Journal of Chemical Physics* 98 (1993), March, No. 6, pp. 4850–4852

[61] DEBYE, P.: Interferenz von Röntgenstrahlen und Wärmebewegung. In: *Annalen der Physik* 348 (1913), No. 1, pp. 49–92

[62] DETSI, Eric ; ONCK, Patrick ; DE HOSSON, Jeff Th. M.: Metallic Muscles at Work: High Rate Actuation in Nanoporous Gold/Polyaniline Composites. In: *ACS Nano* 7 (2013), May, No. 5, pp. 4299–4306

[63] DIMESSO, L. ; FÖRSTER, C. ; JAEGERMANN, W. ; KHANDERI, J. P. ; TEMPEL, H. ; POPP, A. ; ENGSTLER, J. ; SCHNEIDER, J. J. ; SARAPULOVA, A. ; MIKHAILOVA, D. ; SCHMITT, L. A. ; OSWALD, S. ; EHRENBERG, H.: Developments in nanostructured LiMPO4 (M = Fe, Co, Ni, Mn) composites based on three dimensional carbon architecture. In: *Chemical Society Reviews* 41 (2012), No. 15, pp. 5068–5080

[64] DING, Yi ; ZHANG, Zhonghua: *Nanoporous Metals for Advanced Energy Technologies*. Springer International Publishing, 2016

[65] DURAND, G.: Recent advances in nematic and smectic A anchoring on amorphous solid surfaces [1]. In: *Liquid Crystals* 14 (1993), No. 1, pp. 159–168

[66] DYATKIN, Boris: 2015. – private communication

[67] DYATKIN, Boris ; MAMONTOV, Eugene ; COOK, Kevin M. ; GOGOTSI, Yury: Capacitance, charge dynamics, and electrolyte-surface interactions in functionalized carbide-derived carbon electrodes. In: *Progress in Natural Science: Materials International* 25 (2015), December, No. 6, pp. 631–641

[68] DYATKIN, Boris ; OSTI, Naresh C. ; GALLEGOS, Alejandro ; ZHANG, Yu ; MAMONTOV, Eugene ; CUMMINGS, Peter T. ; WU, Jianzhong ; GOGOTSI, Yury: Electrolyte cation length influences electrosorption and dynamics in porous carbon supercapacitors. In: *Electrochimica Acta* 283 (2018), September, pp. 882–893

[69] DYATKIN, Boris ; OSTI, Naresh C. ; ZHANG, Yu ; WANG, Hsiu-Wen ; MAMONTOV, Eugene ; HELLER, William T. ; ZHANG, Pengfei ; ROTHER, Gernot ; CUMMINGS, Peter T. ; WESOLOWSKI, David J. ; GOGOTSI, Yury: Ionic liquid structure, dynamics, and electrosorption in carbon electrodes with bimodal pores and heterogeneous surfaces. In: *Carbon* 129 (2018), April, pp. 104–118

[70] DYATKIN, Boris ; ZHANG, Yu ; MAMONTOV, Eugene ; KOLESNIKOV, Alexander I. ; CHENG, Yongqiang ; MEYER, Harry M. ; CUMMINGS, Peter T. ; GOGOTSI, Yury: Influence of Surface Oxidation on Ion Dynamics and Capacitance in Porous and Non-porous Carbon Electrodes. In: *The Journal of Physical Chemistry C* 120 (2016), April, No. 16, pp. 8730–8741

[71] EFTEKHARI, Ali: Supercapacitors utilising ionic liquids. In: *Energy Storage Materials* 9 (2017), October, pp. 47–69

[72] EFTEKHARI, Ali ; FAN, Zhaoyang: Ordered mesoporous carbon and its applications for electrochemical energy storage and conversion. In: *Materials Chemistry Frontiers* 1 (2017), No. 6, pp. 1001–1027

[73] EGELSTAFF, Peter A. ; LOVESEY, S. W. (Ed.) ; MITCHELL, E. W. J. (Ed.): *An Introduction to the Liquid State*. 2. Oxford University Press, 1992 (Oxford series on neutron scattering in condensed matter 7)

[74] EIDENSCHINK, R. ; GEELHAAR, T. ; MERCK, E. ; ANDERSSON, G. ; DAHLGREN, A. ; FLATISCHLER, K. ; GOUDA, F. ; LAGERWALL, S. T. ; SKARP, K.: Parameter characteristics of a ferroelectric liquid crystal with polarization sign reversal. In: *Ferroelectrics* 84 (1988), August, No. 1, pp. 167–181

[75] EINSTEIN, Albert: Über die von der molekularkinetischen Theorie der Wärme geforderte Bewegung von in ruhenden Flüssigkeiten suspendierten Teilchen. In: *Annalen der Physik* 322 (1905), No. 8, pp. 549–560

[76] EMBS, Jan P. ; BURANKOVA, Tatsiana ; REICHERT, Elena ; HEMPELMANN, Rolf: Cation Dynamics in the Pyridinium Based Ionic Liquid 1-*N*-Butylpyridinium Bis((trifluoromethyl)sulfonyl) As Seen by Quasielastic Neutron Scattering. In: *Journal of Physical Chemistry B* 116 (2012), November, No. 44, pp. 13265–13271

[77] EMBS, Jan Peter ; BURANKOVA, Tatsiana ; REICHERT, Elena ; FOSSOG, Verlaine ; HEMPELMANN, Rolf: QENS Study of Diffusive and Localized Cation Motions of Pyridinium-based Ionic Liquids. In: *Journal of the Physical Society of Japan* 82 (2013), No. Suppl. A, pp. SA003–1–SA003–6

[78] ENGEMANN, S. ; REICHERT, H. ; DOSCH, H. ; BILGRAM, J. ; HONKIMÄKI, V. ; SNIGIREV, A.: Interfacial Melting of Ice in Contact with SiO_2. In: *Physical Review Letters* 92 (2004), May, No. 20, pp. 205701–1–205701–4

[79] FAN, Zhong Xiao ; HAASE, Wolfgang: Determination of the translational order parameter in the liquid crystalline smectic A phase using the x-ray diffraction method. In: *The Journal of Chemical Physics* 95 (1991), October, No. 8, pp. 6066–6074

[80] FENG, Guang ; CHEN, Ming ; BI, Sheng ; GOODWIN, Zachary A. H. ; POSTNIKOV, Eugene B. ; BRILLIANTOV, Nikolai ; URBAKH, Michael ; KORNYSHEV, Alexei A.: Free and Bound States of Ions in Ionic Liquids, Conductivity, and Underscreening Paradox. In: *Physical Review X* 9 (2019), May, No. 2, pp. 021024–1–021024–22

[81] FENG, Guang ; CUMMINGS, Peter T.: Supercapacitor Capacitance Exhibits Oscillatory Behavior as a Function of Nanopore Size. In: *The Journal of Physical Chemistry Letters* 2 (2011), November, No. 22, pp. 2859–2864

[82] FENG, Yanxiao ; ZHANG, Yuechuan ; YING, Cuifeng ; WANG, Deqiang ; DU, Chunlei: Nanopore-based Fourth-generation DNA Sequencing Technology. In: *Genomics, Proteomics & Bioinformatics* 13 (2015), February, No. 1, pp. 4–16

[83] FERDEGHINI, Filippo ; BERROD, Quentin ; ZANOTTI, Jean-Marc ; JUDEINSTEIN, Patrick ; SAKAI, Victoria García ; CZAKKEL, Orsolya ; FOUQUET, Peter ; CONSTANTIN, Doru: Nanostructuration of ionic liquids: impact on the cation mobility. A multi-scale study. In: *Nanoscale* 9 (2017), No. 5, pp. 1901–1908

[84] FERMI, E. ; MARSHALL, J. ; MARSHALL, L.: A Thermal Neutron Velocity Selector and Its Application to the Measurement of the Cross Section of Boron. In: *Physical Review* 72 (1947), August, No. 3, pp. 193–196

[85] FINDON, Alison ; GLEESON, Helen F. ; LYDON, John: An unusual chevron structure in an achiral smectic C liquid crystal device. In: *Liquid Crystals* 25 (1998), No. 5, pp. 631–638

[86] FINDON, Alison ; GLEESON, Helen F. ; LYDON, John E.: The realignment of an achiral smectic C chevron structure with applied field. In: *Liquid Crystals* 29 (2002), No. 1, pp. 79–85

[87] FLETCHER, S. Isobel ; SILLARS, Fiona B. ; HUDSON, Nicholas E. ; HALL, Peter J.: Physical Properties of Selected Ionic Liquids for Use as Electrolytes and Other Industrial Applications. In: *Journal of Chemical & Engineering Data* 55 (2010), February, No. 2, pp. 778–782

[88] FORSE, Alexander C. ; MERLET, Céline ; GRIFFIN, John M. ; GREY, Clare P.: New Perspectives on the Charging Mechanisms of Supercapacitors. In: *Journal of the American Chemical Society* 138 (2016), May, No. 18, pp. 5731–5744

[89] FRICK, B. ; ALBA-SIMIONESCO, C. ; DOSSEH, G. ; LE QUELLEC, C. ; MORENO, A. J. ; COLMENERO, J. ; SCHÖNHALS, A. ; ZORN, R. ; CHRISSOPOULOU, K. ; ANASTASIADIS, S. H. ; DALNOKI-VERESS, K.: Inelastic neutron scattering for investigating the dynamics of confined glass-forming liquids. In: *Journal of Non-Crystalline Solids* 351 (2005), September, No. 33-36, pp. 2657–2667. – Proceedings of 3rd International Conference on Broadband Dielectric Spectroscopy and its Applications; Section 3. Dynamics of nano-confined systems

[90] FRICK, B. ; COMBET, J. ; EIJCK, L. van: New possibilities with inelastic fixed window scans and linear motor Doppler drives on high resolution neutron backscattering spectrometers. In: *Nuclear Instruments and Methods in Physics Research Section A: Accelerators, Spectrometers, Detectors and Associated Equipment* 669 (2012), March, pp. 7–13

[91] FRICK, B. ; MAGERL, A. ; BLANC, Y. ; REBESCO, R.: The new backscattering spectrometer IN16 at the ILL. In: *Physica B: Condensed Matter* 234-236 (1997), pp. 1177–1179. – Proceedings of the First European Conference on Neutron Scattering

[92] FRICK, B. ; SEYDEL, T. ; APPEL, M. ; FARAGO, B.: Instrument review for IN16B / Institut Laue-Langevin. April 2018. – Research Report

[93] FRICK, Bernhard: *Instrument characteristics of IN16B neutron backscattering spectrometer*. – URL `https://www.ill.eu/en/html/instruments-support/instruments-groups/instruments/in16b/characteristics/`. – Institut Laue-Langevin, Grenoble, France – accessed: 11 August 2015 (archived version; current (2019) instrument characteristics are different from those at the time of the experiment)

[94] FRICK, Bernhard: *Neutron Backscattering Spectroscopy*. Chap. 15, pp. 483–527. In: HIPPERT, Françoise (Ed.) ; GEISSLER, Erik (Ed.) ; HODEAU, Jean Louis (Ed.) ; LELIÈVRE-BERNA, Eddy (Ed.) ; REGNARD, Jean-René (Ed.): *Neutron and X-ray Spectroscopy*. Dordrecht : Springer Netherlands, 2006

[95] FRICK, Bernhard ; NEUMANN, Dan: *Neutron Backscattering*. Chap. II.3.2, pp. 183–202. In: IMAE, Toyoko (Ed.) ; KANAYA, Toshiji (Ed.) ; FURUSAKA, Michihiro (Ed.) ; TORIKAI, Naoya (Ed.): *Neutrons in Soft Matter*, John Wiley & Sons, Inc., 2011

[96] FU, Kaiyu ; BOHN, Paul W.: Nanopore Electrochemistry: A Nexus for Molecular Control of Electron Transfer Reactions. In: *ACS Central Science* 4 (2018), January, No. 1, pp. 20–29

[97] Futamura, Ryusuke ; Iiyama, Taku ; Takasaki, Yuma ; Gogotsi, Yury ; Biggs, Mark J. ; Salanne, Mathieu ; Ségalini, Julie ; Simon, Patrice ; Kaneko, Katsumi: Partial breaking of the Coulombic ordering of ionic liquids confined in carbon nanopores. In: *Nature Materials* 16 (2017), pp. 1225–1232

[98] Garland, C. W. ; Iannacchione, G. S.: Effect of Aerosil Gels on de Gennes Nematic–Smectic Coupling. In: *Journal of Physical Chemistry B* 113 (2009), March, No. 12, pp. 3901–3905

[99] Garland, C. W. ; Nounesis, G. ; Stine, K. J.: XY behavior for the heat capacity at nematic–smectic-A_1 liquid-crystal transitions. In: *Physical Review A* 39 (1989), May, No. 9, pp. 4919–4922

[100] Garland, C. W. ; Nounesis, G. ; Stine, K. J. ; Heppke, G.: Heat capacity measurements near the nematic-smectic-A_1 and smectic-A_1-smectic-$\tilde{C}$ transitions in octyloxyphenyl cyanobenzyloxy benzoate. In: *Journal de Physique* 50 (1989), August, No. 16, pp. 2291–2301

[101] Garland, C. W. ; Nounesis, G. ; Young, M. J. ; Birgeneau, R. J.: Critical behavior at nematic–smectic-A_1 phase transtions. II. Preasymptotic three-dimensional XY analysis of x-ray and C_p data. In: *Physical Review E* 47 (1993), March, No. 3, pp. 1918–1930

[102] Garland, Carl W. ; Nounesis, George: Critical behavior at nematic–smectic-A phase transitions. In: *Physical Review E* 49 (1994), April, No. 4, pp. 2964–2971

[103] Gehring, P. M. ; Brocker, C. W. ; Neumann, D. A.: Design of a High-Flux Backscattering Spectrometer for Ultra-High Resolution Inelastic Neutron Measurements. In: *MRS Proceedings* 376 (1995), pp. 113–118. – Symposium BB – Neutron Scattering in Materials Science

[104] de Gennes, P. G.: An analogy between superconductors and smectics A. In: *Solid State Communications* 10 (1972), May, No. 9, pp. 753–756

[105] de Gennes, P. G.: Some Remarks on the Polymorphism of Smectics. In: *Molecular Crystals and Liquid Crystals* 21 (1973), No. 1–2, pp. 49–76

[106] de Gennes, P. G. ; Prost, J.: *The Physics of Liquid Crystals*. 2nd ed. Oxford University Press, 1993 (The International series of monographs on physics; 83)

[107] Göbel, Ronald ; Hesemann, Peter ; Weber, Jens ; Möller, Eléonore ; Friedrich, Alwin ; Beuermann, Sabine ; Taubert, Andreas: Surprisingly high, bulk liquid-like mobility of silica-confined ionic liquids. In: *Physical Chemistry Chemical Physics* 11 (2009), No. 19, pp. 3653–3662

[108] González, M. A. ; Frick, B.: Simulation of the backscattering spectrometer IN16: how much can be gained by using the phase space transformation technique? In: *Applied Physics A* 74 (2002), No. 1, pp. S1474–S1476

[109] GOODBY, J. W.: *Ferroelectricity and Related Phenomena*. Vol. 7: *Properties and Structure of Ferroelectric Liquid Crystals*. Chap. II, pp. 99–247. In: TAYLOR, George W. (Ed.) ; SHUVALOW, Lev A. (Ed.): *Ferroelectric Liquid Crystals: Principles, Properties and Applications* Vol. 7, Gordon and Breach Science Publishers, 1991

[110] GOODBY, John W. ; CHIN, Evelyn ; GEARY, John M. ; PATEL, Jayantilal S. ; FINN, Patrick L.: The ferroelectric and liquid-crystalline properties of some chiral alkyl 4-n-alkanoyloxybiphenyl-4'-carboxylates. In: *Journal of the Chemical Society, Faraday Transactions 1* 83 (1987), No. 11, pp. 3429–3446

[111] GRAPENGETER, H. H. ; ALEFELD, B. ; KOSFELD, R.: An investigation of micro-brownian motions in polydimethylsiloxane by complementary incoherent-neutron-scattering and nuclear-magnetic-resonance experiments below room temperature. In: *Colloid and Polymer Science* 265 (1987), March, No. 3, pp. 226–233

[112] GRAY, G. W. ; MCDONNELL, D. G.: Some Cholesteric Derivatives of S-(+)-4-(2'-Methylbutyl) Phenol. In: *Molecular Crystals and Liquid Crystals* 48 (1978), January, No. 1-2, pp. 37–51

[113] GRIGORIADIS, Christos ; DURAN, Hatice ; STEINHART, Martin ; KAPPL, Michael ; BUTT, Hans-Jürgen ; FLOUDAS, George: Suppression of Phase Transitions in a Confined Rodlike Liquid Crystal. In: *ACS Nano* 5 (2011), November, No. 11, pp. 9208–9215

[114] GUÉGAN, R. ; MORINEAU, D. ; LEFORT, R. ; BÉZIEL, W. ; GUENDOUZ, M. ; NOIREZ, L. ; HENSCHEL, A. ; HUBER, P.: Rich polymorphism of a rod-like liquid crystal (8CB) confined in two types of unidirectional nanopores. In: *The European Physical Journal E* 26 (2008), No. 3, pp. 261–273

[115] HAGA, Hisashi ; GARLAND, Carl W.: Effect of silica aerosil particles on liquid-crystal phase transitions. In: *Physical Review E* 56 (1997), September, No. 3, pp. 3044–3052

[116] HALL, Peter L. ; ROSS, D. K.: Incoherent neutron scattering functions for random jump diffusion in bounded and infinite media. In: *Molecular Physics* 42 (1981), No. 3, pp. 673–682

[117] HALLER, Ivan: Thermodynamic and static properties of liquid crystals. In: *Progress in Solid State Chemistry* 10 (1975), No. Part 2, pp. 103–118

[118] HALPERIN, B. I. ; LUBENSKY, T. C.: On the analogy between smectic a liquid crystals and superconductors. In: *Solid State Communications* 14 (1974), May, No. 10, pp. 997–1001

[119] HARDACRE, Christopher ; HOLBREY, John D. ; MULLAN, Claire L. ; YOUNGS, Tristan G. A. ; BOWRON, Daniel T.: Small angle neutron scattering from 1-alkyl-3-methylimidazolium hexafluorophosphate ionic liquids ([Cnmim][PF6], n=4, 6, and 8). In: *The Journal of Chemical Physics* 133 (2010), August, No. 7, pp. 074510–1–074510–7

[120] HARDACRE, Christopher ; MULLAN, Claire ; YOUNGS, Tristan G. A.: *Investigating the Structure of Ionic Liquids and Ionic Liquid: Molecular Solute Interactions*. Chap. 4, pp. 55–82. In: PLECHKOVA, Natalia V. (Ed.) ; SEDDON, Kenneth R. (Ed.): *Ionic Liquids Completely UnCOILed: Critical Expert Overviews*, John Wiley & Sons, 2015

[121] HAYES, Robert ; WARR, Gregory G. ; ATKIN, Rob: Structure and Nanostructure in Ionic Liquids. In: *Chemical Reviews* 115 (2015), July, No. 13, pp. 6357–6426

[122] HE, Xiaoyun ; ZENG, Min ; BRABAZON, D.: Recent Progress in Fabrication of Nanostructured Carbon Monolithic Materials. In: *Reference Module in Materials Science and Materials Engineering*. Elsevier, 2016

[123] VAN DER HEYDEN, Frank H. J. ; BONTHUIS, Douwe Jan ; STEIN, Derek ; MEYER, Christine ; DEKKER, Cees: Power Generation by Pressure-Driven Transport of Ions in Nanofluidic Channels. In: *Nano Letters* 7 (2007), April, No. 4, pp. 1022–1025

[124] HOFMANN, Tommy ; WALLACHER, Dirk ; MAYOROVA, Maria ; ZORN, Reiner ; FRICK, Bernhard ; HUBER, Patrick: Molecular dynamics of n-hexane: A quasi-elastic neutron scattering study on the bulk and spatially nanochannel-confined liquid. In: *Journal of Chemical Physics* 136 (2012), No. 12, pp. 124505

[125] VAN HOVE, Léon: Correlations in Space and Time and Born Approximation Scattering in Systems of Interacting Particles. In: *Physical Review* 95 (1954), July, No. 1, pp. 249–262

[126] HU, Zhonghan ; MARGULIS, Claudio J.: Heterogeneity in a room-temperature ionic liquid: Persistent local environments and the red-edge effect. In: *Proceedings of the National Academy of Sciences* 103 (2006), January, No. 4, pp. 831–836

[127] HUBER, Patrick: Soft matter in hard confinement: phase transition thermodynamics, structure, texture, diffusion and flow in nanoporous media. In: *Journal of Physics: Condensed Matter* 27 (2015), February, No. 10, pp. 103102

[128] IACOB, C. ; SANGORO, J. R. ; KIPNUSU, W. K. ; VALIULLIN, R. ; KÄRGER, J. ; KREMER, F.: Enhanced charge transport in nano-confined ionic liquids. In: *Soft Matter* 8 (2012), No. 2, pp. 289–293

[129] IACOB, Ciprian ; SANGORO, Joshua Rume ; PAPADOPOULOS, Periklis ; SCHUBERT, Tilman ; NAUMOV, Sergej ; VALIULLIN, Rustem ; KÄRGER, Jörg ; KREMER, Friedrich: Charge transport and diffusion of ionic liquids in nanoporous silica membranes. In: *Physical Chemistry Chemical Physics* 12 (2010), No. 41, pp. 13798–13803

[130] IANNACCHIONE, Germano S.: Review of liquid-crystal phase transitions with quenched random disorder. In: *Fluid Phase Equilibria* 222-223 (2004), August, pp. 177–187

[131] IANNACCHIONE, Germano S. ; FINOTELLO, Daniele: Specific heat dependence on orientational order at cylindrically confined liquid crystal phase transitions. In: *Physical Review E* 50 (1994), December, No. 6, pp. 4780–4795

[132] IMRY, Yoseph ; WORTIS, Michael: Influence of quenched impurities on first-order phase transitions. In: *Physical Review B* 19 (1979), April, No. 7, pp. 3580–3585

[133] INOUE, Yo ; YOSHIDA, Hiroyuki ; INOUE, Kenta ; SHIOZAKI, Yusuke ; KUBO, Hitoshi ; FUJII, Akihiko ; OZAKI, Masanori: Tunable Lasing from a Cholesteric Liquid Crystal Film Embedded with a Liquid Crystal Nanopore Network. In: *Advanced Materials* 23 (2011), No. 46, pp. 5498–5501

[134] JACKSON, Catheryn L. ; MCKENNA, Gregory B.: The melting behavior of organic materials confined in porous solids. In: *The Journal of Chemical Physics* 93 (1990), December, No. 12, pp. 9002–9011

[135] JANG, Won Gun ; KIM, Kyeong Hyeon: Infrared (IR) Spectroscopy, X-ray Scattering, and Optical Microscopy Studies of Ferroelectric Liquid Crystals (FLC) with Polarization Sign-Inversion Characteristics. In: *Journal of the Korean Physical Society* 38 (2001), January, No. 1, pp. 4–9

[136] JANSSEN, S. ; MESOT, J. ; HOLITZNER, L. ; FURRER, A. ; HEMPELMANN, R.: FOCUS: a hybrid TOF-spectrometer at SINQ. In: *Physica B: Condensed Matter* 234–236 (1997), June, pp. 1174–1176. – Proceedings of the First European Conference on Neutron Scattering

[137] JANSSEN, S. ; RUBIO-TEMPRANO, D. ; FURRER, A.: Time versus monochromatic focusing on a cold neutron time-of-flight spectrometer. In: *Physica B: Condensed Matter* 283 (2000), June, No. 4, pp. 355–360

[138] JANSSEN, Stefan ; MESOT, Joel ; HEMPELMANN, Rolf: FOCUS: Time-of-Flight Spectrometer for Cold Neutrons at SINQ. In: FURRER, A. (Ed.): *New instruments and science around SINQ – Lecture notes of the 4 summer school on neutron scattering*. Switzerland : Paul Scherrer Institut, November 1996 (PSI Proceedings 96-02), pp. 45–54

[139] JIANG, De-en ; JIN, Zhehui ; WU, Jianzhong: Oscillation of Capacitance inside Nanopores. In: *Nano Letters* 11 (2011), December, No. 12, pp. 5373–5377

[140] JOHNO, Masahiro ; CHANDANI, A. D. L. ; OUCHI, Yukio ; TAKEZOE, Hideo ; FUKUDA, Atsuo ; ICHIHASHI, Mitsuyoshi ; FURUKAWA, Kenji: Smectic Layer Switching by an Electric Field in Ferroelectric Liquid Crystal Cells. In: *Japanese Journal of Applied Physics* 28 (1989), January, No. 1A, pp. L119–L120

[141] JONES, Cliff: *Bistable Liquid Crystal Displays*. Chap. 7.3.5, pp. 1507–1543. In: CHEN, Janglin (Ed.) ; CRANTON, Wayne (Ed.) ; FIHN, Mark (Ed.): *Handbook of Visual Display Technology*. Berlin, Heidelberg : Springer Berlin Heidelberg, 2012

[142] DE JONGH, Petra E. ; EGGENHUISEN, Tamara M.: Melt Infiltration: an Emerging Technique for the Preparation of Novel Functional Nanostructured Materials. In: *Advanced Materials* 25 (2013), No. 46, pp. 6672–6690

[143] JUHL, Anika C. ; ELVERFELDT, Carl-Philipp ; HOFFMANN, Frank ; FRÖBA, Michael: Porous carbon monoliths with pore sizes adjustable between 10 nm and 2 μm prepared by phase separation – New insights in the relation between synthesis composition and resulting structure. In: *Microporous and Mesoporous Materials* 255 (2018), January, pp. 271–280

[144] KANAKUBO, Mitsuhiro ; HIEJIMA, Yusuke ; MINAMI, Kimitaka ; AIZAWA, Takafumi ; NANJO, Hiroshi: Melting point depression of ionic liquids confined in nanospaces. In: *Chemical Communications* 42 (2006), No. 17, pp. 1828–1830

[145] KAPERNAUM, Nadia ; GIESSELMANN, Frank: Simple experimental assessment of smectic translational order parameters. In: *Physical Review E* 78 (2008), December, No. 6, pp. 062701–1–062701–3

[146] KASHYAP, Hemant K. ; SANTOS, Cherry S. ; ANNAPUREDDY, Harsha V. R. ; MURTHY, N. Sanjeeva ; MARGULIS, Claudio J. ; CASTNER, JR, Edward W.: Temperature-dependent structure of ionic liquids: X-ray scattering and simulations. In: *Faraday Discussions* 154 (2012), No. 26, pp. 133–143

[147] KITYK, Andriy V. ; HUBER, Patrick: Thermotropic nematic and smectic order in silica glass nanochannels. In: *Applied Physics Letters* 97 (2010), October, No. 15, pp. 153124–1–153124–3

[148] KITYK, Andriy V. ; WOLFF, Matthias ; KNORR, Klaus ; MORINEAU, Denis ; LEFORT, Ronan ; HUBER, Patrick: Continuous Paranematic-to-Nematic Ordering Transitions of Liquid Crystals in Tubular Silica Nanochannels. In: *Physical Review Letters* 101 (2008), October, No. 18, pp. 187801–1–187801–4

[149] KITZEROW, Heinz-Siegfried (Ed.) ; BAHR, Christian (Ed.): *Chirality in Liquid Crystals*. Springer-Verlag, 2001 (Partially Ordered Systems)

[150] KLÉMAN, M. ; WILLIAMS, C. E.: Interaction between parallel edge dislocation lines in a smectic A liquid crystal. In: *Le Journal de Physique - Lettres* 35 (1974), April, No. 4, pp. 49–51

[151] KOBAYASHI, K. K.: On the theory of translational and orientational melting with application to liquid crystals. In: *Physics Letters* 31A (1970), February, No. 3, pp. 125–126

[152] KOBAYASHI, Kenji K.: Theory of Translational and Orientational Melting with Application to Liquid Crystals. In: *Molecular Crystals and Liquid Crystals* 13 (1971), No. 2, pp. 137–148

[153] KONDRAT, S. ; GEORGI, N. ; FEDOROV, M. V. ; KORNYSHEV, A. A.: A superionic state in nano-porous double-layer capacitors: insights from Monte Carlo simulations. In: *Physical Chemistry Chemical Physics* 13 (2011), No. 23, pp. 11359–11366

[154] KONDRAT, S. ; KORNYSHEV, A.: Superionic state in double-layer capacitors with nanoporous electrodes. In: *Journal of Physics: Condensed Matter* 23 (2010), December, No. 2, pp. 022201

[155] KONDRAT, Svyatoslav ; WU, Peng ; QIAO, Rui ; KORNYSHEV, Alexei A.: Accelerating charging dynamics in subnanometre pores. In: *Nature Materials* 13 (2014), March, No. 4, pp. 387–393

[156] KRALJ, S. ; SLUCKIN, T. J.: Landau–de Gennes theory of the chevron structure in a smectic-A liquid crystal. In: *Physical Review E* 50 (1994), October, No. 4, pp. 2940–2951

[157] KRALJ, Samo ; CORDOYIANNIS, George ; JESENEK, Dalija ; ZIDANŠEK, Aleksander ; LAHAJNAR, Gojmir ; NOVAK, Nikola ; AMENITSCH, Heinz ; KUTNJAK, Zdravko: Dimensional crossover and scaling behavior of a smectic liquid crystal confined to controlled-pore glass matrices. In: *Soft Matter* 8 (2012), pp. 2460–2470

[158] KUCZYŃSKI, W. ; HOFFMANN, J. ; MAŁECKI, J.: Investigation of ferroelectric modes in liquid crystals using dielectric and optical methods. In: *Ferroelectrics* 150 (1993), No. 1, pp. 279–290

[159] KUSMIN, André ; GRUENER, Simon ; HENSCHEL, Anke ; HOLDERER, Olaf ; ALLGAIER, Jürgen ; RICHTER, Dieter ; HUBER, Patrick: Evidence of a Sticky Boundary Layer in Nanochannels: A Neutron Spin Echo Study of *n*-Hexatriacontane and Poly(ethylene oxide) Confined in Porous Silicon. In: *The Journal of Physical Chemistry Letters* 1 (2010), October, No. 20, pp. 3116–3121

[160] KUTNJAK, Z. ; KRALJ, S. ; LAHAJNAR, G. ; ZUMER, S.: Thermal study of octylcyanobiphenyl liquid crystal confined to controlled-pore glass. In: *Fluid Phase Equilibria* 222–223 (2004), pp. 275–281. – Proceedings of the Fifteenth Symposium on Thermophysical Properites

[161] KUTNJAK, Zdravko ; KRALJ, Samo ; LAHAJNAR, Gojmir ; ŽUMER, Slobodan: Calorimetric study of octylcyanobiphenyl liquid crystal confined to a controlled-pore glass. In: *Physical Review E* 68 (2003), August, No. 2, pp. 021705–1–021705–12

[162] KUTNJAK, Zdravko ; KRALJ, Samo ; LAHAJNAR, Gojmir ; ŽUMER, Slobodan: Influence of finite size and wetting on nematic and smectic phase behavior of liquid crystal confined to controlled-pore matrices. In: *Physical Review E* 70 (2004), November, No. 5, pp. 051703–1–051703–11

[163] LAGERWALL, Jan P. F. ; GIESSELMANN, Frank: Current Topics in Smectic Liquid Crystal Research. In: *ChemPhysChem* 7 (2006), No. 1, pp. 20–45

[164] LAGERWALL, Jan P. F. ; SCALIA, Giusy: A new era for liquid crystal research: Applications of liquid crystals in soft matter nano-, bio- and microtechnology. In: *Current Applied Physics* 12 (2012), November, No. 6, pp. 1387–1412

[165] LAGERWALL, Sven Torbjörn: *Ferroelectric and antiferroelectric liquid crystals*. Weinheim : Wiley-VCH Verlag, 1999

[166] LAI, Feili ; FENG, Jianrui ; YAN, Runyu ; WANG, Gui-Chang ; ANTONIETTI, Markus ; OSCHATZ, Martin: Breaking the Limits of Ionic Liquid-Based Supercapacitors: Mesoporous Carbon Electrodes Functionalized with Manganese Oxide Nanosplotches for Dense, Stable, and Wide-Temperature Energy Storage. In: *Advanced Functional Materials* 28 (2018), No. 36, pp. 1801298

[167] LALL-RAMNARINE, Sharon I. ; HATCHER, Jasmine ; CASTANO, Alejandra ; THOMAS, Marie ; WISHART, James: Exploring the Effect of Structural Modification on the Physical Properties of Various Ionic Liquids. In: *ECS Transactions* 33 (2010), No. 7, pp. 659–665

[168] LAROCHELLE, S. ; RAMAZANOGLU, M. ; BIRGENEAU, R. J.: Effects of disorder on a smectic-A–nematic phase transition. In: *Physical Review E* 73 (2006), June, No. 6, pp. 060702–1–060702–4

[169] LARRIBA, Marcos ; GARCÍA, Silvia ; NAVARRO, Pablo ; GARCÍA, Julián ; RODRÍGUEZ, Francisco: Physical Properties of N-Butylpyridinium Tetrafluoroborate and N-Butylpyridinium Bis(trifluoromethylsulfonyl)imide Binary Ionic Liquid Mixtures. In: *J. Chem. Eng. Data* 57 (2012), April, No. 4, pp. 1318–1325

[170] LASCHAT, Sabine ; BARO, Angelika ; STEINKE, Nelli ; GIESSELMANN, Frank ; HÄGELE, Constanze ; SCALIA, Giusy ; JUDELE, Roxana ; KAPATSINA, Elisabeth ; SAUER, Sven ; SCHREIVOGEL, Alina ; TOSONI, Martin: Discotic Liquid Crystals: From Tailor-Made Synthesis to Plastic Electronics. In: *Angewandte Chemie International Edition* 46 (2007), No. 26, pp. 4832–4887

[171] LEADBETTER, A. J. ; NORRIS, E. K.: Distribution functions in three liquid crystals from X-ray diffraction measurements. In: *Molecular Physics* 38 (1979), No. 3, pp. 669–686

[172] LEADBETTER, A. J. ; RICHARDSON, R. M.: Molecular motions in a smectic A phase by incoherent quasielastic neutron scattering. In: *Molecular Physics* 35 (1978), April, No. 4, pp. 1191–1200

[173] LECHNER, R. E. ; BLEIF, H. J. ; DACHS, H. ; MARX, R . ; STAHN, M. ; ANDERSON, I.: Two-dimensional proton diffusion in CsH_3O_2. In: *Solid State Ionics* 46 (1991), October, pp. 25–32

[174] LECHNER, R. E. ; LONGEVILLE, S.: *Quasielastic Neutron Scattering in Biology, Part I: Methods*. Chap. 15, pp. 309–354. In: FITTER, Jörg (Ed.) ; KATSARAS, John (Ed.) ; GUTBERLET, Thomas (Ed.): *Neutron Scattering in Biology – Techniques and Applications*, Springer-Verlag, 2006

[175] LECHNER, R. E. ; LONGEVILLE, S.: *Quasielastic Neutron Scattering in Biology, Part II: Applications*. Chap. 16, pp. 355–397. In: FITTER, Jörg (Ed.) ; KATSARAS, John (Ed.) ; GUTBERLET, Thomas (Ed.): *Neutron Scattering in Biology – Techniques and Applications*, Springer-Verlag, 2006

[176] LEE, Alpha A. ; VELLA, Dominic ; GORIELY, Alain ; KONDRAT, Svyatoslav: Capacitance-Power-Hysteresis Trilemma in Nanoporous Supercapacitors. In: *Physical Review X* 6 (2016), June, No. 2, pp. 021034–1–021034–11

[177] LEE, Woo ; PARK, Sang-Joon: Porous Anodic Aluminum Oxide: Anodization and Templated Synthesis of Functional Nanostructures. In: *Chemical Reviews* 114 (2014), August, No. 15, pp. 7487–7556

[178] LEFORT, R. ; JEAN, F. ; NOIREZ, L. ; NDAO, M. ; CERCLIER, C. V. ; MORINEAU, D.: Smectic C chevrons in nanocylinders. In: *Applied Physics Letters* 105 (2014), November, No. 20, pp. 203106

[179] LEHENY, R. L. ; PARK, S. ; BIRGENEAU, R. J. ; GALLANI, J.-L. ; GARLAND, C. W. ; IANNACCHIONE, G. S.: Smectic ordering in liquid-crystal–aerosil dispersions. I. X-ray scattering. In: *Physical Review E* 67 (2003), January, No. 1, pp. 011708–1–011708–13

[180] LI, Song ; HAN, Kee Sung ; FENG, Guang ; HAGAMAN, Edward W. ; VLCEK, Lukas ; CUMMINGS, Peter T.: Dynamic and Structural Properties of Room-Temperature Ionic Liquids near Silica and Carbon Surfaces. In: *Langmuir* 29 (2013), August, No. 31, pp. 9744–9749

[181] LI, Tao ; SENESI, Andrew J. ; LEE, Byeongdu: Small Angle X-ray Scattering for Nanoparticle Research. In: *Chemical Reviews* 116 (2016), No. 18, pp. 11128–11180

[182] LIANG, Dennis ; LEHENY, Robert L.: Smectic liquid crystals in an anisotropic random environment. In: *Physical Review E* 75 (2007), March, No. 3, pp. 031705–1–031705–11

[183] LIMAT, L. ; PROST, J.: A model for the chevron structure obtained by cooling a smectic A liquid crystal in a cell of finite thickness. In: *Liquid Crystals* 13 (1993), No. 1, pp. 101–113

[184] LIU, Li ; CHEN, Sow-Hsin ; FARAONE, Antonio ; YEN, Chun-Wan ; MOU, Chung-Yuan ; KOLESNIKOV, Alexander I ; MAMONTOV, Eugene ; LEAO, Juscelino: Quasielastic and inelastic neutron scattering investigation of fragile-to-strong crossover in deeply supercooled water confined in nanoporous silica matrices. In: *Journal of Physics: Condensed Matter* 18 (2006), August, No. 36, pp. S2261–S2284

[185] LIU, Qing-Shan ; YANG, Miao ; YAN, Pei-Fang ; LIU, Xiu-Mei ; TAN, Zhi-Cheng ; WELZ-BIERMANN, Urs: Density and Surface Tension of Ionic Liquids [Cnpy][NTf2] (n = 2, 4, 5). In: *Journal of Chemical & Engineering Data* 55 (2010), November, No. 11, pp. 4928–4930

[186] LOVESEY, Stephen W.: *International Series of monographs on physics No 72*. Vol. 1: *Theory of neutron scattering from condensed matter*. London : Oxford University Press, 1984

[187] LUBENSKY, T. C.: Latent heat of the cholesteric to smectic A transition. In: *Journal de Physique Colloques* 36 (1975), March, No. C1, pp. C1–151–C1–152

[188] MAGASINSKI, A. ; DIXON, P. ; HERTZBERG, B. ; KVIT, A. ; AYALA, J. ; YUSHIN, G.: High-performance lithium-ion anodes using a hierarchical bottom-up approach. In: *Nature Materials* 9 (2010), March, pp. 353–358

[189] MAIER-LEIBNITZ, Heinz: Grundlagen für die Beurteilung von Intensitäts- und Genauigkeitsfragen bei Neutronenstreumessungen. In: *Nukleonik* 8 (1966), February, No. 2, pp. 61–67

[190] MANG, Joseph T. ; SAKAMOTO, Kazutami ; KUMAR, Satyendra: Smectic Layer Orientation in Confined Geometries. In: *Molecular Crystals and Liquid Crystals Science and Technology. Section A. Molecular Crystals and Liquid Crystals* 223 (1992), No. 1, pp. 133–142

[191] MARTINELLI, A. ; MARÉCHAL, M. ; ÖSTLUND, Å. ; CAMBEDOUZOU, J.: Insights into the interplay between molecular structure and diffusional motion in 1-alkyl-3-methylimidazolium ionic liquids: a combined PFG NMR and X-ray scattering study. In: *Physical Chemistry Chemical Physics* 15 (2013), pp. 5510–5517

[192] MARUYAMA, M. ; BIENFAIT, M. ; DASH, J. G. ; CODDENS, G.: Interfacial melting of ice in graphite and talc powders. In: *Journal of Crystal Growth* 118 (1992), March, No. 1, pp. 33–40

[193] MAUNE, Brett ; LONČAR, Marko ; WITZENS, Jeremy ; HOCHBERG, Michael ; BAEHR-JONES, Thomas ; PSALTIS, Demetri ; SCHERER, Axel ; QIU, Yueming: Liquid-crystal electric tuning of a photonic crystal laser. In: *Applied Physics Letters* 85 (2004), July, No. 3, pp. 360–362

[194] MCMILLAN, W. L.: Simple Molecular Model for the Smectic *A* Phase of Liquid Crystals. In: *Physical Review A* 4 (1971), September, No. 3, pp. 1238–1246

[195] MCMILLAN, W. L.: X-Ray Scattering from Liquid Crystals. I. Cholesteryl Nonanoate and Myristate. In: *Physical Review A* 6 (1972), September, No. 3, pp. 936–947

[196] MCMILLAN, W. L.: Measurement of Smectic-Phase Order-Parameter Fluctuations in the Nematic Phase of Heptyloxyazoxybenzene. In: *Physical Review A* 8 (1973), July, No. 1, pp. 328–331

[197] MCNALLY, Ben ; SINGER, Alon ; YU, Zhiliang ; SUN, Yingjie ; WENG, Zhiping ; MELLER, Amit: Optical Recognition of Converted DNA Nucleotides for Single-Molecule DNA Sequencing Using Nanopore Arrays. In: *Nano Letters* 10 (2010), June, No. 6, pp. 2237–2244

[198] MENG, Yan ; GU, Dong ; ZHANG, Fuqiang ; SHI, Yifeng ; YANG, Haifeng ; LI, Zheng ; YU, Chengzhong ; TU, Bo ; ZHAO, Dongyuan: Ordered Mesoporous Polymers and Homologous Carbon Frameworks: Amphiphilic Surfactant Templating and Direct Transformation. In: *Angewandte Chemie International Edition* 44 (2005), November, No. 43, pp. 7053–7059

[199] MERLET, Céline ; ROTENBERG, Benjamin ; MADDEN, Paul A. ; TABERNA, Pierre-Louis ; SIMON, Patrice ; GOGOTSI, Yury ; SALANNE, Mathieu: On the molecular origin of supercapacitance in nanoporous carbon electrodes. In: *Nature Materials* 11 (2012), March, No. 4, pp. 306–310

[200] MESOT, J. ; JANSSEN, S. ; HOLITZNER, L. ; HEMPELMANN, R.: Focus: Project of a Space and Time Focussing Time-of-Flight Spectrometer for Cold Neutrons at the Spallation Source SINQ of the Paul Scherrer Institute. In: *Journal of Neutron Research* 3 (1996), September, No. 4, pp. 293–310

[201] MITRA, Subhankur ; CERCLIER, Carole ; BERROD, Quentin ; FERDEGHINI, Filippo ; OLIVEIRA-SILVA, Rodrigo de ; JUDEINSTEIN, Patrick ; LE BIDEAU, Jean ; ZANOTTI, Jean-Marc: Ionic Liquids Confined in Silica Ionogels: Structural, Thermal, and Dynamical Behaviors. In: *Entropy* 19 (2017), March, No. 4, pp. 1–13

[202] MIYANO, K.: Wall-Induced Pretransitional Birefringence: A New Tool to Study Boundary Aligning Forces in Liquid Crystals. In: *Physical Review Letters* 43 (1979), July, No. 1, pp. 51–54

[203] MONK, Joshua ; SINGH, Ramesh ; HUNG, Francisco R.: Effects of Pore Size and Pore Loading on the Properties of Ionic Liquids Confined Inside Nanoporous CMK-3 Carbon Materials. In: *The Journal of Physical Chemistry C* 115 (2011), February, No. 7, pp. 3034–3042

[204] MORENO, A. J. ; COLMENERO, J. ; ALEGRÍA, A. ; ALBA-SIMIONESCO, C. ; DOSSEH, G. ; MORINEAU, D. ; FRICK, B.: Methyl group dynamics in a confined glass. In: *The European Physical Journal E* 12 (2003), November, No. 1, pp. 43–46

[205] MORSE, A. S. ; GLEESON, H. F.: Observation of a chevron hybrid structure in the smectic A phase of a liquid crystal device. In: *Liquid Crystals* 23 (1997), No. 4, pp. 531–535

[206] MUŠEVIČ, I. ; DREVENŠEK, I. ; BLINC, R. ; KUMAR, S. ; DOANE, J. W.: Temperature Dependence of Molecular Tilt Angle and Rotatory Power in a Ferroelectric Liquid Crystal with Polarization Sign Reversal. In: *Molecular Crystals and Liquid Crystals Incorporating Nonlinear Optics* 172 (1989), July, No. 1, pp. 217–222

[207] MUŠEVIČ, Igor ; NIEUWKERK, Cindy ; RASING, Theo: *Introduction*. Chap. 1, pp. 3–16. In: RASING, Th. (Ed.) ; MUŠEVIČ, I. (Ed.): *Surfaces and Interfaces of Liquid Crystals*, Springer, 2004

[208] NAKAGAWA, M.: On the Polarization Electric Field in Surface-Stabilized Ferroelectric Liquid Crystalst. In: *Molecular Crystals and Liquid Crystals Incorporating Nonlinear Optics* 173 (1989), No. 1, pp. 1–16

[209] NAZET, Andreas ; SOKOLOV, Sophia ; SONNLEITNER, Thomas ; FRIESEN, Sergej ; BUCHNER, Richard: Densities, Refractive Indices, Viscosities, and Conductivities of Non-Imidazolium Ionic Liquids [Et3S][TFSI], [Et2MeS][TFSI], [BuPy][TFSI], [N8881][TFA], and [P14][DCA]. In: *Journal of Chemical & Engineering Data* 62 (2017), April, No. 9, pp. 2549–2561

[210] NEIMARK, Alexander V. ; LIN, Yangzheng ; RAVIKOVITCH, Peter I. ; THOMMES, Matthias: Quenched solid density functional theory and pore size analysis of micro-mesoporous carbons. In: *Carbon* 47 (2009), June, No. 7, pp. 1617–1628

[211] NODA, Akihiro ; HAYAMIZU, Kikuko ; WATANABE, Masayoshi: Pulsed-Gradient Spin-Echo ^{1}H and ^{19}F NMR Ionic Diffusion Coefficient, Viscosity, and Ionic Conductivity of Non-Chloroaluminate Room-Temperature Ionic Liquids. In: *The Journal of Physical Chemistry B* 105 (2001), May, No. 20, pp. 4603–4610

[212] NOMURA, Kenji ; TERAUCHI, Hikaru ; KASATANI, Hirofumi ; ITOH, Nobuyuki ; MIYOSHI, Shuji: Electric Field Effect on Layer Structure in Surface-Stabilized Ferroelectric Liquid Crystals. In: *Japanese Journal of Applied Physics* 34 (1995), October, No. 10, pp. 5689–5693. – Part I

[213] NOUNESIS, G. ; BLUM, K. I. ; YOUNG, M. J. ; GARLAND, C. W. ; BIRGENEAU, R. J.: Critical behavior at nematic–smectic-A_1 phase transitions. I. High-resolution x-ray-scattering and calorimetric study of the liquid-crystal octyloxyphenylnitrobenzoyloxy benzoate. In: *Physical Review E* 47 (1993), March, No. 3, pp. 1910–1917

[214] OHBA, Tomonori ; CHABAN, Vitaly V.: A Highly Viscous Imidazolium Ionic Liquid inside Carbon Nanotubes. In: *The Journal of Physical Chemistry B* 118 (2014), June, No. 23, pp. 6234–6240

[215] OLIVEIRA, Filipe S. ; FREIRE, Mara G. ; CARVALHO, Pedro J. ; COUTINHO, João A. P. ; LOPES, José N. Canongia ; REBELO, Luís P. N. ; MARRUCHO, Isabel M.: Structural and Positional Isomerism Influence in the Physical Properties of Pyridinium NTf2-Based Ionic Liquids: Pure and Water-Saturated Mixtures. In: *Journal of Chemical & Engineering Data* 55 (2010), October, No. 10, pp. 4514–4520

[216] OUCHI, Yukio ; LEE, Ji ; TAKEZOE, Hideo ; FUKUDA, Atsuo ; KONDO, Katsumi ; KITAMURA, Teruo ; MUKOH, Akio: Smectic C* Chevron Layer Structure Studied by X-Ray Diffraction. In: *Japanese Journal of Applied Physics* 27 (1988), May, No. 5A, pp. L725–L728

[217] OUCHI, Yukio ; TAKANISHI, Yoichi ; TAKEZOE, Hideo ; FUKUDA, Atsuo: Chevron Layer Structure and Parabolic Focal Conics in Smectic A Liquid Crystals. In: *Japanese Journal of Applied Physics* 28 (1989), December, No. 12R, pp. 2547–2551

[218] PANESAR, K. S. ; HUGON, C. ; AUBERT, G. ; JUDEINSTEIN, P. ; ZANOTTI, J.-M. ; SAKELLARIOU, D.: Measurement of self-diffusion in thin samples using a novel one-sided NMR magnet. In: *Microporous and Mesoporous Materials* 178 (2013), September, pp. 79–83

[219] PATEL, J. S. ; GOODBY, J. W.: Contributions of the molecular species to the magnitude of the spontaneous polarization in ferroelectric liquid crystals. In: *Philosophical Magazine Letters* 55 (1987), June, No. 6, pp. 283–287

[220] PATTIE, R. W. ; CALLAHAN, N. B. ; CUDE-WOODS, C. ; ADAMEK, E. R. ; BROUSSARD, L. J. ; CLAYTON, S. M. ; CURRIE, S. A. ; DEES, E. B. ; DING, X. ; ENGEL, E. M. ; FELLERS, D. E. ; FOX, W. ; GELTENBORT, P. ; HICKERSON, K. P. ; HOFFBAUER, M. A. ; HOLLEY, A. T. ; KOMIVES, A. ; LIU, C.-Y. ; MACDONALD, S. W. T. ; MAKELA, M. ; MORRIS, C. L. ; ORTIZ, J. D. ; RAMSEY, J. ; SALVAT, D. J. ; SAUNDERS, A. ; SEESTROM, S. J. ; SHARAPOV, E. I. ; SJUE, S. K. ; TANG, Z. ; VANDERWERP, J. ; VOGELAAR, B. ; WALSTROM, P. L. ; WANG, Z. ; WEI, W. ; WEAVER, H. L. ; WEXLER, J. W. ; WOMACK, T. L. ; YOUNG, A. R. ; ZECK, B. A.: Measurement of the neutron lifetime using a magneto-gravitational trap and in situ detection. In: *Science* 360 (2018), May, No. 6389, pp. 627–632

[221] PELZL, G. ; KOLBE, P. ; PREUKSCHAS, U. ; DIELE, S. ; DEMUS, D.: Tilt Angle Determination of a Smectic C Phase by Field-Induced Freedericksz Transition and x ray Investigations. In: *Molecular Crystals and Liquid Crystals* 53 (1979), No. 3-4, pp. 167–179

[222] PENDLEBURY, J. M. ; AFACH, S. ; AYRES, N. J. ; BAKER, C. A. ; BAN, G. ; BISON, G. ; BODEK, K. ; BURGHOFF, M. ; GELTENBORT, P. ; GREEN, K. ; GRIFFITH, W. C. ; GRINTEN, M. van der ; GRUJIĆ, Z. D. ; HARRIS, P. G. ; HÉLAINE, V. ; IAYDJIEV, P. ; IVANOV, S. N. ; KASPRZAK, M. ; KERMAIDIC, Y. ; KIRCH, K. ; KOCH, H.-C. ; KOMPOSCH, S. ; KOZELA, A. ; KREMPEL, J. ; LAUSS, B. ; LEFORT, T. ; LEMIÈRE, Y. ; MAY, D. J. R. ; MUSGRAVE, M. ; NAVILIAT-CUNCIC, O. ; PIEGSA, F. M. ; PIGNOL, G. ; PRASHANTH, P. N. ; QUÉMÉNER, G. ; RAWLIK, M. ; REBREYEND, D. ; RICHARDSON, J. D. ; RIES, D. ; ROCCIA, S. ; ROZPEDZIK, D. ; SCHNABEL, A. ; SCHMIDT-WELLENBURG, P. ; SEVERIJNS, N. ; SHIERS, D. ; THORNE, J. A. ; WEIS, A. ; WINSTON, O. J. ; WURSTEN, E. ; ZEJMA, J. ; ZSIGMOND, G.: Revised experimental upper limit on the electric dipole moment of the neutron. In: *Physical Review D* 92 (2015), November, No. 9, pp. 092003–1–092003–22

[223] PERRONE DONNORSO, M. ; MIELE, E. ; ANGELIS, F. De ; ROCCA, R. La ; LIMONGI, T. ; ZANACCHI, F. Cella ; MARRAS, S. ; BRESCIA, R. ; FABRIZIO, E. Di: Nanoporous silicon nanoparticles for drug delivery applications. In: *Microelectronic Engineering* 98 (2012), October, pp. 626–629. – Special issue MNE 2011 - Part II

[224] PEVNYI, Mykhailo Y. ; SELINGER, Jonathan V. ; SLUCKIN, Timothy J.: Modeling smectic layers in confined geometries: Order parameter and defects. In: *Physical Review E* 90 (2014), September, No. 3, pp. 032507–1–032507–8

[225] POLLMANN, P. ; VOSS, E.: High pressure optical studies of the chirality and phase behaviour of liquid crystalline blue phases. In: *Liquid Crystals* 23 (1997), No. 2, pp. 299–307

[226] PRESSER, Volker ; HEON, Min ; GOGOTSI, Yury: Carbide-Derived Carbons – From Porous Networks to Nanotubes and Graphene. In: *Advanced Functional Materials* 21 (2011), March, No. 5, pp. 810–833

[227] QIAN, Sihai ; IANNACCHIONE, Germano S. ; FINOTELLO, Daniele: Critical behavior of a smectic-*A* to nematic phase transition imbedded in a random network of voids. In: *Physical Review E* 57 (1998), April, No. 4, pp. 4305–4315

[228] RICHARD, D. ; FERRAND, M. ; KEARLEY, G. J.: Analysis and visualisation of neutron-scattering data. In: *Journal of Neutron Research* 4 (1996), No. 1-4, pp. 33–39

[229] RIEKER, T. P. ; CLARK, N. A. ; SMITH, G. S. ; PARMAR, D. S. ; SIROTA, E. B. ; SAFINYA, C. R.: "Chevron" Local Layer Structure in Surface-Stabilized Ferroelectric Smectic-*C* Cells. In: *Physical Review Letters* 59 (1987), December, No. 23, pp. 2658–2661

[230] ROH, J. H. ; CURTIS, J. E. ; AZZAM, S. ; NOVIKOV, V. N. ; PERAL, I. ; CHOWDHURI, Z. ; GREGORY, R. B. ; SOKOLOV, A. P.: Influence of Hydration on the Dynamics of Lysozyme. In: *Biophysical Journal* 91 (2006), October, No. 7, pp. 2573–2588

[231] ROLAND, C. M.: Characteristic relaxation times and their invariance to thermodynamic conditions. In: *Soft Matter* 4 (2008), September, No. 12, pp. 2316–2322

[232] ROUQUEROL, J. ; AVNIR, D. ; FAIRBRIDGE, C. W. ; EVERETT, D. H. ; HAYNES, J. M. ; PERNICONE, N. ; RAMSAY, J. D. F. ; SING, K. S. W. ; UNGER, K. K.: Recommendations for the characterization of porous solids (Technical Report). In: *Pure and Applied Chemistry* 66 (1994), January, No. 8, pp. 1739–1758

[233] RYU, Seong Ho ; GIM, Min-Jun ; LEE, Wonsuk ; CHOI, Suk-Won ; YOON, Dong Ki: Switchable Photonic Crystals Using One-Dimensional Confined Liquid Crystals for Photonic Device Application. In: *ACS Applied Materials & Interfaces* 9 (2017), No. 3, pp. 3186–3191

[234] RYU, Seong Ho ; YOON, Dong Ki: Liquid crystal phases in confined geometries. In: *Liquid Crystals* 43 (2016), No. 13-15, pp. 1951–1972

[235] RYU, Seong Ho ; YOON, Dong Ki: Switchable Plasmonic Film Using Nanoconfined Liquid Crystals. In: *ACS Applied Materials & Interfaces* 9 (2017), July, No. 29, pp. 25057–25061

[236] SALANNE, Mathieu: Ionic Liquids for Supercapacitor Applications. In: *Topics in Current Chemistry* 375 (2017), May, No. 3, pp. 63

[237] SCHEIDLER, P. ; KOB, W. ; BINDER, K.: Cooperative motion and growing length scales in supercooled confined liquids. In: *Europhysics Letters* 59 (2002), September, No. 5, pp. 701–707

[238] SCHELTEN, J. ; ALEFELD, B.: Backscattering Spectrometer with Adapted Q-Resolution at the Pulsed Neutron Source. In: SCHERM, R. (Ed.) ; STILLER, H. (Ed.): *Proceedings of the Workshop on Neutron Scattering Instrumentation for SNQ, Maria Laach, 3-5 Sept. 1984* Vol. 1954 Kernforschungsanlage Jülich (Org.), Kernforschungsanlage Jülich, October 1984, pp. 378–389. – Berichte der Kernforschungsanlage Jülich - Nr. 1954 Spallations-Neutronenquelle Jül-1954

[239] SCHERM, Reinhard H. ; KRÜGER, Eckhard: Bragg optics – focusing in real and *k*-space. In: *Nuclear Instruments and Methods in Physics Research Section A: Accelerators, Spectrometers, Detectors and Associated Equipment* 338 (1994), January, No. 1, pp. 1–8

[240] SCHÖNHALS, A. ; GOERING, H. ; SCHICK, Ch. ; FRICK, B. ; ZORN, R.: Polymers in nanoconfinement: What can be learned from relaxation and scattering experiments? In: *Journal of Non-Crystalline Solids* 351 (2005), September, No. 33, pp. 2668–2677. – Proceedings of 3rd International Conference on Broadband Dielectric Spectroscopy and its Applications

[241] SEARS, V. F.: Thermal-Neutron Scattering Lengths and Cross Sections for Condensed-Matter Reasearch / Atomic Energy of Canada Limited - Chalk River Nuclear Laboratories. 1984. – Research Report. AECL-8490

[242] SEARS, Varley F.: Neutron scattering lengths and cross sections. In: *Neutron News* 3 (1992), January, No. 3, pp. 26–37

[243] SEEBOTH, Arno (Ed.) ; LÖTZSCH, Detlef (Ed.): *Thermochromic and Thermotropic Materials*. New York : Pan Stanford, 2013

[244] SERGEYEV, Sergey ; PISULA, Wojciech ; GEERTS, Yves Henri: Discotic liquid crystals: a new generation of organic semiconductors. In: *Chemical Society Reviews* 36 (2007), No. 12, pp. 1902

[245] SHALAGINOV, A. N. ; HAZELWOOD, L. D. ; SLUCKIN, T. J.: Dynamics of chevron structure formation. II. Permeation-dominated phenomena. In: *Physical Review E* 60 (1999), October, No. 4B, pp. 4199–4209

[246] SHENG, Ping: Phase Transition in Surface-Aligned Nematic Films. In: *Physical Review Letters* 37 (1976), October, No. 16, pp. 1059–1062

[247] SHENG, Ping: Boundary-layer phase transition in nematic liquid crystals. In: *Physical Review A* 26 (1982), September, No. 3, pp. 1610–1617

[248] SHI, Wenqing ; FRIEDMAN, Alicia K. ; BAKER, Lane A.: Nanopore Sensing. In: *Analytical Chemistry* 89 (2017), January, No. 1, pp. 157–188

[249] SIMON, P. ; GOGOTSI, Y.: Capacitive Energy Storage in Nanostructured Carbon–Electrolyte Systems. In: *Accounts of Chemical Research* 46 (2013), May, No. 5, pp. 1094–1103

[250] SIMON, Patrice ; GOGOTSI, Yury: Materials for electrochemical capacitors. In: *Nature Materials* 7 (2008), November, No. 11, pp. 845–854

[251] SINGH, Ramesh ; MONK, Joshua ; HUNG, Francisco R.: A Computational Study of the Behavior of the Ionic Liquid [BMIM$^+$][PF$_6^-$] Confined Inside Multiwalled Carbon Nanotubes. In: *The Journal of Physical Chemistry C* 114 (2010), September, No. 36, pp. 15478–15485

[252] SINGH, Ramesh ; MONK, Joshua ; HUNG, Francisco R.: Heterogeneity in the Dynamics of the Ionic Liquid [BMIM$^+$][PF$_6^-$] Confined in a Slit Nanopore. In: *The Journal of Physical Chemistry C* 115 (2011), August, No. 33, pp. 16544–16554

[253] SINGWI, K. S. ; SJÖLANDER, Alf: Diffusive Motions in Water and Cold Neutron Scattering. In: *Physical Review* 119 (1960), August, No. 3, pp. 863–871

[254] SIWY, Zuzanna S. ; HOWORKA, Stefan: Engineered voltage-responsive nanopores. In: *Chemical Society Reviews* 39 (2010), pp. 1115–1132

[255] SKARP, K. ; HANDSCHY, M. A.: Ferroelectric Liquid Crystals. Material Properties and Applications. In: *Molecular Crystals and Liquid Crystals Incorporating Nonlinear Optics* 165 (1988), December, No. 1, pp. 439–509

[256] SON, Sang Jun ; BAI, Xia ; LEE, Sang Bok: Inorganic hollow nanoparticles and nanotubes in nanomedicine: Part 1. Drug/gene delivery applications. In: *Drug Discovery Today* 12 (2007), August, No. 15, pp. 650–656

[257] SOUSA, C. T. ; LEITAO, D. C. ; PROENCA, M. P. ; VENTURA, J. ; PEREIRA, A. M. ; ARAUJO, J. P.: Nanoporous alumina as templates for multifunctional applications. In: *Applied Physics Reviews* 1 (2014), No. 3, pp. 031102–1–031102–22

[258] SPRINGER, Tasso ; HÖHLER, G. (Ed.): *Springer Tracts in Modern Physics*. Vol. 64: *Quasielastic Neutron Scattering for the Investigation of Diffusive Motions in Solids and Liquids*. Springer-Verlag Berlin Heidelberg, 1972

[259] SRAJER, George ; PINDAK, Ron ; PATEL, Jay S.: Electric-field-induced layer reorientation in ferroelectric liquid crystals: An x-ray study. In: *Physical Review A* 43 (1991), May, No. 10, pp. 5744–5747

[260] STENNER, Charlotte ; SHAO, Li-Hua ; MAMEKA, Nadiia ; WEISSMÜLLER, Jörg: Piezoelectric Gold: Strong Charge-Load Response in a Metal-Based Hybrid Nanomaterial. In: *Advanced Functional Materials* 26 (2016), July, No. 28, pp. 5174–5181

[261] TAGUCHI, Akira ; SCHÜTH, Ferdi: Ordered mesoporous materials in catalysis. In: *Microporous and Mesoporous Materials* 77 (2005), January, No. 1, pp. 1–45

[262] TAKANISHI, Yoichi ; OUCHI, Yukio ; TAKEZOE, Hideo ; FUKUDA, Atsuo: Chevron Layer Structure in the Smectic A Phase of 8CB. In: *Japanese Journal of Applied Physics* 28 (1989), March, No. 3A, pp. L487–L489

[263] TANG, Jing ; LIU, Jian ; TORAD, Nagy L. ; KIMURA, Tatsuo ; YAMAUCHI, Yusuke: Tailored design of functional nanoporous carbon materials toward fuel cell applications. In: *Nano Today* 9 (2014), June, No. 3, pp. 305–323

[264] TELL, J. L. ; MARIS, H. J.: Specific heats of hydrogen, deuterium, and neon in porous Vycor glass. In: *Physical Review B* 28 (1983), November, No. 9, pp. 5122–5125

[265] THOMAS, John Meurig ; RAJA, Robert: Nanopore and nanoparticle catalysts. In: *The Chemical Record* 1 (2001), No. 6, pp. 448–466

[266] TIDSWELL, I. M. ; OCKO, B. M. ; PERSHAN, P. S. ; WASSERMAN, S. R. ; WHITESIDES, G. M. ; AXE, J. D.: X-ray specular reflection studies of silicon coated by organic monolayers (alkylsiloxanes). In: *Physical Review B* 41 (1990), January, No. 2, pp. 1111–1128

[267] TOKUDA, Hiroyuki ; ISHII, Kunikazu ; SUSAN, Md. Abu Bin Hasan ; TSUZUKI, Seiji ; HAYAMIZU, Kikuko ; WATANABE, Masayoshi: Physicochemical Properties and Structures of Room-Temperature Ionic Liquids. 3. Variation of Cationic Structures. In: *Journal of Physical Chemistry B* 110 (2006), February, No. 6, pp. 2833–2839

[268] TOKUDA, Hiroyuki ; TSUZUKI, Seiji ; SUSAN, Md. Abu Bin Hasan ; HAYAMIZU, Kikuko ; WATANABE, Masayoshi: How Ionic Are Room-Temperature Ionic Liquids? An Indicator of the Physicochemical Properties. In: *Journal of Physical Chemistry B* 110 (2006), October, No. 39, pp. 19593–19600

[269] TRIOLO, Alessandro ; MANDANICI, Andrea ; RUSSINA, Olga ; RODRIGUEZ-MORA, Virginia ; CUTRONI, Maria ; HARDACRE, Christopher ; NIEUWENHUYZEN, Mark ; BLEIF, Hans-Jurgen ; KELLER, Lukas ; RAMOS, Miguel Angel: Thermodynamics, Structure, and Dynamics in Room Temperature Ionic Liquids: The Case of 1-Butyl-3-methyl Imidazolium Hexafluorophosphate ([bmim][PF_6]). In: *Journal of Physical Chemistry B* 110 (2006), October, No. 42, pp. 21357–21364

[270] TRIOLO, Alessandro ; RUSSINA, Olga ; BLEIF, Hans-Jurgen ; DI COLA, Emanuela: Nanoscale Segregation in Room Temperature Ionic Liquids. In: *The Journal of Physical Chemistry B* 111 (2007), May, No. 18, pp. 4641–4644

[271] TSUZUKI, Seiji ; SHINODA, Wataru ; SAITO, Hiroaki ; MIKAMI, Masuhiro ; TOKUDA, Hiroyuki ; WATANABE, Masayoshi: Molecular Dynamics Simulations of Ionic Liquids: Cation and Anion Dependence of Self-Diffusion Coefficients of Ions. In: *Journal of Physical Chemistry B* 113 (2009), August, No. 31, pp. 10641–10649

[272] VATAMANU, Jenel ; BORODIN, Oleg ; OLGUIN, Marco ; YUSHIN, Gleb ; BEDROV, Dmitry: Charge storage at the nanoscale: understanding the trends from the molecular

scale perspective. In: *Journal of Materials Chemistry A* 5 (2017), No. 40, pp. 21049–21076

[273] VAUPOTIČ, N. ; KRALJ, S. ; ČOPIČ, M. ; SLUCKIN, T. J.: Landau–de Gennes theory of the chevron structure in a smectic liquid crystal. In: *Physical Review E* 54 (1996), October, No. 4, pp. 3783–3792

[274] VINEYARD, George H.: Scattering of Slow Neutrons by a Liquid. In: *The Physical Review* 110 (1958), June, No. 5, pp. 999–1010

[275] VINUTHA, N. ; USHA, M. K. ; SOMASHEKAR, R. ; REVANNASIDDAIAH, D.: Smectic translational order parameter in two liquid crystalline compounds. In: *Phase Transitions* 88 (2015), No. 5, pp. 540–546

[276] VOETS, G. ; DAEL, W. van: Investigation of the chirality dependence of thermal properties in chiral-racemic mixtures of the cholesteric ester CE6. In: *Liquid Crystals* 14 (1993), January, No. 3, pp. 617–627

[277] DE VRIES, Adriaan ; EKACHAI, Arun ; SPIELBERG, N.: Why the Molecules are Tilted in all Smectic A Phases, and How the Layer Thickness Can be Used to Measure Orientational Disorder. In: *Molecular Crystals and Liquid Crystals* 49 (1979), January, No. 5, pp. 143–152

[278] ŠKARABOT, M. ; KRALJ, S. ; BLINC, R. ; MUŠEVIČ, I.: The smectic A-smectic C* phase transition in submicron confined geometry. In: *Liquid Crystals* 26 (1999), May, No. 5, pp. 723–729

[279] ŠKARABOT, M. ; MUŠEVIČ, I. ; BLINC, R.: Solitonlike dynamics in submicron ferroelectric liquid-crystal cells. In: *Physical Review E* 57 (1998), June, No. 6, pp. 6725–6731

[280] WALLER, Ivar: Zur Frage der Einwirkung der Wärmebewegung auf die Interferenz von Röntgenstrahlen. In: *Zeitschrift für Physik* 17 (1923), No. 1, pp. 398–408

[281] WANG, Chun-Ta ; CHEN, Chun-Wei ; YANG, Tzu-Hsuan ; NYS, Inge ; LI, Cheng-Chang ; LIN, Tsung-Hsien ; NEYTS, Kristiaan ; BEECKMAN, Jeroen: Electrically assisted bandedge mode selection of photonic crystal lasing in chiral nematic liquid crystals. In: *Applied Physics Letters* 112 (2018), No. 4, pp. 043301–1–043301–4

[282] WANG, Liang ; XIAO, Feng-Shou: Nanoporous catalysts for biomass conversion. In: *Green Chemistry* 17 (2015), pp. 24–39

[283] WANG, Xiqing ; LIANG, Chengdu ; DAI, Sheng: Facile Synthesis of Ordered Mesoporous Carbons with High Thermal Stability by Self-Assembly of Resorcinol–Formaldehyde and Block Copolymers under Highly Acidic Conditions. In: *Langmuir* 24 (2008), July, No. 14, pp. 7500–7505

[284] WEBSTER, Richard E. ; MOTTRAM, Nigel J. ; CLEAVER, Douglas J.: Molecular simulation of chevrons in confined smectic liquid crystals. In: *Physical Review E* 68 (2003), August, No. 2, pp. 021706–1–021706–9

[285] WEINGARTH, Daniel ; DRUMM, Robert ; FOELSKE-SCHMITZ, Annette ; KÖTZ, Rüdiger ; PRESSER, Volker: An electrochemical in situ study of freezing and thawing of ionic liquids in carbon nanopores. In: *Physical Chemistry Chemical Physics* 16 (2014), No. 39, pp. 21219–21224

[286] WILLIAMS, C. E. ; KLEMAN, M.: Observation of edge dislocation lines in an A-phase smectic. In: *Le Journal de Physique - Lettres* 35 (1974), March, No. 3, pp. 33–35

[287] WU, Peng ; HUANG, Jingsong ; MEUNIER, Vincent ; SUMPTER, Bobby G. ; QIAO, Rui: Complex Capacitance Scaling in Ionic Liquids-Filled Nanopores. In: *ACS Nano* 5 (2011), November, No. 11, pp. 9044–9051

[288] XIANG, Jie ; VARANYTSIA, Andrii ; MINKOWSKI, Fred ; PATERSON, Daniel A. ; STOREY, John M. D. ; IMRIE, Corrie T. ; LAVRENTOVICH, Oleg D. ; PALFFY-MUHORAY, Peter: Electrically tunable laser based on oblique heliconical cholesteric liquid crystal. In: *Proceedings of the National Academy of Sciences* 113 (2016), November, No. 46, pp. 12925–12928

[289] XUE, Yahui ; MARKMANN, Jürgen ; DUAN, Huiling ; WEISSMÜLLER, Jörg ; HUBER, Patrick: Switchable imbibition in nanoporous gold. In: *Nature Communications* 5 (2014), July, pp. 4237

[290] YAMAMURO, Osamu ; YAMADA, Takeshi ; KOFU, Maiko ; NAKAKOSHI, Masamichi ; NAGAO, Michihiro: Hierarchical structure and dynamics of an ionic liquid 1-octyl-3-methylimidazolium chloride. In: *The Journal of Chemical Physics* 135 (2011), No. 5, pp. 054508–1–054508–7

[291] YANG, Haifeng ; SHI, Qihui ; LIU, Xiaoying ; XIE, Songhai ; JIANG, Decheng ; ZHANG, Fuqiang ; YU, Chengzhong ; TU, Bo ; ZHAO, Dongyuan: Synthesis of ordered mesoporous carbon monoliths with bicontinuous cubic pore structure of Ia3d symmetry. In: *Chemical Communications* (2002), No. 23, pp. 2842–2843

[292] YETHIRAJ, Anand ; BECHHOEFER, John: Using Nematic Director Fluctuations as a Sensitive Probe of the Nematic-Smectic-A Phase Transition in Liquid Crystals. In: *Molecular Crystals and Liquid Crystals Science and Technology. Section A. Molecular Crystals and Liquid Crystals* 304 (1997), No. 1, pp. 301–307

[293] YUNUS, Normawati M. ; MUTALIB, M. I. Abdul ; MAN, Zakaria ; BUSTAM, Mohamad Azmi ; MURUGESAN, T.: Thermophysical properties of 1-alkylpyridinum bis(trifluoromethylsulfonyl)imide ionic liquids. In: *The Journal of Chemical Thermodynamics* 42 (2010), April, No. 4, pp. 491–495

[294] ZELEŇÁK, Vladimír ; BEŇOVÁ, Eva ; ALMÁŠI, Miroslav ; HALAMOVÁ, Dáša ; HORNEBECQ, Virginie ; HRONSKÝ, Viktor: Photo-switchable nanoporous silica supports for controlled drug delivery. In: *New Journal of Chemistry* 42 (2018), pp. 13263–13271

[295] ZHAI, Yunpu ; DOU, Yuqian ; ZHAO, Dongyuan ; FULVIO, Pasquale F. ; MAYES, Richard T. ; DAI, Sheng: Carbon Materials for Chemical Capacitive Energy Storage. In: *Advanced Materials* 23 (2011), No. 42, pp. 4828–4850

[296] ZHANG, Rui ; HUA, Hong: Design of a polarized head-mounted projection display using ferroelectric liquid-crystal-on-silicon microdisplays. In: *Applied Optics* 47 (2008), May, No. 15, pp. 2888–2896

[297] ZHANG, Shiguo ; ZHANG, Jiaheng ; ZHANG, Yan ; DENG, Youquan: Nanoconfined Ionic Liquids. In: *Chemical Reviews* 117 (2017), May, No. 10, pp. 6755–6833

[298] ZHANG, Suojiang ; SUN, Ning ; HE, Xuezhong ; LU, Xingmei ; ZHANG, Xiangping: Physical Properties of Ionic Liquids: Database and Evaluation. In: *Journal of Physical and Chemical Reference Data* 35 (2006), October, No. 4, pp. 1475–1517

[299] ZHOU, B. ; IANNACCHIONE, G. S. ; GARLAND, C. W. ; BELLINI, T.: Random-field effects on the nematic–smectic-A phase transition due to silica aerosil particles. In: *Physical Review E* 55 (1997), March, No. 3, pp. 2962–2968

[300] ZHU, Da-Ming ; DASH, J. G.: Surface Melting and Roughening of Adsorbed Argon Films. In: *Physical Review Letters* 57 (1986), December, No. 23, pp. 2959–2962

[301] ZOLLIKER, Markus ; FISCHER, Stephan ; WHITE, Jon: *SINQ Wiki: Closed-CycleRefrigerators*. – URL `http://lns00.psi.ch/sinqwiki/Wiki.jsp?page=ClosedCycleRefrigerators`. – Paul Scherrer Institute, Villigen, Switzerland – accessed 2 August 2019

[302] ZORN, Reiner: Multiple scattering correction of neutron scattering elastic scans. In: *Nuclear Instruments and Methods in Physics Research Section A: Accelerators, Spectrometers, Detectors and Associated Equipment* 572 (2007), March, No. 2, pp. 874–881

[303] ZORN, Reiner: On the evaluation of neutron scattering elastic scan data. In: *Nuclear Instruments and Methods in Physics Research Section A: Accelerators, Spectrometers, Detectors and Associated Equipment* 603 (2009), May, No. 3, pp. 439–445

[304] ZWETKOFF, W.: Über die Molekülanordnung in der anisotrop-flüssigen Phase. In: *Acta Physicochimica U.R.S.S.* 16 (1942), No. 3-4, pp. 132–147

List of Figures

List of Tables

List of own publications

Publications in peer-reviewed journals

A. In direct relation to the dissertation

1 **Ionic liquid dynamics in nanoporous carbon: A pore-size- and temperature-dependent neutron spectroscopy study on supercapacitor materials**
M. Busch, T. Hofmann, B. Frick, J. P. Embs, B. Dyatkin & P. Huber
[under review] (2019).

2 **A ferroelectric liquid crystal confined in cylindrical nanopores: Reversible smectic layer buckling, enhanced light rotation and extremely fast electro-optically active Goldstone excitations**
M. Busch, A. V. Kityk, W. Piecek, T. Hofmann, D. Wallacher, S. Całus, P. Kula, M. Steinhart, M. Eich & P. Huber
Nanoscale **9** (48), 19086–19099 (2017).

3 **Chiral Phases of a Confined Cholesteric Liquid Crystal: Anchoring-Dependent Helical and Smectic Self-Assembly in Nanochannels**
S. Całus, M. Busch, A. V. Kityk, W. Piecek & P. Huber
The Journal of Physical Chemistry C **120** (21), 11727–11738 (2016).

B. Without direct relation to the dissertation

1 **Natural and Chemically Modified Post-Mining Clays — Structural and Surface Properties and Preliminary Tests on Copper Sorption**
B. Jabłońska, M. Busch, A. V. Kityk & P. Huber
Minerals **9** (11), 704 (2019).

2 **The structural and surface properties of natural and modified coal gangue**
B. Jabłońska, A. V. Kityk, M. Busch & P. Huber
Journal of Environmental Management **190**, 80–90 (2017).

3 **Hydraulic transport across hydrophilic and hydrophobic nanopores: Flow experiments with water and *n*-hexane**
S. Gruener, D. Wallacher, S. Greulich, M. Busch & P. Huber
Physical Review E **93** (1), 013102-1–013102-13 (2016).

4 **Thermotropic interface and core relaxation dynamics of liquid crystals in silica glass nanochannels: a dielectric spectroscopy study**
S. Całus, L. Borowik, A. V. Kityk, M. Eich, M. Busch & P. Huber
Physical Chemistry Chemical Physics **17** (34), 22115–22124 (2015).

5 **High-resolution dielectric study reveals pore-size-dependent orientational order of a discotic liquid crystal confined in tubular nanopores**
S. Całus, A. V. Kityk, L. Borowik, R. Lefort, D. Morineau, C. Krause, A. Schönhals, M. Busch & P. Huber
Physical Review E **92** (1), 012503-1–012503-6 (2015).

6 **Paranematic-to-nematic ordering of a binary mixture of rodlike liquid crystals confined in cylindrical nanochannels**
S. Całus, B. Jabłońska, M. Busch, D. Rau, P. Huber & A. V. Kityk
Physical Review E **89** (6), 062501-1–062501-12 (2014).

7 **Thermotropic orientational order of discotic liquid crystals in nanochannels: an optical polarimetry study and a Landau–de Gennes analysis**
A. V. Kityk, M. Busch, D. Rau, S. Całus, C. V. Cerclier, R. Lefort, D. Morineau, E. Grelet, C. Krause, A. Schönhals, B. Frick & P. Huber
Soft Matter **10** (25), 4522–4534 (2014).

8 **Towards bio-silicon interfaces: Formation of an ultra-thin self-hydrated artificial membrane composed of dipalmitoylphosphatidylcholine (DPPC) and chitosan deposited in high vacuum from the gas-phase**
M. J. Retamal, M. A. Cisternas, S. E. Gutierrez-Maldonado, T. Pérez-Acle, B. Seifert, M. Busch, P. Huber & U. G. Volkmann
Journal of Chemical Physics **141** (10), 104201-1–104201-7 (2014).

9 **Thermotropic nematic order upon nanocapillary filling**
P. Huber, M. Busch, S. Całus & A. V. Kityk
Physical Review E **87** (4), 042502-1–042502-6 (2013).

Bookchapter

1 **Liquid Crystals Confined in Nanoporous Solids: From Fundamentals to Functionalities**
P. Huber, K. Sentker, M. Busch & A. V. Kityk
Chapter 11 in *Soft Condensed Matter on the Nanoscale: The WSPC Reference On Functional Nanomaterials*, Volume 2: *Soft Matter Under Confinements and at the Interfaces* (2020).

Conference contributions in direct relation to the dissertation

(presenting author underlined)

1 **Smectic C* layer buckling and fast electro-optics of a LC confined in anodic aluminium oxide nanochannels** *(talk)*
M. Busch, A. V. Kityk, T. Hofmann, D. Wallacher, and P. Huber
45th German liquid crystal conference, Luxembourg (March 2018).

2 **Reversible smectic layer buckling of a ferroelectric liquid crystal confined in anodic aluminium oxide nanochannels** *(talk)*
M. Busch, A. V. Kityk, T. Hofmann, D. Wallacher, and P. Huber
Frühjahrstagung der Deutschen Physikalischen Gesellschaft (Sektion kondensierte Materie), Regensburg (March 2018).

3 **Quasi-elastic neutron scattering study of a room-temperature ionic liquid confined in nanoporous carbon** *(talk)*
M. Busch, P. Huber & T. Hofmann
QENS 2016 (14th International conference on applications of quasielastic neutron scattering), Potsdam (September 2016).

4 **Quasi-elastic neutron scattering study of an ionic liquid confined in nanoporous carbon** *(invited talk)*
M. Busch, T. Hofmann, B. Dyatkin, Y. Gogotsi, A. Kornyshev, J. Embs, B. Frick & P. Huber
Frühjahrstagung der Deutschen Physikalischen Gesellschaft (Sektion kondensierte Materie), Regensburg (March 2016).